# ADVANCED CT-BASED RESERVOIR CHARACTERISATION FOR $CO_2$ STORAGE:

# MULTI-SCALE ANALYSIS AND GEOMECHANICAL MODELING OF TÁZLÁR FIELD, HUNGARY

A Dissertation Submitted for the Degree of Doctor of Philosophy

By

**Gábor Pál Veres**
MS Petroleum Engineer, Economist

Scientific supervisor:
Dr. István Szunyog

Industrial supervisor:
Dr. Béla Kelemen

MIKOVINY SÁMUEL DOCTORAL SCHOOL OF EARTH SCIENCES
Head of the doctoral school: Prof. Dr. Péter Szűcs

Budapest, Hungary
2025

# TABLE OF CONTENTS

# TABLE OF FIGURES

# TABLE OF TABLES

# Scientific Supervisor's recommendation for doctoral (PhD) thesis of

**Gábor Pál VERES**

Advanced CT-based reservoir characterization for $CO_2$ storage:
Multi-scale analysis and geomechanical modeling of the Tázlár field, Hungary

The fight against climate change is a top priority for the European Union and Hungary. In order to achieve this, a package of measures and spectacular emission reduction indicators have been formulated in several areas. The most important climate strategic goal is to reduce carbon dioxide emissions, which cannot be achieved on an industrial scale yet, or only with a very significant financial sacrifice. An alternative is the capture of carbon dioxide produced during the industrial processes and its storage in depleted hydrocarbon fields. One of Hungary's largest energy companies has also embarked on this path and has started to explore storage options. It has not yet been implemented, it is currently a pilot project plan. In order to be able to achieve this technically and to keep the stored carbon dioxide safely in the designated layer for many decades, complex geological and reservoir mechanical investigations are necessary.

In the framework of this thesis, the Candidate undertook to complement the traditional rock testing procedures with a novel possibilities provided by human CT and microCT, and to analyze the results obtained in this way with the help of a reservoir mechanical modeling software. The aim of the investigations was not to fully assess and re-evaluate the selected field, but to develop a new methodology that can be used to update and refine the currently known storage data. The complex modeling of the field is a very significant task, not a “one-man” task, so its complete analysis and interpretation was not a set goal in the available time interval. A further goal was to develop the test procedure based on real data, so the rock samples used for the measurements actually came from the examined reservoir. It was not possible to analyze all storage and overhead rock sections of each well, as the core samples were no longer fully available. The available 23 samples were further selected in order to ensure that all characteristic extreme parameters are represented among the examined data. Laboratory porosity and permeability measurements were also carried out, as well as planned carbon dioxide flooding tests. These measurements were supplemented and raised to a new dimension by static and dynamic flood testing with human CT and microCT. The resulting refined rock physics parameters were fed into the dynamic modeling software, as a result of which the currently known parameters of the field could be further refined. Based on this, new conclusions and findings could be outlined.

The direction of the research has changed continuously over the years, partly because of the industrial background, and partly because of the cost-intensive laboratory and simulation tests presented in the thesis. In the thesis, a new test concept for the storage of carbon dioxide was developed, which provides a more accurate picture of the physical processes taking place in the rock not only on the basis of traditional but also on CT scans. In my opinion, the developed method is novel, but its clarification and further validation will mean new tasks for industry and researchers. A D1 (SJR) international publication has also been published on the topic of the thesis.

The Candidate summarized his research work in five thesis points. The structure of the PhD thesis is logical, it follows the individual phases of the research work. The formulations, interpretations and conclusions used are clear, and the format of the dissertation is appropriate. The available measurement results created a significant amount of databases, which significantly increased the scope of the thesis. In my opinion, the dissertation can also be applied in industrial practice, and it contains new scientific results that significantly clarify the existing data. The results of the research clearly prove the Candidate's high-quality professional knowledge and suitability for independent research work.

It can be stated that the PhD thesis contains new scientific results based on credible data, and the thesis meets the content and formal requirements of the Mikoviny Sámuel Doctoral School of Earth Sciences in all respects. The supervisor recommends that the dissertation be submitted for public defense and that the Candidate be awarded the title of PhD.

Miskolc, 29 August 2025

**István SZUNYOG (PhD)**
Associate Professor
Scientific Supervisor

# Industrial Supervisor's recommendation for doctoral (PhD) thesis of

**Gábor Pál VERES**

Advanced CT-Based Reservoir Characterization for $CO_2$ Storage:
Multi-Scale Analysis and Geomechanical Modeling of Tázlár Field, Hungary

One of the greatest global challenges of our time is climate change, namely, how to stop it. The almost unlimited and ever-increasing emissions of greenhouse gases – primarily $CO_2$ and $CH_4$ – are one of the main reasons of this trend. Reducing $CO_2$ emissions seems to be a mission impossible task for now, but even stopping the growth has only been possible for a while. Among the world's primary energy sources, fossil energy sources still represent over 80%, resulting annually ca 35 billion tons $CO_2$ emissions. According to our current knowledge, the only certain point of the energy transition is that there will be no silver bullet, no single solution and no single type of energy that will replace fossil energy sources. That is why, every step that reduces the atmospheric concentration of greenhouse gases contributes to the ultimate goal of stopping climate change.
CCS technology (Carbon Capture and Storage) may be one of these solutions. No matter how simple the technology is, which involves capturing $CO_2$, transporting the enriched gas and storing it in depleted hydrocarbon fields - there are many technological uncertainties and unknown factors in a scientific sense. One of these is the long-term behaviour of $CO_2$ in depleted fields, its "sustainability" measured in years, hundreds or thousands of years.

The candidate started from the examination of the hydrogen value chain, which is extremely important for the oil and gas industry. Methane-based hydrogen production accounts for 30-40% of a petroleum refinery's $CO_2$ emissions and is essential for the production of sulphur-free fuels. At the same time, the concentration of $CO_2$ in the by-product is relatively high (30+%), which facilitates the capture of $CO_2$.

However, mapping the entire process and answering its scientific questions went far beyond the scope of a doctoral thesis. Thus, by coordinating the methods outlined in the title, the candidate finally developed a new approach for the evaluation and selection of potential fields for $CO_2$ storage. The annual amount to be stored was determined in accordance with the strategy of the MOL Group and company commitment towards the state and it was taken into account during the work.

Through specific samples of a specific field, he scientifically analyzed the behaviour of the rock and $CO_2$ gas, their interaction under static and dynamic conditions, using the most modern tools (CT, microCT and simulation software).
He managed some measurements to a limited extent due to their complexity and cost, but these also provided sufficient data to substantiate the theses.

The thesis estimates extremely important parameters from an industrial perspective with scientific rigor, under laboratory conditions, and supports them with measurements. The most important of these are the volume, which can be stored, the critical pressure that can lead to cracking of the cap rock, the duration that represents the optimal time for storage, and the possibility of damage to the rocks, which can be related to the long-term “stability” of the storage facility. It seems clear that the measurement system compiled by the candidate, although expensive, allows for the evaluation of the fields in terms of $CO_2$ storage, and leads a better and more complex understanding.

The thesis is written with sufficient precision, the figures suggest a demanding execution, and all this is backed by thorough literature. During the doctoral work, he not only fulfilled his university teaching duties, but also published his results in significant journals. Based on this, as an industrial consultant, I clearly recommend the thesis to be submitted for public discussion and the candidate be awarded a doctoral degree after its success.

Budapest, 29 August 2025.

Dr. Béla Kelemen
Industrial Supervisor
MOL Nyrt.
VP Business Excellence

# 1. LIST OF ABBREVIATIONS

| | | |
|---|---|---|
| BHP | - | Bottom Hole Pressure |
| CBM | - | Coal Bed Methane |
| CCS | - | Carbon Capture and Storage |
| CCUS | - | Carbon Capture, Utilization, and Storage |
| $CH_4$ | - | Methane |
| $CO_2$ | - | Carbon-dioxide |
| CT | - | Computed Tomography (human) |
| DRP | - | Digital Rock Physics |
| EGR | - | Enhanced Gas Recovery |
| EGS | - | Enhanced Geothermal System |
| EOR | - | Enhanced Oil Recovery |
| EWR | - | Enhanced Water Recovery |
| EU | - | European Union |
| FDD | - | Focus-Detector Distance |
| FEM | - | Finite Element Method |
| GHG | - | Greenhouse Gas |
| H.U. | - | Hounsfield Unit |
| He | - | Helium |
| IEA | - | International Energy Agency |
| IPCC | - | Intergovernmental Panel on Climate Change |
| mCT | - | Micro Computed Tomography |
| MIP | - | Mercury Intrusion Porosimeter |
| MMV | - | Monitoring, Measurement, and Verification |
| $N_2$ | - | Nitrogen |
| NMR | - | Nuclear Magnetic Resonance |
| OGIP | - | Original Gas in Place |
| OOIP | - | Original Oil in Place |
| PVT | - | Pressure-Volume-Temperature |
| SEM | - | Scanning Electron Microscopy |
| UCS | - | Uniaxial Compressive Strength |
| UoM | - | University of Miskolc |
| $tCO_2e$ | - | Tons of carbon dioxide equivalent |
| 3D | - | Three-Dimensional |

# 2. ABSTRACT

Climate change mitigation is among the major technical and policy challenges of the 21st century. Atmospheric carbon dioxide ($CO_2$) concentrations have increased from pre-industrial levels of approximately 280 parts per million (ppm) to over 415 ppm in recent years. This rise underscores the need for effective carbon capture and storage (CCS) technologies as part of broader emission reduction strategies aligned with international climate agreements.

This dissertation presents a multidisciplinary study integrating advanced computed tomography (CT) techniques with geomechanical modeling to evaluate $CO_2$ sequestration potential in depleted hydrocarbon reservoirs. The research focuses on the Tázlár field in Hungary's Pannonian Basin, applying multi-scale characterization across four orders of magnitude in spatial resolution to assess storage capacity, containment integrity, and long-term behavior of injected $CO_2$.

High-resolution X-ray micro-computed tomography (mCT) with spatial resolution of 0.0097 mm enabled detailed analysis of pore structures, mineral distributions, and rock-fluid interactions under reservoir conditions typical of the Tázlár field (~ 200 bar pressure, ~100°C temperature). Standard CT imaging at 0.21 x 0.21 x 0.6 mm resolution complemented this by characterizing core-scale heterogeneity across 18 samples from five wells at depths of 1,833–2,138 meters.

Laboratory experiments on selected core samples showed methane ($CH_4$) recovery rates of 87–95% via $CO_2$ injection under near-miscible displacement conditions. Approximately 60–75% of the injected $CO_2$ remained stored through residual trapping mechanisms. Three-dimensional saturation visualizations revealed fluid distribution patterns and flow pathways relevant to field-scale injection modeling.

Characterization of three lithological units—metamorphic basement rocks (average porosity 0.29%, mean Hounsfield value 2,117 HU), breccia units (average porosity 3.45%, mean Hounsfield value 2,012 HU), and sandstone reservoirs (average porosity 5.48%, mean Hounsfield value 1,828 HU)—provided input parameters for geomechanical simulations using tNavigator software. Sensitivity analyses of Young's modulus (5–50 GPa), Poisson's ratio (0.15–0.45), friction angle (20–45°), and cohesion (5–50 MPa) helped define safe operational limits for $CO_2$ injection.
Modeling results indicated mechanical stability of reservoir and cap rock formations under injection pressures below 200 bar, with no mechanical failure observed across scenarios with friction angles above 0°. Optical microscopy identified $CO_2$-rock interactions,

including fracture development and selective mineral dissolution (notably of plagioclase feldspars), while quartz remained stable under exposure conditions.

The integrated analysis estimates a $CO_2$ storage capacity of ~7 million tons, with structural and residual trapping mechanisms dominating initially, followed by gradual increases in solubility and mineral trapping over time. The findings support the technical feasibility of commercial-scale CCS deployment in the Pannonian Basin and contribute to Hungary's climate neutrality goals while enhancing understanding of subsurface $CO_2$ dynamics.

# 3. ÖSSZEFOGLALÓ

A klímaváltozás elleni küzdelem a 21. század egyik legjelentősebb kihívását jelenti, amelyben az atmoszférikus szén-dioxid ($CO_2$) koncentráció a preindusztriális körülbelül 280 milliomod részről (ppm) napjainkra, 415 ppm feletti szintre emelkedett. Ez a drasztikus növekedés szükségessé teszi a szén-dioxid-leválasztási és -tárolási (CCS) technológiák fejlesztését és alkalmazását az átfogó kibocsátáscsökkentési stratégiák részeként, a nemzetközi klímamegállapodásokkal összhangban, a globális hőmérséklet-emelkedés korlátozása érdekében.

Ez a disszertáció egy multidiszciplináris vizsgálatot mutat be, amely fejlett számítógépes tomográfiás (CT) technikákat ötvöz kifinomult geomechanikai modellezéssel, hogy betekintést nyújtson a kimerült szénhidrogén-tárolókban történő $CO_2$ megkötés lehetőségeibe. A kutatás a magyarországi Pannon-medencében található Tázlár mezőre összpontosít, térbeli felbontásban négy nagyságrendet átfogó többléptékű jellemzést alkalmazva a tárolókapacitás, a tárolás biztonsága és a besajtolt $CO_2$ hosszú távú viselkedésének értékelésére.

A 0,0097 mm-es térbeli felbontást elérő nagy felbontású röntgen mikroszámítógépes tomográfiás (mCT) elemzés lehetővé tette a pórusszerkezet, az ásványeloszlás és a kőzet-folyadék kölcsönhatások részletes vizsgálatát a Tázlár mezőre jellemző tárolási körülmények között (~200 bar nyomás, ~100°C hőmérséklet). A 0,21 x 0,21 x 0,6 mm felbontású standard CT-mérések kiegészítő elemzést biztosítottak a maglléptékű heterogenitásról 18 magmintán keresztül, amelyek öt kútból származnak 1 833-2 138 méteres mélységtartományban.

A kiválasztott magmintákon végzett laboratóriumi kísérletek, melyek során metán és $CO_2$ elárasztás történt, a kiszorítási folyamatok során bekövetkező telítettségi változások háromdimenziós vizualizációja összetett folyadékeloszlási mintázatokat és preferenciális áramlási útvonalakat tárt fel, amelyek kritikus fontosságúak a mezőléptékű besajtolási viselkedés megértéséhez.

Három különböző litológiai egység átfogó jellemzése—metamorf alapkőzetek (átlagos porozitás 0,29%, átlagos Hounsfield-érték 2 117 HU), breccsa egységek (átlagos porozitás 3,45%, átlagos Hounsfield-érték 2 012 HU) és homokkő tárolók (átlagos porozitás 5,48%, átlagos Hounsfield-érték 1 828 HU) —alapvető paramétereket biztosított a fejlett tNavigator szoftverrel történő geomechanikai modellezéshez. A Young-modulus (5-50 GPa), a Poisson-arány (0,15-0,45), a súrlódási szög (20-35°) és a kohézió

(5-50 MPa) hatásait vizsgáló érzékenységi elemzés meghatározta a $CO_2$-besajtolás biztonságos üzemeltetési paramétereit.

A geomechanikai modellezési eredmények megerősítették a tároló és fedőkőzet formációk mechanikai stabilitását a $CO_2$-besajtolási műveletek során, ahol a taroló 200 bar rétegnyomás alatti tartása megakadályozta a mechanikai tönkremenetelt minden modellezési változatban, ahol a súrlódási szög > 0°. Az optikai mikroszkópos vizsgálatok kiértékelése dokumentálta a $CO_2$ kőzet kölcsönhatásokat, feltárva a fokozott repedésfejlődést és a szelektív ásványi oldódást, különösen a plagioklász földpátok esetében, miközben megerősítette a kvarc stabilitását $CO_2$-expozíciós körülmények között.

Az integrált értékelés konzervatív becslések alapján jelentős, ~ 7 millió tonnás $CO_2$-tárolási kapacitást jelez (~3,3 milliárd $nm^3$), ahol a strukturális és maradványos csapdázódás dominál a korai szakaszokban, majd az oldhatósági és ásványi csapdázódás fokozatos növekedése következhet be hosszabb időtávokon. A kutatás átfogó technikai keretrendszereket hoz létre a kereskedelmi léptékű CCS megvalósításához a Pannon-medence régióban, hozzájárulva Magyarország klímasemlegességi célkitűzéseihez, miközben előmozdítja a felszín alatti $CO_2$ viselkedés nemzetközi megértését.

# 4. INTRODUCTION AND RESEARCH OBJECTIVES

## 4.1 BACKGROUND AND GLOBAL CONTEXT

The European Climate Law, a key component of the European Green Deal, aims to achieve climate neutrality in the European Union (EU) by 2050. This overview highlights the primary objectives, mechanisms, and provisions of the law, underscoring the EU's commitment to reducing greenhouse gas emissions and enhancing adaptive measures. The necessity of such legislation is emphasized by historical increases in atmospheric $CO_2$ levels and the urgent global need to mitigate climate change effects. (European Climate Law, 2021). Since the late 18th century, industrial activities have significantly increased atmospheric $CO_2$ levels, rising from 280 parts per million (ppm) before the industrial revolution to an unprecedented 415 ppm in 2019 (IPCC, 2019). Major sources of $CO_2$ include large fossil fuel power stations, cement and steel manufacturing plants, biomass energy operations, and synthetic fuel facilities. These elevated $CO_2$ levels, along with other greenhouse gases, have led to a global rise in land and ocean surface temperatures, which are now approximately 1.0°C above pre-industrial levels, with a range of 0.8°C to 1.2°C (IPCC, 2019). According to the latest United Nations Intergovernmental Panel on Climate Change (IPCC) report, urgent and effective measures are needed globally to limit the temperature rise to 1.5°C by 2050 to prevent catastrophic consequences (IPCC, 2019).

The European Climate Law is central to the EU's strategy to confront these challenges, being an integral part of the European Green Deal framework. The law legally commits the EU to achieve climate neutrality by 2050, establishing intermediate targets and comprehensive measures to ensure progress and adaptability.
In line with European Climate Law, the Ministry of Innovation and Technology (ITM) of Hungary released the finalized energy and climate policy strategy documents, outlining Hungary’s short- and long-term energy strategies. The primary objectives of this strategy align with the European Council's conclusions from 12 December 2019, which emphasize increasing global climate action. In accordance with the Paris Agreement, Hungary has committed to reducing its GHG emissions by at least 40% by 2030 compared to 1990 levels (93.7 million $tCO_2e$). This commitment will shape the Hungarian energy sector and the most energy-intensive industries for the foreseeable future. (Veres, 2021)

One of the most promising strategies to enhance $CO_2$ capture and reduce atmospheric emissions is Carbon Capture Utilization and Storage (CCUS). This approach involves injecting large quantities of $CO_2$ into deep underground formations, either to boost the extraction of fossil fuels and other natural resources or to permanently store the $CO_2$.

CCUS is considered one of the best available technologies to significantly increase $CO_2$ sequestration and curb emissions into the atmosphere (Bachu and Adams, 2003).
CCUS necessitates capturing $CO_2$ from major point sources, such as fossil fuel power plants, and storing it in the subsurface for periods spanning hundreds to thousands of years. According to the IPCC, achieving emission reduction targets is infeasible without the implementation of CCUS.

Potential geological formations suitable for CCUS include oil and gas reservoirs, deep saline aquifers, salt caverns, and not mineable coal beds.
In Hungary, the application of CCS technology is primarily feasible in depleted hydrocarbon reservoirs. These geological formations offer potential storage sites due to their prior use in storing hydrocarbons, which suggests they have suitable structural integrity and capacity for $CO_2$ sequestration. Effective CCS implementation could significantly contribute to Hungary's climate goals by reducing $CO_2$ emissions from industrial sources.

Depleted hydrocarbon fields are considered optimal for CCS due to their proven capacity to contain fluids over geological timescales. These reservoirs typically have the necessary porosity and permeability to store $CO_2$ efficiently.
Recent studies indicate that Hungary's Pannonian Basin, which has been heavily exploited for hydrocarbon production, presents significant opportunities for $CO_2$ storage. The structural geology and existing infrastructure in these fields can be utilized for CCS (Szabó et al., 2020).

Preliminary assessments suggest that the storage capacity of Hungary's depleted hydrocarbon fields could be substantial. For instance, the Algyő field, one of the largest oil fields in Hungary, has been identified as a promising site for long-term $CO_2$ storage (Szabó et al., 2019). There are other promising fields in Hungary, where further investigation needed, from capacity, HSE and technical point of view. To have a clarified storage capacity and well-known caprock and storage reservoir material composition and structure is essential.
Implementing CCS in Hungary will require advancements in monitoring and verification technologies to ensure the safety and efficacy of $CO_2$ storage. (European Commission, 2019).

To understand the CCUS limitations, the migration patterns of injected $CO_2$ and the interactions between $CO_2$, and the formation rocks, also the wellbore cement is vital for estimating storage capacity and predicting the long-term stability of the stored $CO_2$

(Cheng et al., 2016; Scherer et al., 2005; Steefel et al., 2013; Zhang et al., 2011). Thus, advanced techniques are required to analyze the pore structure, wettability, and mineralogical composition of these materials when exposed to $CO_2$. Various characterization methods are available, all relevant will be introduced in the next chapters. The area has many exciting and research-worthy topics. In this thesis, the previously unexplored parameters of a depleted gas field in Hungary are examined. Utilizing available resources, laboratory and field results are combined with digital simulations and findings in an attempt to reach new and previously unestablished conclusions. The results obtained should only be interpreted with due caution and under appropriate conditions. The following chapters provide a theoretical overview and methodological descriptions, followed by a detailed presentation of the structure and content of the dissertation.

## 4.2 RESEARCH OBJECTIVES

The objectives aim to address knowledge gaps in geological $CO_2$ sequestration processes, focusing on depleted gas reservoirs with complex pore structures and heterogeneous properties. The research integrates scientific investigation with engineering applications, enhancing both theoretical understanding and technological progress in carbon capture and storage. This research focuses on the geological and technical aspects of $CO_2$ injection and storage, specifically reservoir characterization, storage mechanisms, and operational feasibility. Although economic and regulatory considerations are mentioned, detailed economic modeling and policy analysis are beyond this dissertation's scope.

The research objectives are processed by identifying the importance of the designated area as described in Chapter 4.1, in agreement and in line with the medium and long-term goals and strategy of my workplace, MOL Plc. According to these goals, it is also important for the company to reduce its $CO_2$ emissions and carbon footprint in the coming years and decades. There are numerous areas for development and opportunities in line with this objective. My previous studies and the intersection of the company's objectives have resulted in an upstream-relevant research topic, and this thesis is the final product of it.

A fundamental aspect of the research was to ensure that the theoretical data and measurements would enable practical findings and conclusions to be drawn.

At the inception of my doctoral studies, I was a member of a project team investigating the potential of CCS in Hungary. The extant knowledge, conclusions, and decisions available at that time were used as a basis for narrowing down the research area. At the time, the

most promising depleted hydrocarbon field in Hungary was identified based on our existing knowledge.

The initial phase of the research focused on acquiring knowledge about the available information within the company, as well as on the processing of production data and geological information. These will be summarized in the following chapters.

A thorough review of the extant literature on the selected field revealed the necessity of additional laboratory measurements on core samples to attain a more profound understanding of the field. The available drilling core samples were extracted during the 1970s and have since been stored at the core repository in Szolnok. Due to the inherent challenges associated with their long-term preservation, particular attention had to be devoted to reassessing their current condition and identifying viable measurement opportunities. Then must be accepted; no new samples were available for this research. The present study involved the analysis of 18 distinct core samples.

The laboratory measurements were determined, so that their results could be used as inputs for various types of computer modeling. Another objective and subject of this phase of the research was to model the reactions occurring in reality on a laboratory scale. Consequently, at the University of Miskolc, the drill core samples were prepared and the mineral composition of the samples taken from them was examined. Subsequent to the preparation stage, the core samples were subjected to a process of "static" $CO_2$ injection, thereby simulating the various processes presumed to occur in a real-world laboratory setting.

The scope of the research endeavors entailed the meticulous measurement of the physical parameters of diverse rock specimens in their initial and final states. This was followed by a comparative analysis of these parameters, with a view to explaining the mineral transformations that transpired between the initial and final states.

Parallel, CT scans were conducted to ascertain the physical parameters of the rocks through an alternative method. Given the physical parameters of the rock identified in this study, the drill core sample that was subjected to the so-called dynamic $CO_2$ flooding test was selected for analysis. This investigation was conducted by means of mCT, a technique that facilitated the observation of fluid flow in various phases. It also provided an opportunity to modify and refine the correlations based on practical experience. It is important to emphasize that, due to their physical extent and duration, these measurements are only suitable for drawing conclusions about the field under strict boundary conditions.

The findings from the laboratory measurements also enabled the creation of new digital models, thereby facilitating the updating of existing ones. The field history fit was derived based on field data, including production history and reservoir pressure measurements. This was accomplished by using the PETEX software package and Irap RMS. The initial fit was refined using laboratory data. This previous fit subsequently served as the foundation for the dynamic model that was devised in the tNavigator program by Rock Flow Dinamics®. The utilization of this software enabled the execution of simulations that addressed the geomechanical stability of the site. The structure and updating of the fundamental model, the recognized parameters relating to the site — such as the location of wells, geological layer sequences, perforation locations, etc.—were also an integral part of the research. The creation of a model with more realistic and extreme scenarios was informed by the available knowledge and data. Simulations were conducted and the results were evaluated. No one had ever done this kind of simulation at the site before, so the conclusions were drawn from them promised new results under the previously mentioned boundary conditions. This was particularly evident in the initial estimation of the hydrocarbon depletion process and the desired $CO_2$ injection into the depleted field.

The research work, which encompasses the previously mentioned subjects, was conducted over the course of several years, involving measurements and simulations. The subsequent chapters offer a comprehensive presentation of the research findings, accompanied by a thorough exposition of the theoretical foundations and practical applications.

# 5. LITERATURE REVIEW

## 5.1 THEORETICAL INTRODUCTION OF CARBON CAPTURE AND STORAGE

### 5.1.1 CARBON CAPTURE AND STORAGE – IN GENERAL

The International Energy Agency (IEA) projects that carbon capture and storage (CCS) could independently account for about a 19% reduction in global $CO_2$ emissions by 2050; in the absence of CCS, the cost of achieving $CO_2$ emission reduction targets would rise by 70% ("IEA - Publication:-Technology Roadmap: Carbon Capture and Storage," 2019). This highlights the economic importance of CCS in reducing $CO_2$ emissions and addressing climate change (Sharma et al., 2021). There are 51 CCS projects planned worldwide, with most located in Western Europe, China, North America, and Australia, yet only 19 are currently operational (GCCSI, 2019). Expanding existing CCS projects and initiating new ones are essential steps toward a sustainable future.

Currently, fossil fuels are the dominant source meeting global energy requirements, supporting economic growth and being indispensable for electricity generation, agriculture, industry, and transportation. The rapid pace of economic development has resulted in an unprecedented rise in fossil fuel consumption, which is the chief contributor to $CO_2$ emissions (Patra et al., 2021). CCS involves the capture of $CO_2$ from major emission sources such as cement plants, steel mills, fossil-fuel power stations, and oil refineries, followed by secure and efficient storage, thereby preventing large quantities of $CO_2$ from exerting adverse effects on the global environment (Francis et al., 2023).

There are several technical approaches for carbon capture, including chemical looping combustion (CLC) (Alalwan and Alminshid, 2021), pre-combustion, oxy-fuel combustion, and post-combustion capture, with the selection depending on the type of fuel and the characteristics of the combustion exhaust gases (Dixit et al., 2022).

In post-combustion capture, $CO_2$ is separated from the flue gas after burning a carbon-based fuel, with $CO_2$ concentrations ranging from 3 to 20 vol% (Liu et al., 2020). The pre-combustion method partially converts a carbonaceous fuel into syngas, allowing $CO_2$ to be captured at concentrations between 15 and 60 vol% (Zhou et al., 2021). Oxy-fuel combustion utilizes pure oxygen instead of air, generating a flue gas with up to 90 vol% $CO_2$, which is the basis for this capture technique (Koohestanian and Shahraki, 2021). CLC operates in two stages: first, fossil fuels are oxidized by oxygen from a metal oxide, producing $CO_2$ and water; after condensing the water, $CO_2$ is captured, and the

metal oxide is regenerated in the second stage, resulting in a $CO_2$ stream of 100% purity (Alalwan and Alminshid, 2021).

Once $CO_2$ has been captured, it must be transported either to storage sites or to facilities for industrial use. Pipelines are generally considered the most efficient and cost-effective means for transporting large amounts of $CO_2$ over long distances (Liu et al., 2020). These transportation networks deliver the $CO_2$ to storage or sequestration sites, which may include mineral carbonation, underground geological formations, or ocean sequestration.

CCS is recognized as a sustainable, low-carbon energy technology that is rapidly advancing to mitigate the growing climate crisis. This review comprehensively assesses the effectiveness of $CO_2$ capture and sequestration strategies in reducing significant volumes of anthropogenic $CO_2$ from major emission sources. Alongside an overview of current capture technologies—including post-combustion, pre-combustion, oxy-fuel combustion, and CLC—it also details efficient and secure sequestration strategies, focusing on geological, oceanic, and mineral carbonation storage, all supported by reliable $CO_2$ transport systems. The exceptional storage facilities and associated sequestration risks distinguish this review from previous studies. The analysis concludes with a thorough examination of cost-effective CCS applications, including enhanced oil recovery (EOR), enhanced gas recovery (EGR), and enhanced water recovery (EWR) using sequestered $CO_2$, as the research's culmination. By assigning equal importance to both capture and sequestration methods, this review introduces a new perspective on the CCS value chain.

### 5.1.2 $CO_2$ CAPTURE METHODS

Despite ongoing efforts to reduce emissions, vast quantities of $CO_2$ are still released each year. $CO_2$ is responsible for the majority (65%) of all greenhouse gas emissions, with power and heat production accounting for 25% and industry for 21% of the global total. The manufacture of steel, iron, and non-metallic minerals such as cement contributes 44% of all industrial $CO_2$ emissions (Intergovernmental Panel on Climate Change, 2015). This underscores the increasing need for $CO_2$ capture technologies (Korde and Kandasubramanian, 2019). The main technologies used for $CO_2$ capture include oxy-fuel combustion, pre-combustion, chemical looping combustion, and post-combustion, which are discussed below.

### 5.1.3 $CO_2$ TRANSPORT

After $CO_2$ has been separated from other exhaust gases, it needs to be transported to sequestration sites or to industrial facilities for use. Onshore transport options include pipelines, highways, and railways, while offshore transport is accomplished via ships and

pipelines. Pipelines made mainly from carbon steel are considered the most practical and cost-effective solution for transporting large quantities of $CO_2$, particularly from power plants with operational lives exceeding 23 years (Lu et al., 2020). When pipeline transport is not feasible, $CO_2$ is shipped as a dense liquid using specially designed tanker vessels (Al Baroudi et al., 2021). For short distances, road and rail transport using tanker trucks or specialized railcars is used where shipping and pipelines are impractical (Trevisan and Bordignon, 2020).

### 5.1.4 $CO_2$ SEQUESTRATION

$CO_2$ sequestration has become a major technological approach in strategies aimed at reducing high levels of emissions. This process involves isolating $CO_2$ from the atmosphere or anthropogenic sources for long-term or permanent storage. Potential storage options include the deep ocean, subsurface geological formations, and mineral carbonation, with geological sinks comprising hydrate storage, depleted oil and gas reservoirs, not mineable coal seams, and saline aquifers (Bachu, 2000).

### 5.1.5 UNDERGROUND GEOLOGICAL $CO_2$ STORAGE

Geological $CO_2$ sequestration, also known as geological carbon storage, is widely regarded as the most viable long-term storage method. In this approach, large amounts of captured $CO_2$, transported by ship or pipeline, are injected into geological formations for extended storage. The vast storage capacity and widespread availability of suitable formations make geological storage one of the most common carbon storage methods (Pan et al., 2021a; Pan et al., 2022). To ensure efficient transport and injection, captured $CO_2$ is compressed to a supercritical state. Geological formations with high porosity and permeability are ideal for storing large $CO_2$ volumes, but careful site selection is necessary to guarantee safety and effectiveness. Safety measures include monitoring pressure and temperature, as well as tracking the movement of stored $CO_2$ to prevent leaks into the atmosphere or other subsurface areas. Major geological formations used for secure $CO_2$ storage include deep saline aquifers, depleted oil and gas reservoirs, not mineable coal seams, and basalt formations (Kumar et al., 2020), as illustrated in Figure 1.

It has been demonstrated that depleted oil and gas reservoirs, which are well-characterized and equipped with efficient $CO_2$ storage infrastructure, can retain hydrocarbons over geological timeframes. Enhanced oil recovery (EOR) or enhanced gas recovery (EGR) techniques applied to these reservoirs improve oil and gas production through $CO_2$ injection while maintaining reservoir pressure for effective storage. Although these sites have moderate storage capacity, their well-developed infrastructure and

moderate to high security make them attractive options for sequestration, despite the risk of potential $CO_2$ leakage and the limitation of suitable reservoir availability (Paluszny et al., 2020).

Deep saline aquifers, with their enormous storage potential, can securely store about 10,000 Gt of $CO_2$ for over a century, mainly in saline water (Celia et al., 2015; De Silva et al., 2015). Injected $CO_2$ becomes trapped or dissolved in the rock's pore spaces, enabling storage. Enhanced water recovery (EWR) associated with this storage method not only facilitates active storage but also yields saline water that can be used for power plant cooling, agriculture, and other applications (Feng et al., 2018, 2021). While deep saline aquifers offer moderate to high storage security and high capacity, issues such as pressure buildup and $CO_2$ plume migration—which can fracture formations, reactivate faults, and cause leakage—remain significant concerns (Orlic, 2016).

Injecting $CO_2$ into not mineable coal seams displaces $CH_4$, promoting enhanced coal bed methane (CBM) recovery, with the recovered $CH_4$ serving as a fuel source (Zhao et al., 2018). Coal's greater affinity for $CO_2$ compared to $CH_4$ means that initially adsorbed $CH_4$ is replaced, allowing for substantial $CO_2$ storage while improving the efficiency and profitability of CBM production (Gilliland et al., 2013).

Basalt formations, rich in minerals such as calcium, magnesium, and iron silicates, enable $CO_2$ to react and form stable mineral carbonates through mineral trapping. However, challenges related to $CO_2$ injection, monitoring, and the scarcity of suitable formations limit their use, despite moderate storage capacity and high security (Raza et al., 2022).

Key requirements for optimal geological storage sites include the following:
– The reservoir (cap) rock must possess sufficient thickness, permeability, and porosity, along with robust sealing properties, to prevent leakage and migration of $CO_2$ from storage locations.
– The site should be capable of accepting $CO_2$ at a rate proportional to the supplier's injection.
– Adequate storage capacity is essential (Bachu, 2000).

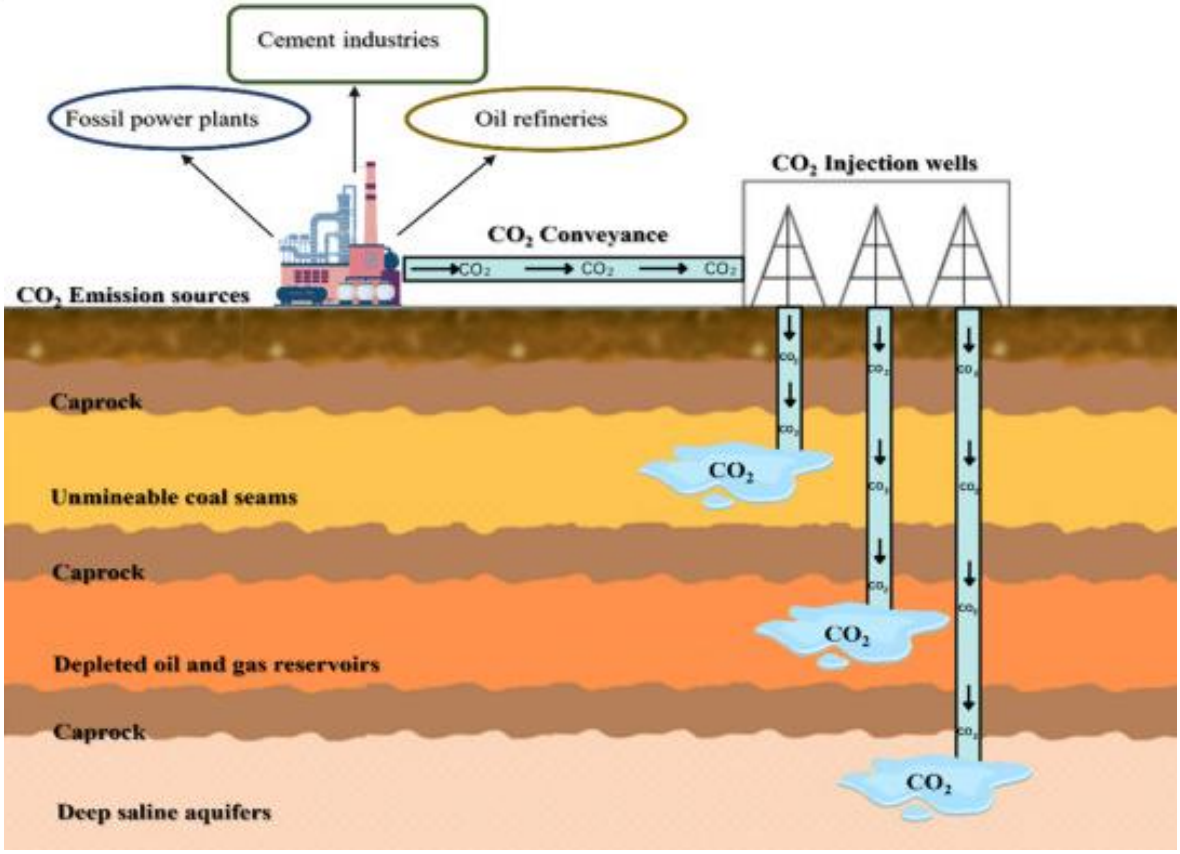


Figure 1. Underground $CO_2$ geological sequestration sites and $CO_2$ sequestration (source: Krishnan et al., 2023)

Existing industries such as cement and steel manufacturing, oil and gas extraction, and power generation can operate with a reduced carbon footprint by utilizing geological storage (Rissman et al., 2020). Advancements and implementation of geological storage technologies may generate employment and business opportunities in the construction, management, and maintenance of storage infrastructure. Developing countries might adopt geological storage to curb greenhouse gas emissions while fostering economic development, as these technologies are suitable for large-scale $CO_2$ emitters and heavy industries (Lee et al., 2018). However, successful deployment is often limited by challenges such as potential leakage, monitoring difficulties, and public acceptance, all of which must be addressed to enable broader adoption for achieving net-zero carbon goals (Pawar et al., 2015). High construction and operational costs for injection wells and monitoring systems, as well as concerns about public perception, long-term safety, and possible environmental impacts, are also among the obstacles associated with geological sequestration (Jenkins et al., 2015). Ongoing improvements in geological storage technology are expected to enhance its effectiveness, scalability, and security.

### 5.1.6 PROPERTIES OF GEOLOGICAL $CO_2$

At standard atmospheric conditions, $CO_2$ is a kinetically stable gas with a density greater than air. When subjected to its critical pressure and temperature—7.38 MPa and 31.18 C, $CO_2$ shifts from a gaseous to a supercritical state. $CO_2$ phase diagram shown on Figure 2. In this supercritical phase, $CO_2$ is immiscible with water, has a liquid-like density (200 – 900 kg/m³), and exhibits gas-like viscosity. Under low temperatures and high pressures, supercritical $CO_2$ can form hydrates, which are denser than water, and it demonstrates a strong affinity for coal—approximately twice that of $CH_4$ in coal seams. This high affinity facilitates enhanced CBM recovery, while the increased miscibility with saline water, oil, and gas benefits EWR, EGR, and EOR applications. These $CO_2$ properties are critical when selecting suitable methods and locations for geological disposal and sequestration. Depending on reservoir pressure and temperature, $CO_2$ may be stored as a gas, liquid, or supercritical fluid (Hendriks and Blok, 1993; Holloway and Savage, 1993).

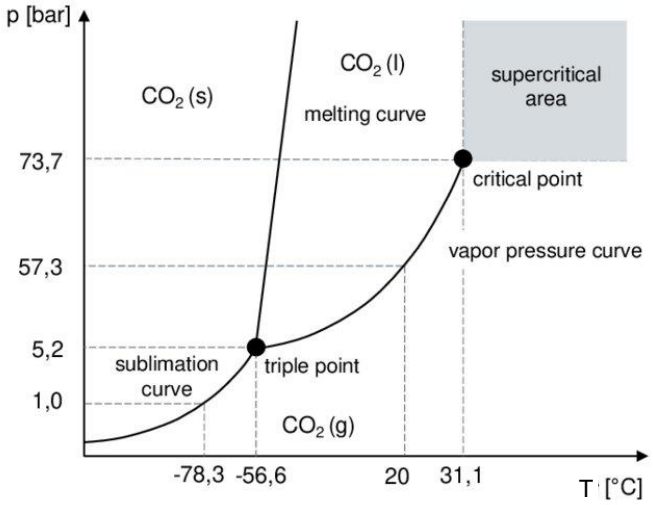


Figure 2. The phase diagram of $CO_2$
(source: Meier et al, 2021)

### 5.1.7 RISKS FACTORS OF GEOLOGICAL SEQUESTRATION

The behavior of $CO_2$ in storage reservoirs is governed by mineralogy, geochemistry, fractures, mineral precipitation and dissolution, and pore fluid dynamics of the reservoir system, persisting over years until the $CO_2$ is transformed into stable solid carbonates (Wei et al., 2015). Variables such as injection-induced seismicity, interactions between $CO_2$ and rock, and the potential for leakage influence how well $CO_2$ remains confined. Effective risk assessment and monitoring are essential for ensuring the secure containment of sequestered $CO_2$ (Aminu et al., 2017). Addressing these risk factors reliably through innovative strategies is crucial for advancing toward a pollution-free environment.

### 5.1.8 INTERACTIONS OF BRINE-ROCK, AND $CO_2$

When $CO_2$ dissolves in brine, it forms acidic mineral carbonates, triggering a series of geochemical reactions that can ultimately immobilize the $CO_2$. At higher pH, secondary carbonate minerals may precipitate from the dissolution of Mg- or Ca-rich silicates, further trapping $CO_2$. The acidic conditions alter displacement pressure, rock permeability, and pore structure, affecting $CO_2$ migration, which can continue for years until carbonate formation is complete (Aminu et al., 2017).

### 5.1.9 SEISMICITY INDUCED BY INJECTION

Injecting $CO_2$ can alter in-situ fluid pressures and subsurface stresses, potentially triggering seismic events (Aminu et al., 2017). To minimize the risk of induced seismicity, it is advisable to select sites with no evidence of faulting and with high permeability and porosity, evaluate the stress state of potential sites, and prioritize areas with low natural seismic activity (Nicol et al., 2011).

### 5.1.10 DIFFUSIVE LOSS

$CO_2$ can slowly diffuse through water-saturated pores in cap rocks due to concentration gradients, leading to gradual mineral responses in the reservoir. Enhanced degradation can significantly modify caprock porosity and permeability. However, pressure-driven flow through porous host rocks allows for greater volumes of $CO_2$ to pass, making long-term reactions and mineral trapping particularly impactful (Gaus, 2010; MacQuarrie and Mayer, 2005).

### 5.1.11 CAPILLARY LEAKAGE

Capillary leakage occurs if the pressure of stored $CO_2$ exceeds the capillary entry pressure of the caprock, allowing $CO_2$ to penetrate caprock pores. Thus, the capillary entry pressure defines the maximum allowable overpressure and serves as a measure of sealing effectiveness. Factors such as caprock wettability, pore size, and the interfacial tension between $CO_2$ and brine influence capillary entry pressure, and changes in these parameters can affect the seal's performance (CHIQUET et al., 2007; Farrell et al., 2014).

### 5.1.12 WELL INTEGRITY

Effective $CO_2$ sequestration requires high-quality well seals. However, alkaline cement used for sealing can degrade when exposed to mildly acidic $CO_2$-brine, leading to dissolution of cement components and formation of silica and carbonate minerals, which may reduce porosity. The durability of cement is influenced by rock type, temperature fluctuations, cement composition, and the presence of contaminants, with these effects being more pronounced in older wells (Scherer et al., 2005).

### 5.1.13 FRACTURE AND FAULT NETWORKS

Existing fractures and faults represent possible leakage pathways, as they may act as rapid fluid conduits or barriers. High injection rates can reactivate pre-existing fractures or generate new ones. The sealing ability of faults and fractures may also be compromised by mineral dissolution processes within the caprock and reservoir (Beaubien et al., 2013; Li et al., 2013).

### 5.1.14 GEOLOGICAL $CO_2$ UTILIZATION

Despite the risks associated with subsurface geological $CO_2$ sequestration, it also provides a cost-effective pathway for supporting technologies such as Enhanced Oil Recovery (EOR), Enhanced Gas Recovery (EGR), and Enhanced Water Recovery (EWR). Schematic representation seen in Figure 3.

#### 5.1.14.1 EOR

Enhanced Oil Recovery (EOR) involves injecting $CO_2$ into hydrocarbon reservoirs to increase oil extraction while simultaneously storing $CO_2$ underground, thus helping to reduce greenhouse gas emissions (Al-Shargabi et al., 2022; Hamza et al., 2021). Injecting $CO_2$ raises reservoir pressure and lowers oil viscosity, maximizing production, improving recovery rates, and extending oil field lifespans advantages leveraged by oil companies (Liu and Rui, 2022). There are two main EOR types: miscible EOR, suitable for light oil reservoirs with high permeability, where $CO_2$ and oil mix at or above minimum miscibility pressure to enhance mobility and recovery (Czarnota et al., 2017); and immiscible EOR, applicable to a broader range of reservoirs, where $CO_2$ is injected below minimum miscibility pressure, causing oil to swell and become more mobile, though less efficiently than miscible EOR (Li-ping et al., 2015). Advanced EOR methods include foam-assisted EOR, carbonated water injection, water-alternating-gas injection, and hybrid techniques. In water-alternating-gas processes, water and gas are alternately injected to improve sweep efficiency and oil mobility (Al-Bayati et al., 2018). Foam-assisted EOR uses foaming agents to create viscous $CO_2$ foam, reducing gas channeling and improving sweep (Xu et al., 2017). Carbonated water injection lowers oil viscosity and displace oil, but may result in $CO_2$ loss to the atmosphere and lower recovery (Nowrouzi et al., 2020). Hybrid EOR combines $CO_2$-EOR with other techniques (e.g., steam, low-salinity water, chemicals), but operational complexity is a drawback (Mogensen and Masalmeh, 2020). Although EOR is a mature technology offering simultaneous storage, it requires significant infrastructure and its long-term impact depends on the global transition to renewable energy (Kalair et al., 2021).

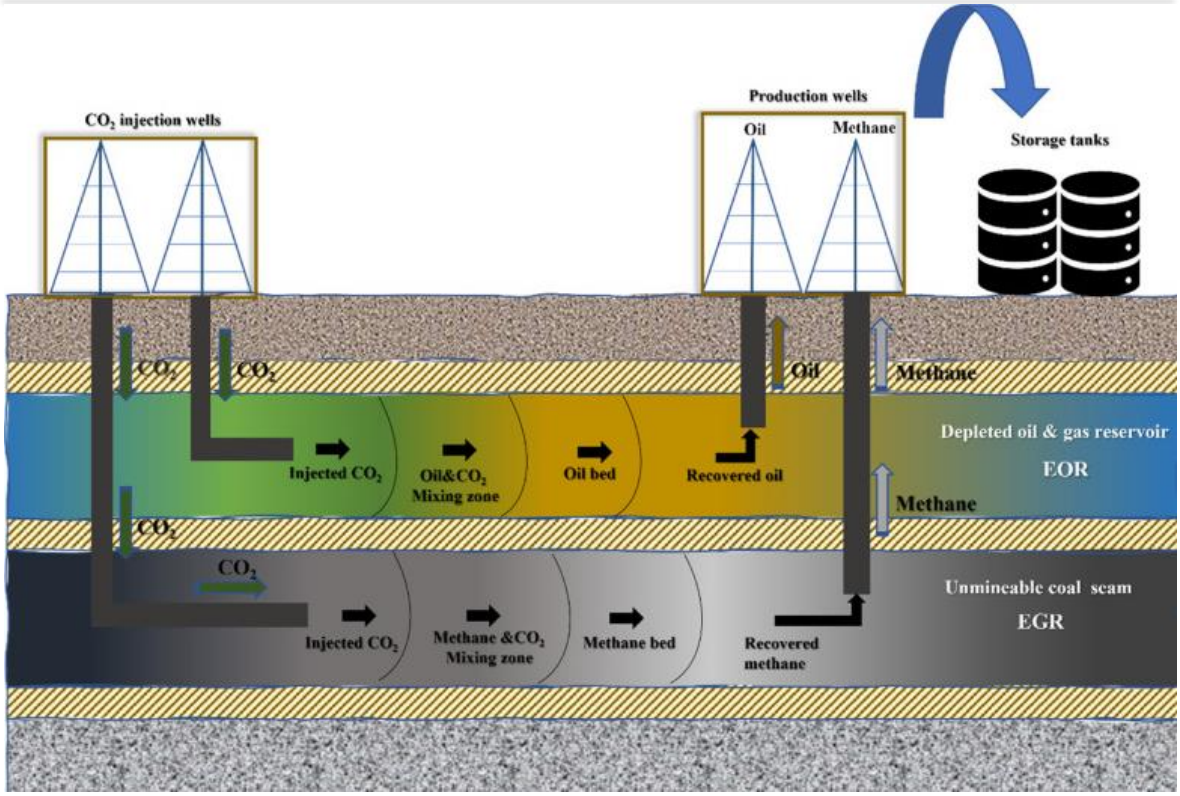


Figure 3. Schematic representation of Enhanced oil recovery & Enhanced gas recovery (source: Krishnan et al., 2023)

### 5.1.14.2 EGR

Enhanced Gas Recovery (EGR) is less developed than EOR due to lower global gas demand and the complex behavior of gas reservoirs (Burrows et al., 2020; ZOU et al., 2023). Gas reservoir compositions vary, necessitating specialized $CO_2$ management and treatment. Continuous $CO_2$ injection into gas reservoirs is the most straightforward and widely used method to increase reservoir pressure and push natural gas toward production wells (Bongole et al., 2019). This approach is used to boost productivity in mature or $CO_2$-rich gas fields, providing a viable $CO_2$ reduction strategy and supporting CCTUS industries (Mikulčić et al., 2019). While this technique improves gas output and extends reservoir life, it may hinder the shift to cleaner energy sources (Kalair et al., 2021). Raising awareness of EGR's benefits can encourage broader adoption among gas producers to enhance recovery and reduce environmental impact (Dudek et al., 2021). Ongoing research will improve efficiency, reduce costs, and advance monitoring, making the technology more accessible and attractive for diverse projects.

### 5.1.14.3 EWR

Enhanced Water Recovery (EWR) can reduce $CO_2$ emissions by injecting $CO_2$ into saline aquifers and extracting brine, achieving efficient sequestration (Ranaee et al., 2022).

Injecting $CO_2$ into deep saline aquifers increases pressure, raises the risk of induced seismicity, caprock fracturing, and potential leaks. To maximize storage and manage pressure, EWR involves extracting brine to control pressure buildup and $CO_2$ migration. Optimizing well placement and injection rates can improve $CO_2$ injection efficiency and saline water production. Closer spacing between injection and production wells accelerates $CO_2$ recovery and concentrates pressure drops at the injection well base. Re-injecting brine into overlying shallower aquifers can boost storage capacity by 30% or more, increase injectivity, and lower leakage risk. Pressure shifts to higher layers when all produced brine is injected into the upper aquifer. High porosity and permeability enhance dissolution and storage effectiveness. (Yang et al., 2021). EWR also offers economic benefits by supplying cooling water to power plants. (Alsarhan et al., 2021).

#### 5.1.14.4 EGS

As a renewable energy source, an effective method for harnessing dry-hot rock resources involves the development of an enhanced geothermal system (EGS). This technology is pivotal for enabling the exploitation and utilization of geothermal energy from dry-hot rock formations. In contrast to conventional water-based EGS, the emerging $CO_2$-based EGS—where carbon dioxide serves as the heat transfer fluid—offers several advantages, including improved energy efficiency, reduced greenhouse gas emissions, and enhanced thermal performance. $CO_2$ exhibits strong heat extraction capabilities, minimal chemical reactivity with reservoir rocks, and the added benefit of geological carbon sequestration.

Due to these distinctive benefits, dry-hot rock geothermal energy is anticipated to play a strategic role in addressing future energy challenges. As conventional fossil fuel reserves dwindle, attention is increasingly turning toward sustainable alternatives such as high-efficiency dry-rock geothermal systems, particularly within the oil and gas industry. The question of how to optimize the development of these resources has become a central concern. The unique thermophysical and chemical properties of $CO_2$ make it a particularly promising medium for heat transfer. Given the widespread availability of dry-hot rock formations globally, utilizing $CO_2$ in geothermal applications not only mitigates reliance on fossil fuels but also contributes to climate change mitigation through carbon storage. (Liu, Tao & Zhao, Guanghui., 2025)

## 5.2 THEORETICAL INTRODUCTION OF COMPUTER TOMOGRAPHY MEASUREMENTS AND INTERPRETATION

### 5.2.1 INTRODUCTION

CCUS comprehending the migration patterns of injected $CO_2$ and the interactions between $CO_2$, formation rocks, and wellbore cement is vital for estimating storage

capacity and predicting the long-term stability of the stored $CO_2$ (Cheng et al., 2016; Scherer et al., 2005; Steefel et al., 2013; Zhang et al., 2011). Thus, advanced techniques are required to analyze the pore structure, wettability, and mineralogical composition of these materials when exposed to $CO_2$. Various characterization methods are available to study the pore structures of rock and cement samples, including mercury intrusion porosimeter (MIP), nuclear magnetic resonance (NMR), scanning electron microscopy (SEM), gas adsorption techniques, and neutron imaging (M Gan et al., 2020).

Each method, however, has its own limitations. For instance, while MIP can measure total porosity, it does not effectively assess pore heterogeneity. NMR imaging is restricted to fluids and minerals that contain hydrogen. SEM provides detailed two-dimensional images of microstructures but fails to offer three-dimensional perspectives essential for understanding interconnected pores and 3D heterogeneity. Moreover, SEM's in-situ analysis capabilities are limited. Gas adsorption can only determine the volume of open pores, not isolated ones. Neutron imaging is effective for examining hydrogen-rich fluids in non-aquatic porous media, though it is hampered by the limited availability of high-intensity neutron sources and the high costs associated with the equipment.

Due to these limitations, there is a pressing need for an advanced technique capable of accurately evaluating the three-dimensional connectivity and spatial heterogeneity of pores in rock and wellbore cement samples. Human X-ray computed tomography (CT) emerges as a fitting solution, offering non-invasive and non-destructive imaging that can directly reveal and reconstruct the 3D architecture of these materials. Modern CT scanners provide high-resolution, three-dimensional images that allow detailed visualization of the internal features of samples. This capability is essential for identifying fine-scale structures such as pore spaces, fractures, and mineral compositions. (M Gan et al., 2020).

### 5.2.2 COMPUTED TOMOGRAPH MEASUREMENT

The main parts are the following “gantry” , “test desk” , “High voltage generator” , “control panel” , the computer can be divided into two main parts: “imager” and “host".
The task of the host computer is to run all the necessary processes required (such as the operating system, user applications, etc.). The imager analyses the signs sent by the gantry. It also performs the required corrections, displays the image and does the calculation of secondary processing (3D reconstruction, reconstruction, redisplaying of raw images). Illustrated on Figure 4.

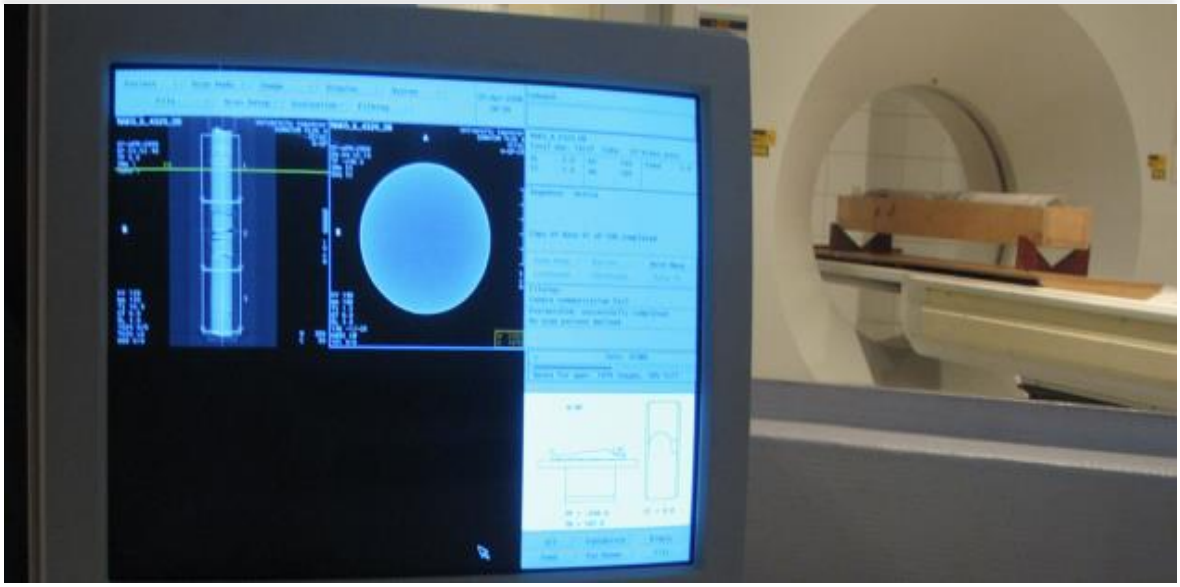

Figure 4. CT control panel and Siemens Somatom Plus S40 spiral CT during the measurement
(source: G.P. Veres et al., 2024)

High voltage generator:
It is the energy supplier of the Xray tube during the time of the various measurement types.
Control panel:
With the help of the above part of the CT the operator can manage and control the measurements and the post-processing work. The pictures generated by the imager are displayed on the monitor of the control panel.
Test desk:
The object in question can be positioned with high precision (mm) with the help of it.
The gantry: The Xray tube and the detectors are situated inside the gantry. The latter are positioned face to face and during the data collection process they turn around 360° within the gantry. (Kalender, W. A. 1994).

Siemens Somatom Plus S40 is a spiral CT scanner. There is a bifocal, rotating-anode Xray tube in it with 768 Xenon gas detectors on the opposite side. The signals of the detectors get out of the gantry's spinning part through the generator brushes following the enhancement and analogue/ digital transformation of these. Then, with the help of an optic cable the signals are sent to the imager through an optocoupler. (Kalender et al. 1999; Siemens Healthcare, 2024).
Xray is weakening as it goes through different materials and textures. The degree of absorption is smaller or higher in materials of different densities and therefore it depends

on the attributes of the measured materials. The capability of Xray absorption can be characterized by the coefficient of Xray absorption.

If the transfer of energy is constant, the absorption of Xray depends only on the material through which it goes. This degraded radiation reaching the detectors generates electrical signals dependent on the intensity of radiation.

As the system of tube detector turns around the analyzed object during the time of data collection, hundreds or thousands of measurements are made by the CT while the incoming data is organized into a matrix. At the end of the process the imager calculates each element of the matrix and assigns a scale to the points of the matrix whose points are actually the coefficients of Xray absorption. This scale is the so-called Hounsfield scale, its unit is the Hounsfield unit. Assigning the different values of the matrix to the appropriate values of the Hounsfield scale, the image can be displayed. Can visualize the image using predefined color tables or own color ones. The Hounsfield scale calibrated where the value of vacuum is -1,024, and the value of water is 0. The software running on PCs shifts to this scale with a value of +1,024, so the value of vacuum is 0.

A CT can be operated in two different modes. Using different commands, only one slice or a predefined number of slices within a certain distance can be measured at a time. The thickness of one slice can be 1, 2, 3, 5 or 10 mm using our Siemens Somatom Plus S40 spiral CT scanner. The size of the matrix with regard to a slice is $512 \cdot 512$ pieces.
The resolution of a matrix depends on several factors. Using the best resolution of our CT the smallest size of a cell of a slice can be 0.1·0.1·1 mm in reality. The duration of time of the measurement can be set within the range of 0.11 second for one slice.

In summary, if a sequence of slices on a sample measured, a 3D lattice network will be, where the size of one cell is derived from the resolution of the slice and its thickness. In general, the size of the cells is 0.1·0.1·0.1 mm.

The feed motion of the test desk with 1 mm precision can be handled manually or programmed by a computer application. If the target object is fixed on the test desk, the back-and-forth positioning of the object has no effect on the result and accuracy of the measurement. (Földes et al., 2014)

### 5.2.3 STRUCTURE AND WORKING PRINCIPLE OF MCT MEASUREMENT AND TECHNIQUES

The mCT is prepared from a micro focused X-ray tube, optionally applicable consists of a filter, a movable sample holder, and a detector array (Stock 2009). The micro-focused X-ray source illuminates the measured sample, the photons forming the X-ray beam interact with the sample material (absorbed, scattered), thus weakening the beam, i.e. decreasing its intensity.

The intensity attenuation of the beam depends on the number of atoms in the sample and the density of the material. The detector matrix determines the intensity distribution of the X-ray beam passing through the sample, which contains an enlarged projection image of the sample.

During the rotation of the sample (in the case of mCT, the sample rotates, the detector and the X-ray source are fixed) Hundreds of projection images are made, from which a computer algorithm reconstructs the virtual sections of the sample. (Figure 5.) In the case of cone-beam geometry, when the beam is divergent in the vertical direction as well, the most common is the so-called The Feldkamp algorithm is used for reconstruction (Feldkamp et al. 1984), which is a version of Filtered Back Projection (FBP) adapted to cone-beam geometry.

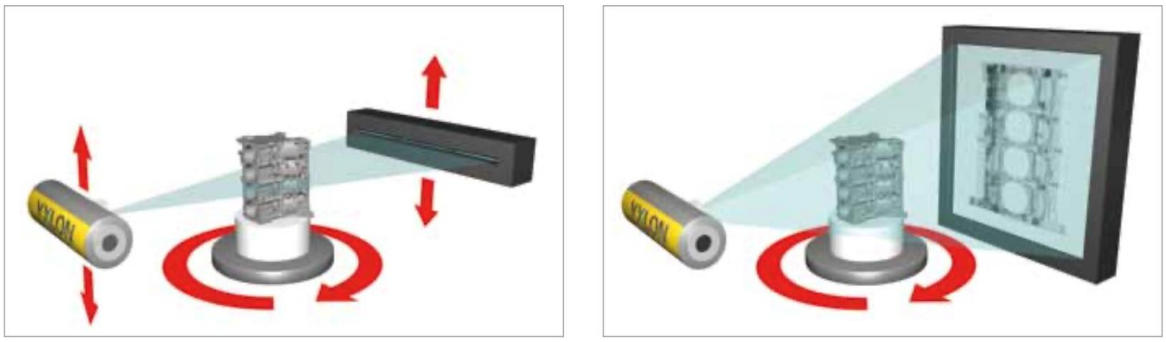

Principle of fan-beam CT: Rotation of part is followed by a vertical movement. This sequence is repeated until the desired area is scanned.

Principle of cone-beam CT: The 3D model comprises all information acquired by the detector during the rotation.

Figure 5. Principle of fan-beam and cone-beam CT techniques
(source: Földes, 2024)

### 5.2.4 BASIS OF GEOLOGICAL INTERPRETATION OF CT MEASUREMENTS

With the help of CT measurements rock samples can be measured in their original state (even in a closed case) without any destruction. The CT measurement also makes it possible to study dynamic systems which can vary in time and to determine the various parameters of these systems. (Földes et al. 2010)

The Hounsfield values of the different minerals were determined (in the same standard volume) and it was found that there was a strong - but not perfect - linear relationship between the Hounsfield unit of the minerals and their densities. (Figure 6.) The Hounsfield value can be identified as “CT number” in some literature.

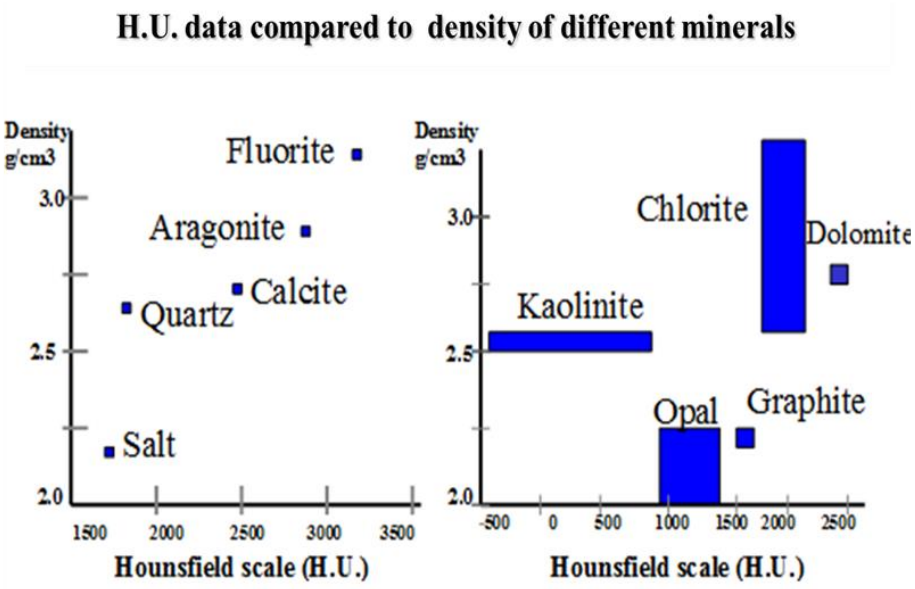


Figure 6. Hounsfield Unit data compared to density of different minerals (source: G.P. Veres et al., 2024)

In CT scanning, X-ray absorption by the sample is determined by both the atomic number and the density of the material within each volume element (3D voxel) of the sample. The relationship between the intensity of transmitted radiation (I), the intensity of incident radiation ($I_0$), the material’s attenuation coefficient (μ), and the X-ray path length through the material (x) is described by Lambert-Beer's Law, as shown in Equation (1):

$$I = I_0 e^{-\mu x} \tag{1}$$

In equation (1), $I_0$ and $x$ are known values, while $I$ is measured by the X-ray detector within the CT scanning system. Consequently, the attenuation coefficient (μ) for each voxel in the material can be calculated from these measurements. Equation (2): (Akin and Kovscek, 2003)

$$A \sim \lambda^3 \cdot Z^4 \cdot d \cdot D \tag{2}$$

where:

A: the absorption, $\lambda^3$: the wavelength (the absorption of the lower energy radiations is higher), Z the order number (the absorption is proportional with the fourth power), d the density, D the layer thickness.

CT image reconstruction involves resolving the spatial distribution of the material's attenuation coefficients using CT projection values, P(i, j). To reconstruct an N·M CT image, one must solve at least an N·M set of independent equations to determine all the μ (i, j) values. By varying the direction of X-rays, projection values from different angles can be obtained.

After reconstruction, the signal in each pixel of the reconstructed images is represented as the CT number, which is defined by Akin and Kovscek (2003) as, Equation (3):

$$CT = 1{,}000 \cdot \frac{\mu - \mu_w}{\mu_w} \quad (3)$$

Where, $\mu$ is the attenuation coefficient of the scanned sample, while $\mu_w$ is the attenuation coefficient of pure water. Most industrial CT scanners allow operators to utilize the full 16-bit CT number range (0–65,535), accommodating the dynamic range of the scanned material. Consequently, the CT number scale is somewhat arbitrary, influenced by the scanned material and reconstruction parameters. Standard CT numbers are -1,000 for air (corresponding to a μ air of 0) and 0 for water. Higher CT numbers indicate denser materials and vice versa. (M. Gan et al. 2020)

Considering these challenges, the image derived from the data matrix of a CT scan can be treated as a density map of the specified slice of the rock sample. By displaying this density map, the main features of the sample, such as granularity, joints, fractures, sedimentological characteristics, or lithological changes, can be clearly observed.
Sequentially displaying the images of the slices reveals the internal characteristics of the rock samples (core samples). Hounsfield values of cells are influenced by two factors: the Hounsfield value of the mineral grains within the cell and the Hounsfield value of the pore space filled with liquid and/or gas (air). (Földes et al. 2012)

Properly preparing a rock sample, including draining, vacuuming, and saturating it with liquid, allows the effective porosity to be determined through CT measurement. This involves quantifying the effective pore space within the cells, which can be filled with liquid or gas, thus defining the effective porosity of each cell.

CT measurements can monitor not only the final stage of saturation but also the behavior and state of saturation of each cell at regular intervals. By measuring the saturation over time, the complexity of the cells' internal structures can be elucidated. The saturation process might also flush out residual dry materials, such as drilling mud, within the samples, which can be studied using CT techniques.
Once the effective porosity of a cell is known, the Hounsfield value of its mineral grains can be calculated. This enables the determination of mineral composition in coarse-grained rocks, where grain size exceeds resolution, and estimation in fine-grained samples where grain sizes are smaller than the applied resolution (Schembre and Kovscek, 2001).

Further studies can involve using different liquids, acids, or gels. Repeated measurements at the same positions can reveal insights into the mineral composition and petrophysical properties of rock samples and their interactions with various substances.
CT data processing facilitates extensive interpretation across the full length of a borehole, necessitating high levels of cooperation among CT data processing and interpretation experts and core and wireline analysis specialists. This collaboration is crucial for comprehensive analyses and accurate conclusions.

### 5.2.5 TYPES AND RESULTS OF MEASUREMENTS-BASIC MEASUREMENTS ON ROCK SAMPLES

Core samples chosen by a geologist are measured on selected intervals by CT with the requested slice thickness. Doing all the adequate data processing, several interpretations can be made on the basis of the scope of information gathered.

The following types of analyses and results can be obtained by CT measurements:

Digitalization of the full length of the core in 3D preserving the original state of the sample (fragmented or poorly cemented core samples also can be measured in their original state). As a result, the selection of representative core plugs from the cored interval becomes more reliable.

Qualitative and quantitative processing and interpretation of cores in their full length and diameter (macro-examination, structure, estimation of mineral composition, estimation of rock composition, determination of continuous sedimentary sequence, heterogeneity, grading (depends on applied resolution), fractures, cavities, orientation, minerals filling of fractures, dip direction of strata, sedimentological features, etc.)

Determination of petrophysical parameters and a flow profile (estimation of 3D effective volume, porosity, permeability, and determination of flow profile with the help of saturating the samples)

Running simulations and scale model experiments to better understand the processes within the various types of rocks and in the borehole. (modeling of path lines, formation damage, rock mechanics, etc.)

- Examination of the behavior of various drilling fluids, gels, polymers
- Possibility of calibration of well bore logs
- With the help of other measurements (e.g. Formation Imagers) the original orientation of the cores can be reconstructed
- Technology of processing the CT measurements supporting the geological interpretations

The flowchart below (Figure 7.) introduces the process of CT measurement, the interpretation and its relationship with core analyses and with other mainly wellbore and petrophysical interpretation methodologies.

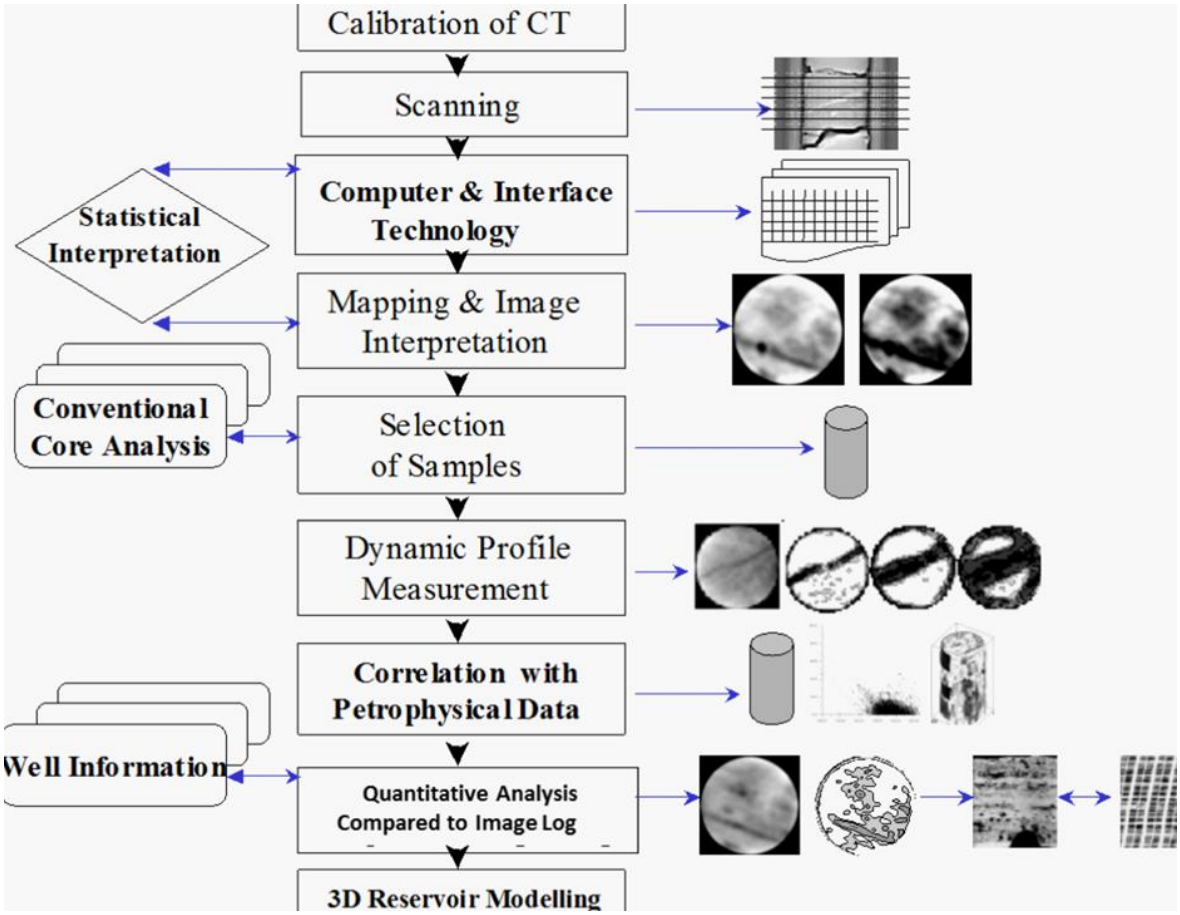


Figure 7. Geological interpretations supporting technology process chart (source: G. P. Veres et al, 2024)

### 5.2.5.1 Total porosity calculation

To acquire reservoir petrophysical properties, such as porosity, nondestructive techniques like X-ray computed tomography (CT) can provide precise and accurate results, particularly when displacement tests are feasible under CT measurement conditions. Typically, Hounsfield Unit (H.U.) data is influenced by both porosity and mineral composition. When mineral composition remains unchanged, H.U. values can be robustly correlated with laboratory porosity data. Nondestructive methods such as X-ray computed tomography (CT) appear to be precise and accurate in determining the physical properties of reservoir rocks, such as porosity, when displacement testing is available in addition to the CT measurement. Generally, H.U. data depends on porosity and mineral composition. If the mineral composition does not change, it can be strongly correlated with the porosity laboratory data. The total porosity values were calculated in the unbroken (non-fractured) volume. The basis of the processing is the change in the character of the 3D H.U. cumulative distributions made per measurement slice. This character changes at lithological boundaries, or at those porous sections where the rock matrix content is small in voxels. (Figure 8.) These voxels with high porosity (where the H.U. value is so low that it no longer corresponds to the H.U. value resulting from the mineral composition) may have connected each other. The shape and size of such subareas can be examined.

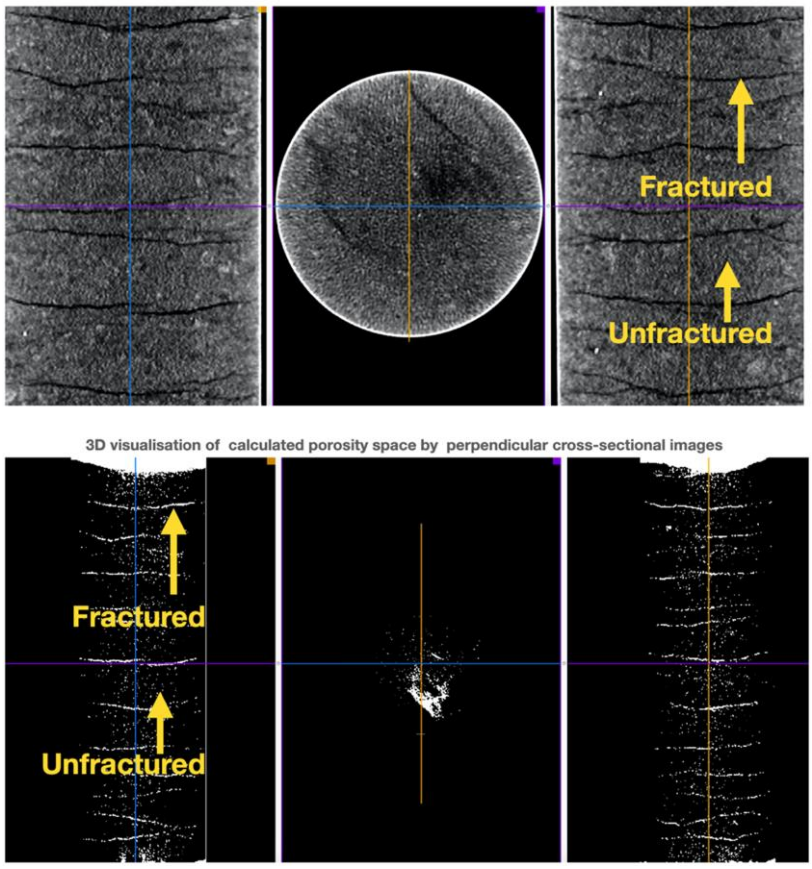


Figure 8. Unfractured and macro fractured areas in 3D CT slices
(Edited by the author, source TOMOGEO Ltd.)

Fractal dimension calculation

The value of the fractal dimension on the fractured samples were determined, which expresses the complexity of the fracture system mainly. The higher value also means greater extension. Using the box counting method, the fractal dimension is again the slope of the line when the log (n) value is represented on the Y axis with the log (r) value of the x axis. The same equation is used to determine the fractal dimension, D.

#### 5.2.5.2 Shape parameter calculation

The shape parameters were summarized in the following parameter form based on the calculated porosity areas measurement slice by slice:

- Perimeter: Calculated perimeter of porosity area element.
- Circularity:

$$\frac{4 \cdot \pi \cdot \text{Area}}{\text{Perimeter}^2} \tag{4}$$

with a value of 1.0 indicating a perfect circle. As the value approaches 0.0, it indicates an increasingly elongated shape. The number of the elements in the volume where the value was below 0.7 (Count%) were also determined.

- Solidity:

$$\frac{\text{Area}}{\text{Convex Area}} \tag{5}$$

#### 5.2.5.3 Feret's diameter:

The longest distance between any two points along the selection boundary, also known as maximum caliper. Uses the heading Feret. The angle (0–180°) of the Feret's diameter is displayed as FeretAngle, as well as the minimum caliper diameter (MinFeret). The starting coordinates of the Feret diameter (FeretX and FeretY) are also displayed.

## 5.3 THEORETICAL BACKGROUND OF GEOMECHANICAL MODELING

### 5.3.1 MECHANICAL PROPERTIES

It is fundamental to geomechanics and rock mechanics to understand the mechanical properties of rocks. These properties govern the manner in which rock materials respond to external forces and are of paramount importance for the modeling and design of rock structures such as tunnels, foundations, and slopes. The key mechanical properties that

are of relevance in this context include stress and strain, in addition to the various stress states (e.g. shear stress and hydrostatic compression) and the elastic constants that are indicative of a rock's elastic behavior. The elastic constants, which include Young's modulus (stiffness in tension/compression), shear modulus (stiffness in shear), bulk modulus (stiffness under uniform pressure) and Poisson's ratio (lateral vs. axial strain ratio), are critical in describing the deformation of rocks under load within the elastic range. Fundamental principles, such as Hooke's law, facilitate the application of these constants to establish relationships between stress and strain in elastic materials. Beyond the concept of elasticity, the field of rock mechanics encompasses the study of rock strength and failure criteria. The Mohr–Coulomb theory, defined by parameters of cohesion and internal friction angle, provides a simple model for the failure envelope of rocks under shear and normal stresses. This section provides a comprehensive review of this theoretical background, offering precise definitions, detailed descriptions, and illustrative examples drawn from authoritative sources in the field of geomechanics. The text is enriched by the incorporation of relevant figures and tables from the extant literature, which serve to provide a visual context for the explanations. (S. Peng and J. Zhang 2007). Table 1. summarizes the primary mechanical properties and stress measures for rocks.

Table 1. Summarizes the primary mechanical properties and stress measures for rocks, including their definitions and typical units
(source: Askaripour et al., 2022)

| Quantity | Definition | Typical Units |
|---|---|---|
| **Stress (σ)** | Force per unit area within a rock (can be normal or shear). Describes the intensity of internal forces acting on rock planes. | Pa $\left(\frac{\mathrm{N}}{\mathrm{m}^2}\right)$ (also MPa in practice) |
| **Strain (ε)** | Deformation of the rock normalized to original dimensions (dimensionless change in length, shape, or volume). | – (dimensionless) |
| **Hydrostatic stress** | Equal stress in all directions ($\sigma_1 = \sigma_2 = \sigma_3$). Causes uniform volume change (dilation/compression) with no shape distortion. | Pa $\left(\frac{\mathrm{N}}{\mathrm{m}^2}\right)$ |
| **Deviatoric stress** | Difference between a given principal stress and the hydrostatic mean stress. Causes distortion (shape change) in the material. | Pa $\left(\frac{\mathrm{N}}{\mathrm{m}^2}\right)$ |
| **Uniaxial compressive strength (UCS)** | Maximum axial stress a rock specimen can withstand under unconfined compression before failure. Indicates rock's compressive strength. | Pa (often MPa) |

#### 5.3.1.1 Stress and strain

The mechanical properties of rocks are defined by their response to various forces. Stress is defined as the internal force per unit area within a rock, while strain is defined as the deformation (change in shape or size) in the rock caused by stress. In the field of rock mechanics, stress is defined as a tensor quantity, characterized by normal and shear components acting on any plane within the material. The symbol used to denote normal stress is "σ", whereas "τ" is used to denote shear stress. The application of an external force to a rock induces an internal stress field and corresponding strains.

Stress and strain are two key factors that must be considered in this analysis. In situations where a rock is subjected to a load, the rock experiences stress, denoted by the symbol σ. This stress leads to strain, denoted by the symbol ε.

Types of Stress: In the field of geology, stresses in rocks can be complex, but two end-member states are often considered: hydrostatic compression and pure shear. In a hydrostatic stress state, the stress is equal in all directions ($\sigma_1 = \sigma_2 = \sigma_3$). This is analogous to a uniform pressure being exerted on the rock (as if it were situated at a great depth underwater). Hydrostatic compression induces a change in volume without causing any distortion to the shape of the object. Furthermore, no shear stresses are present on any plane. Conversely, under conditions of pure shear, there is no alteration in volume (the mean stress is zero); however, distortion does occur – shear stresses are present while the algebraic sum of normal stresses is zero. The majority of practical stress states are located between these two endmembers and can be decomposed into a hydrostatic component (the average of the three principal stresses) and a deviatoric component (the differential part of stress that causes shape change). (Askaripour et al., 2022)

For visualization, see the Figure 85. at Appendix 1.

It is imperative to comprehend these components, as hydrostatic stress (also referred to as confining pressure) has the tendency to compact the rock and, as a rule, augment its strength. Conversely, deviatoric stress (shear stress) has the capacity to distort the rock, which can ultimately result in failure when it surpasses the rock's shear strength. (Zhang 2005)

#### 5.3.1.2 Elastic vs. Plastic Behavior

The mechanical behavior of rock can be categorized as either elastic, where deformations are reversible, or inelastic (plastic or brittle), where permanent deformation or fracture occurs. For strains of a smaller magnitude, intact rocks frequently demonstrate a linear elastic response in accordance with Hooke's law. In situations of elevated stress, there is a possibility of yield (i.e. the development of inelastic strain). Brittle failure is a common

occurrence in low-porosity strong rocks, while ductile yielding has been observed to occur in softer rocks or in conditions of high pressure and high temperature. The transition from elastic to inelastic behavior is characterized by the rock's yield point. (S. Peng and J. Zhang 2007).

#### 5.3.1.3 Elastic constants

Within the elastic range, four elastic constants characterize how a rock deforms under load: Young's modulus (E), Shear modulus (G), Bulk modulus (K), and Poisson's ratio (ν). These constants assume the rock behaves as a linear elastic, homogeneous, and (often) isotropic material. Under those assumptions, the elastic constants are related, and each has a specific physical meaning:

Elastic modulus (also called Young's modulus) is an important parameter to describe stress and strain relationships. For most rocks, the uniaxial stress-strain curve before failure takes approximately the linear form. (Figure 9.)

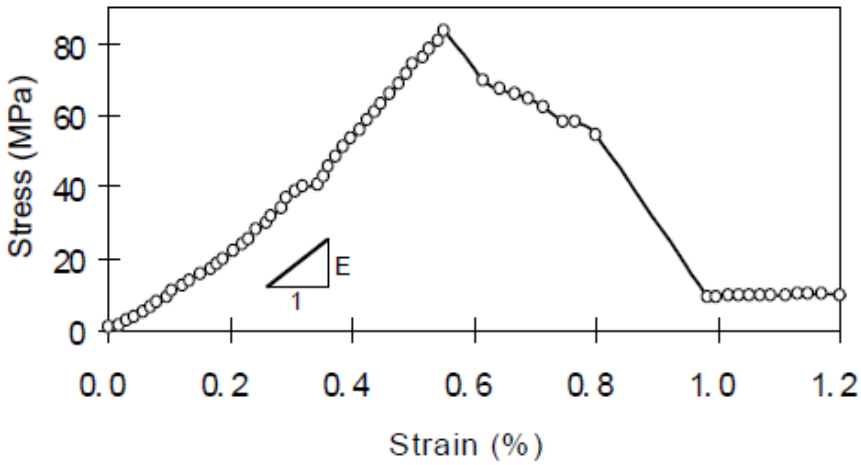


Figure 9. Elastic modulus and stress-strain relationship for a medium-grained sandstone under uniaxial compressive test
(source: Peng and Wang, 2001)

This can be presented by (Jaeger and Cook 1979):

$$\sigma = E \cdot \varepsilon \tag{6}$$

where $\sigma$ is the stress; $\varepsilon$ is the strain; the constant, E, is called elastic modulus. The material is linearly elastic if the above relation holds accurately.

Elastic modulus describes the capacity of rock deformation, or the stiffness of a rock. For a high elastic modulus rock, it is less deformable (i.e. stiff). The initial part of the complete stress-strain curve will be steep. For a low elastic modulus (soft) rock, it is more deformable, and the initial part of the complete stress-strain curve will be gentle (Hudson and Harrison 1997).

Shear Modulus (G): Also known as the rigidity modulus, G relates shear stress to shear strain under elastic conditions. It measures the rock's resistance to shearing deformation. In an isotropic material, G is related to E and ν by:

$$G = \frac{E}{2 \cdot (1+\nu)} \tag{7}$$

For most rocks, G is on the same order of magnitude as E (typically roughly 0.4–0.5 times E). For example, using the above relation, a rock with E = 40 GPa and ν = 0.25 has G ≈ 16 GPa. Shear modulus is directly measured in laboratory torsion tests or inferred from wave velocities (since the velocity of shear waves through rock depends on G and density).

Bulk Modulus (K): K defines the rock's compressibility—the resistance to uniform compression. It is the ratio of hydrostatic pressure change to the resulting volumetric strain (fractional change in volume). An isotropic material's bulk modulus is related to E and ν by:

$$K = \frac{E}{3 \cdot (1 - 2 \cdot \nu)} \tag{8}$$

A high bulk modulus indicates the rock is hard to compress (incompressible). For instance, a granite with E ~60 GPa and ν = 0.25 would have a bulk modulus on the order of 40 GPa. Bulk modulus is relevant for problems involving volumetric deformation, such as compaction of reservoirs or closure of caverns under high external pressure. (Esterhuizen et al, 2013)

Poisson's Ratio (ν): Poisson's ratio is the ratio of lateral (transverse) strain to axial (longitudinal) strain in the elastic regime. It reflects the rock's tendency to expand or contract laterally when compressed or stretched longitudinally. A higher ν means the material undergoes relatively large lateral deformation when compressed. Typical ν values for rocks range from about 0.1 (very low, for highly cracking-prone rocks) up to about 0.35 (for very ductile or rubbery materials); most rocks fall in the 0.15–0.30 range. For

example: sedimentary rocks like sandstones often have ν ≈ 0.2, limestones around 0.25–0.30, and shales can be 0.30 or higher. Laboratory measurements and seismic velocity data support these ranges. A set of tests on different rocks found Poisson's ratios of approximately 0.22 for an andesite, 0.30 for a basalt, and 0.21 for a tuff, illustrating variation even among volcanic rocks. Poisson's ratio influences how stress waves propagate and is an important parameter in numerical models of rock behavior. (S. Peng and J. Zhang 2007)

These elastic constants are summarized in Table 2-3-4. below, along with their typical ranges and significance in geomechanics.

Table 2. Elastic Constants of Intact Rocks and Their Typical Ranges
(source: Schön, 2015)

| **Constant** | **Symbol** | **Definition (for isotropic, linear elastic rock)** | **Typical Range in Rocks** | **Geomechanical Significance** |
|---|---|---|---|---|
| Young's Modulus | E | Ratio of axial stress to axial strain (slope of stress–strain curve in elastic region) | ~5–70 GPa (higher for crystalline rocks, lower for weak porous rocks) e.g., Basalt ~40 GPa, Tuff ~12 GPa. | Stiffness in tension/compression; controls deformation underload and structural rigidity. |
| Shear Modulus | G | Ratio of shear stress to shear strain under elastic deformation. Related by $G = \frac{E}{2\cdot(1+\nu)}$ | ~2–30 GPa (varies similarly to E; often ~0.4E to 0.5E). | Resistance to shearing; affects distortion, controls shear wave velocity in rock. |
| Bulk Modulus | K | Ratio of hydrostatic pressure changes to volumetric strain (compressibility). $K = \frac{E}{3\cdot(1 - 2\cdot\nu)}$ | ~5–50 GPa (high for low-porosity rocks; lower for highly compressible porous rocks). | Incompressibility; resistance to uniform compression; important for volume change behavior and P-wave velocity. |
| Poisson's Ratio | *ν* | Ratio of lateral strain to axial strain under uniaxial stress Dimensionless (0–0.5 for stable materials). | 0.15–0.35 for most rocks. e.g., Sandstone ~0.20, Limestone ~0.25, Shale ~0.30 | Lateral deformation tendency; influences dilation, crack propagation, and stress wave propagation. |

Table 3. Some Elastic Constants with Rock Type and Confining Pressure (P = 1 bar)
(source: Karagianni et al., 2017)

| Rock type | Bulk modulus | Young's modulus | Shear modulus | Poisson's ratio |
|---|---|---|---|---|
| granite | 0.10 | 0.30 | 0.20 | 0.05 |
| gabbro | 0.30 | 0.90 | 0.60 | 0.10 |
| dunite | 1.10 | 1.50 | 0.50 | 0.30 |
| obsidian | 0.40 | 0.70 | 0.30 | 0.08 |
| basalt | 0.50 | 0.80 | 0.30 | 0.23 |
| gneiss | 0.10 | 0.20 | 0.10 | 0.05 |
| marble | 0.10 | 0.40 | 0.20 | 0.10 |
| quartzite | 0.20 | 0.60 | 0.20 | 0.30 |
| sandstone | 0.07 | 0.20 | 0.08 | 0.10 |
| shale | 0.04 | 0.10 | 0.05 | 0.04 |
| limestone | 0.80 | 0.60 | 0.20 | 0.30 |

Table 4. Some Elastic Constants with Rock Type and Confining Pressure (P=3000 bar)
(source: Karagianni et al., 2017)

| Rock type | Bulk modulus | Young's modulus | Shear modulus | Poisson's ratio |
|---|---|---|---|---|
| granite | 0.50 | 0.60 | 0.40 | 0.25 |
| gabbro | 0.90 | 0.80 | 0.50 | 0.20 |
| dunite | 1.20 | 1.70 | 0.70 | 0.27 |
| obsidian | - | - | - | - |
| basalt | 0.80 | 1.20 | 0.40 | 0.25 |
| gneiss | 0.50 | 0.70 | 0.30 | 0.25 |
| marble | 0.80 | 0.70 | 0.30 | 0.30 |
| quartzite | 0.50 | 1.00 | 0.40 | 0.07 |
| sandstone | - | - | - | - |
| shale | - | - | - | - |
| limestone | - | - | - | - |

### 5.3.2 TRIAXIAL COMPRESSION TESTING

Triaxial compression testing represents the most valuable experimental approach for investigating rock mechanical behavior across extensive parameter ranges (Jeager and Cook 1979). Visualization of the influence of specimen size on the strength of intact rocks on Figure 10. During this testing procedure, a cylindrical rock sample experiences axial loading through the major principal stress ($\sigma_1$), while fluid confinement applies uniform minor principal stress ($\sigma_3$) to the specimen's lateral surfaces. A servo-controlled triaxial testing system manufactured by MTS Systems exemplifies typical equipment used for such investigations (Peng et al. 2000).

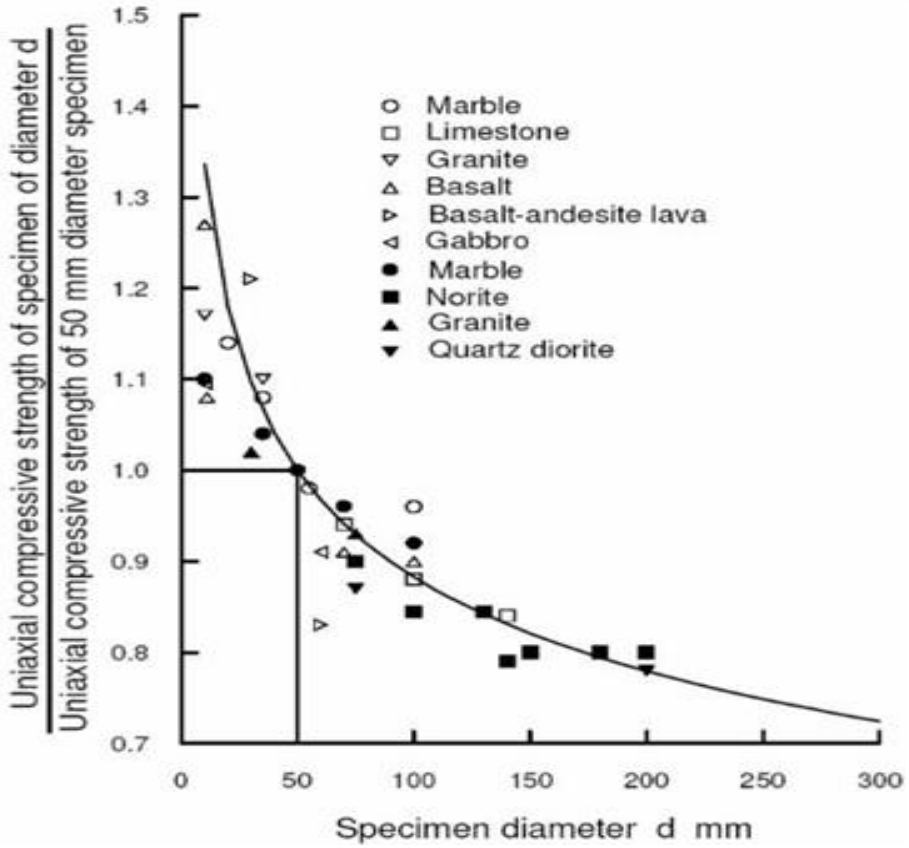


Figure 10. Influence of specimen size on the strength of intact rocks (source: Hoek and Brown, 1980)

#### 5.3.2.1 Test Results and Mechanical Property Determination

When sufficient rock specimens undergo triaxial compression testing, both unconfined compressive strength (UCS) and failure envelopes can be established. Complete stress-strain relationships under varying confining pressures are illustrated for medium-grained sandstone samples from the Huinan coal mines within Eastern China's Permian coal formations (Peng and Meng 2002). This experimental data demonstrates that increasing confining pressure correlates with enhanced rock strength. Consequently, rocks exhibit superior mechanical performance under three-dimensional stress states compared to uniaxial conditions.

Triaxial testing reveals that elastic modulus values are not constant parameters but increase proportionally with confining pressure, as demonstrated in Figure 11. The elastic modulus (Young's modulus) corresponds directly to the gradient of stress-strain curves measured before peak loading conditions. Experimental findings establish a non-linear correlation between elastic modulus and confining pressure for various rock types (Meng et al. 2006).

This relationship follows the mathematical expression:

$$E = b_2 \cdot \sigma_3^2 + b_2 \cdot \sigma_3 + b_0 \quad (9)$$

where E represents the rock elastic modulus in GPa; σ3 denotes the confining pressure in MPa; $b_0$, $b_1$, and $b_2$ are lithology-dependent parameters. These parameters vary significantly among different rock types. (Table 5.) The elastic modulus and confining pressure relationship in Huainan coalfield rocks of eastern China exhibits a distinct power-law correlation, optimally described by the equation developed by Brown et al. (1989), utilizing an exponent value of c = 2:

$$E = (a \cdot \sigma_3 + b)^c \quad (10)$$

where a , b, and c are the constants.

Table 5. The parameters for different lithologies in Eq. 9.
(source: Peng and Zhang, 2007)

| Lithology | $b_2$ | $b_1$ | $b_0$ | $\sigma_3$ (MPa) |
|---|---|---|---|---|
| Medium- and fine-grained sandstone | 0.016 | - 0.121 | 38.113 | <50 |
| Sandy mudstone | 0.040 | - 0.678 | 26.909 | <40 |
| Mudstone | 0.006 | 0.254 | 28.876 | <50 |

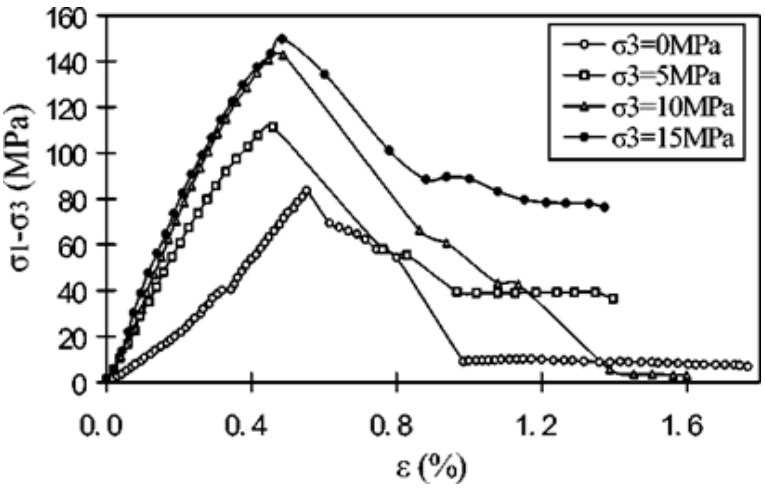


Figure 11. Complete stress-strain curves for different confining pressures under the triaxial tests in a medium-grained sandstone
(source: Peng and Zhang, 2007)

By applying the Mohr-Coulomb strength criterion to the triaxial test results, can be obtain the Mohr circle and rock failure envelope. The Mohr-Coulomb strength criterion indicates

that the normal stress (σ), shear stress (τ), and principal stresses ($\sigma_1$ and $\sigma_3$) have the following relationship for dry rocks:

$$\left(\sigma - \frac{\sigma_1 + \sigma_3}{2}\right)^2 + \tau^2 = \left(\frac{\sigma_1 - \sigma_3}{2}\right)^2 \quad (11)$$

It is a circle in the (σ, τ) plane with the center at $\left(\frac{\sigma_1 + \sigma_3}{2}, 0\right)$ and the radius is $\frac{\sigma_1 - \sigma_3}{2}$. This circle can be used to determine rock failure envelope, cohesive strength (*c*) and internal friction angle ($\varphi$). This circle is called Mohr circle, shown in Figure 12.

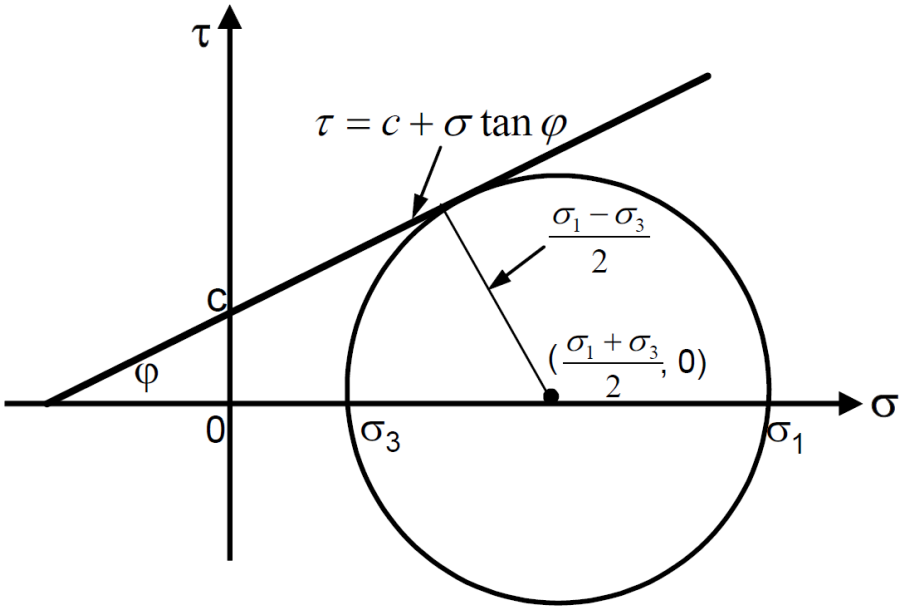


Figure 12. Mohr circle and strength envelope for dry materials
(source: Peng and Zhang, 2007)

At Appendix 1. Figures 86-89. illustrate the Mohr circles and failure envelopes from a series of triaxial compressive tests conducted on various rocks sampled from Eastern China's Permian coal measures (Peng and Zhang, 2007). These tests allow for the determination of rock cohesion and internal friction angle from the Mohr circles and strength envelopes. The experimental results indicate that mudstone and sandy shale exhibit cohesions ranging from 10.7 to 11.6 MPa and internal friction angles varying from 30.7 to 40.3°. In contrast, sandstones display cohesions ranging from 16.5 to 22.1 MPa and internal friction angles ranging from 40.6 to 46.23°. It is evident that mudstone and shale possess significantly lower cohesion compared to sandstones. Consequently, mudstones are more susceptible to compressive/shear failure than sandstones. (Meng Z, Peng S, Ling B 2000)

### 5.3.3 ROCK FAILURE CRITERIA

#### 5.3.3.1 Rock failure types

Rock failure happens when the surrounding stress exceeds the rock's tensile, compressive, or shear strengths, reaching whichever limit first. The types of failure vary depending on rock lithology, microstructures, and the applied stresses. Jaeger and Cook (1979) described rock failures under different confining pressures, as illustrated in Figure 13.

In unconfined compression (Figure 13a), irregular longitudinal splitting occurs. With moderate confining pressure, a single fracture plane inclined at less than 45° to the direction of σ1 characterizes rock failure, as seen in Figure 13b and Figure 14. (Peng and Zhang, 2007), indicating typical shear failure under compressive stresses, leading to shear displacement along the fracture. Increasing the confining pressure until the material becomes fully ductile results in a shear fracture network with plastic deformation, depicted in Figure 13c. (Jaeger and Cook 1979). Tensile failure, another primary type, usually arises in uniaxial tension, marked by a clean separation with no offset between surfaces (Figure 13d). When a slab is compressed between line loads, as shown in Figure 13e, a tensile fracture appears between the loads.

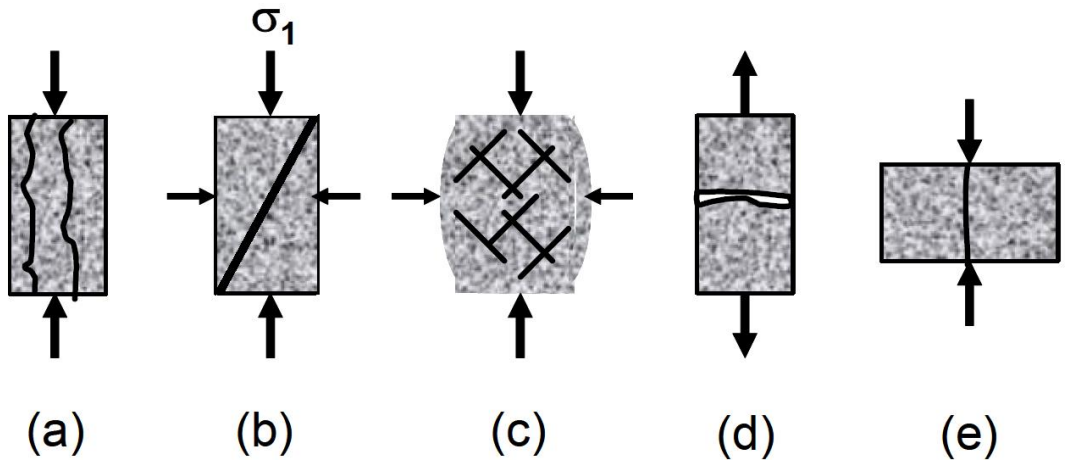


Figure 13. Rock failure types: a. splitting; b. shear failure; c. multiple shear fractures; d. tensile failure; e. tensile failure induced by point loads
(source: Peng and Zhang, 2007)

Different failure/strength criteria are employed to compare rock stresses and strengths for explaining rock failures. Effective stress concentrations in porous media close to underground engineering must be considered for initiating failure. Rock failure follows Terzaghi's effective stress concept, since Biot's effective stress coefficient nears 1.0 when failure is imminent. Terzaghi's effective stress is expressed as follows:

$$\sigma'_{ij} = \sigma_{ij} - \delta_{ij} \cdot p \quad (12)$$

where $\sigma'_{ij}$ represents the effective stress tensor, $p$ is the pore pressure, and δ is the Kronecker delta (δ = 1 when i = j; δ = 0 when i ≠ j).

Various failure criteria, such as tensile, Mohr-Coulomb, and Drucker-Prager, apply to different underground engineering types. (Hoek E 2007) The Mohr-Coulomb criterion will be the subject of the following part.

**Mohr-Coulomb criterion**

Shear failure occurs when the formation's shear strength is surpassed. The Mohr-Coulomb failure criterion can determine this failure mechanism for a porous medium, expressed as:

$$\tau = c + \sigma' \tan\phi \quad (13)$$

where σ' is the normal effective stress; τ is the shear stress; ϕ is the angle of internal friction; and c is the material's cohesion (inherent shear strength). In the principal space ($\sigma'_1$, $\sigma'_2$, $\sigma'_3$), the Mohr-Coulomb failure criterion is expressed as:

$$\sigma'_1 = UCS + q \cdot \sigma'_3 \quad (14)$$

with $\sigma'_1$, $\sigma'_3$ representing the maximum and minimum effective principal stresses, respectively, in

$$q = \frac{1 + \sin\phi}{1 - \sin\phi} \quad (15)$$

$$UCS = \frac{2 \cdot c \cos\phi}{1 - \sin\phi} \quad (16)$$

Figure 14. illustrates the Mohr circle and Mohr-Coulomb strength envelope. a) shear failure plane under triaxial compression, and in the shear plane, $\tan 2\beta = \frac{-1}{\tan\phi}$; b) Mohr circles and strength criterion. (Zhang, 2005) Failure does not occur if σ' and τ values lie below the strength envelope. In the Mohr-Coulomb criterion, it is important to note: (1) the intermediate principal stress $\sigma'_2$ does not affect failure, possibly leading to an overestimation of failure; (2) the shear fracture plane passes through the intermediate stress direction. This conclusion helps determine the direction of in-situ intermediate stress when the stress regime is known.

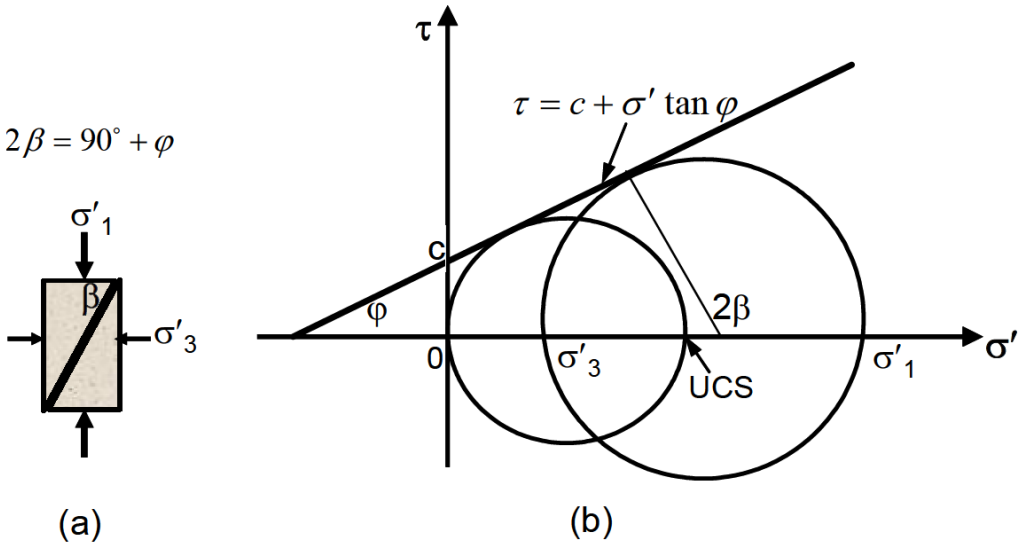


Figure 14. Mohr-Coulomb strength in effective stress domain
(source: Peng and Zhang, 2007)

The value of internal friction of different rock types based on some literature data are the following:

Table 6. Rock physical and mechanical parameters in the models
(source: Esterhuizen et al., 2013)

| Lithology | Density $\left(\frac{g}{cm^3}\right)$ | UCS (MPa) | Tensile strength (MPa) | Friction angle (°) | Cohesion (MPa) | Young's modulus (MPa) | Poisson's ratio |
|---|---|---|---|---|---|---|---|
| Medium-grained sandstone | 2.630 | 116.680 | 2.200 | 36.000 | 12.110 | 36,104 | 0.178 |
| Sandy mudstone | 2.300 | 71.400 | 1.000 | 35.000 | 10.200 | 19,566 | 0.216 |
| Mudstone | 2.630 | 66.110 | 0.800 | 42.000 | 1.430 | 18,261 | 0.268 |
| Coal | 1.520 | 22.300 | 0.880 | 38.400 | 3.500 | 18,480 | 0.303 |
| Sandstone with mudstone | 1.520 | 11.500 | 0.880 | 38.400 | 3.500 | 18,480 | 0.268 |
| Fine-grained sandstone | 2.610 | 104.120 | 3.200 | 40.000 | 11.600 | 36,410 | 0.143 |
| Siltstone | 2.500 | 94.540 | 1.200 | 37.000 | 11.000 | 20,871 | 0.164 |
| Faulted zone | 1.320 | 3.310 | 0.0400 | 30.000 | 0.072 | 913.100 | 0.268 |

### 5.3.4 THEORETICAL BACKGROUND OF GEOMECHANICS IN TNAVIGATOR

The study of deformation resulting from the strain of rocks in response to stress is called rock mechanics. When the scale of the deformation is extended to large geologic structures in the crust of the Earth, the field of study is known as geotectonic.

**Rock mechanics**

It is a theoretical and applied science of the mechanical behavior of rock and rock masses; is used to issue recommendations for hydrocarbon extraction, well engineering, etc.

#### 5.3.4.1 Geomechanical Modeling

A geomechanical model of a rock mass is a set of parameters that define the mechanical and structural features of a particular rock mass and its reaction to external impact.

To predict the irreversible reservoir deformation, to define the optimal operation conditions in order to avoid destruction of the bottomhole region and prevent damage to the tubing, to predict the deterioration of filtration-capacity formation properties and to predict the possible fracturing direction, geomechanical modeling is the right approach.

#### 5.3.4.2 Fundamentals of Geomechanical Modeling

In the dynamic model simulator, the geomechanical processes are approximated by changing the pore volume under the influence of compressibility, either as a constant or pressure-dependent parameter.

- As the deposits deplete and the injection wells operate, the rock stress field changes, which leads to various processes in the rock:
- consolidation,
- fractures,
- natural fracture system propagation,
- faults activation.

The movement of rock has a direction. It can affect the permeability and transmissibility of the faults in addition to changing the porosity of the structure. For such cases, scalar pressure-compressibility dependence may not be sufficient. It is sometimes necessary to couple hydrodynamic and geomechanical calculations, with the above-mentioned mechanical parameters.

# 6. GENERAL OVERVIEW OF TÁZLÁR FIELD

## 6.1 GEOLOGICAL CONDITIONS

Looking at Hungary's pre-Cenozoic surface, the Tázlár area is located in the Villány-Bihari Unit, as shown in Figure 15.

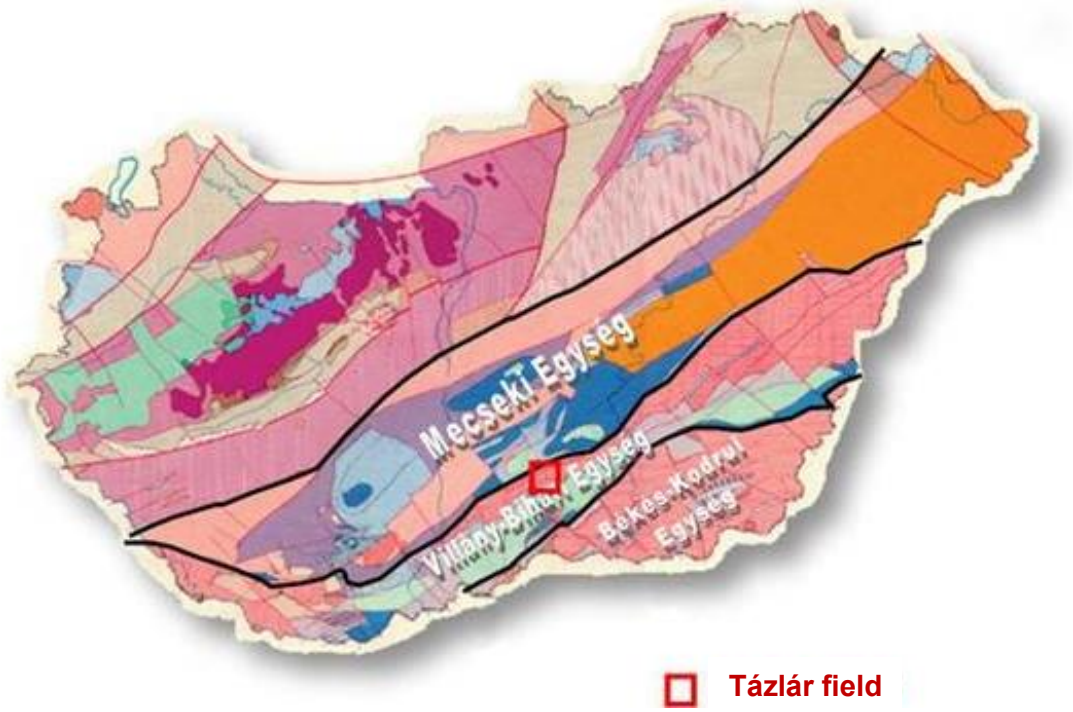


Figure 15. Location of Tázlár field
(source: MOL Plc.)

## 6.2 DRILLING RESEARCH

Table 7. Information on wells belonging to the storage layers of the Tázlár oil fields
(source: MOL Plc. ; Edited by the author)

| Well Nr. | Year of drilling | Initial qualification | Discovered part | Productive layer |
|---|---|---|---|---|
| Táz-2 | 1967 | Oil producer | Tázlár No. 1. rétegtelep | Miocene |
| Táz-3 | 1967 | Oil producer | Tázlár No. 1/a. halmaztelep | Miocene |
| | | Oil layer inspect. | Tázlár No. 1/a. halmaztelep | Paleozoic-Precambrian |
| Táz-5 | 1967 | Oil producer | Tázlár No. 2 halmaztelep | Paleozoic-Precambrian |
| Táz-8 | 1967 | Dry (water) | Tázlár No. 1/a. halmaztelep | Miocene |
| Táz-12 | 1969 | Dry (water) | Tázlár 1. sz. rétegtelep | Miocene |
| Táz-14 | 1969 | Oil producer | Tázlár No. 1. rétegtelep | Paleozoic-Precambrian |
| Táz-20 | 1971 | Dry (water) | Tázlár No. 1/a. halmaztelep | Miocene |

Drilling exploration began in the Tázlár area in 1966, when the location of the Táz-1 exploratory well was marked out and deepening began. The drilling point of the well was determined on the basis of seismic reflection measurements carried out between 1963 and 1966 at the maximum point of the Tázlár structure. The drilling found the No. 1 halmaztelep. The Táz-2, -3, -4, and -5 further development exploration wells drilled in 1967 all intersected hydrocarbon reservoirs. While Táz-4 reached the already known No. 1 cluster, the Táz-2, -3, -5 wells discovered new unsaturated oil deposits on the northern side of the structure. The Táz-6, -7, -8, -9, -10, -11, -12, -13, -16, -17, -18, -19, and -25 were drilled between 1967 and 1975, partly for detailed exploration and further development. These, together with the delineation wells drilled during the same period, Táz-20, -23, -24, -26, refined the hydrocarbon geology knowledge available at the time. Between 1969 and 1980, wells Táz-14, -15, -21, -22, -27, -28, -29, -30, -31, -33, -34, and -35 were installed in the field for production purposes. Of these, only Táz-14 reached the storage layer of one of the unsaturated oil deposits. The other wells were directed at No. 1 halmaztelep, which is still the largest occurrence in the field today. The basic location of the 35 wells in the Tázlár area are shown on Figure 16. The storage layers of the unsaturated crude oil deposits in Tázlár that are the subject of our study were intersected by the wells shown in Table 7.

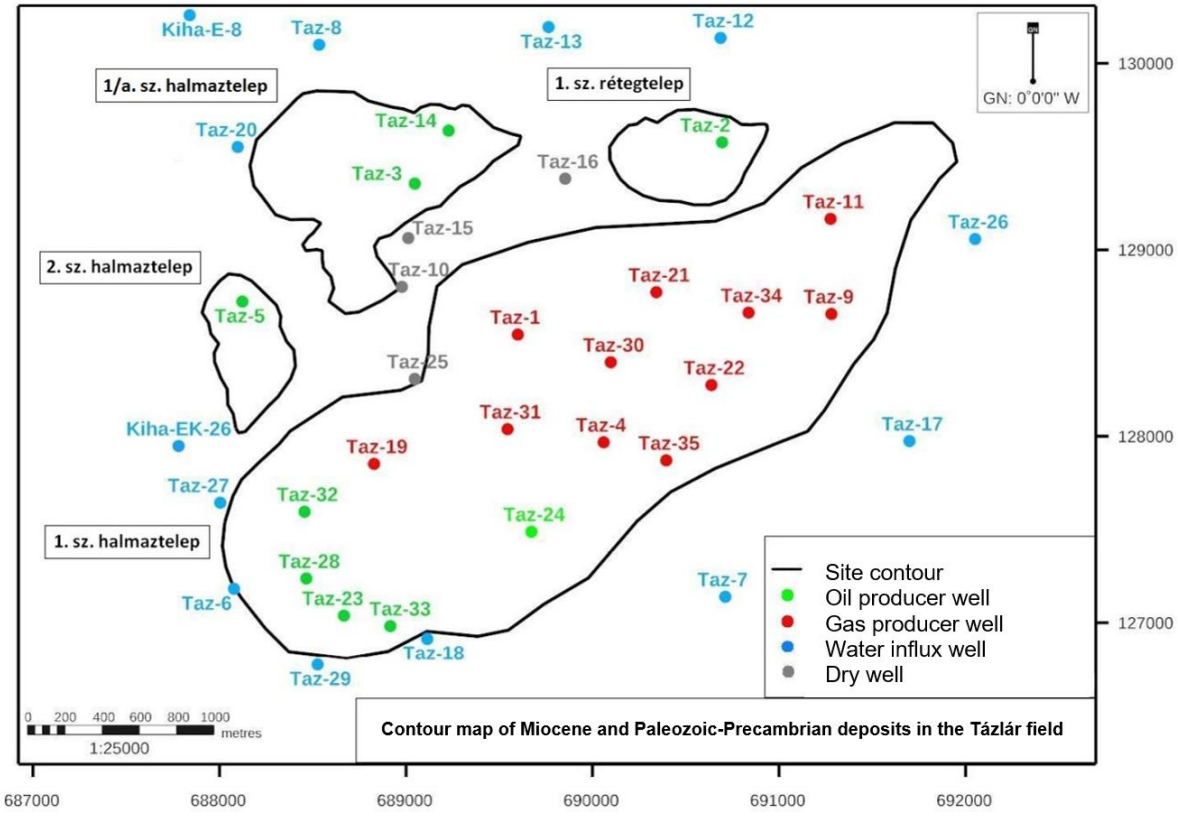


Figure 16. Contour map of Tázlár
(source: MOL Plc.)

## 6.3 LITHOLOGICAL CONDITIONS

To understand the lithological conditions of the Tázlár area, 37 well profiles and nearly 350 successful core samples were available. The information used from 35 wells (Táz-1-35) and two wells in Kiskunhalas (Kiha-É-8, Kiha-ÉK-26), which also fell within the study area, to determine the distribution of formations and stratigraphic assemblages of different ages and types. The layer identification is shown in Table 7., which lists the top values of the formations of different ages in the drilled wells. These were determined on the basis of the deep drilling base profiles (specific resistance, natural gamma, natural potential), core drilling, and the daily operational geological reports. The stratigraphic conditions are well illustrated in Figure 17., which shows a NW-SE (1) and a NE-SW (2) geological section and their section lines. The sections show the basin floor consisting of Paleozoic and Precambrian metamorphic rocks (marked in purple) and the discordantly overlain Miocene sedimentary sequence (marked in yellow). (MOL Plc, 2014)

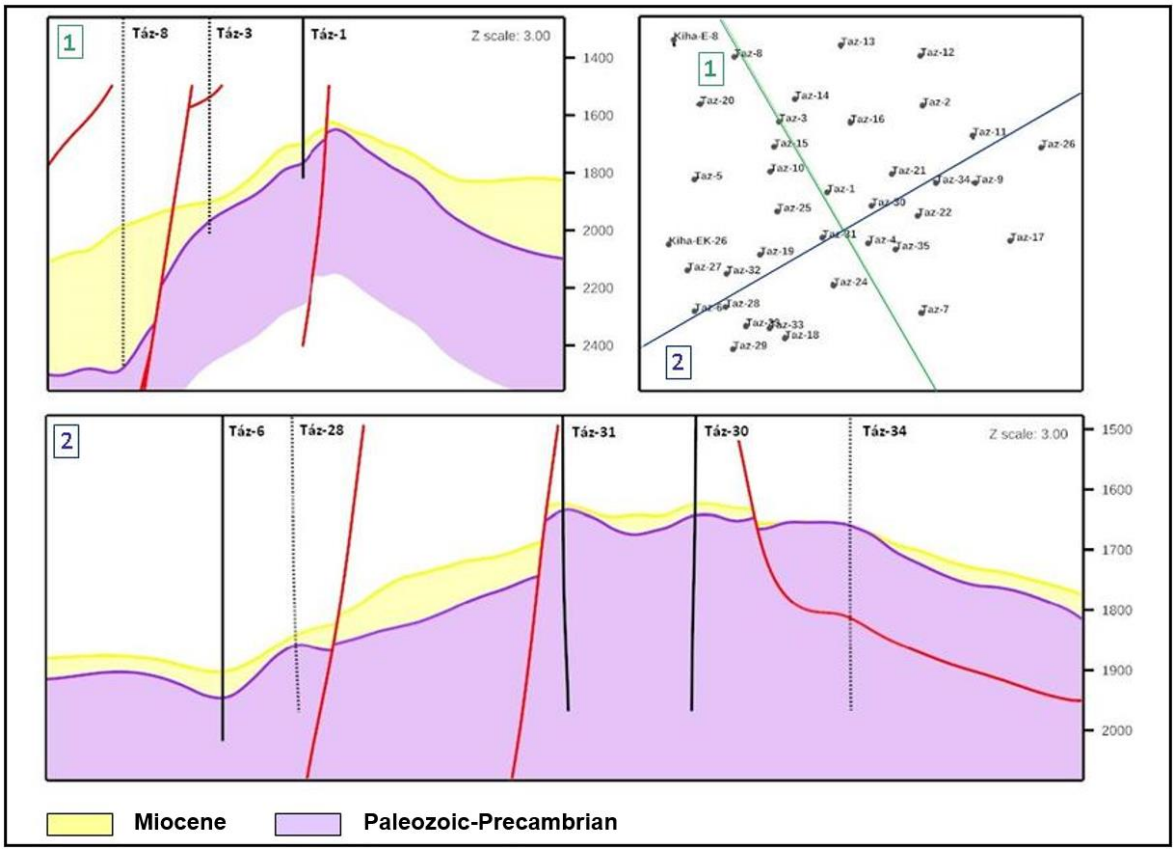


Figure 17. Geological cross-sections of the Tázlár area
(source: MOL Plc.)

## 6.4 LITHOLOGICAL AND STORAGE PROPERTIES MODEL

One of the aims of the modeling was to place the oil fields in their geological environment, and another was to model the spatial distribution of different rock types, thus providing a more comprehensive understanding of the geological conditions of the area. First, a lithological section (indicators) for the 35 Táz wells and the Kiha-É-8 and Kiha-ÉK-26 wells were determined, which created by combining the core drilling data, geological daily reports and the stratigraphic sequence provided in the final reports. Then the effective sections of the petrophysical interpretation into the sections were inserted, assigning a separate code to each site. Distinguished the following rock types and reservoir properties in the modeled area (discrete codes are given in parentheses):

0. marga, marl, clay marl
1. sandstone
2. conglomerate, breccia
3. limestone
4. metamorphic
5. No 1/a halmaztelep Miocene
6. No 1/a halmaztelep Precambrian
7. No 1 halmaztelep Miocene
8. No 2 halmaztelep Precambrian
9. Precambrian effective

The extension was performed using the RMS indicators module, which allows for stochastic modeling of heterogeneity. The individual rock types in the area show certain trends, confirming our geological assumptions. Breccia and conglomerate are the lowest rock types in the Miocene zone (Zone 1), thicker in the deeper structural parts and thinning towards the top. For the extension, was created an auxiliary surface based on well data (37 wells) below which only the given rock type can occur. In the case of the pelite rock type closing the Miocene sequence, the lowest surface was determined, above which only pelite occurs. For the lithothamnion limestone discovered in the area, a 3D trend based on its proportion in the wells (limestone thickness/total Miocene thickness) was created.

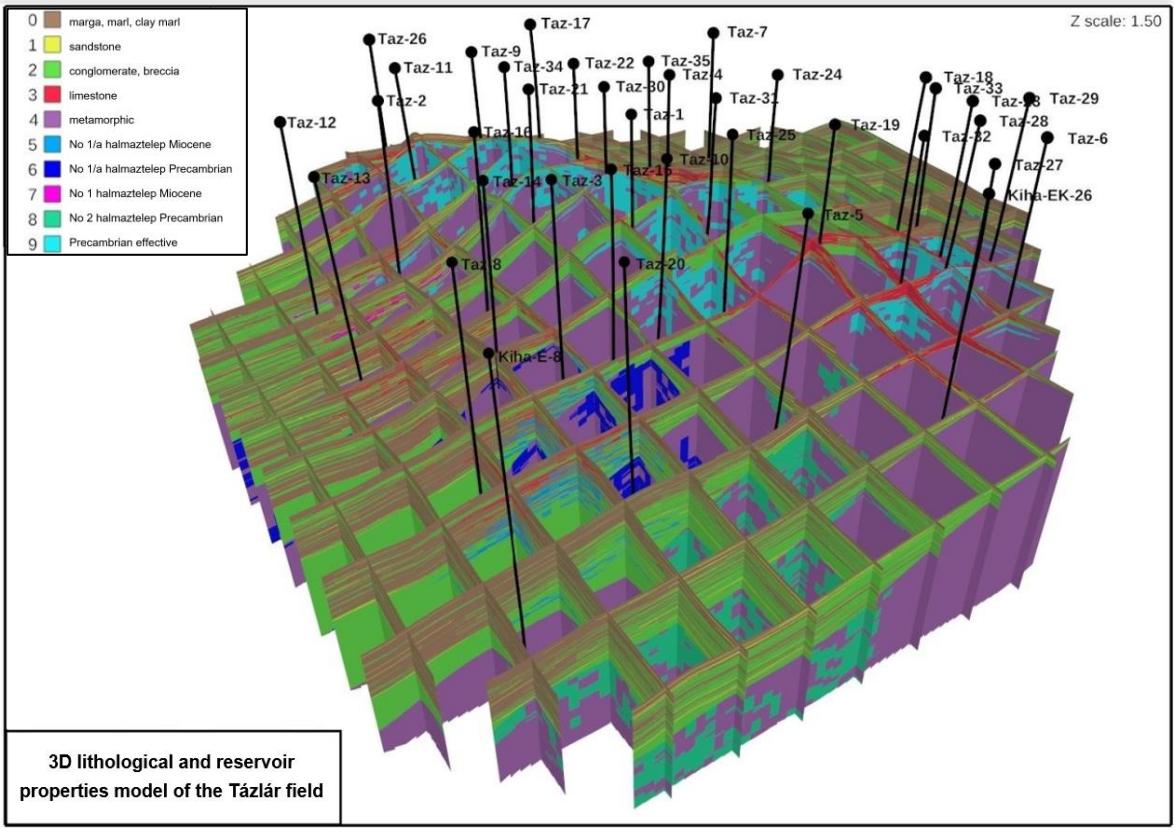


Figure 18. 3D lithological and reservoir properties model of the Tázlár area (source: MOL Plc.)

The lithological and reservoir property model was created in order to delimit the deposits by extending their effective rock volume. In order to separate the hydrodynamic systems formed above or below each other, the effective sections of the deposits were defined and extended as separate regions. The completed 3D lithological and reservoir property model is shown in a grid view in Figure 18.

# 7. LABOR MEASUREMENTS

## 7.1 DESIGNING ROCK CORES

The original drilling core samples were ensured by MOL Plc. They were selected based on the following criteria: physical condition, well type and location in the field, depth of origin, and known or probable mineral structure.

For the measurements, the 1.5" long cores were formed (drilling, end facing) in the research, at Research Institute of Applied Earth Sciences, University of Miskolc. The geometric and measured dry weight of the cylindrical cores are summarized in Table 8. The formation process of the used rocks for $CO_2$ flooding, there is an example shown in Figure 19. Based on time and facility limitations, the number of the cores had to be decreased. The selection criteria were: different type of wells, the location of origin and the known porosity, and if it is possible different lithology.

Some of the rock cores cracked during the formation process, others were damaged during the cutting of the endplates and had to be classified as incomplete. The formation of the damage was basically caused by the inhomogeneity of the rocks, which is clearly visible by eye in the photos. (Figures 90 to 108. in Appendix 2.)

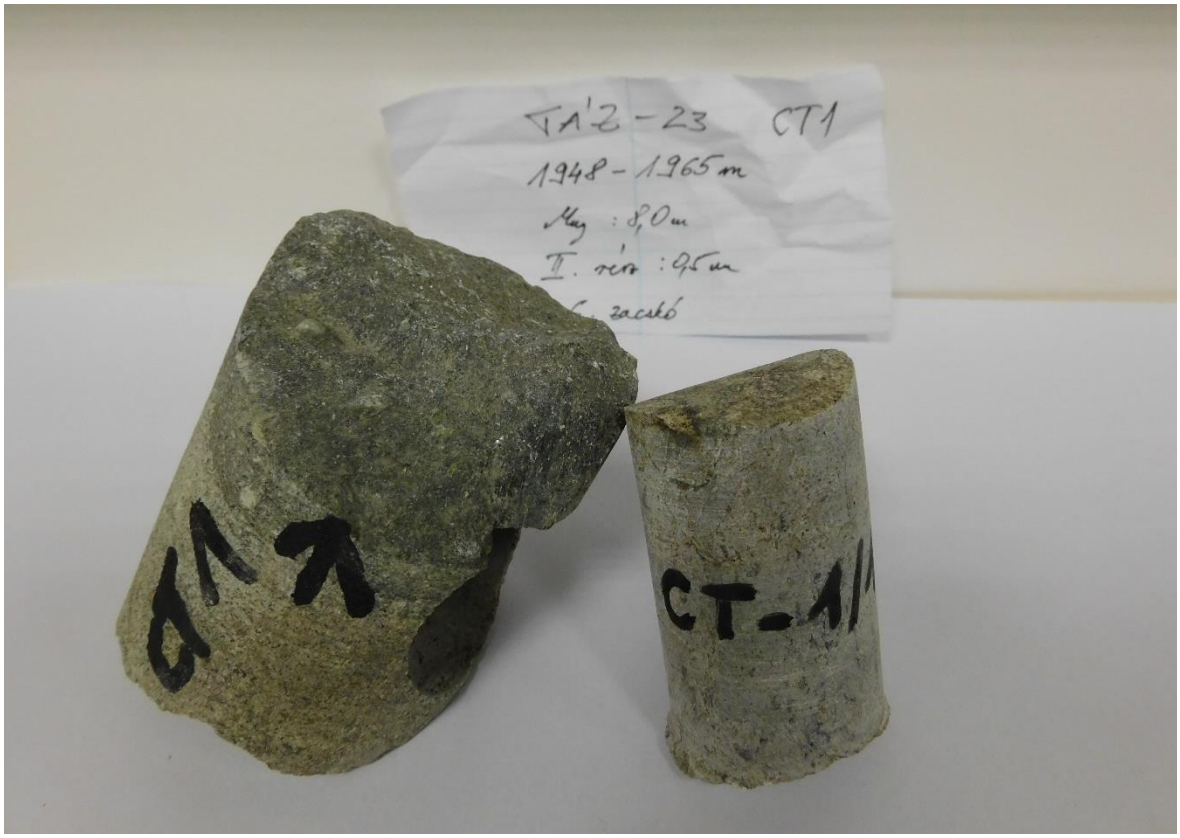


Figure 19. Design of the CT-1/1 rock core
(Recorded by the author)

Table 8. Geometric dry mass data for natural rock cores
(Edited by the author)

| Rocks | Length (cm) | Diameter (cm) | Volume ($cm^3$) | Dry mass (g) |
|---|---|---|---|---|
| **CT-1/1** | 4.552 | 3.811 | 51.924 | 139.540 |
| **CT-1A/1** | 4.306 | 3.822 | 49.402 | 132.780 |
| **CT-1B/1** | 4.849 | 3.815 | 55.428 | 148.250 |
| **CT-2/1** | 4.515 | 3.808 | 51.421 | 132.390 |
| **CT-2/2** | 4.350 | 3.814 | 49.698 | 128.730 |
| **CT-2/3** | 4.491 | 3.807 | 51.121 | 131.400 |
| **CT-3/1** | 4.619 | 3.811 | 52.688 | 120.700 |
| **CT-3/2** | 3.801 | 3.810 | 43.335 | 99.560 |
| **CT-4/1** | 4.269 | 3.808 | 48.619 | 125.970 |
| **CT-4/2** | 4.904 | 3.814 | 56.028 | 145.710 |
| **CT-5/1** | 4.712 | 3.808 | 53.665 | 137.200 |
| **CT-5/2** | 4.707 | 3.808 | 53.608 | 137.930 |
| **CT-5/3** | 4.704 | 3.809 | 53.602 | 137.540 |
| **CT-6/1** | 3.913 | 3.810 | 44.612 | 117.080 |
| **CT-7/1** | 4.043 | 3.810 | 46.094 | 106.110 |
| **CT-8/1** | 4.598 | 3.816 | 52.587 | 126.750 |
| **CT-10/1** | 5.178 | 3.809 | 59.003 | 142.920 |
| **CT-10A/1** | 6.254 | 3.805 | 71.114 | 171.090 |
| **CT-11/1** | 6.474 | 3.796 | 73.268 | 141.810 |
| **CT-11/2** | 6.789 | 3.813 | 77.523 | 162.570 |
| **CT-12/1** | 6.712 | 3.810 | 76.523 | 174.570 |
| **CT-12A/1** | 6.814 | 3.808 | 77.604 | 195.850 |
| **CT-12A/2** | 6.899 | 3.811 | 78.696 | 197.270 |

## 7.2 DETERMINATION OF HE POROSITY

### 7.2.1 HE POROSITY MEASUREMENT PRINCIPLE

The He pycnometer is used to measure the matrix density (rock particle density) or matrix volume (solid volume) of solid or powdered samples. The measurement is carried out by filling a reference cell of known volume $V_R$ with He gas up to a given pressure $p_1$ and then opening the reference cell by opening a valve to a cell of known volume $V_C$ containing the sample to be measured. As the volume increases, the gas undergoes an expansion which occurs as the initial pressure decreases, resulting in a pressure $p_2$. Before measurement, the system is calibrated at a given temperature using a calibration sphere of known volume. Using Boyle's Law for Ideal Gases, the volume occupied by a gas can be calculated from the pressure of a constant molar quantity of gas at a given volume ($p_1$; $V_R$) , and from its steady-state pressure following expansion ($p_2$). If the temperature is constant during the measurement, the volume occupied by the gas after expansion is the volume inside the cells ($V_R$ + $V_C$) minus the true pore-free volume of the sample $V_S$. (Iglauer et al. 2015; McPhee et al. 2015)

The equations used in the measurement are as follows:

The state of a cell containing a core sample at normal (atmospheric) pressure $p_a$ and $T_a$ at thermostatic temperature can be described as follows:

$$p_a \cdot (V_C - V_S) = n_a \cdot R \cdot T_a, \tag{17}$$

where $n_a$ is the number of moles of gas filling the cell volume $V_C - V_S$, where $V_S$ is the rock core is the volume of solid matter; R is the universal gas constant; $T_a$ is thermostatic temperature; $p_a$ is the normal (atmospheric) pressure in the laboratory.

When the reference volume $V_R$, which is known exactly, is filled with He gas (up to a pressure of approximately 17 psi ≈ 1.17 bar), the gas in the reference cell of volume $V_R$ can be described by the following equation:

$$p_1 \cdot V_R = n_1 \cdot R \cdot T_a \tag{18}$$

where, $p_1$ is the overpressure measured in the reference cell; $n_1$ is the number of moles of gas in a reference cell of volume $V_R$.

If the cell containing the core sample and the reference cell are compressed, the pressure decreases to a lower value, $p_{(2)}$, after a certain time, so that the following equation can be written for the compressed cells:

$$p_2 \cdot (V_C - V_S + V_R) = n_a \cdot R \cdot T_a + n_1 \cdot R \cdot T_a \tag{19}$$

Substituting $n_a \cdot R \cdot T_a$, or $n_1 \cdot R \cdot T_a$ in Equation 18, substitute $p_a \cdot (V_C - V_S)$, or $p_1 \cdot V_R$, and rearranging the equation.

$$V_C - V_S = \frac{(p_1 - p_2)}{(p_2 - p_a)} \cdot V_R \tag{20}$$

During the measurement, the atmospheric pressure is constant, and taking this into account, the equation can be simplified to Equation 21. This gives the solid volume $V_{(S)}$ of the rock sample in the sample container:

$$V_S = V_C - V_R \cdot \left[\left(\frac{p_1}{p_2}\right) - 1\right] \tag{21}$$

From the known dry mass of the rock sample $m_{dry}$ and the measured volume of solids in the sample $V_S$, the density of the solids in the rock sample, called the matrix density $\rho_{matrix}$, can be determined $\left(\frac{g}{cm^3}\right)$ (21). Knowing the true volume of the sample and its total volume $V_{total}$ calculated from its geometric data (diameter, length), the porosity $\phi_{He}$ can be determined using Equation 23.

$$\rho_{matrix} = \frac{m_{dry\ sample}}{V_S} \tag{22}$$

$$\phi_{He} = \frac{V_{dry\ sample} - V_S}{V_{dry\ sample}} \cdot 100\ \% \tag{23}$$

(Tanikawa & Shimamoto, 2006)

### 7.2.2 MEASURING HE POROSITY OF NATURAL ROCK CORES

The pre-designed rock cores with regular cylindrical geometry were dried in a drying oven to a constant weight. Afterwards, the He porosity of the samples was determined using an Ultra-pycnometer 1200e (Quanta chrome) at 21°C. The instrument is used to take 5 to 11 parallel measurements on the samples, of which the arithmetic means of five measurements (within a specified margin of error) is used to calculate the solid volume and matrix density of the rock sample. The difference between the volume resulting from the geometrical size of the sample and the volume of the solids (matrix) of the sample gives the pore volume, i.e. the He porosity of the sample. The porosity values determined for natural rock cores are summarized in Table 9. and plotted in Figure 20.

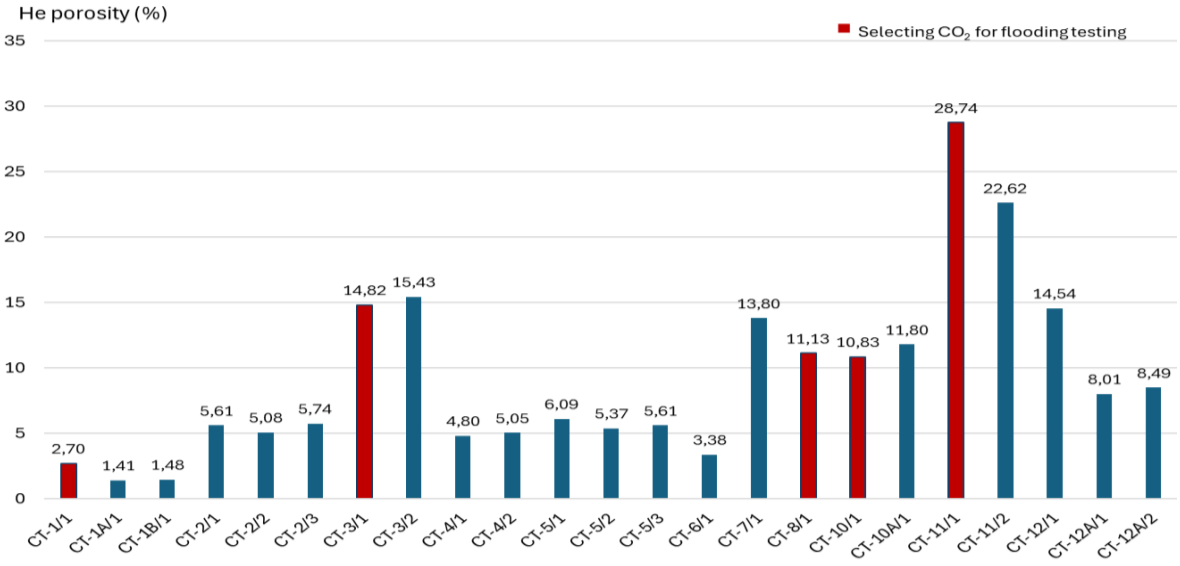


Figure 20. Porosity of natural rock cores He
(Edited by the author)

Table 9. Natural rock cores He porosity measurement data
(Edited by the author)

| Rocks | Matrix volume ($cm^3$) | Matrix density $\left(\frac{g}{cm^3}\right)$ | Booth. Dev (%) | He porosity (%) | Comment |
|---|---|---|---|---|---|
| **CT-1/1** | 50.5244 | 2.7618 | 0.0191 | 2.7000 | $CO_2$ flooding |
| CT-1A/1 | 48.7065 | 2.7261 | 0.0181 | 1.4100 | |
| CT-1B/1 | 54.6058 | 2.7149 | 0.0411 | 1.4800 | |
| CT-2/1 | 48.5345 | 2.7278 | 0.0075 | 5.6100 | |
| CT-2/2 | 47.1748 | 2.7288 | 0.0076 | 5.0800 | |
| CT-2/3 | 48.1883 | 2.7268 | 0.0094 | 5.7400 | |
| **CT-3/1** | 44.8790 | 2.6895 | 0.0050 | 14.8200 | $CO_2$flooding |
| CT-3/2 | 36.6469 | 2.7167 | 0.0065 | 15.4300 | incomplete |
| CT-4/1 | 46.2840 | 2.7217 | 0.0157 | 4.8000 | |
| CT-4/2 | 53.1997 | 2.7389 | 0.0073 | 5.0500 | |
| CT-5/1 | 50.3964 | 2.7224 | 0.0100 | 6.0900 | |
| CT-5/2 | 50.7270 | 2.7191 | 0.0061 | 5.3700 | |
| CT-5/3 | 50.5955 | 2.7184 | 0.0088 | 5.6100 | |
| CT-6/1 | 43.1036 | 2.7162 | 0.0051 | 3.3800 | cracked |
| CT-7/1 | 39.7327 | 2.6706 | 0.0086 | 13.8000 | incomplete |
| **CT-8/1** | 46.7357 | 2.7133 | 0.0061 | 11.1300 | $CO_2$ flooding |
| **CT-10/1** | 52.6149 | 2.7163 | 0.0093 | 10.8300 | $CO_2$ flooding |
| CT-10A/1 | 62.7263 | 2.7276 | 0.0085 | 11.8000 | |
| **CT-11/1** | 52.2100 | 2.7160 | 0.0041 | 28.7400 | $CO_2$ flooding |
| CT-11/2 | 59.9897 | 2.7100 | 0.0096 | 22.6200 | |
| CT-12/1 | 65.3939 | 2.6695 | 0.0033 | 14.5400 | |
| CT-12A/1 | 71.3889 | 2.7434 | 0.0095 | 8.0100 | |
| CT-12A/2 | 72.0125 | 2.7394 | 0.0100 | 8.4900 | incomplete |

## 7.3 DETERMINATION OF $N_2$ PERMEABILITY

The permeability to $N_2$ gas of rock samples pre-dried to mass permeability was determined using the procedure described below.

### 7.3.1 TOOLS

The gas permeability of samples is determined by using $N_2$ gas to investigate the flow resistances in the pore system of the samples. The core samples are placed in a Hassler - type cell, which is connected to the measuring device to record the inlet and outlet pressures during flow in the samples.

### 7.3.2 GAS PERMEABILITY MEASUREMENT PRINCIPLE

In the case of the Hassler-type core collector, the samples are placed in a rubber tube to which hydrostatic pressure is applied from the outside. This ensures that the pressure drop recorded for the set flow rate will be the value corresponding to the flow through the sample pore system. Increasing volume flow rates are obtained by incrementally

increasing the initial low pressure. Using the recorded data and the geometric parameters of the sample, the permeability of the rock sample to $N_2$ can be easily calculated using an Excel spreadsheet. The calculations are performed using the following rearrangement of Darcy's equation for gas flow (compressible fluids):

$$k_g = \frac{q_{ga} \cdot p_a \cdot \mu_g \cdot L}{A} \cdot \frac{2}{p_1^2 - p_a^2} \cdot \frac{1000}{0.9869} \quad [mD] \tag{24}$$

where $k_g$ is the permeability of the rock sample at a given pressure difference, (mD); A is the cross section of the rock sample perpendicular to the gas flow direction, ($cm^2$) ; L is the length of the rock sample (cm); $p_a$ outlet pressure of the gas flow (normal atmospheric pressure), atm; $q_{ga}$ measured volumetric flow rate of the gas at the outlet pressure$\left(\frac{cm^3}{s}\right)$, $\mu_g$ the viscosity of $N_2$, measured at average pressure and temperature, cP, and (mPa.s); $p_1$ measured inlet pressure of the gas (atm).

Plotting the $k_g$ values at each pressure difference $\Delta p$ as a function of the reciprocal of the mean pressure of the measurement $\frac{1}{p_{av}}$, fitting a line to the resulting points using the method of least squares, obtain the following relation 25. The relation allows to determine the constants $k_\infty$ , b describing the so-called Klinkenberg gas permeability of the rock sample under investigation.

$$k_g = k_\infty \cdot \left(1 + \frac{b}{p_{av}}\right) = k_\infty + k_\infty \cdot b \frac{1}{p_{av}} = k_\infty + m \cdot \frac{1}{p_{av}} \tag{25}$$

where, $k_\infty$ is the Klinkenberg equivalent permeability of the fluid (mD), b is the Klinkenberg constant $\left(\frac{1}{atm}\right)$, $k_g$ measured gas or air permeability (mD), $p_{av}$ average pressure of the gas permeability measurement $\frac{P_1+P_a}{2}$, (atm).

Equation 26, is a linear equation with the axis intercept $k_\infty$, of the liquid equivalent permeability k of the rock sample under investigation, and the slope m of the line (which is a function of the gas used in the measurement) allows the parameter b of the Klinkenberg equation to be determined.

$$b = \frac{m}{k_\infty} \tag{26}$$

where m is the slope (tangent) of the line, (mD atm). (Bobok 2012 ; R. Rezaee. and M. Lebedev 2015 ; Anovitz & Cole, 2024)

### 7.3.3 MEASUREMENT OF $N_2$ PERMEABILITY OF NATURAL ROCK CORES

The pre-designed rock cores with regular cylindrical geometry were dried in a drying oven to a constant weight. The $N_2$ permeability of the samples was then determined as described in the previous sections. The $N_2$ permeability values determined for the natural rock cores are summarized in Table 10. and plotted graphically in Figures 21 and 22.

Table 10. $N_2$ permeability of natural rock cores
(Edited by the author)

| Rocks | $N_2$ permeability (mD) | Comment |
|---|---|---|
| **CT-1/1** | **0.0159** | **$CO_2$ flooding** |
| CT-1A/1 | 0.0005 | |
| CT-1B/1 | 0.0009 | |
| CT-2/1 | 0.0110 | |
| CT-2/2 | 0.0150 | |
| CT-2/3 | 0.0180 | |
| **CT-3/1** | **44.8900** | **$CO_2$ flooding** |
| CT-3/2 | 12.8000 | incomplete |
| CT-4/1 | 0.0990 | |
| CT-4/2 | 0.0170 | |
| CT-5/1 | 0.0260 | |
| CT-5/2 | 0.0150 | |
| CT-5/3 | not assessable | |
| CT-6/1 | 0.0730 | cracked |
| CT-7/1 | 7.1500 | incomplete |
| **CT-8/1** | **0.1560** | **$CO_2$ flooding** |
| **CT-10/1** | **0.0560** | **$CO_2$ flooding** |
| CT-10A/1 | 0.0640 | |
| **CT-11/1** | **1.7390** | **$CO_2$ flooding** |
| CT-11/2 | 1.2300 | |
| CT-12/1 | 5.3500 | |
| CT-12A/1 | 0.0240 | |
| CT-12A/2 | 0.0790 | incomplete |

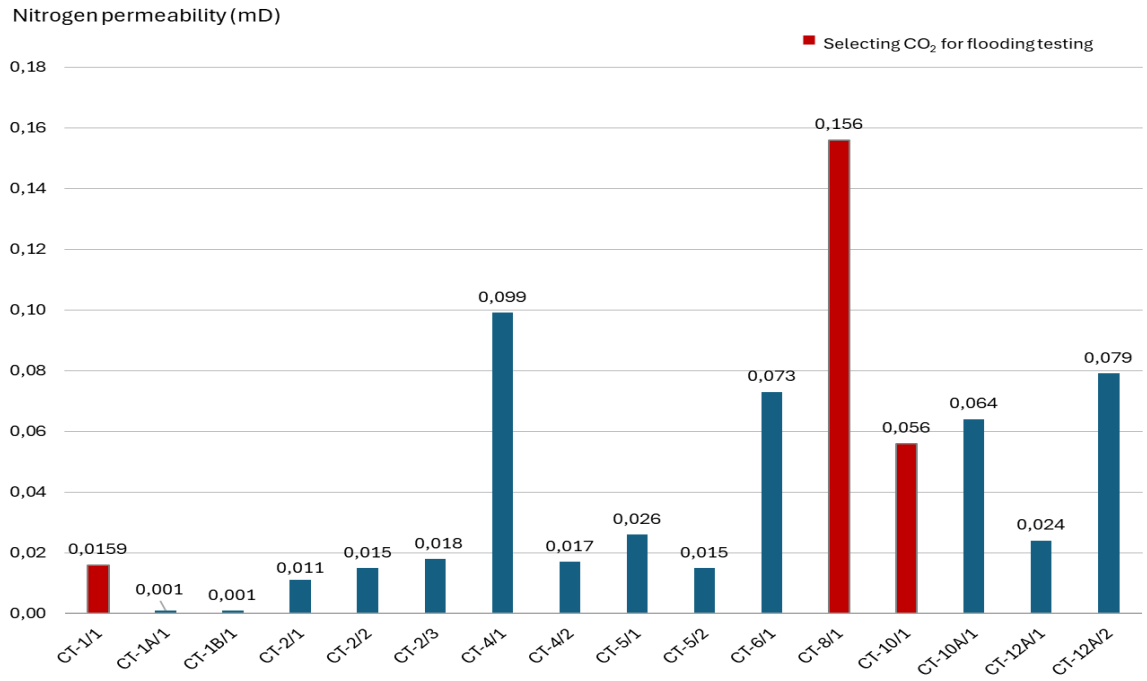


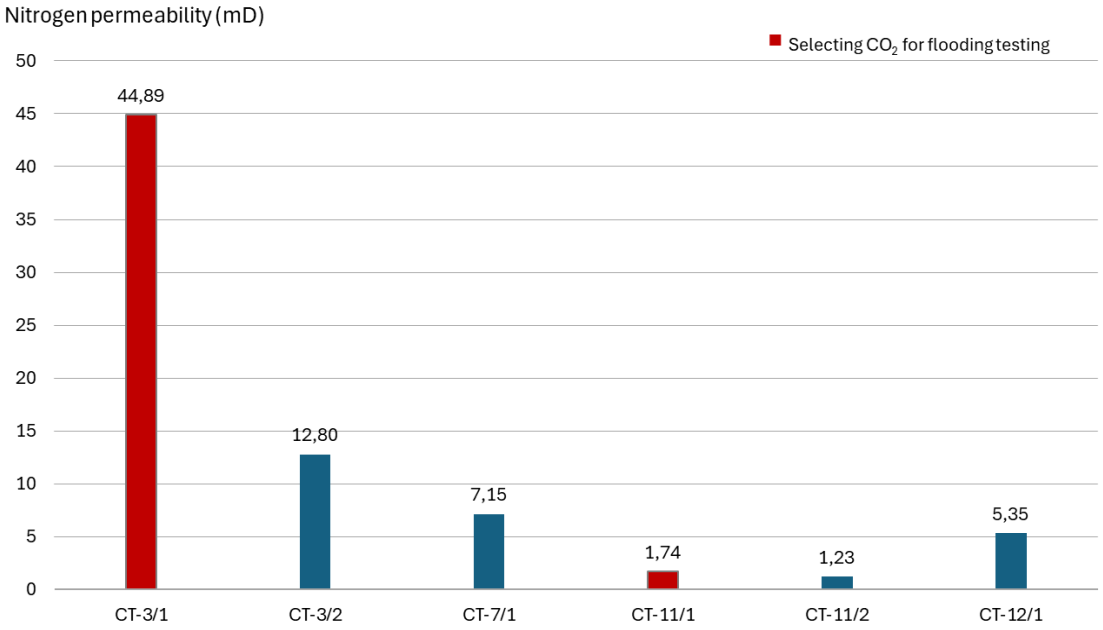


Figure 21 & 22. $N_2$ permeability of natural rock cores
(Edited by the author)

## 7.4 $CO_2$ FLOODING TESTS

Five cores have been designated to carry out $CO_2$ flooding tests. After placing the selected rocks in a pressure cell (Figure 23.), the cell was placed in a thermostat with the rocks and the desired temperature and $CO_2$ pressure were set. After the contact time, the cores were removed, dried again, and the He porosity and $N_2$ permeability measurements were performed again. The cores were then placed back in the pressure cell and the next flooding cycle was started. The contact time, temperature and pressure conditions used for each flooding are summarized in Table 11.

The flooding times, temperature and pressure values were determined taking into account the resources and laboratory equipment (cell, $CO_2$ gas cylinder, manometer) of the Research Institute of Applied Earth Sciences at the University of Miskolc. In the first flooding cycle, considered it important that $CO_2$ saturation also takes place in the gaseous state, and then, at the maximum achievable pressure (90 barg), several temperatures above the critical point of $CO_2$ were determined.

Table 11. Time, temperature and pressure data for $CO_2$ flooding cycles
(Edited by the author)

| **$CO_2$ flooding** | **Duration (weeks)** | **Temperature (°C)** | **Pressure (bar)** |
|---|---|---|---|
| Before $CO_2$ flooding | - | 23 | - |
| I. cycle of $CO_2$ flooding | 1 | 50 | 65 |
| II. cycle of $CO_2$ flooding | 1 | 100 | 90 |
| III. cycle of $CO_2$ flooding | 2 | 100 | 90 |
| IV. cycle of $CO_2$ flooding | 1 | 135 | 90 |
| V. cycle of $CO_2$ flooding | 1 | 135 | 90 |
| VI. cycle of $CO_2$ flooding | 2 | 135 | 90 |

Figure 23. The cell used for $CO_2$ flooding
(Recorded by the author)

## 7.5 RESULTS OF POROSITY AND PERMEABILITY MEASUREMENTS

After measuring the basic rock parameters, five samples were selected from 18 core samples based on their porosity and permeability, as well as their origin from different storage areas and lithology.

After the $CO_2$ treatment contact time had elapsed, the cores were removed from the pressure cell and the rock samples were dried in a drying oven until they reached a constant weight, after which repeated He porosity and $N_2$ permeability measurements were performed. The cores were then returned to the cell, and the next flooding cycle began.

After six measurement cycles, an increase in porosity and permeability was observed between the initial and final states for the CT-1/1 (quartz clay), CT-3/1 (conglomerate), and CT-8/1 (sandstone) samples. This was also confirmed by thin section examinations. $CO_2$ initiated dissolution in these samples from the Tázlár field, but no crystallization/carbonation process was observed. No clear pattern was observed in the case of CT-10/1 (bioclastic marl) and CT-11/1 (bioclastic limestone).

In the CT-10/1 sample, the He porosity increased after the first saturation cycle, then decreased under the influence of the second and third cycles. After treatments IV-V-VI, a clear increase was observed again. In the case of the measured $N_2$ permeability, there was initially a minimal decrease, followed by a clear increase after treatments IV-V-VI.
In sample CT-11/1, the He porosity values increased after the first and second $CO_2$ flooding, followed by a decrease and stagnation in the subsequent cycles. While the measured $N_2$ permeability decreased after treatments I and V, a slight increase was observed after the other cycles.

### 7.5.1 CT-1/1 SAMPLE

The results of the tests carried out are summarized in the table and figure below for the CT-1/1 natural rock core. It can be seen that there was a decrease and then an increase in He porosity due to the effect of the consecutive $CO_2$ flooding. (Figure 24.) A similar trend was observed for the measured $N_2$ permeabilities. (Figure 25.)

Table 12. Porosity and permeability data after $CO_2$ flooding: CT-1/1
(Edited by the author)

| Sample name | Length (cm) | Diameter (cm) | Dry mass (g) | He porosity (%) | $N_2$ permeability (mD) |
|---|---|---|---|---|---|
| CT-1/1 | 4.552 | 3.811 | 139.540 | 2.700 | 0.0159 |
| CT-1/1-I | 4.552 | 3.811 | 139.590 | 2.630 | 0.0168 |
| CT-1/1-II | 4.552 | 3.811 | 139.540 | 2.530 | 0.0162 |
| CT-1/1-III | 4.552 | 3.811 | 139.570 | 2.480 | 0.0161 |
| CT-1/1-IV | 4.552 | 3.811 | 139.480 | 2.660 | 0.0200 |
| CT-1/1-V | 4.552 | 3.811 | 139.480 | 2.720 | 0.0370 |
| CT-1/1-VI | 4.552 | 3.811 | 139.480 | 2.850 | 0.0284 |

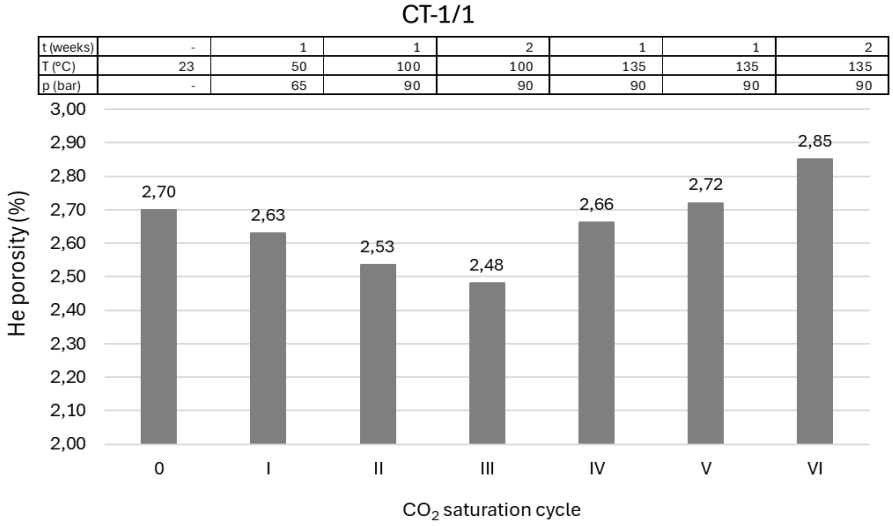


Figure 24. Measured He porosity values: CT-1/1 rock core
(Edited by the author)

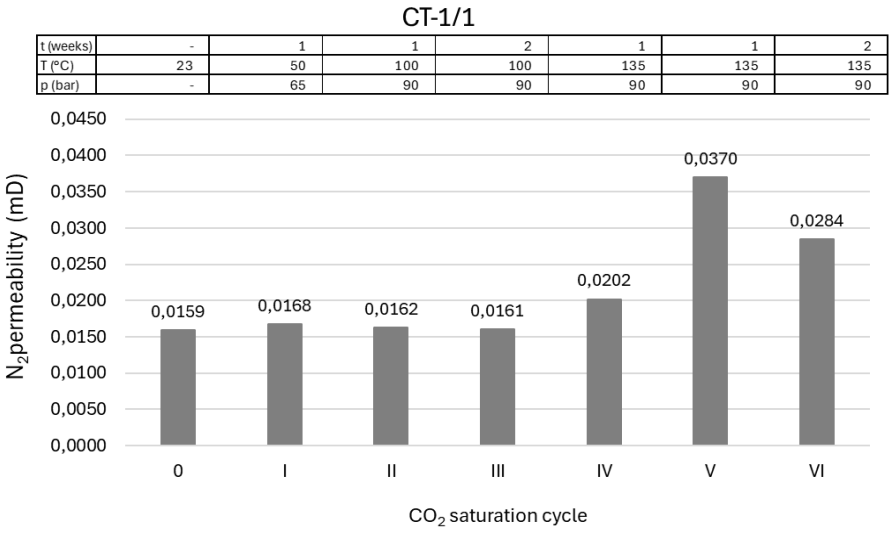


Figure 25. Measured $N_2$ permeability values: CT-1/1 rock core
(Edited by the author)

### 7.5.2 CT-3/1 SAMPLE

The results of the tests carried out are summarized in the table and figure below for CT-3/1 natural rock core. It can be seen that there was a clear increase in He porosity after treatments IV-V-VI. (Figure 26.) The same was even more pronounced for the measured $N_2$ permeabilities. (Figure 27.)

Table 13. Porosity and permeability data after $CO_2$ flooding: CT-3/1
(Edited by the author)

| Sample name | Length (cm) | Diameter (cm) | Dry mass (g) | He porosity (%) | $N_2$ permeability (mD) |
|---|---|---|---|---|---|
| CT-3/1 | 4.619 | 3.811 | 120.700 | 14.820 | 44.880 |
| CT-3/1-I | 4.619 | 3.811 | 120.700 | 15.020 | 44.480 |
| CT-3/1-II | 4.619 | 3.811 | 120.660 | 14.790 | 43.760 |
| CT-3/1-III | 4.619 | 3.811 | 120.650 | 14.780 | 44.860 |
| CT-3/1-IV | 4.619 | 3.811 | 120.580 | 14.920 | 53.340 |
| CT-3/1-V | 4.619 | 3.811 | 120.570 | 14.900 | 55.330 |
| CT-3/1-VI | 4.619 | 3.811 | 120.350 | 15.100 | 58.310 |

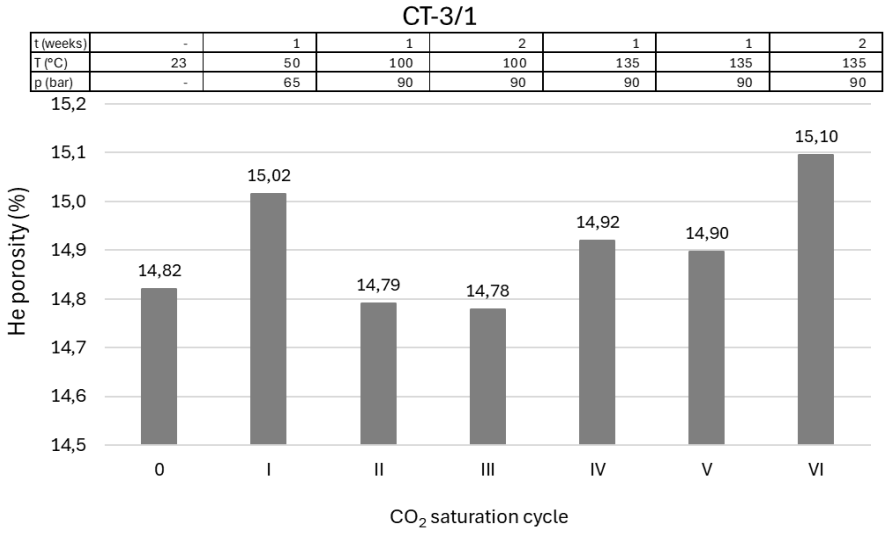


Figure 26. Measured He porosity values: CT-3/1 rock core
(Edited by the author)

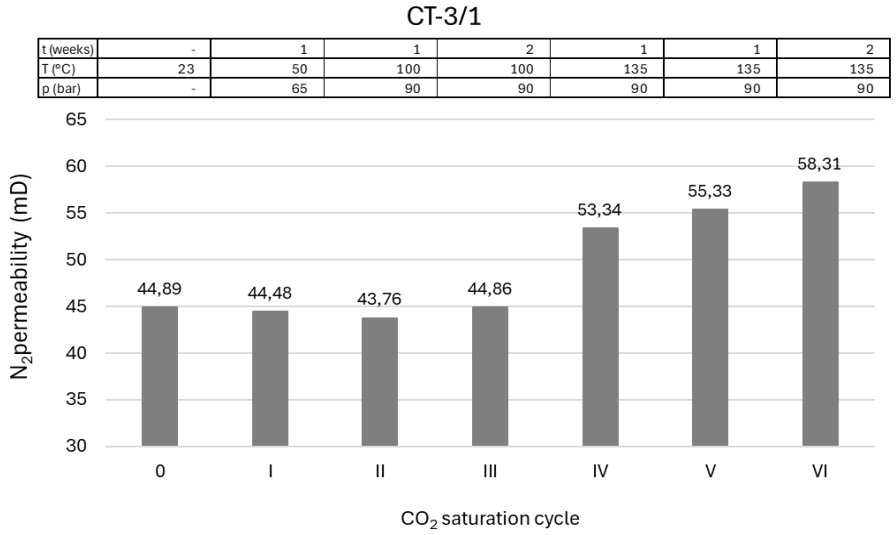


Figure 27. Measured $N_2$ permeability values: CT-3/1 rock core
(Edited by the author)

### 7.5.3 CT-8/1 SAMPLE

The results of the tests carried out are summarized in the following table and figures for the CT-8/1 natural rock core. It can be seen that the He porosity increased after the first and second $CO_2$ flooding treatments. and then decreased after the third treatment. After treatments IV-V-VI there was again a clear increase. (Figure 28.) While for the measured $N_2$ permeabilities. a minimal decrease was initially observed. followed by a clear increase after treatments IV-V-VI (Figure 29.).

Table 14. Porosity and permeability data after $CO_2$ flooding: CT-8/1
(Edited by the author)

| Sample name | Length (cm) | Diameter (cm) | Dry mass (g) | He porosity (%) | $N_2$ permeability (mD) |
|---|---|---|---|---|---|
| CT-8/1 | 4.598 | 3.816 | 126.750 | 11.130 | 0.156 |
| CT-8/1-I | 4.598 | 3.816 | 126.810 | 11.240 | 0.150 |
| CT-8/1-II | 4.598 | 3.816 | 126.750 | 11.230 | 0.151 |
| CT-8/1-III | 4.598 | 3.816 | 126.740 | 11.150 | 0.158 |
| CT-8/1-IV | 4.598 | 3.816 | 126.760 | 11.170 | 0.168 |
| CT-8/1-V | 4.598 | 3.816 | 126.710 | 11.200 | 0.169 |
| CT-8/1-VI | 4.598 | 3.816 | 126.70 | 11.280 | 0.195 |

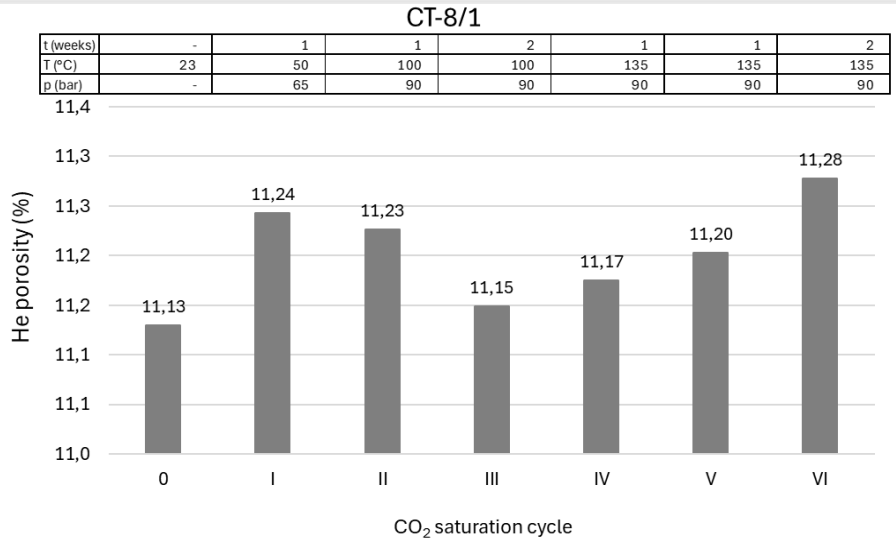


Figure 28. Measured He porosity values: CT-8/1 rock core
(Edited by the author)

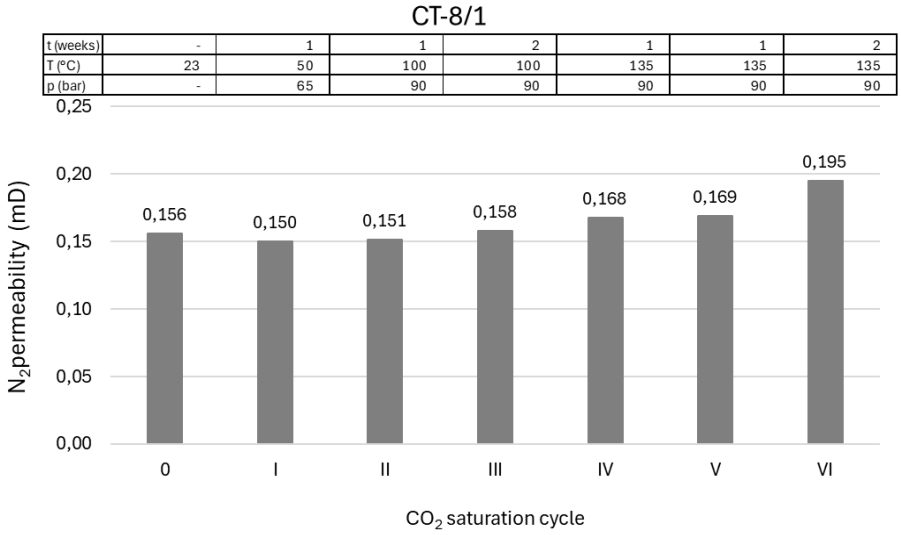


Figure 29. Measured $N_2$ permeability values: CT-8/1 rock core
(Edited by the author)

### 7.5.4 CT-10/1 SAMPLE

The results of the tests carried out are summarized in the following table and figures for the CT-10/1 natural rock core. It can be seen that the porosity of He increased after the first $CO_2$ flooding and decreased after the second and third treatments. After treatments IV-V-VI there was again a clear increase. (Figure 30.) While the measured $N_2$ permeabilities showed a minimal decrease initially. followed by a clear increase after treatments IV-V-VI. (Figure 31.)

Table 15. Porosity and permeability data after $CO_2$ flooding: CT-10/1
(Edited by the author)

| Sample name | Length (cm) | Diameter (cm) | Dry mass (g) | He porosity (%) | $N_2$ permeability (mD) |
|---|---|---|---|---|---|
| CT-10/1 | 5.178 | 3.809 | 142.920 | 10.830 | 0.056 |
| CT-10/1-I | 5.178 | 3.809 | 142.920 | 10.880 | 0.051 |
| CT-10/1-II | 5.178 | 3.809 | 142.90 | 10.750 | 0.054 |
| CT-10/1-III | 5.178 | 3.809 | 142.900 | 10.680 | 0.053 |
| CT-10/1-IV | 5.178 | 3.809 | 142.920 | 10.750 | 0.061 |
| CT-10/1-V | 5.178 | 3.809 | 142.900 | 10.810 | 0.064 |
| CT-10/1-VI | 5.178 | 3.809 | 142.820 | 10.860 | 0.069 |

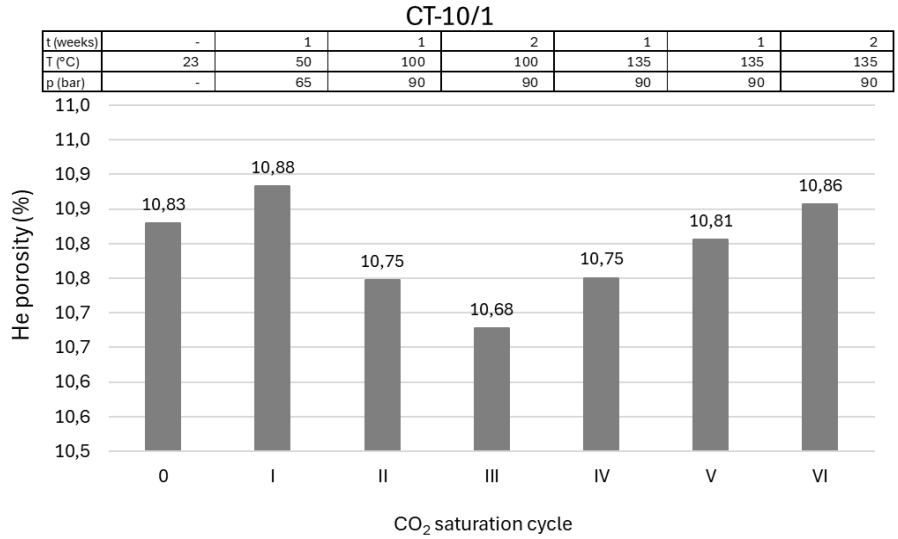


Figure 30. Measured He porosity values: CT-10/1 rock core
(Edited by the author)

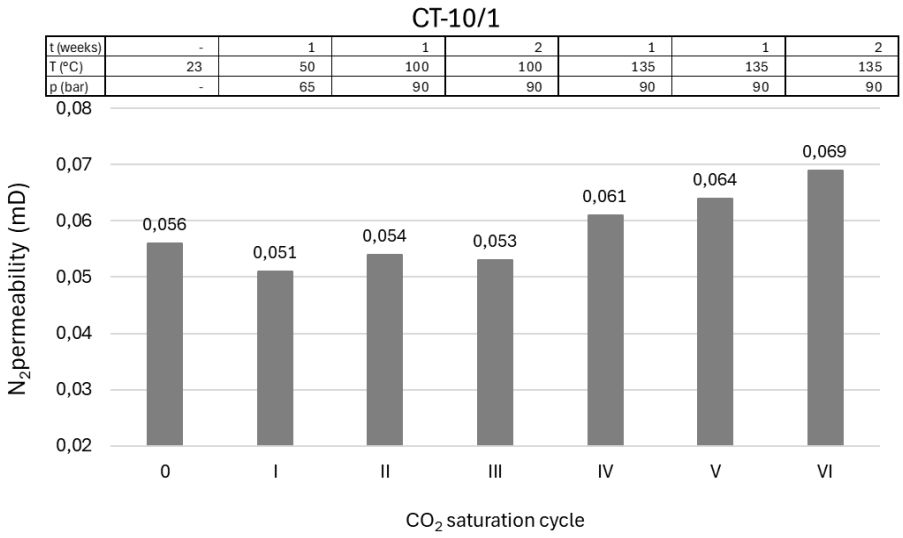


Figure 31. Measured $N_2$ permeability values: CT-10/1 rock core
(Edited by the author)

### 7.5.5 CT-11/1 SAMPLE

The results of the tests carried out are summarized in the following table and figures for the CT-11/1 natural rock core. It can be seen that the evolution of the He porosity values showed a decrease after the first and second $CO_2$ flooding and a decrease-stagnation after the subsequent treatments. (Figure 32.) While the measured $N_2$ permeabilities showed a decrease after treatments I and V. the others showed a slight increase. (Figure 33.)

Table 16. Porosity and permeability data after $CO_2$ flooding: CT-11/1
(Edited by the author)

| Sample name | Length (cm) | Diameter (cm) | Dry mass (g) | He porosity (%) | $N_2$ permeability (mD) |
|---|---|---|---|---|---|
| CT-11/1 | 6.474 | 3.796 | 141.810 | 28.740 | 1.739 |
| CT-11/1-I | 6.474 | 3.796 | 141.810 | 28.810 | 1.729 |
| CT-11/1-II | 6.474 | 3.796 | 141.730 | 28.830 | 1.807 |
| CT-11/1-III | 6.474 | 3.796 | 141.730 | 28.750 | 1.810 |
| CT-11/1-IV | 6.474 | 3.796 | 141.740 | 28.750 | 1.832 |
| CT-11/1-V | 6.474 | 3.796 | 141.810 | 28.710 | 1.765 |
| CT-11/1-VI | 6.474 | 3.796 | 141.800 | 28.710 | 1.958 |

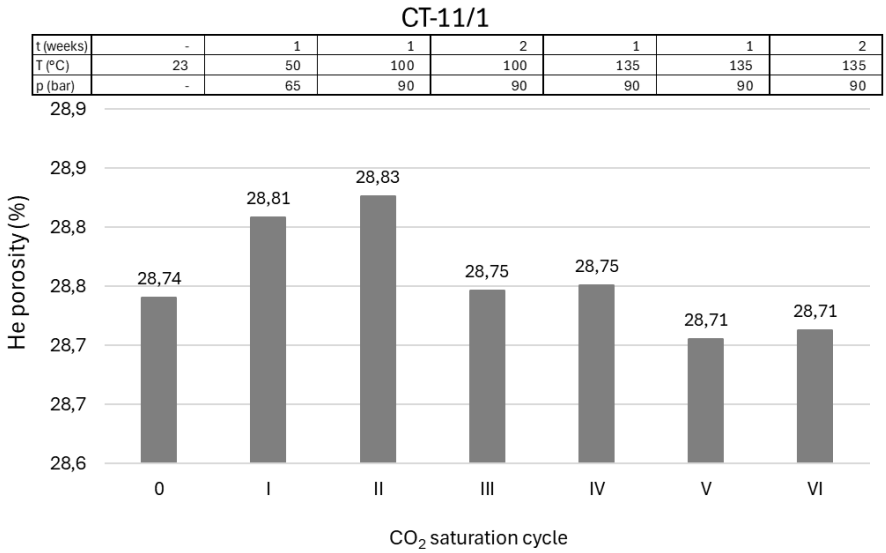


Figure 32. Measured He porosity values: CT-11/1 rock core
(Edited by the author)

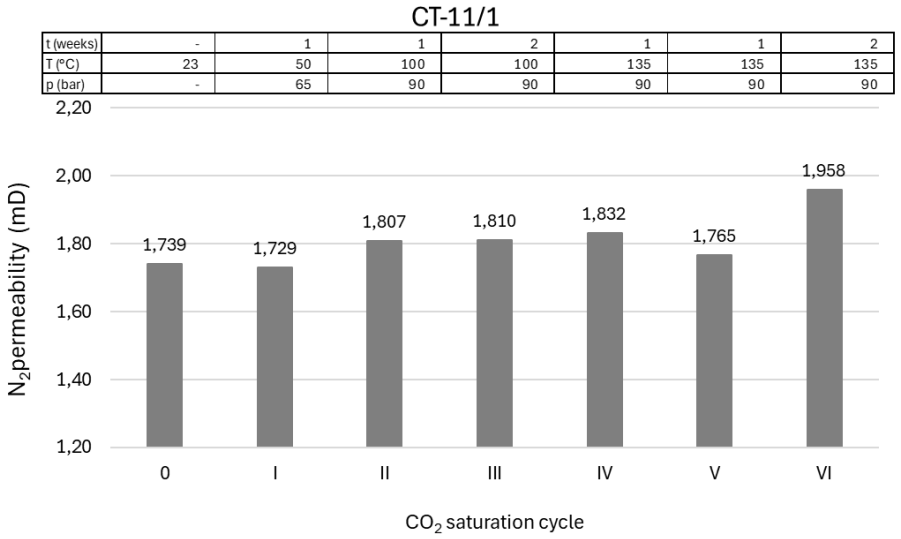


Figure 33. Measured $N_2$ permeability values: CT-11/1 rock core (Edited by the author)

## 7.6 OPTICAL MICROSCOPIC EXAMINATION OF THE THIN SECTIONS

### 7.6.1 PROCESS DESCRIPTION OF THIN SECTION PREPARATION FOR MICROSCOPIC ANALYSIS

The sample preparation for microscopic analysis was systematically carried out at the Department of Applied Mineralogy, part of the Institute of Exploration Geosciences in University of Miskolc. The thin-section preparation followed a rigorous protocol designed to ensure high-quality results suitable for petrographic and mineralogical investigation.

**Drying**: Samples were dried for a minimum of 12 hours in a drying oven set to a maximum of 60 °C. This step is essential to remove moisture that could interfere with resin embedding and subsequent polishing stages.

**Embedding:** The dried samples were embedded in Araldite 2020, a two-component epoxy resin, mixed with a blue pore-staining powder. The mixture was prepared in precise proportions to ensure uniform penetration and visibility of pore structures. The curing period was three days, allowing full polymerization of the resin.

**Trimming and Surface Grinding:** After curing, the samples were trimmed to appropriate dimensions using a precision cutting machine. Surface grinding was performed using silicon carbide (SiC) abrasive papers in sequential grit sizes: 500, 800, 1,000, 1,200 and 2,000. Between each grinding stage, samples were ultrasonically cleaned in distilled water to prevent cross-contamination of abrasive particles.

**Mounting:** The polished surface of each sample was mounted onto a matte glass slide using the Araldite 2020 resin. Another three-day drying period followed to ensure strong adhesion.

**Final Trimming and Polishing:** The top layer of the sample was removed using a precision cutter to achieve the desired final thickness of approximately 30 µm, suitable for transmitted light microscopy. The surface was then re-polished using the same sequence of SiC papers. Final polishing was conducted on a RotoPol-35 machine using diamond polishing compounds with decreasing particle sizes: 6 µm, 3 µm, 1 µm, and finally ¼ µm. Between each polishing stage, ultrasonic cleaning in petroleum ether was performed.

**Microscopic Analysis:** Thin sections were analyzed using a Zeiss Imager, A2m AXIO polarizing microscope, equipped with a Zeiss Axio Cam MRc5 camera for high-resolution image capture.

### 7.6.2 RESULTS

In this chapter, the results of the mineralogical analysis of thin sections, prepared before and after $CO_2$ flooding, were summarized. In the appendices (see Appendix 3.) there are included some very impressive photographs in which the individual sections are clearly visible on Figures 109 – 146.

#### 7.6.2.1 CT 1/1 sample

**Untreated sample**

Mineral creators:

- Quartz: The presence of xenomorphic grains with a size range of 100–500 µm is observed, accompanied by undulatory staining and cracked grains. The formation of polycrystalline clusters and lenses is also noted.
- Calcite: observed as a crack filler or vein filler and forming irregularly shaped polycrystalline clusters, sometimes polysynthetic twinned
- Chlamydia: platy appearance, biotite and muscovite residues, Fe-oxidized
- Olivine: 1 ~100 µm grain, compact, intact, unbroken crystal
- Plagioclase: 200-800 µm in size, hypidiomorphic/xenomorphic, highly disaggregated, polysynthetically veined, quartz-confined, calcitised
- Fe-oxide: vascular microscopy shows goethite, the sample is highly Fe-oxidized, especially along the mica plates and cracks
- Pyrite: 10-50 µm particles, observed in cracks/veins through the sample with Fe oxide

Tissue: metamorphic, larger mineral clusters/lenses in microcrystalline matrix, directional fabric, lineation, mineral clusters and fissures are directionally positioned in the sample, angled to form secondary fissures (filled with calcite)
Fissures, veins: veins parallel to orientation filled with Fe oxide, veins parallel to orientation filled with calcite

**$CO_2$ treated sample:**

- Mineral constituents: same as in the untreated sample
  - In several places, a microcrystalline calcitic cluster can be observed in place of disintegrated minerals (plagioclase)
- Fabric: same as untreated sample
- Fissures, veins: more unfilled cracks (new), they are located in line with the orientation

The name of the rock: quartz clay shale

#### 7.6.2.2 CT 3/1 sample

**Untreated sample:**

Mineral creators:

- Quartz: xenomorphic grains of 100-800 μm, undulatory spotting, cracked grains, also forming polycrystalline clusters/lenses, and polycrystalline clusters of grain size 10-20 μm
- Calcite: xenomorphous particles of 50-200 μm and pore-filling microcrystalline aggregates
- Muscovite: 100-400 μm in size, lamellar appearance
- Olivine: 1-2 ~100 μm grains, chunky, prismatic in shape, intact, not disintegrated
- Plagioclase: 200-800 μm in size, hypidiomorphic/xenomorphic, polysynthetically clotted, disintegrated, often calcitised
- Fe-oxide: Fe-oxide weathering is characteristic of the sample

Fabric: highly porous, cracked rock and cracked grains
Cracks, pores: unfilled, pores up to 300 μm in size, but usually <100 μm

**$CO_2$ treated sample:**

- Mineral constituents: same as in the untreated sample
- The rock is also heavily fractured, the raw material and the minerals
- Fabric: same as untreated sample
- Cracks, pores: more pores, increased interstitial space, wider cracks (100-500 μm wide)

Rock name: Conglomerate

### 7.6.2.3 CT 8/1 sample

**Untreated sample:**

Mineral creators:

- Quartz: xenomorphic grains 100-500 µm, undulatory staining, slightly fissured grains, also forming polycrystalline clusters
- Calcite: pore filler, microcrystalline aggregates, cementitious material?
- Muscovite: 100-400 µm in size, plate-like, lath-like appearance

Fabric: solid fabric

Cracks, pores: few in the sample, unfilled pores between the grains are generally <100 µm

**$CO_2$ treated sample:**

- Mineral constituents: same as in the untreated sample
- Another rock-forming mineral:
- Plagioclase: 200-500 µm in size, hypidiomorphic/xenomorphic, polysynthetically clotted, disintegrated, calcitised
- More degraded material, and a higher proportion of it than in the untreated sample
- Fabric: same as untreated sample
- Cracks, pores: more pores and cracks, increased interstitial space, wider cracks

Rock name: Sandstone

### 7.6.2.4 CT 10/1 sample

**Untreated sample:**

Mineral creators:

- Quartz:
  - Two types of particle size: polycrystalline clusters of 100-500 µm and <30 µm
  - Xenomorphic granules, undulatory efflorescence, cracked
- Calcite:
  - xenomorphous granules of 100-300 µm, sometimes polysynthetic and sometimes increased
  - Limestone fossil skeleton and filler material
  - Pore- and crack-filling microcrystalline aggregates
- Muscovite: 100-500 µm in size, platy appearance
- The sample contains calcareous fossils
- Cracks, pores: 1-1 grain may have fallen out, polycrystalline quartz clusters have larger cracks and pores (20-50 µm), fossils and calcitic fillings are microporous

**$CO_2$ treated sample:**

- Mineral constituents: same as in the untreated sample
  - A larger clast Fe-oxidized
  - In Muscovite, undulating extinction can also be observed
  - Plagioclase: 500-1000 µm in size, hypidiomorphic, polysynthetically twinned, slightly broken, inclusions
- The sample contains calcareous fossils
- Cracks. pores: cracks and pores within the granules are more open

Rock name: Bioclastic marble

#### 7.6.2.5 CT 11/1 sample

**Untreated sample:**

Mineral creators:

- Calcite:
  - xenomorphous granules of 100-200 µm, sometimes polysynthetic and increased
  - Limestone fossil skeleton and filler material
  - Pore- and crack-filling microcrystalline aggregates
  - Cement: microcrystalline calcite
  - Quartz: occasionally 1-1 xenomorphic grains, 100-200 µm in size, cracked

The sample contains calcareous fossils

Cracks, pores: microporous (hence blue sample), larger pores/cracks filled with calcite

**$CO_2$ treated sample:**

- Mineral constituents: same as in the untreated sample
  - More about quartz grains
- The sample contains calcareous fossils
- Fissures, pores: larger intergranular space (bluer pattern), there are unfilled cracks between the grains, within the grains and through the grains

Rock name: Bioclastic limestone

# 8. RESULTS OF COMPUTER TOMOGRAPHY MEASUREMENTS

## 8.1 HUMAN COMPUTED TOMOGRAPHY INTERPRETATIONS OF CORE SAMPLES

The (human) CT processing and interpretation were carried out by the Institute of Radiology at the University of Pécs in collaboration with TOMOGEO Ltd. Hungary. The objective was to acquire comprehensive data on the porosity and structural system of the core samples. Additionally. it aimed to ensure the digital documentation of the material in the form of a 3D density block. 18 samples were measured, the rock samples were selected to have “as much heterogeneous overall picture, as it possible” regarding all the relevant storage tanks caprock and reservoir rock formations.

In the next section, it can be found, based on CT measurement interpretation and the most important average data of the measured data profile and the porosity profile. The average of contiguous small subareas inside the porosity total area in the measurement slices determined in the pixel unit. The CT processing was carried out with Siemens computer tomograph on core material the high resolution of the data set was 0.21 · 0.21 · 0.6 mm (slice thickness).

The observations and evaluations for each sample were summarized in the following form:
It was performed a simple statistical interpretation for the different samples of the whole core from the survey data, in the course of which defined the mean -, minimum -, maximum value and the standard deviation. The 3D visual (color coded) mapping of the measurement and porosity data on the basis of the statistical interpretation done. The average data of the most important parameter distributions(Porosity, Lithology, Avg size, Perimeter, Fractal D) were compared, see below in Tables 17,18 and Appendix 4.

Table 17. Comparison of average data for samples
(Edited by the author, source TOMOGEO Ltd.)

| Mean [H.U.] | Min [H.U.] | Max [H.U.] | POR % | Sample ID | Lithology | Avg Size [px] | Perimeter | FractalD |
|---|---|---|---|---|---|---|---|---|
| 2,140 | 1,285 | 3,120 | 0.500 | **CT1** | metamorphic | 0.600 | 1.570 | 0.780 |
| 2,160 | 1,275 | 3,134 | 0.170 | **CT1A** | metamorphic | 0.200 | 1.310 | 0.770 |
| 2,130 | 1,399 | 3,120 | 0.060 | **CT1/B** | metamorphic | 0.120 | 1.170 | 0.440 |
| 2,040 | 1,111 | 3,150 | 0.430 | **CT6** | metamorphic | 0.210 | 1.620 | 0.580 |
| 2,192 | 923 | 2,952 | 1.780 | **CT2** | breccia | 0.640 | 2.740 | 0.900 |
| 2,108 | 550 | 2,944 | 4.660 | **CT2A** | breccia | 0.960 | 3.590 | 1.090 |
| 1,650 | -5 | 2,814 | 3.770 | **CT3** | breccia | 0.550 | 2.680 | 1.190 |
| 2,186 | 868 | 3,053 | 2.590 | **CT4** | breccia | 0.590 | 2.700 | 1.150 |
| 2,164 | 938 | 2,905 | 2.240 | **CT5** | breccia | 0.640 | 2.830 | 0.930 |
| 1,774 | -76 | 3,199 | 5.660 | **CT12A** | breccia | 1.350 | 3.980 | 1.140 |
| 1,708 | -78 | 3,199 | 5.900 | **CT7** | sandstone | 0.510 | 2.470 | 1.450 |
| 1,772 | 1,133 | 2,700 | 4.840 | **CT8** | sandstone | 0.320 | 1.850 | 0.620 |
| 2,002 | 418 | 3,054 | 2.410 | **CT9** | sandstone | 0.300 | 1.890 | 0.690 |
| 2,091 | 887 | 3,084 | 2.180 | **CT10** | sandstone | 0.260 | 1.750 | 0.630 |
| 2,016 | 435 | 3,026 | 5.290 | **CT10A** | sandstone | 0.320 | 1.900 | 0.730 |
| 1,583 | -171 | 2,653 | 10.920 | **CT11** | sandstone | 8.950 | 8.900 | 1.350 |
| 1,623 | -485 | 2,678 | 6.790 | **CT12** | sandstone | 2.150 | 6.100 | 1.120 |
| 2,049 | 1,264 | 2,729 | 0.940 | **CT13** | siltstone | 0.160 | 1.370 | 0.900 |

Table 18. Comparison of average data of samples
(Edited by the author, source TOMOGEO Ltd.)

| Count % | Circle | Circle (0.7) | Sample id | Lithology |
|---|---|---|---|---|
| 16.500 | 0.848 | 0.496 | **CT1** | metamorphic |
| 29.800 | 0.745 | 0.352 | **CT1A** | metamorphic |
| 12.700 | 0.871 | 0.531 | **CT1/B** | metamorphic |
| 19.700 | 0.819 | 0.518 | **CT6** | metamorphic |
| 24.000 | 0.795 | 0.511 | **CT2** | breccia |
| 28.800 | 0.767 | 0.492 | **CT2A** | breccia |
| 25.200 | 0.787 | 0.525 | **CT3** | breccia |
| 22.500 | 0.803 | 0.512 | **CT4** | breccia |
| 23.500 | 0.795 | 0.509 | **CT5** | breccia |
| 30.500 | 0.770 | 0.481 | **CT12A** | breccia |
| 19.800 | 0.800 | 0.537 | **CT7** | sandstone |
| 16.000 | 0.838 | 0.532 | **CT8** | sandstone |
| 16.500 | 0.814 | 0.517 | **CT9** | sandstone |
| 15.900 | 0.829 | 0.491 | **CT10** | sandstone |
| 12.500 | 0.848 | 0.530 | **CT10A** | sandstone |
| 34.800 | 0.744 | 0.465 | **CT11** | sandstone |
| 37.000 | 0.726 | 0.454 | **CT12** | sandstone |
| 10.300 | 0.887 | 0.559 | **CT13** | siltstone |

### 8.1.1 METAMORPHIC ROCK MATERIAL SAMPLES

Well: Táz-23 Core#1 1,948-1,965 m: CT1, CT1A, CT1B samples
Well: Táz-15 Core#6 2,031-2,035 m: CT6 sample

They have low porosity (average: 0.29 %) and high density (H.U. average: 2,117). 20 % of the porosity elements are elongated – cracks, but the full-volume cracks are all closed and filled. (Figure 34.) More important average data in Table 19. contains. Porosity-increasing factors cannot be decided on the basis of the measurements. Based on the available samples, the matrix porosity is very low, so the permeability cannot be evaluated.

The evaluation of measurements highlights the inherently low porosity and high density of metamorphic rocks. These core samples, potentially originating from the cap rock, offer crucial insights. Further investigation of these samples could address key questions regarding the integrity of Carbon Capture and Storage (CCS) and inform subsequent research activities.

Metamorphic rocks, such as schist and gneiss, typically exhibit low porosity due to the recrystallization processes that fill pore spaces with denser minerals. Their high density often results from the presence of heavy minerals like garnet and pyroxene.
The core samples' potential origin as cap rock is significant for CCS applications, as effective cap rocks are essential in preventing the escape of stored $CO_2$. Metamorphic rocks, with their low permeability and high mechanical strength, can serve as excellent barriers.
Understanding the integrity of cap rocks is crucial for ensuring the long-term security of $CO_2$ storage sites. Studies focusing on the geo-mechanical properties, mineral composition, and potential fracturing of cap rocks can provide valuable data.

Further analysis of these metamorphic rock samples will likely involve sophisticated techniques such as X-ray computed tomography (CT) and scanning electron microscopy (SEM). These methods can offer detailed 3D imaging and mineralogical analysis, essential for assessing the potential for $CO_2$ leakage and the overall stability of the storage formation. (Figure 34.)

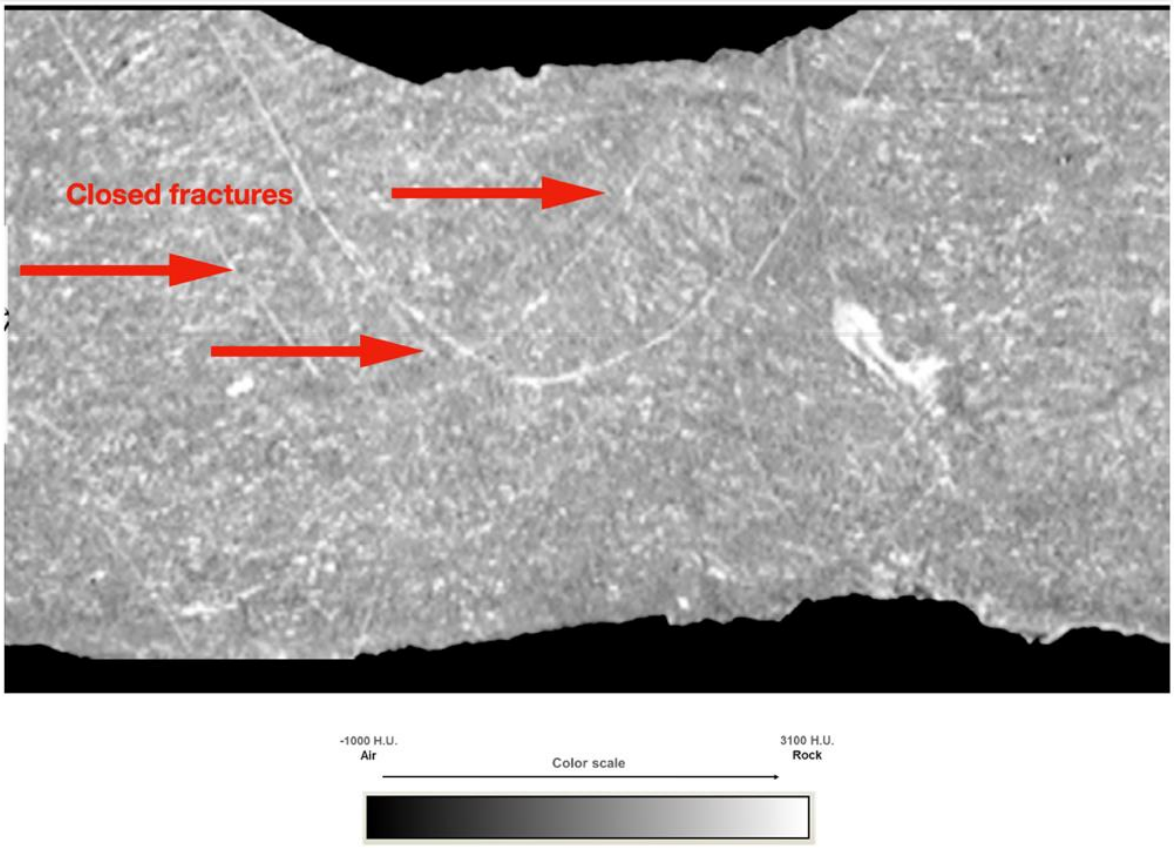


Figure 34. 3D visualization of core sample surface (sample CT1B)
(Edited by the author, source TOMOGEO Ltd.)

### 8.1.2 BRECCIA SAMPLES

Well: Táz-23 Core#1 1,948-1,965 m: CT2, CT2A, CT3, CT4, CT5 samples
Well: Táz-2 Core#10 2,121-2,138 m: CT12A sample

They have medium porosity (average: 3.45 %) and high density (H. U. average: 2,012). 26 % of the porosity elements are elongated - cracks mainly on surfaces of pebbles. (Figure 35.)
More important average data in Table 19. contain. Porosity-increasing factor is the surfaces of the pebbles based on the measurements. Based on the available samples. the porosity system is a very complex fracture-matrix system, so the permeability depends on the tortuosity system. Because of this, the fractal dimension is the highest for these samples (average: 1.07).

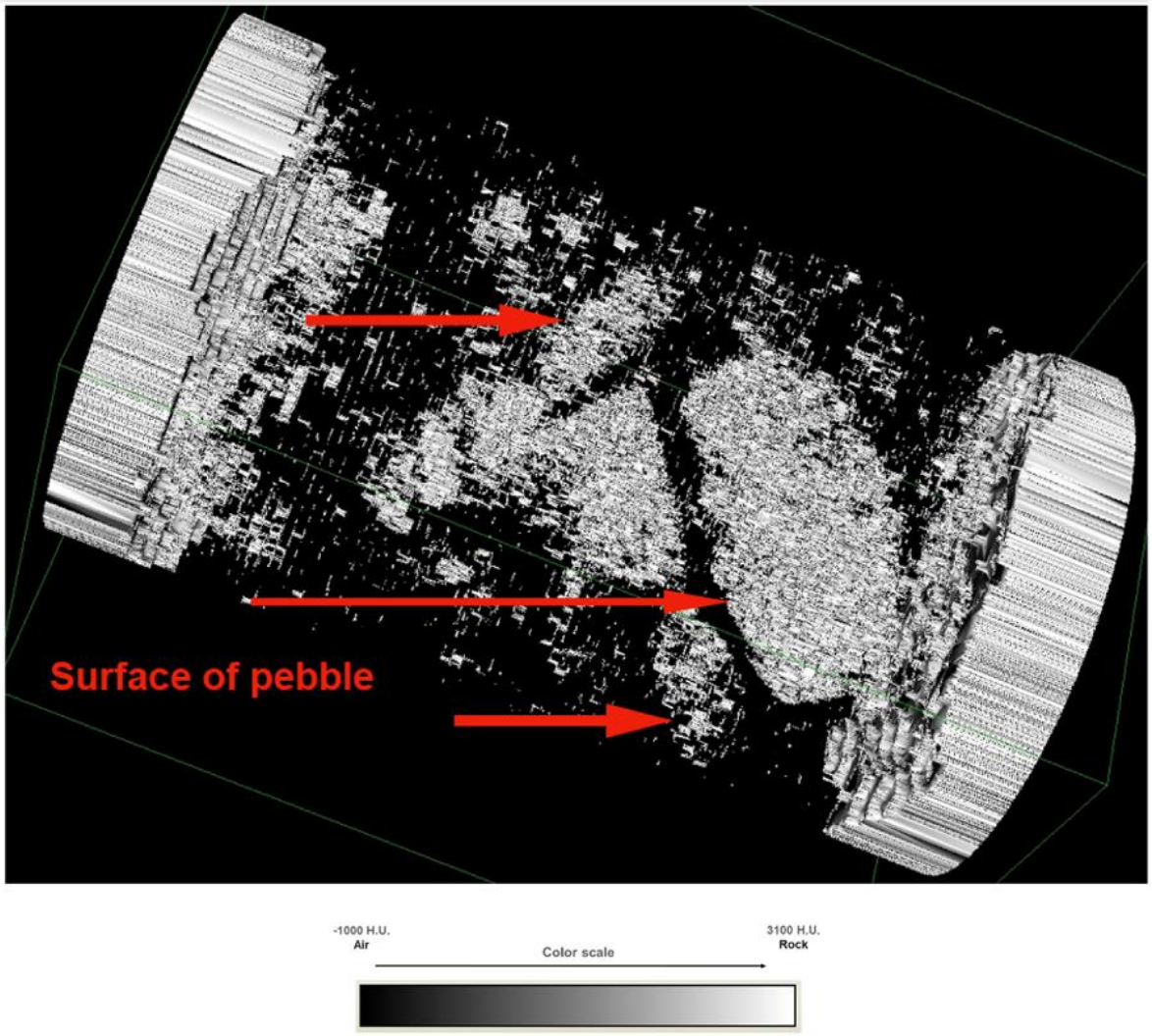


Figure 35. 3D visualization of calculated porosity space (sample CT2A)
(Edited by the author, source TOMOGEO Ltd.)

### 8.1.3 SANDSTONE SAMPLES

Well: Táz-15 Core#6 2,031-2,035 m: CT7 sample
Well: Táz-11 Core#9 1,918-1,928 m: CT8 sample
Well: Táz-18 Core#8 2,029-2,033.5 m: CT9, CT10 and CT10A samples
Well: Táz-19 Core#5 1,833.5-1,842.5 m: CT11 sample
Well: Táz-2 Core#10 2,121-2,138 m: CT12 sample

They have medium and high porosity (average: 5.48 %) and medium density (H.U. average: 1,828). 22 % of the porosity elements are elongated - mainly algal encrustations on the surface of smaller pebbles and sand grains. (Figure 36.) The more important average data can be found in Table 19. Porosity-increasing factors are the increase in the size of the sand grains and the cracking of the algal encrustation. Based on the available

samples, the porosity system is a matrix system containing very complex cracks, so the permeability also depends on the tortuous system. Fractal dimension (average: 1)

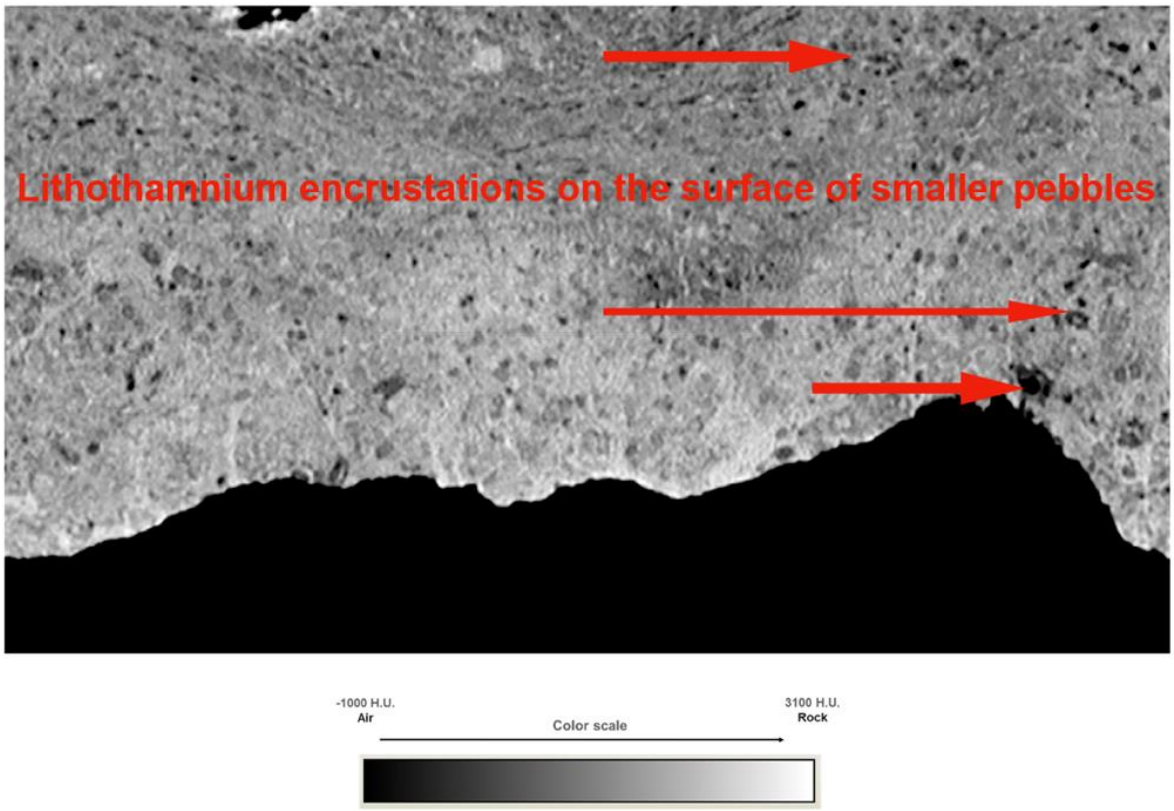


Figure 36. 3D visualization of core sample surface (sample CT11)
(Edited by the author, source TOMOGEO Ltd.)

### 8.1.4 SILTSTONE SAMPLE

Well: Táz-4 Core#6 1,814.5–1,816 m: sample CT13

They have low porosity (average: 0.94 %) and high density (H.U. average: 2,049). 10% of the porosity elements are elongated - cracks, only. Porosity-increasing factors cannot be decided on the basis of the measurements. Based on the available samples, the matrix porosity is very low, so the permeability cannot be evaluated. The comparison of average data of different rock types was attached on Figure 147-151. Appendix 4.

Table 19. CT measurement evaluation average data
(Edited by the author)

| Lithology | Sample Id | Mean [H.U.] | Minimum [H.U.] | Maximum [H.U.] | POR % | Average Size | Perimeter | Fractal D | Count % | Circ | Circ (0.7) |
|---|---|---|---|---|---|---|---|---|---|---|---|
| metamorphic | CT1, CT1A, CT1B, CT6 | 2,117 | 1,267 | 3,131 | 0.290 | 0.280 | 1.420 | 0.640 | 19.700 | 0.821 | 0.460 |
| breccia | CT2, CT2A, CT3, CT4, CT5, CT12A | 2,012 | 533 | 2,978 | 3.450 | 0.790 | 3.090 | 1.070 | 25.800 | 0.786 | 0.503 |
| sandstone | CT7, CT8, CT9, CT10, CT10A, CT11, CT12 | 1,828 | 306 | 2,914 | 5.480 | 1.830 | 3.550 | 0.940 | 21.800 | 0.800 | 0.498 |
| siltstone | CT13 | 2,049 | 1,264 | 2,729 | 0.940 | 0.160 | 1.370 | 0.900 | 10.300 | 0.89 | 0.560 |

## 8.2 MICROCOMPUTED TOMOGRAPH MEASUREMENT

### 8.2.1 TECHNICAL DATA

The measurements were performed with a special portable device developed by TOMOGEO LTD., together with the associated measurement technology and processing system. (All rights reserved)

The technology provides the measurement of the parameters of the displacement process (flow rate, fluid density, pressure, temperature) and the archiving of the data. During this, X-ray microCT or CT measurements are performed on the core sample in 3D, partly continuously or in key positions.

The displacement equipment is calibrated altogether with the CT equipment. During the measurement, the parameters and CT images can be displayed with a two-screen system, enabling continuous monitoring of the flow conditions. (Figure 37.)

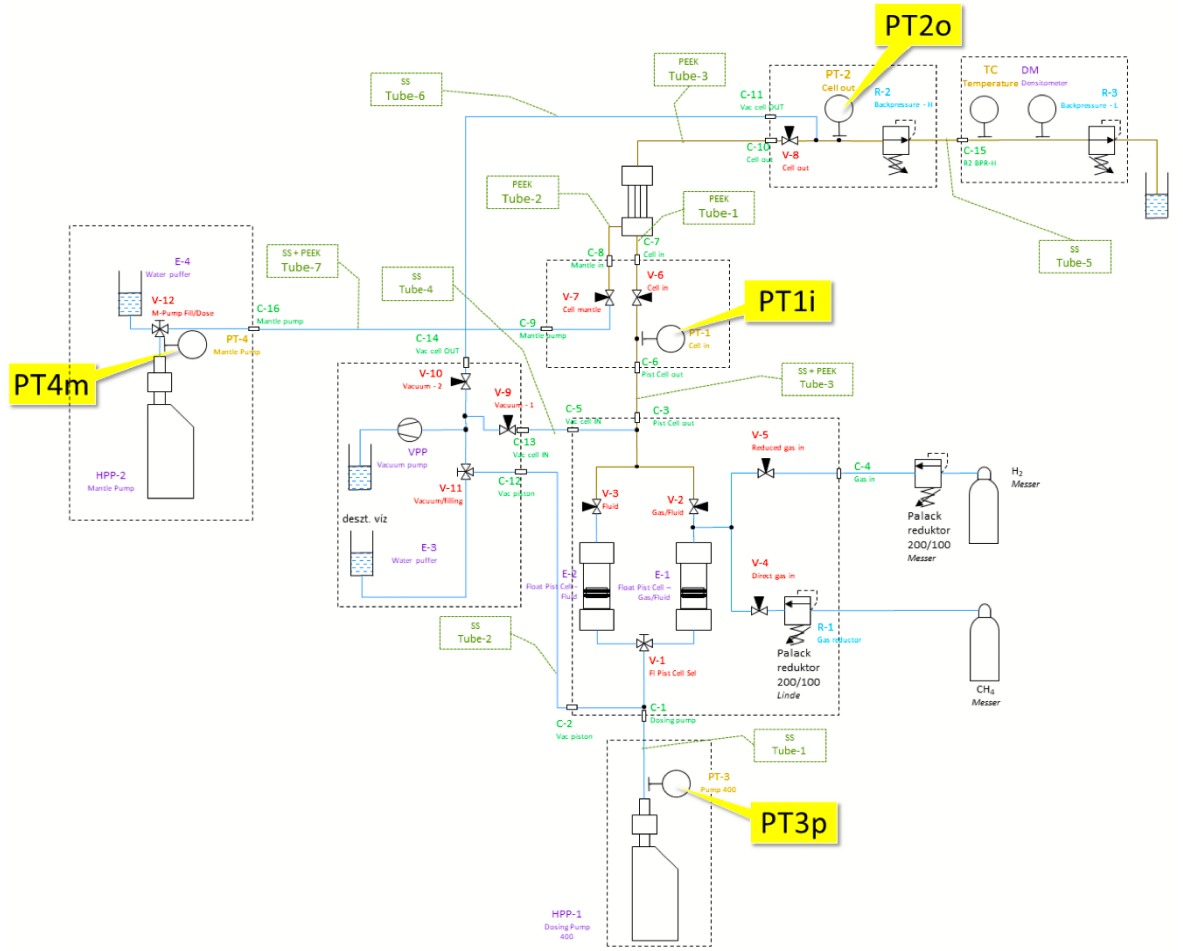


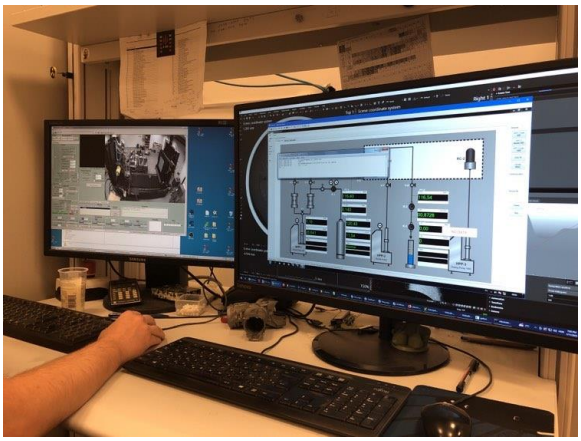

Figure 37. Network diagram and photos of the displacement device which was coordinated with the mCT device
(Recorded by TOMOGEO Ltd.)

The microCT processing was carried out with YXILON MODULAR CT (microCT) machine on plug material. The best resolution of the data set was 0.0097 x 0.0097 x 0.097 mm.

Measurement and calibration data set:

- 190.00 kV tube voltage
- 0.13 mA tube current
- 7 um focus size
- 1,440 projections
- 750.00 ms exposure time
- 1,024 · 1,024 detector pixel number (2,048 · 2,048 2 · 2 binning)
- 409.60 · 409.60 mm detector size
- 1,249.07 mm FDD

The summary diagrams of the measurement processes are contained in Figure 38.

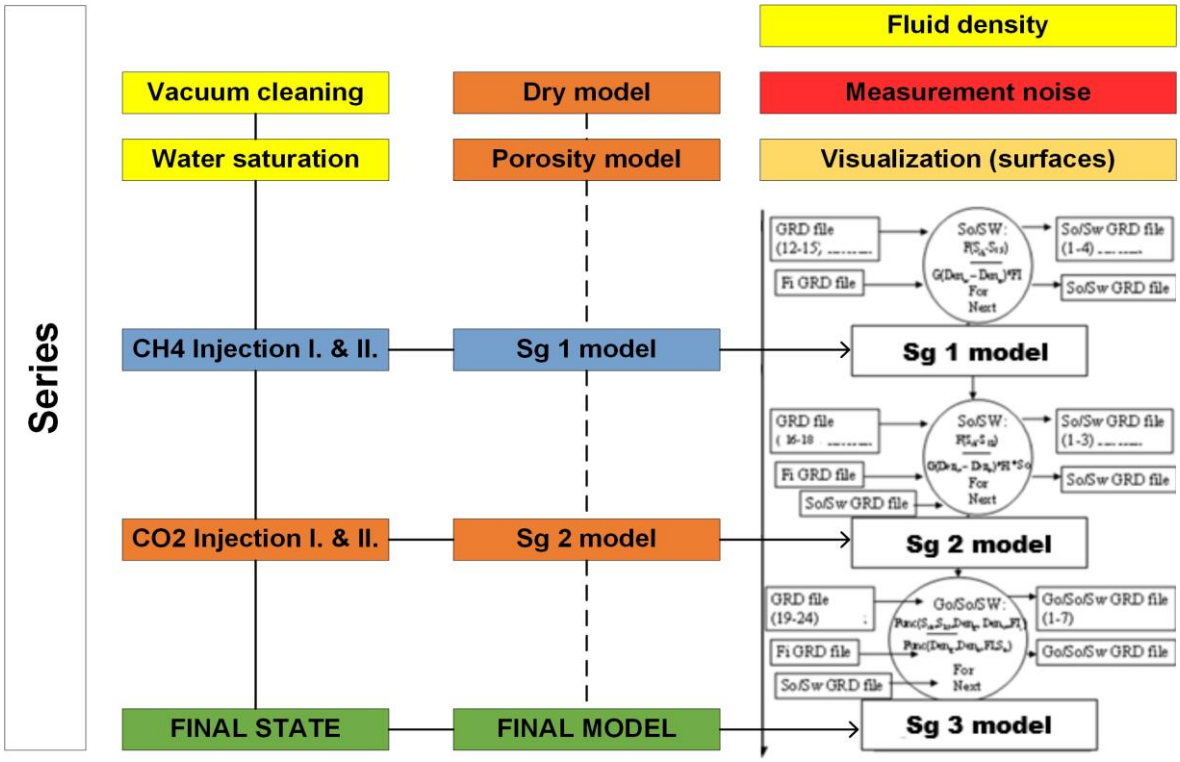


Figure 38. $CO_2$ Displacement Test Processing Software Schematic Process Diagram (Edited by the author, source TOMOGEO Ltd.)

### 8.2.2 SELECTION OF CORE SAMPLE

The sample to be examined was selected based on the results of the previous chapter. According to the studies, the main reservoir rocks in the area are sandstones. Based on these the following can be stated:

Sandstone samples:

Well: Táz-15 Core#6 2,031-2,035 m: CT7 sample
Well: Táz-11 Core#9 1,918-1,928 m: CT8 sample
Well: Táz-18 Core#8 2,029-2,033.5 m: CT9, CT10 and CT10A samples
Well: Táz-19 Core#5 1,833.5-1,842.5 m: CT11 sample
Well: Táz-2 Core#10 2,121-2,138 m: CT12 sample

They have medium and high porosity (average: 5.48%) and medium density (H.U. average: 1,828). 22% of the porosity elements are elongated - mainly algal encrustations on the surface of smaller pebbles and sand grains. (Figure 39). The most important average data can be found in the Table 19. Porosity-increasing factors are the increase in the size of the sand grains and the cracking of the algal encrustation. Based on the available samples, the porosity system is a matrix system containing very complex cracks, so the permeability also depends on the tortuous system. The attached appendix contains further detailed data. (See Appendix 4.)

Finally, based on these results, the mini core used for measurement was a sample with good rock physics parameters, which also contained parts with weaker parameters. (see Figure 39.)

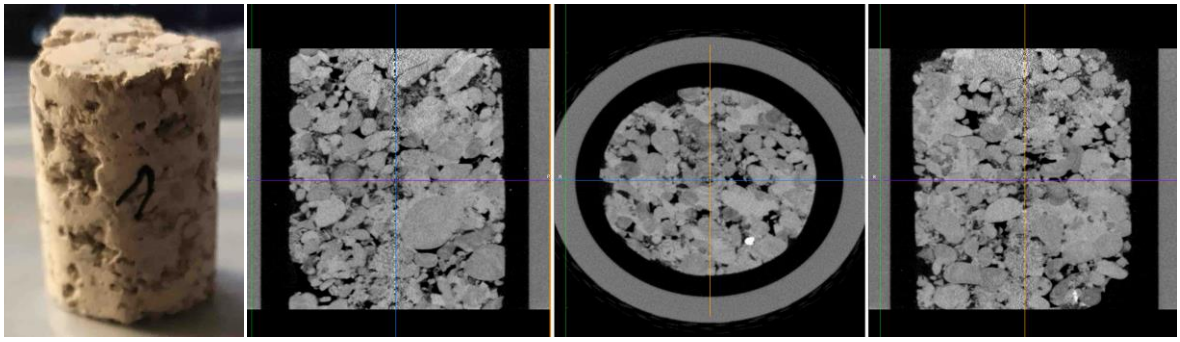

Figure 39. 3D CT images and cylinder images of the core sample
(Edited by the author, source TOMOGEO Ltd.)

### 8.2.3 THE AIM OF THE MEASUREMENT

The aim of the measurement was to know about the efficiency of $CH_4$ displacement by $CO_2$ gas and determine the following parameters:

- 3D porosity changes due to pressure changes
- 3D saturation distributions and changes in different (water - $CH_4$ - $CO_2$) in displacement processes
- determination of recovery value due to $CO_2$ injection in $CH_4$ displacement
- learning and determining permeability relationships

The measurement program was defined for dynamic $CO_2$ flooding micro-CT rock analysis. The goal was to reproduce the initial reservoir conditions and layer fluids, then model hydrocarbon extraction under laboratory conditions, and then model $CO_2$ injection under actual field conditions, as we would do in a real field of this size. The mCT tool and technology made it possible to determine the flow patterns, porosity, and permeability values occurring during the processes (measurement process summarized in Table 27, at Appendix 5.) :

- Creation of the initial state: keeping the sample in a vacuum
- Flooding the dry sample with ion-exchanged water at room temperature. The injected volume is 10 $cm^3$, with a calculated pore volume of 0.8 $cm^3$.
- Performing mCT measurement on the water-saturated sample.
- To ensure complete flooding, inject an additional 10 $cm^3$ of ion-exchange water while increasing the pressure to 100 barg.
- Performing mCT measurement on the water-saturated sample.
- Increase the pressure to the initial layer pressure value: 207 barg.
- Perform mCT measurement.
- Increase the temperature to 90°C. (The initial layer temperature was 128°C, but it was not possible to reach this temperature during the mCT measurement. $CO_2$ injection and supercritical conditions were achieved at 90°C.)
- Perform mCT measurement.
- First $CH_4$ flooding cycle at a pressure of 207 barg and a temperature of 90°C. The injected volume is 10 $cm^3$.
- Performing mCT measurement.
- Second $CH_4$ flooding cycle at a pressure of 207 barg and a temperature of 90°C. The injected volume was 10 $cm^3$.
- Performing mCT measurement.
- Set the current layer pressure to 30 barg.
- Perform mCT measurement.

- Increase the pressure to 100 barg. First, the $CO_2$ flooding cycle at a pressure of 100 barg and a temperature of 90°C. The injected volume is 10 $cm^3$.
- Perform mCT measurement.
- Increase pressure to 207 barg. Second, the $CO_2$ flooding cycle at a pressure of 207 barg and a temperature of 90°C. The injected volume is 10 $cm^3$.
- Perform mCT measurement.

The values set in the measurement program are based on the „reality", from production history to the $CO_2$ injection. The initial reservoir pressure is 207 bar(a), and the initial reservoir temperature is 128°C. The current reservoir pressure is 30 bar(a), and the current reservoir temperature is 128°C. Due to the limitations of the measuring instruments, the maximum temperature is 90°C. This does not actually affect the measurement, as $CO_2$ will be in a supercritical phase, anyway. Water is injected into the dried core, then the pressure and temperature are increased and $CH_4$ is flooded in. Then the pressure reduced, followed by an increase in pressure due to the injection of $CO_2$ and the displacement of the water and $CH_4$.

### 8.2.4 DETERMINATION OF POROSITY AND POROSITY CHANGE

The measurement series started with two mCT measurement series after vacuuming, from which the distribution of measurement noise value was ascertained—a prerequisite for precise calculations. During these measurements and the flooding processes too, the slice positions in the mCT measurement series were always the same. The evaluation of total porosity began with the determination of the pore space within the measurement resolution limit (9 microns). The mapping of the effective porosity was determined by saturation process with water. The resulting framework provided the basis for the determination of porosity changes at different pressures.

The calculations are given together with the saturation values by representing the averages of the measurement slices. In addition, the various calculations were performed for the upper denser and thus lower average porosity effective volumes of 100%, 25%, 12% and 2%. In this way, the saturation and permeability relations of the space with worse rock physical parameters became known. The visualization of the 3D total porosity of the sample in 3D and in three perpendicular slices is shown in Figure 40. The distributions of the porosity values calculated per slice average at different pressures (0, 100 and 207 bar) and at different effective volumes (100%, 25%, 12%, 2%) are shown in Figure 41. The change of the average porosity values at different pressures is shown in Table 20. Further detailed results can be found in the Appendix 4.

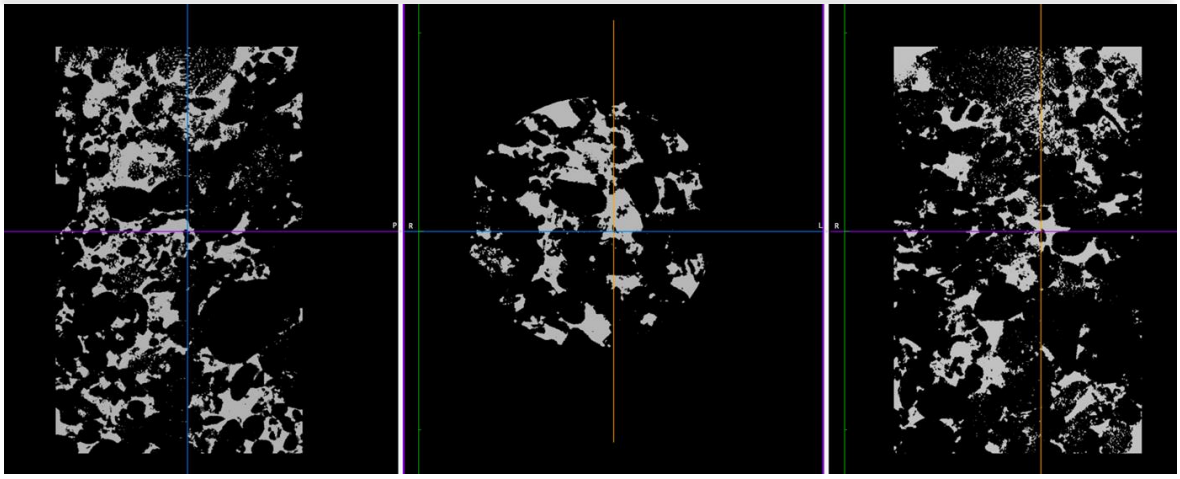

Figure 40. 3D porosity visualizations (white color is the porosity range) based on CT images
(Edited by the author, source TOMOGEO Ltd.)

Table 20. The change of the averaged porosity values at different pressures
(Edited by the author, source TOMOGEO Ltd.)

| $V_{porosity}$ @ 0 barg | $\Delta V_{porosity}$ 100-0 barg (%) | $V_{porosity}$ @ 100 barg | $\Delta V_{porosity}$ 207-100 barg (%) | $V_{porosity}$ @ 207 barg | $\Delta V_{porosity}$ 207-0 barg (%) |
|---|---|---|---|---|---|
| 21.99 | - 4.32 | 21.04 | - 10.03 | 18.93 | - 13.92 |
| $V_{porosity\ 25\%eff}$ @ 0 barg | $\Delta V_{porosity\ 25\%\ eff}$ 100-0 barg (%) | $V_{porosity\ 25\%eff}$ @ 100 barg | $\Delta V_{porosity\ 25\%\ eff}$ 207-100 barg (%) | $V_{porosity\ 25\%eff}$ @ 207 barg | $\Delta V_{porosity\ 25\%\ eff}$ 207-0 barg (%) |
| 16.54 | - 7.80 | 15.25 | - 17.70 | 12.55 | - 24.12 |
| $V_{porosity\ 12\%eff}$ @ 0 barg | $\Delta V_{porosity\ 12\%\ eff}$ 100-0 barg (%) | $V_{porosity\ 12\%eff}$ @ 100 barg | $\Delta V_{porosity\ 12\%\ eff}$ 207-100 barg (%) | $V_{porosity\ 12\%eff}$ @ 207 barg | $\Delta V_{porosity\ 12\%\ eff}$ 207-0 barg (%) |
| 10.92 | - 8.70 | 9.97 | - 19.76 | 8.00 | - 26.74 |
| $V_{porosity\ 2\%eff}$ @ 0 barg | $\Delta V_{porosity\ 2\%\ eff}$ 100-0 barg (%) | $V_{porosity\ 2\%eff}$ @ 100 barg | $\Delta V_{porosity\ 2\%\ eff}$ 207-100 barg (%) | $V_{porosity\ 2\%eff}$ @ 207 barg | $\Delta V_{porosity\ 2\%\ eff}$ 207-0 barg (%) |
| 3.56 | - 10.11 | 3.20 | - 24.06 | 2.43 | - 31.74 |

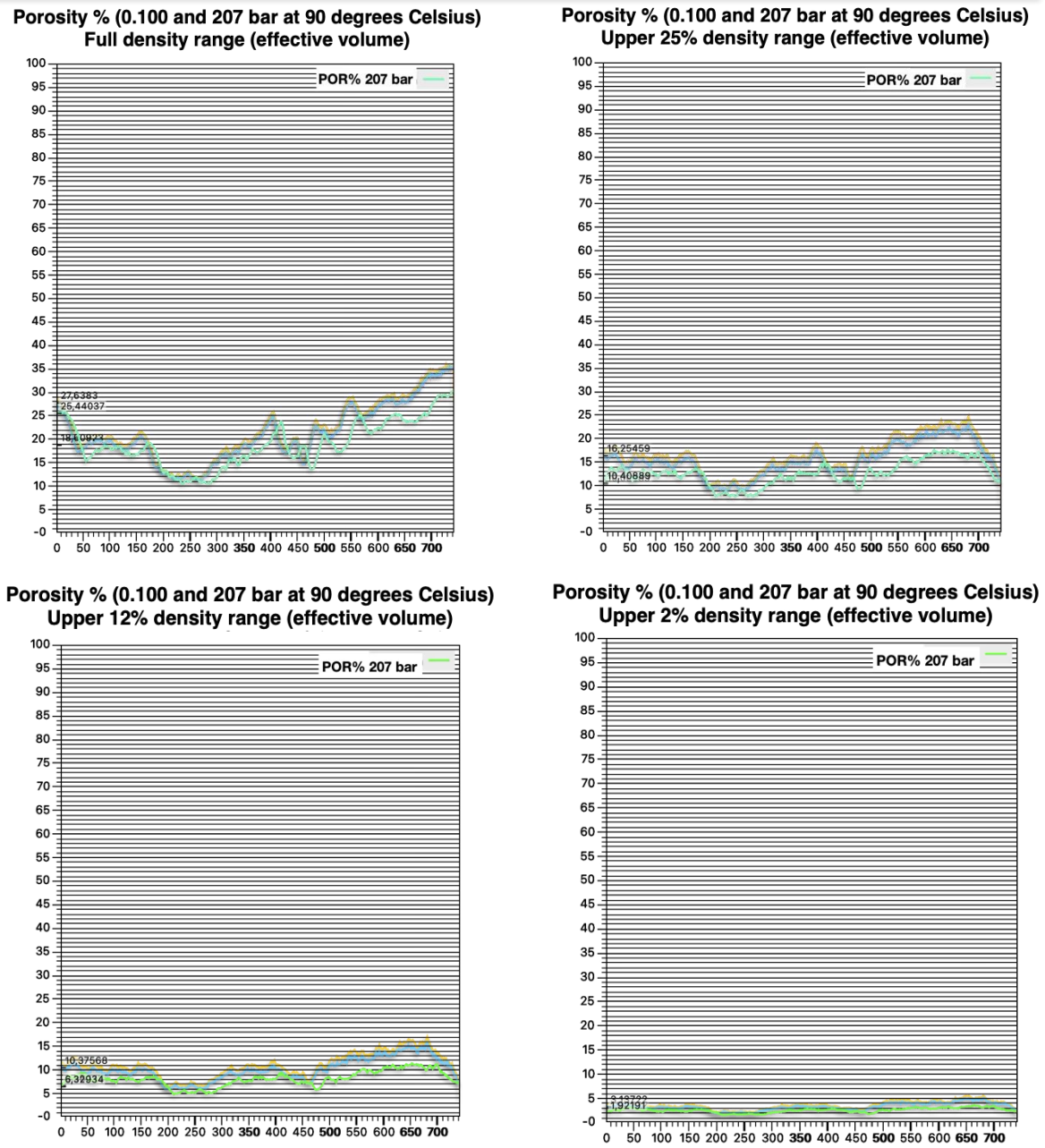


Figure 41. Porosity % change due to pressure and temperature
(Edited by the author, source TOMOGEO Ltd.)

### 8.2.5 WATER DISPLACEMENT BY $CH_4$ INJECTION

The water displacement was made by volume of $CH_4$ (10 $cm^3$) included more than ten times the pore volume of sample (0.8 $cm^3$) in two processes. The 3D saturation conditions were measured by mCT. Based on this, a higher $CH_4$ saturation - lower water saturation was developed on the injection side of the sample. The injection process parameters and the developed saturation averages in the different effective volumes are shown in Figures 42&43 and Figures 152&153. (Appendix 5.)

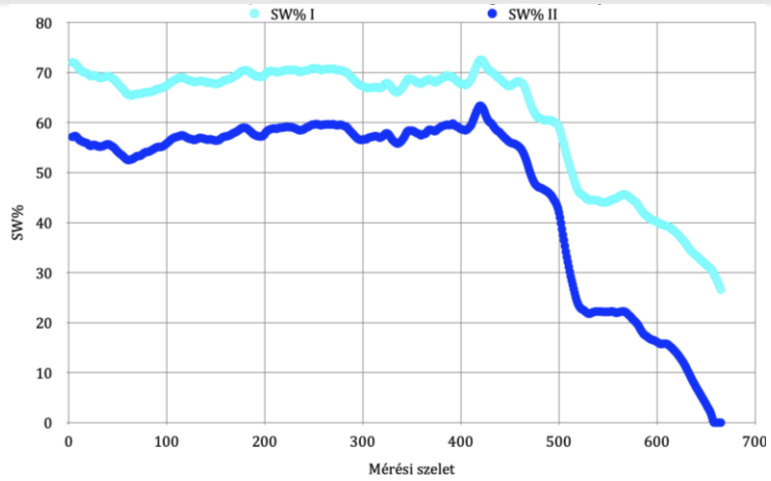


Figure 42. Average SW% per measurement slice in state I. and II. after $CH_4$ injection
(Edited by the author, source TOMOGEO Ltd.)

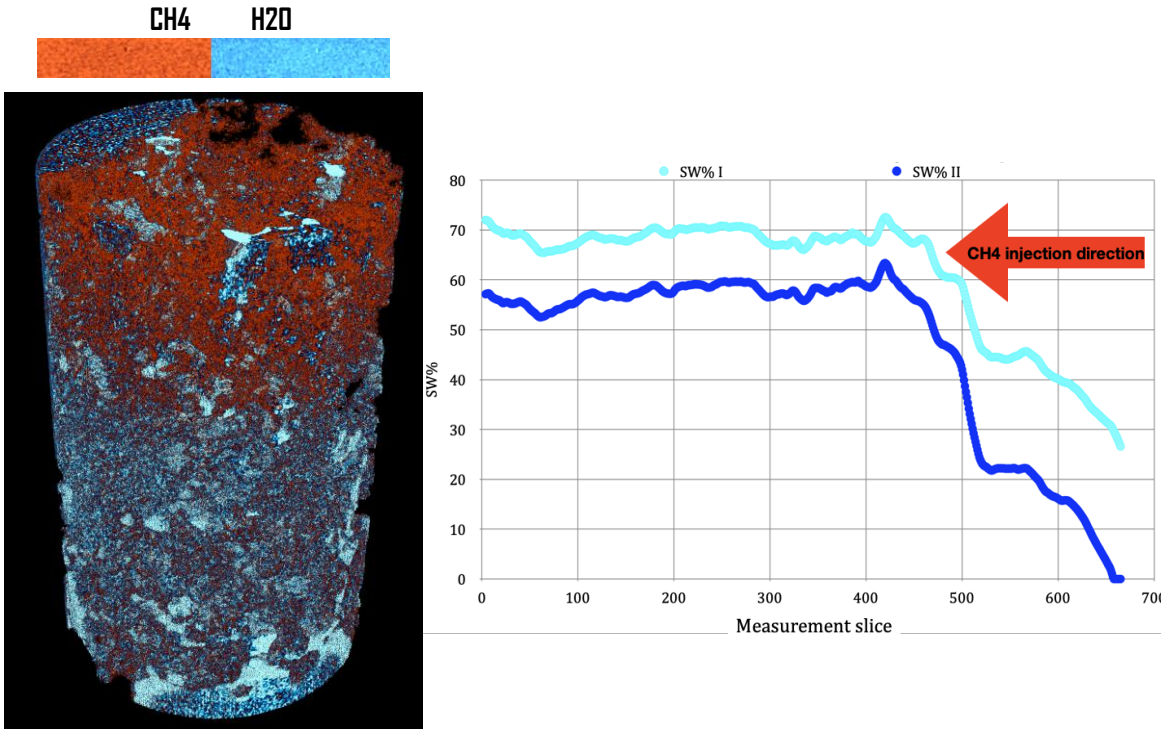


Figure 43. Comparison of average SW% per measurement slice and 3D mCT data visualization after $CH_4$ injection
(Edited by the author, source TOMOGEO Ltd.)

### 8.2.6 $CH_4$ DISPLACEMENT BY $CO_2$ INJECTION

$CH_4$ displacement was performed in two procedures with a $CO_2$ volume (10 $cm^3$) containing more than ten times the pore volume (0.8 $cm^3$) of the sample. The 3D saturation relationships were measured with mCT. Based on this, a higher $CH_4$ displacement - higher $CO_2$ saturation was developed on the injection side of the sample.

The injection process parameters and the obtained saturation averages at different effective volumes are shown in Figure 44. after the finished $CO_2$ injection process and the $CH_4$ displacement by $CO_2$.

Based on Figures 45-46-47. visible, the $CO_2$ only able to flood between 495 and 700. slices, where the 700. slice is the injection point.

In case of repeat measurements, the measurement duration and/or the amount of $CO_2$ injected must be increased. No financial resources were available for repeat measurements. The amount injected was determined based on estimates, so it cannot be determined in situ whether the injected fluid completely flooded the pore space.

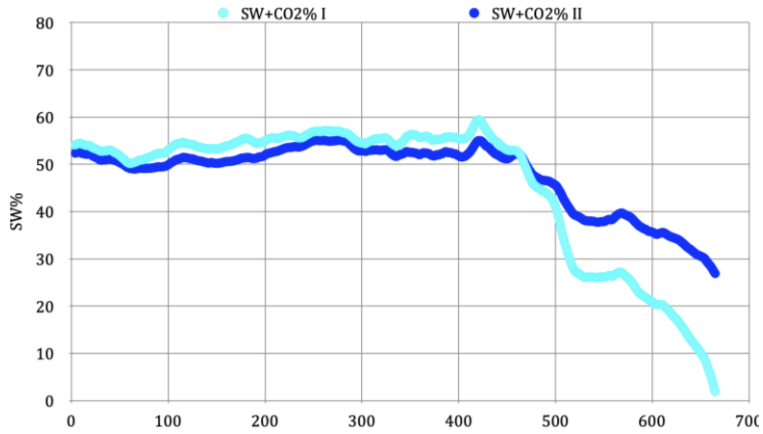


Figure 44. Average (SW+$CO_2$ )% per measurement slice in state I. and II. after $CO_2$ injection

(Edited by the author, source TOMOGEO Ltd.)

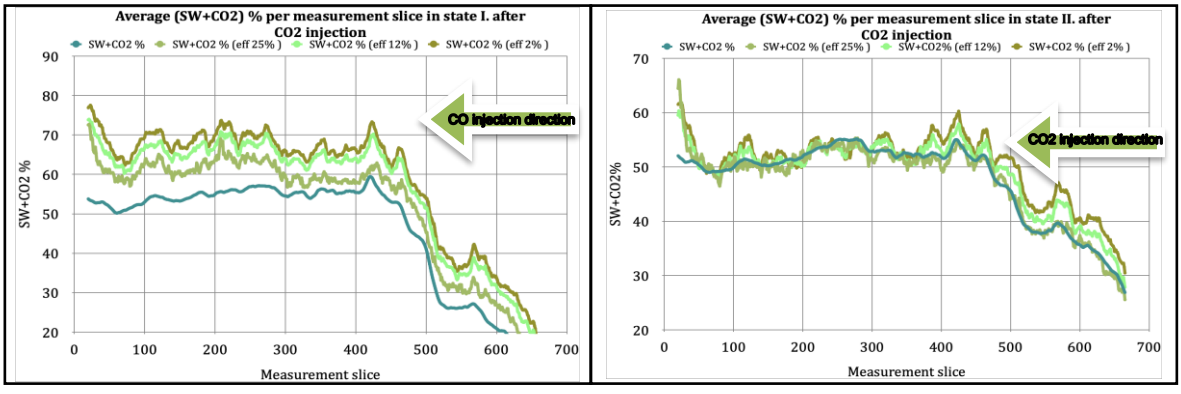


Figure 45. Average (SW+ $CO_2$) % per measurement slice in states I. and II. with different effective volumes after $CO_2$ injection

(Edited by the author, source TOMOGEO Ltd.)

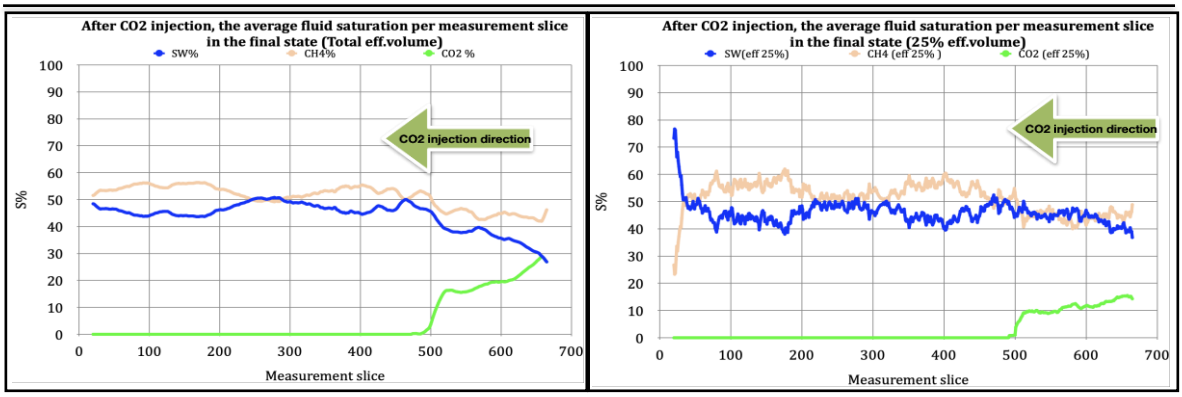


Figure 46. Fluid saturation distributions in the final state
(Edited by the author, source TOMOGEO Ltd.)

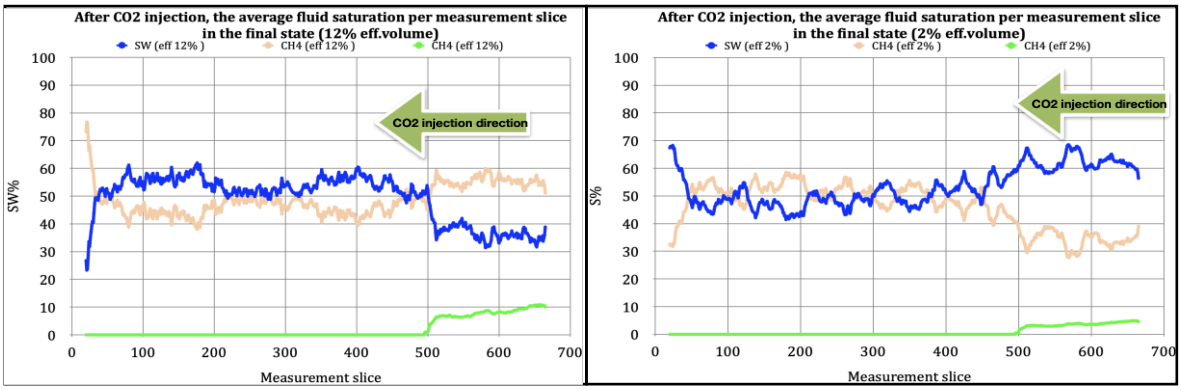


Figure 47. Fluid saturation distributions in the final state
(Edited by the author, source TOMOGEO Ltd.)

### 8.2.7 RECOVERY RESULT DURING $CH_4$ DISPLACEMENT BY $CO_2$

The displacement results were calculated in selected effective volume- assuming that $CO_2$ completely displaced $CH_4$ from each pore, these are the slides between 700 and 495. (Figure 48.) It is visible from the figures that $CO_2$ displaced $CH_4$ mainly, on the injection side of the sample, shown with green color on the left mCT picture. The Table 21. shows the average data of sample - in the total volume of the sample and in the injection side volume of the sample separately, projected to the effective volumes.

Table 21. Average $CH_4$ recovery % in final state
(Edited by the author, source TOMOGEO Ltd.)

| $CH_4$ recovery % @ $V_{eff\ 2\%}$ | $CH_4$ recovery % @ $V_{eff\ 12\%}$ | $CH_4$ recovery % @ $V_{eff\ 25\%}$ | $CH_4$ recovery % @ $V_{eff\ 100\%}$ |
|---|---|---|---|
| 3.49 | 7.56 | 10.78 | 18.22 |

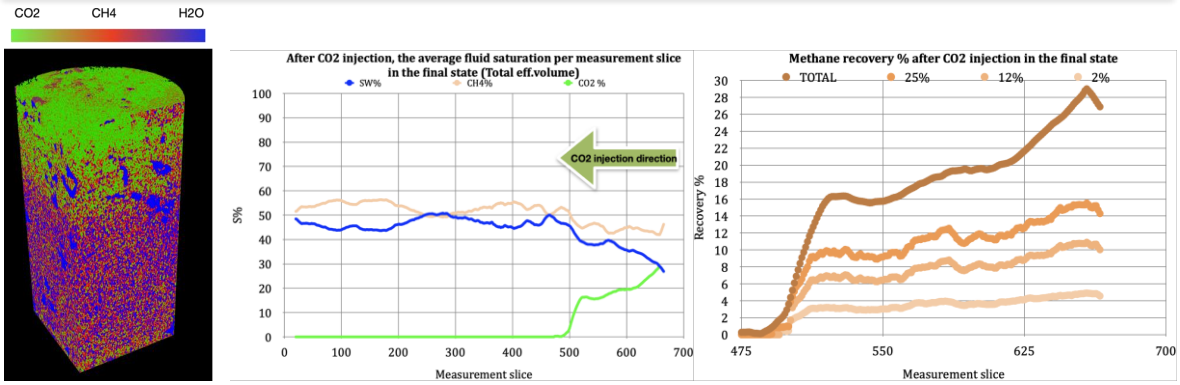


Figure 48. $CH_4$ recovery % in final state

### 8.2.8 PERMEABILITY INTERPRETATION

Permeability was calculated by the displacement equipment measurement data for the entire volume. The average permeability data per slice of $CH_4$ and $CO_2$ displacement were determined by the weight of the average porosity per measurement slice. Since the effective porosity data was calculated from the water saturation data, the porosity-permeability relationship here is linear. Because of all only possible to give permeability-porosity correlation for $CH_4$ - water and $CO_2$ - $CH_4$ displacement. The correlation for each effective volume is different because the porosity distribution within the volume is different. Several values can be associated with each porosity average because there may be volumes with exceptionally good porosity within a given slice, despite the fact that the slice average is the same. With all this, increasingly smaller effective volumes mean an increasingly definite relationship and better correlation. The calculations were made for the volume on the injection side.

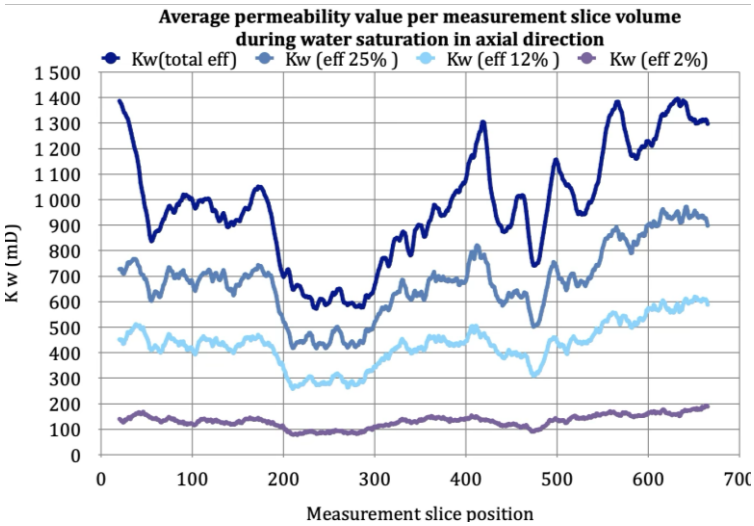


Figure 49. Permeability interpretation value during water saturation for the whole sample (Edited by the author, source TOMOGEO Ltd.)

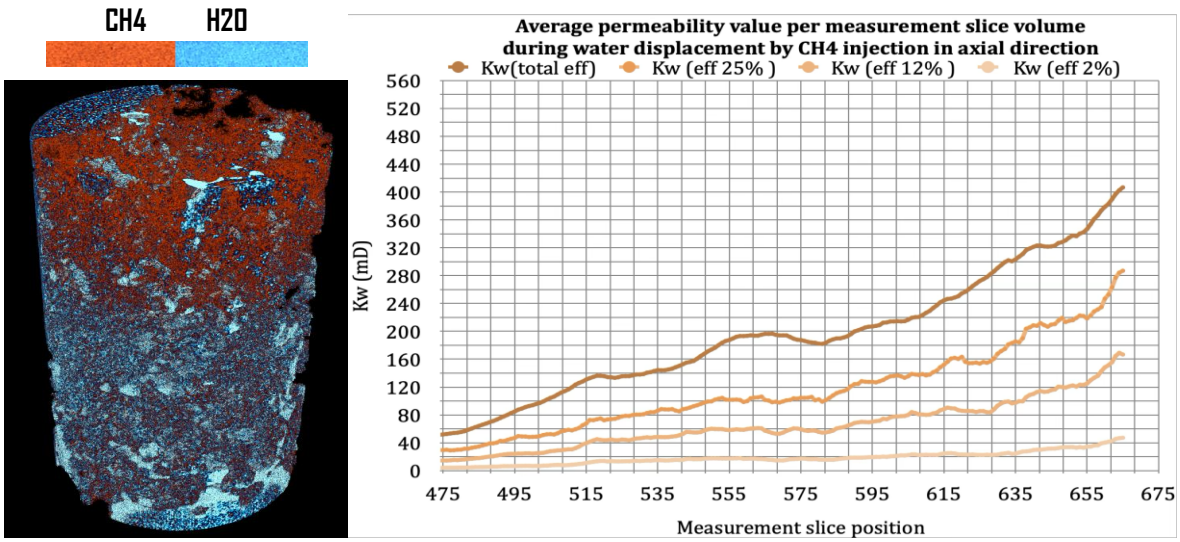


Figure 50. Permeability interpretation value during water displacement between 700 and 495 slices

(Edited by the author, source TOMOGEO Ltd.)

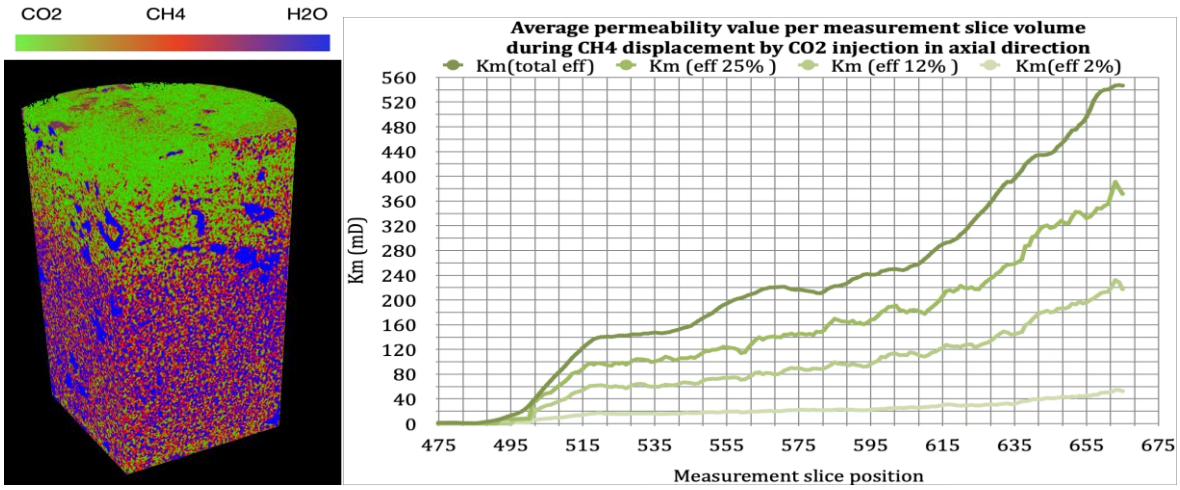


Figure 51. Permeability interpretation value during $CH_4$ displacement between 700 and 495 slices

(Edited by the author, source TOMOGEO Ltd.)

Since no steady state occurred and the $CO_2$ did not completely pass through the pore space, it is not possible to define relative permeability values, but possible to calculate permeabilities with new in-situ observations on the slices. For a given porosity, several permeability values can be associated, but there are some slices that behave in the same way. For different percentages of effective volume (2, 12, 25, 100%), different new porosity-permeability relationships have been defined as shown in the Table 22, below.

Table 22. Calculated Porosity-permeability correlations
(Edited by the author)

| Effective volume | Porosity-permeability relationship |
|---|---|
| 100% | $K = 23.291 \cdot e^{0.0994 \cdot \varphi}$ |
| 25% | $K = 6.8474 \cdot e^{0.1887 \cdot \varphi}$ |
| 12% | $K = 2.7628 \cdot e^{0.3329 \cdot \varphi}$ |
| 2% | $K = 0.3436 \cdot e^{1.3884 \cdot \varphi}$ |

Where: e - Euler number and φ - porosity (%).

The calculated Porosity-permeability correlations and the different porosity and permeability values during the different process steps visualized below on Figures 52-55.

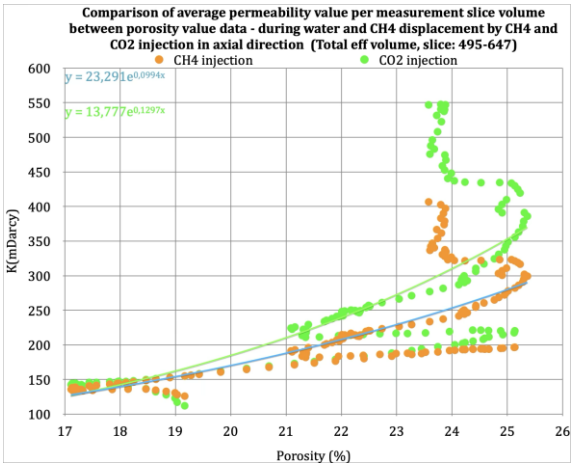


Figure 52. Porosity-permeability correlation @ $V_{eff\ 100\%}$ between 495 and 700 slices
(Edited by the author, source TOMOGEO Ltd.)

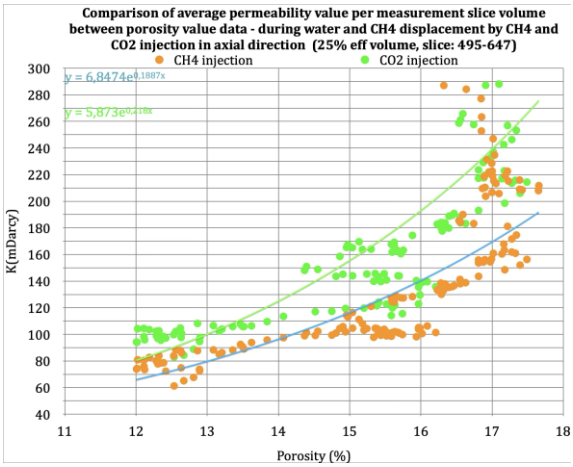


Figure 53. Porosity-permeability correlation @ $V_{eff\ 25\%}$ between 495 and 700 slices
(Edited by the author, source TOMOGEO Ltd.)

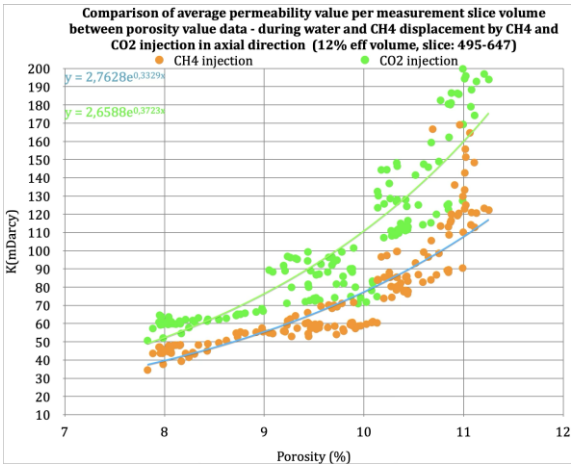


Figure 54. Porosity-permeability correlation @ $V_{eff\ 12\%}$ between 495 and 700 slices
(Edited by the author, source TOMOGEO Ltd.)

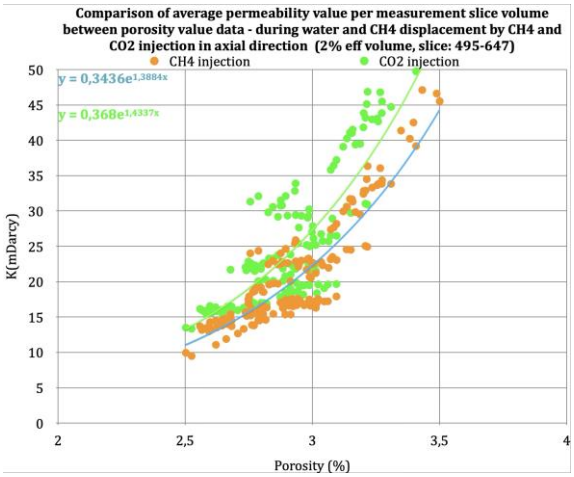


Figure 55. Porosity-permeability correlation @ $V_{eff\ 2\%}$ between 495 and 700 slices
(Edited by the author, source TOMOGEO Ltd.)

### 8.2.9 REMARKS

The samples were carefully selected for the measurements. Nevertheless, in order to reliably determine the expected result of $CO_2$ displacement in the reservoir, the behavior of fluids and the distribution of saturation conditions, similar tests should be performed on several samples, since the porosity ratios may be different in rocks of different facies. For this reason, calculations on the parameters of the pore sizes did not perform either.

The 3D saturation results were obtained under the control of the mCT measurement at the measurement times. However, it is only possible to draw conclusions about the flow conditions between these states from the measurement data of the displacement equipment for the entire sample. Thus, the pressure distribution, diffusion and non-laminar flow phenomena developing inside the sample were unknown factors in the permeability calculations.

Permeability calculations were performed from the average porosity of the measurement slices, based on the permeability values measured for the total volume.

Digital rock calculation was not performed, because not only a simple mCT baseline measurement was performed a mCT-controlled displacement measurement was performed.

The relative permeability of the individual fluids was not determined. The two-day measurement could not provide time for this. However, was obtained important results from the $CH_4$ and water displacement data regarding the combined behavior of the three fluids.

In the absence of a water sample from field, ion-exchange freshwater was used during the measurements. The use of salt water can also provide insight into salt precipitation processes.

# 9. DYNAMIC MODELING WITH TNAVIGATOR

The information provided in all previous chapters is necessary for the dynamic modeling summarized in this chapter. This is the nexus where all elements converge. The outcomes of laboratory measurements. the production history and field data, geology, rock physics parameters, and microCT measurement results are all integrated in this section. Despite the abundance of known data, it was necessary to rely on literature data or approximate values in many cases.

## 9.1 STATIC MODEL

The basis of modeling was a 3D static model developed in 2009 by MOL Plc. using Irap RMS, which was imported into tNavigator by Rock Flow Dynamics®. (Figure 56.) This static model encompasses the entire field, including the metamorphic basement; however, the analysis focused specifically on the upper section of the structure, where the target reservoir is located. The static model includes all necessary parameters for conducting numerical simulations, apart from the permeability distribution.

Taking into account the geodetic data and the static model data, the model's extent of the 3D storage model is: ***5,092 m x 4,730 m x 955 m (Length x Width x Depth)***. The average cell division in the *Length* x *Width* x *Depth* dimensions are *100 x 100 x 5 m*, meaning that the storage model consists of ***51 x 47 x 190 cells***. (Visualization on Figure 154. at Appendix 6.) The storage model was later covered with a coherent 100-meter-thick cap rock, with a thickness of 33.33 meters along the Z-axis.

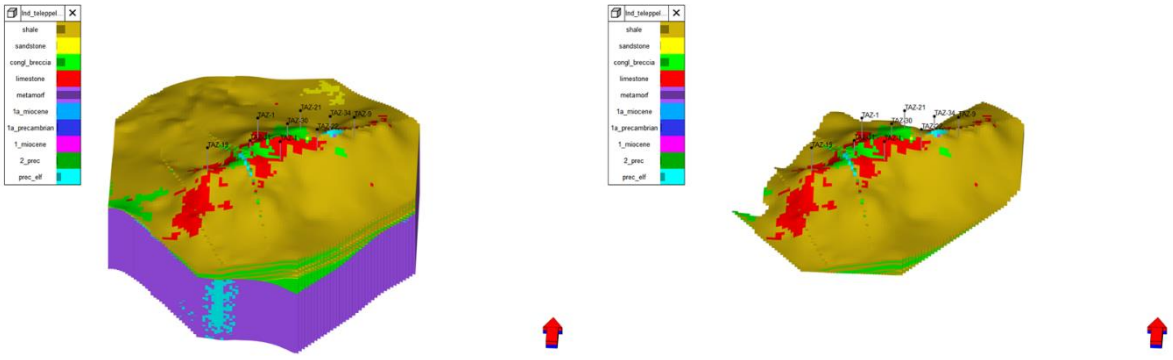


Figure 56. 3D model of Tázlár field with lithology
(source: tNavigator ; Edited by the author)

## 9.2 PRODUCTION HISTORY

The reservoir is an oil reservoir with a substantial gas cap, and production commenced in 1974 and continues to this day.

The initial step in the modeling process involved conducting a history match in parallel to determine the optimal average permeability value. This was done to accurately model the pressure drop within the reservoir and the wells. During the research, the primary focus was on the gas cap wells and the gas production.

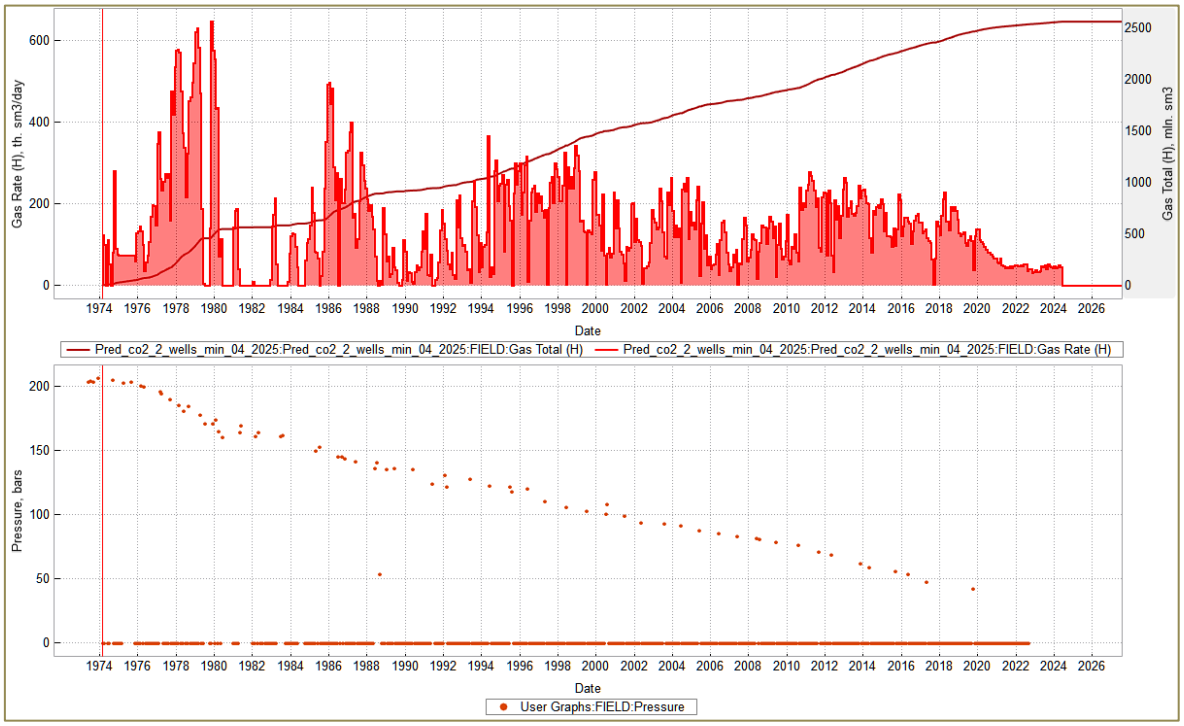


Figure 57. Production and reservoir pressure history
(source: tNavigator ; Edited by the author)

The production and pressure data were available until May 2024.

The field total gas production was **2,557.78 Mm³ gas**.

### 9.2.1 HISTORY MATCH

The static model was the basis of the dynamic modeling.

All necessary dynamic input parameters, including the compositional PVT model and relative permeability curves, were provided by MOL Plc.

Due to the unavailability of a detailed permeability distribution within the static model, sensitivity analyses were performed to constrain the lower bound of average permeability, in addition to the 30 mD baseline value utilized by the model provider.

The evaluation concluded that the minimum average permeability is 10mD while the base case permeability was 30mD. Considering that the reservoir modeled as homogeneous due to the unknown location and extent of the fractures, the wells therefore communicate with each other to an extent corresponding to the permeability of the reservoir.

Relative permeability characterizes fluid flow within fractures, which plays a significant role in contributing to overall fluid movement.

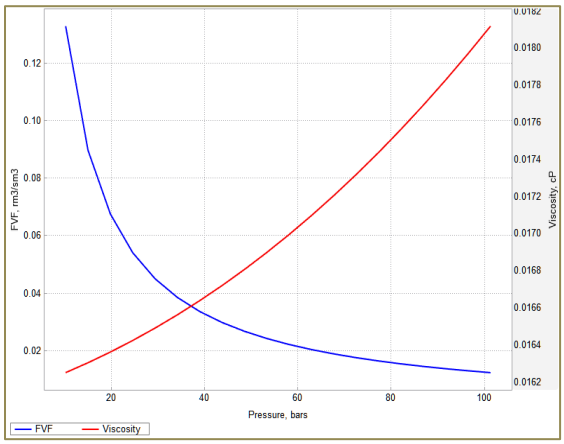


Figure 58. Gas formation volume factor and viscosity vs. pressure
(source: Irap RMS ; Edited by the author)

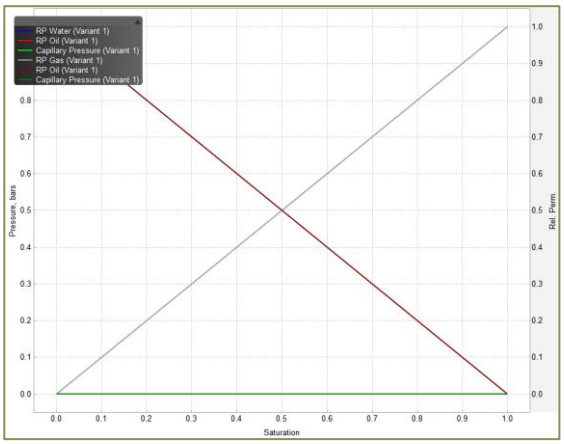


Figure 59. Relative permeability curve for fluid flow within fractur system
(source: Irap RMS ; Edited by the author)

#### 9.2.1.1 History match results on field level

1. **case**: Assumed, that the reservoir did not have an active aquifer and that there was no pressure support.

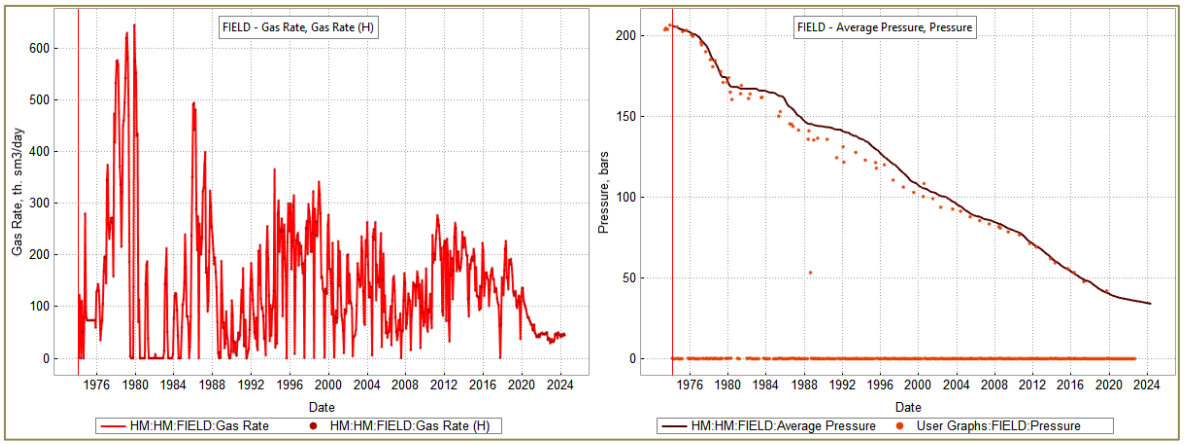


Figure 60. History matching without aquifer connection
(source: tNavigator ; Edited by the author)

All the available gas production data rate and the reservoir pressure measurement data were fitted to the history matching, assuming there is no active aquifer, an accurate fit was achieved, as shown in Figure 60. The initial and current reservoir pressure values are

shown in the 3D layer model in Figure 61, confirming the measured data. (Initial reservoir pressure: 207 barg, current reservoir pressure: 30 barg)

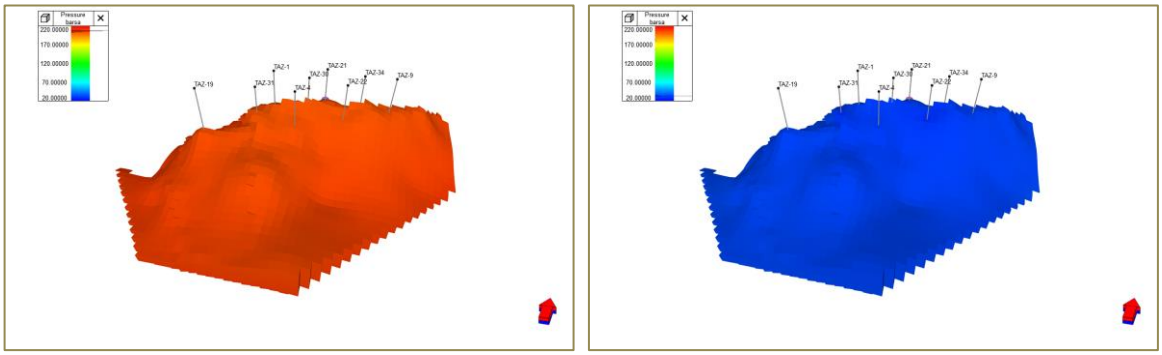

Figure 61. Initial and current reservoir pressure simulation without aquifer
(source: tNavigator ; Edited by the author)

2. **case**: Assumed, that the reservoir has an active aquifer and that there is pressure support.

Although its obvious from the closed reservoir model, and its pressure match, that there is no additional pressure support of the reservoir besides the gas expansion, created a simulation run with an aquifer connecting to the reservoir. The pressure match of this run and the comparison of the two cases are shown on the graphs below. (Figure 62.)

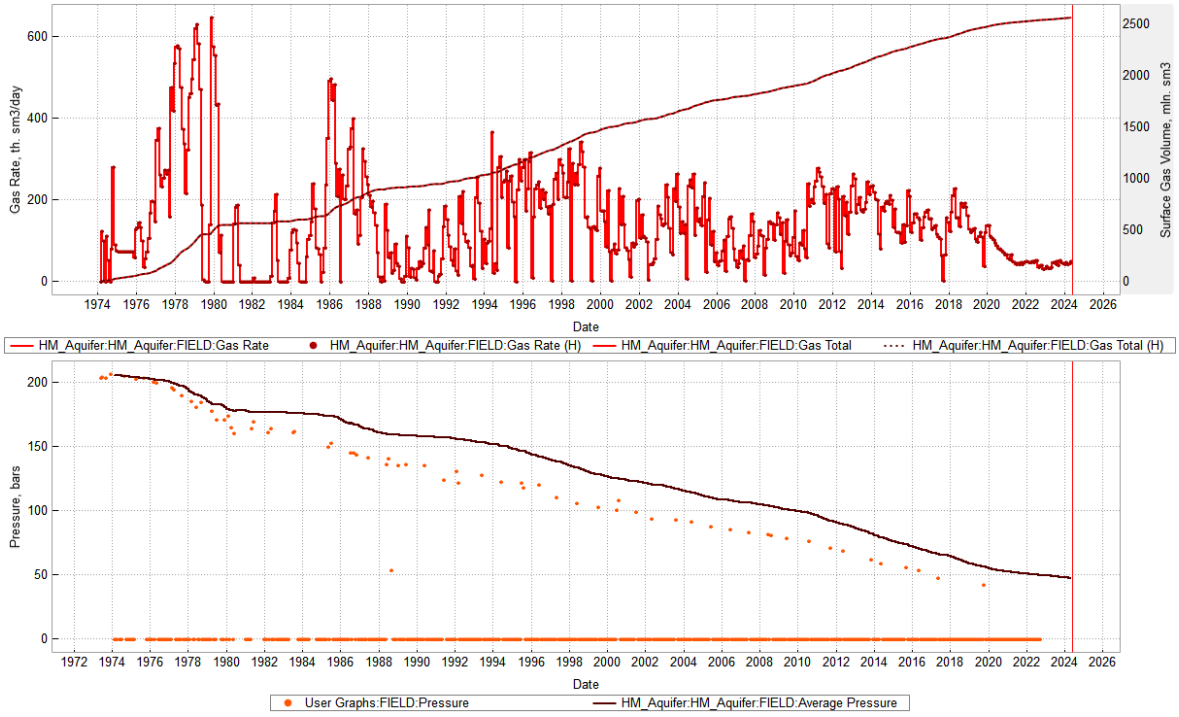


Figure 62. History matching with aquifer connection
(source: tNavigator ; Edited by the author)

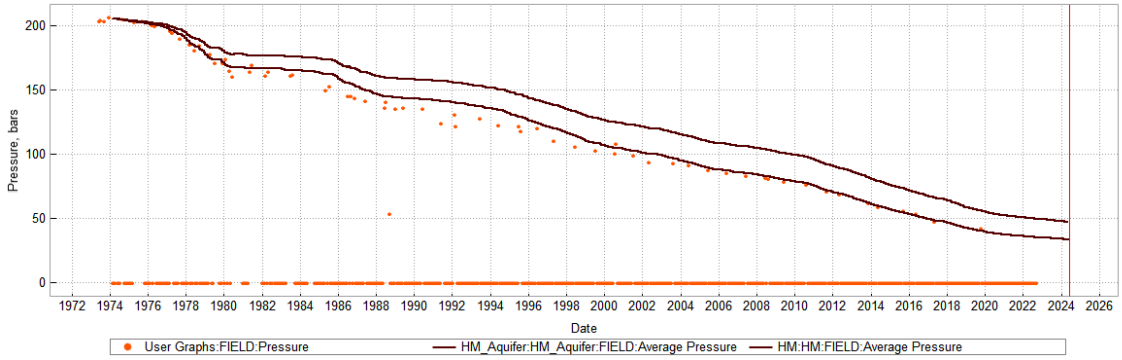


Figure 63. Pressure difference 1. vs. 2. case
(source: tNavigator ; Edited by the author)

#### 9.2.1.2 History match result of those wells which had pressure data

In the previous subsection, confidently and accurately demonstrated that a successful history match was achieved at the field scale, under the assumption of there is no aquifer connection. In order to further substantiate this conclusion, the history matching was executed at the individual well level, specifically for those wells where reservoir pressure measurements were recorded during production over the past decades and where production data are available. These well-level simulations were likewise performed under the assumption there is no aquifer connection. In all cases, as illustrated in Figure 64, the history matching results exhibit a high degree of accuracy, confirming the robustness of the model not only at the field scale but also at the well scale. Further well-level history matching results shown in Appendix 7, Figures 155-159.

**Táz-1 well**

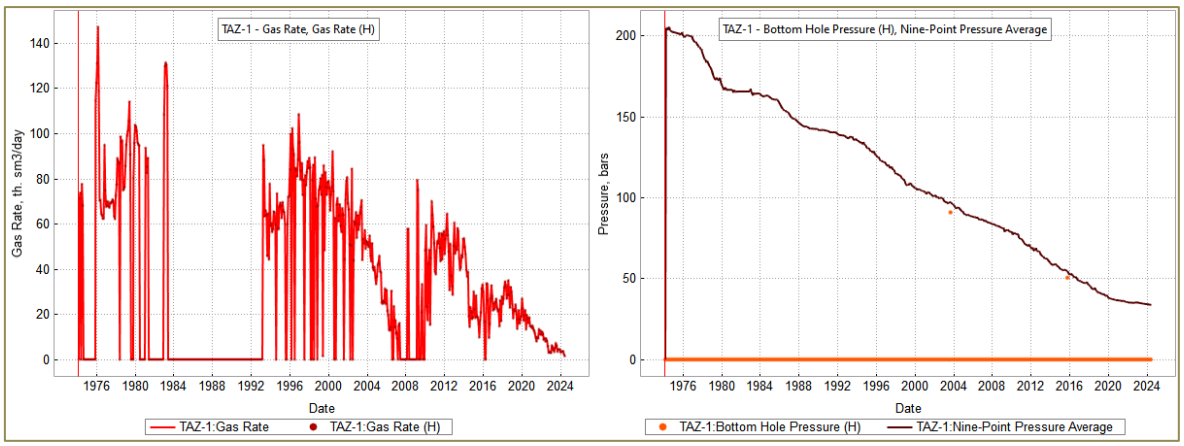


Figure 64. History matching of Táz-1 well
(source: tNavigator ; Edited by the author)

The main conclusion of the history match is that the reservoir is a closed reservoir based on the pressure drop during its production history, therefore on the following the model does not calculate with the pore volume loss due to water influx or $CO_2$ solution to the aqueous phase. All the further rock mechanics runs were based on these two permeability cases 10mD and 30 mD.

## 9.3 SENSITIVITY RUNS

In the numerical simulation model, 3 additional layers were added to the static model, representing the cap rock, with extreme low porosity and permeability values. The thickness of the coherent cap rock was 100m.

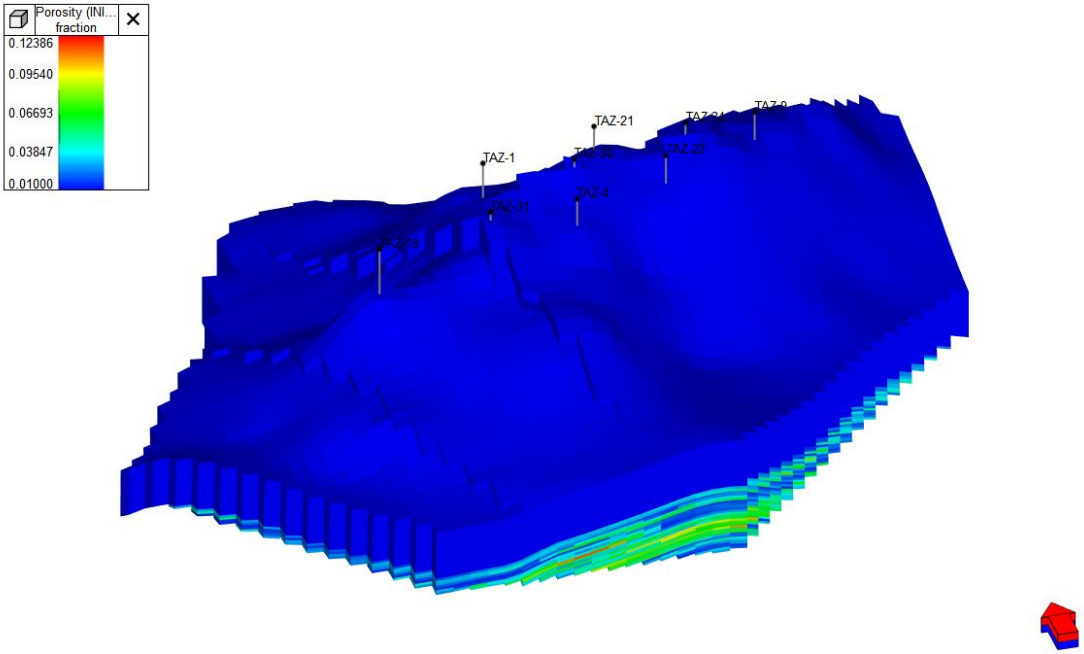


Figure 65. Upgraded model with 3 additional layers
(source: tNavigator ; Edited by the author)

As in previous chapters mentioned, the most critical geomechanical values are Young's modulus, Poisson's ratio, internal friction angle and cohesion numbers.
From these 4 critical parameter were selected the min-max values for the cap rock as the main focus of the sensitivity study was to determine whether the caprock had/have had any failure during the depletion period – initial reservoir pressure of 207 bar was decreased to an average of 30 bars by now – and the aim was to identify whether any failure occurs during the $CO_2$ injection.

Due to lack of rock mechanics property measurements in Tázlár field, analogies were used. The closest well which had such measurements was the KihaD-1 well. This well is ~14 km far from the selected block and the rock is similar than in case of Tázlár field.

There measured mechanical properties shown in Table 23.

Table 23. KihaD-1 well rock parameters
(Edited by the author, source MOL Plc.)

| No. Sample | UCS ($\sigma_c$) MPa | Young's modulus (E) GPa | Poisson's ratio (ν) |
|---|---|---|---|
| 3.mf. 2,656 m | 28.51 | 458 | 0.11 |
| 4.mf. 2,829 m/I | 85.23 | 1,989 | 0.28 |
| 6.mf. 3,192 m/I | 28.77 | 632 | n/a |
| 6.mf. 3,192 m/III | 22.80 | 249 | 0.02 |
| 6.mf. 3,192 m/IIb | 46.37 | 2,112 | 0.10 |
| 8.mf. 3,424 m | 9.50 | 158 | 0.50 |
| 9.mf 3,578 m | 66.34 | 2,683 | 0.17 |
| 11.mf. 3,933 m | 39.90 | 1,718 | 0.14 |
| 12.mf. 4,070 m | 23.38 | 285 | 0.02 |
| 13.mf. 4,225 m /3za | 81.46 | 2,780 | 0.18 |
| 13.mf. 4,225 m /3zb | 46.26 | 1,527 | n/a |
| 13.mf. 4,225 m /5z | 75.83 | 2,041 | 0.11 |
| 14.mf. 4,441 m/II | 102.55 | 3,257 | 0.10 |
| 15.mf. 4,497 m | 75.68 | 2,478 | 0.08 |

Subsequent to the measurement, no reliable data was available for the storage facility, and thus, $CO_2$ injection was modeled using values determined based on data found in the literature. (see Appendix 8.)

### 9.3.1 PARAMETERS

The parameter combination of the runs were the following. (on Table 24.) There are six different combinations, to check all limiting values :

Table 24. Parameters of six run scenarios
(Edited by the author)

| | | Permeability | Young modulus [MPa] | Poisson ratio | Friction angel (theta) [°] | cohesion [MPa] |
|---|---|---|---|---|---|---|
| **1. Case - min** | Reservoir | 30 | 300,000 | 0.17 | 0 | 6 |
| | Cap rock | 0.00001 | 50,000 | 0.10 | 0 | 14 |
| **2. Case - max** | Reservoir | 30 | 900,000 | 0.35 | 32 | 40 |
| | Cap rock | 0.00001 | 300,000 | 0.10 | 14 | 40 |
| **3. Case - min** | Reservoir | 10 | 300,000 | 0.17 | 0 | 6 |
| | Cap rock | 0.00001 | 50,000 | 0.10 | 0 | 14 |
| **4. Case - max** | Reservoir | 10 | 900,000 | 0.35 | 32 | 40 |
| | Cap rock | 0.00001 | 300,000 | 0.10 | 14 | 40 |
| **5. Case - combination 1** | Reservoir | 30 | 300,000 | 0.17 | 32 | 40 |
| | Cap rock | 0.00001 | 50,000 | 0.10 | 14 | 40 |
| **6. Case - combination 2** | Reservoir | 30 | 900,000 | 0.35 | 0 | 6 |
| | Cap rock | 0.00001 | 300,000 | 0.10 | 0 | 14 |

### 9.3.2 WELL INJECTION CONSTRAINTS

In every case there were two gas injector wells.

Different well locations were tested, the wells which were used were grouped:

Táz-19 & Táz-30 ; Táz-19 & Táz-21 and Táz-19 & Táz-4 wells. (Figure 66.)

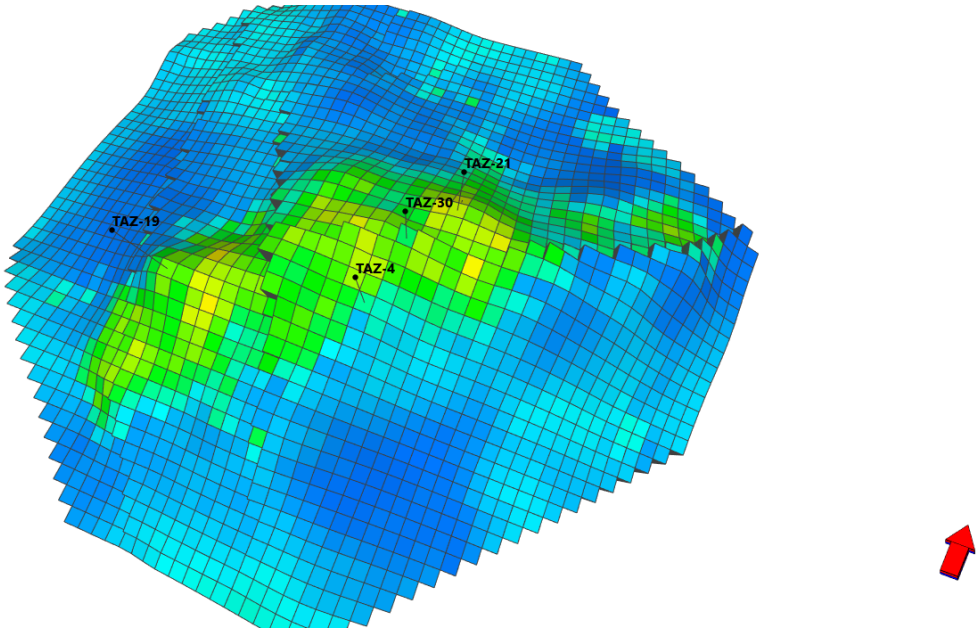


Figure 66. Location of the injection wells
(source: tNavigator ; Edited by the author)

As there were no well models and vertical lift performance curves available, or well test data to be able to create the curves. Bottom Hole Pressure (BHP) constraints were used to control the injection. This number was defined to not to increase the reservoir pressure above the initial reservoir pressure to avoid fracking the formation or the cap rock. $P_{BHPmax}$ = 207 barg.

The injected amount was 1.2 Mtons/year. That amount is identified and harmonized with the strategy of MOL Plc.

There was only a small difference in the results indicating that the average permeability model is not sensitive to the well location.

There were runs with higher BHP controls with the Táz-19 & Táz-21 wells.
If the maximal field reservoir pressure of 200 bar was used, the injection was stopped after reaching the 200 bar reservoir average pressure.

Without this limit the reservoir pressure was increased till 400 bar, in which case the fracking was probable. (See Figure 67.) Take it to consideration, that the surface launch pressure would have had to be unimaginably high for this to manner.

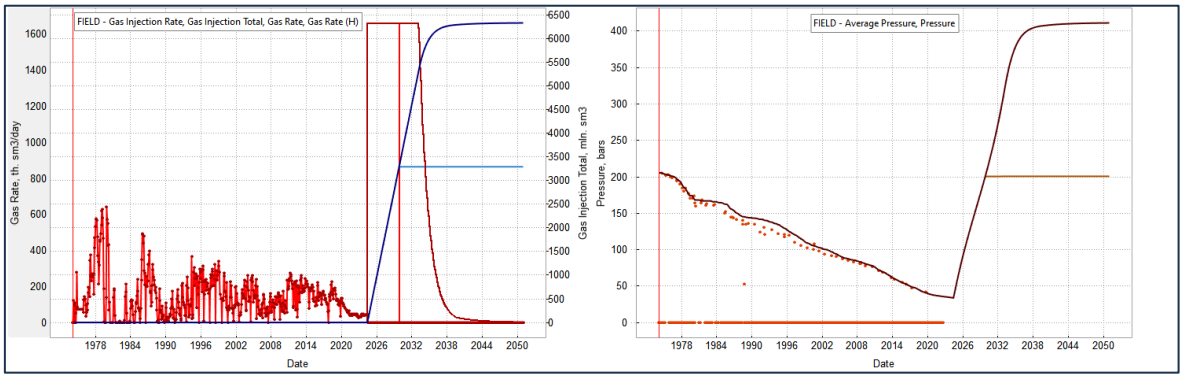


Figure 67. Results of unlimited BHP
(source: tNavigator ; Edited by the author)

If the reservoir pressure constraint was removed, the high pressure caused more rock failure in the cap rock.

If the reservoir is more heterogenous, and the injection pressure is high, rock failure can happen anywhere in the reservoir and the structures and well sites of the injection wells are also destroyed. (See Táz-31 on Figure 68.)

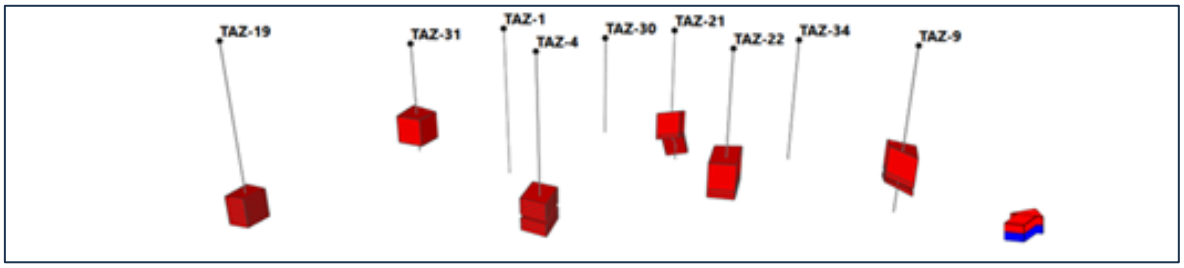


Figure 68. Destroyed well structure during the “unlimited” injection
(source: tNavigator ; Edited by the author)

Higher injected amount was also evaluated, instead of 1.2 Mtons/year, 2.4 Mtons/year was injected in case of the next two versions. The constraints were the same as before, one with reservoir pressure limitation, the other without is. (Shown on Figure 69.)

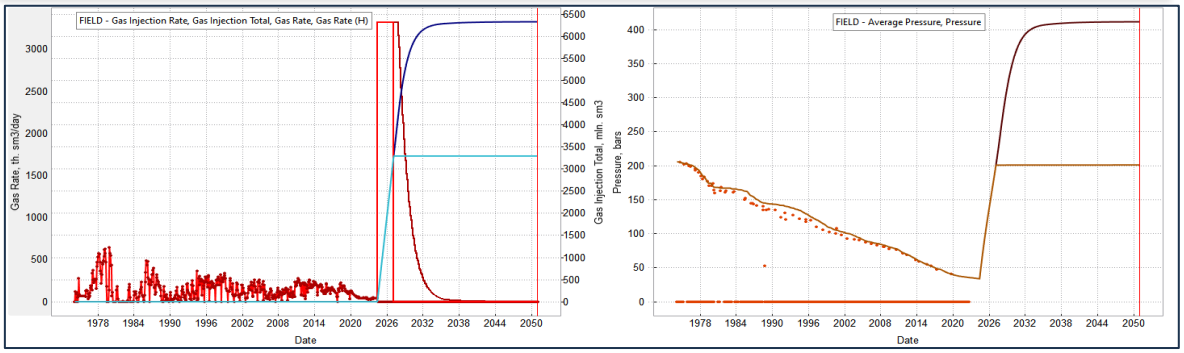


Figure 69. Injection rate and reservoir pressure trends @ 2.4 Mtons/year injection (source: tNavigator ; Edited by the author)

During the simulation if the injection rate was increased and the reservoir pressure constraint was removed, the high pressure caused more rock failure in the cap rock, similarly to the previous case. Within 5 years the reservoir pressure reached the 400 barg.

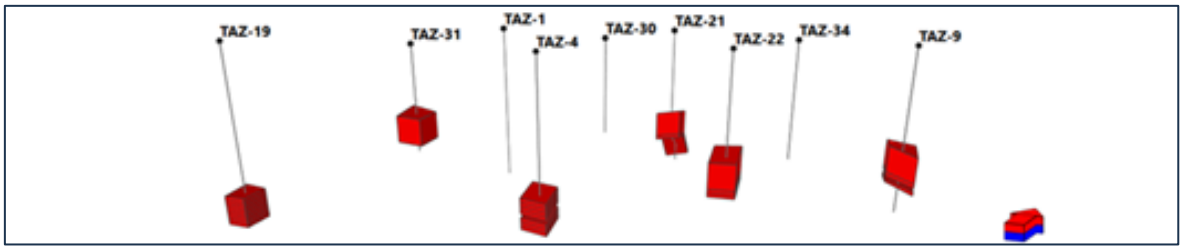


Figure 70. Well damages @ 2.4 Mtons/year injection (source: tNavigator ; Edited by the author)

### 9.3.3 RESULTS AND CONCLUSIONS

The main conclusion of the runs is that the result does not depend on the permeability. Using average permeability makes the model homogeneous, which does not describe the reservoir properly. The only difference is caused by using the minimum and maximum permeability was the injection rate – in case of 10 mD average permeability, the injection rate of the wells is much lower than in case of the 30 mD. (Shown on Figure 71&72.) The total injected amount is also slightly different, even after almost 75 years of injection the total injected $CO_2$ volume is less, due to the BHP constraint of the injectors.

Table 25. Simulation based specified values of Tázlár field reservoir properties (source: tNavigator ; Edited by the author)

| **The calculated total injected $CO_2$ after 25 years** | **@10 mD** | **@30 mD** |
|---|---|---|
| Total injected $CO_2$ volume | 3.08 billion $m^3$ | 3.36 billion $m^3$ |
| Total injected $CO_2$ mass | 6.31 Mt | 6.89 Mt |

| | |
|---|---|
| **Original Gas in Place** | 3.02 billion $m^3$ |
| **Pore Volume @ Reservoir Conditions** | 21.20 $Mm^3$ |

At reservoir conditions, above $CO_2$ critical pressure and temperature, $CO_2$ behaves like a supercritical fluid, with a density often 2–3 times that of methane at the same reservoir pressure. This means that for the same pore space, more standard cubic meters of $CO_2$ molecules are storable than methane molecules.

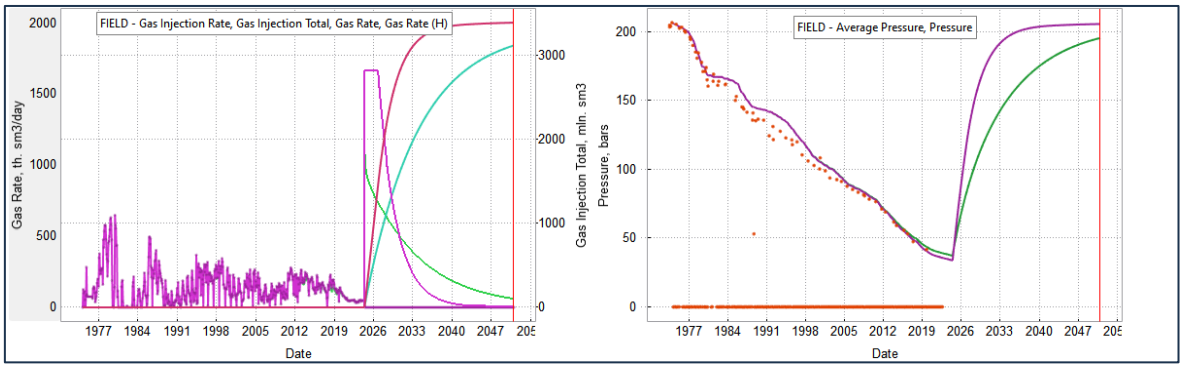


Figure 71. Injection rate and pressure @ 30 mD
(source: tNavigator ; Edited by the author)

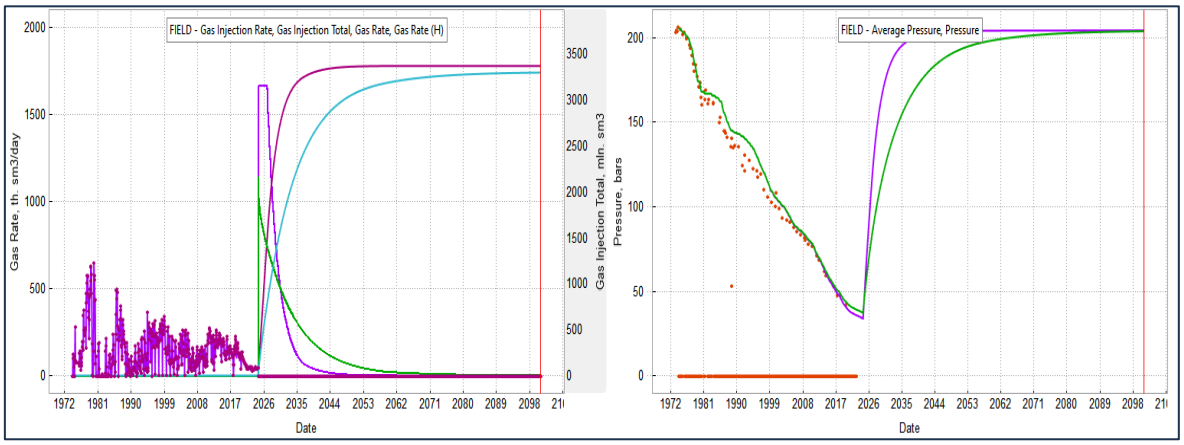


Figure 72. Injection rate and pressure @ 10 mD
(source: tNavigator ; Edited by the author)

### 9.3.4 SIMULATION OF THE 6 CASES

#### 9.3.4.1 Case 1

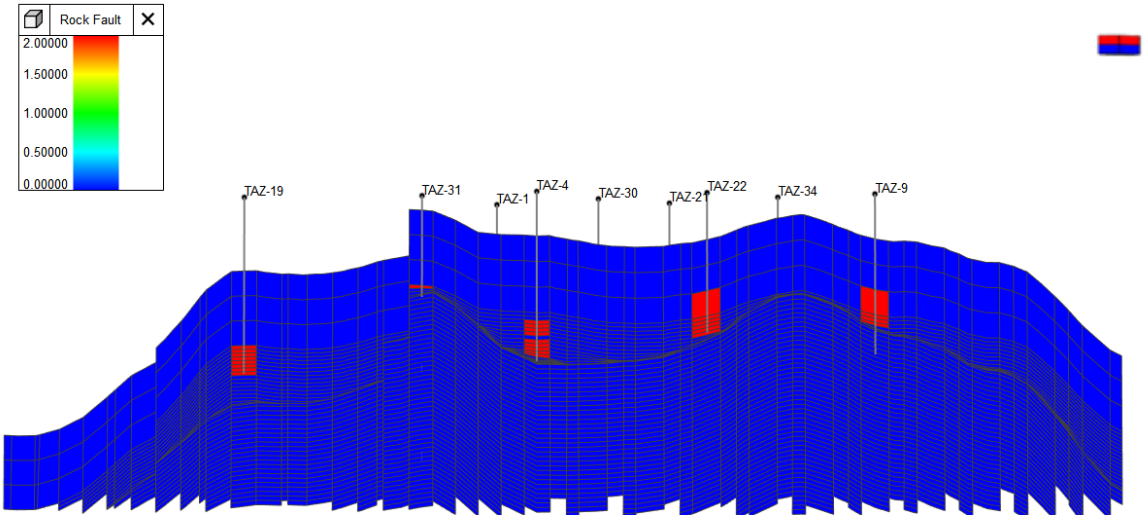


Figure 73. Cross-sectional view of Tázlár wells @ Case 1

(source: tNavigator ; Edited by the author)

| | Permeability | Young modulus [MPa] | Poisson ratio | Friction angel (theta) [°] | cohesion [MPa] |
|---|---|---|---|---|---|
| Reservoir | 30 | 300,000 | 0.17 | 0 | 6 |
| Cap rock | 0.00001 | 50,000 | 0.10 | 0 | 14 |

In case of “Case 1” when the friction angle is 0°, visible on Figure 73 and 74. several well location and the caprock damaged (with color red).

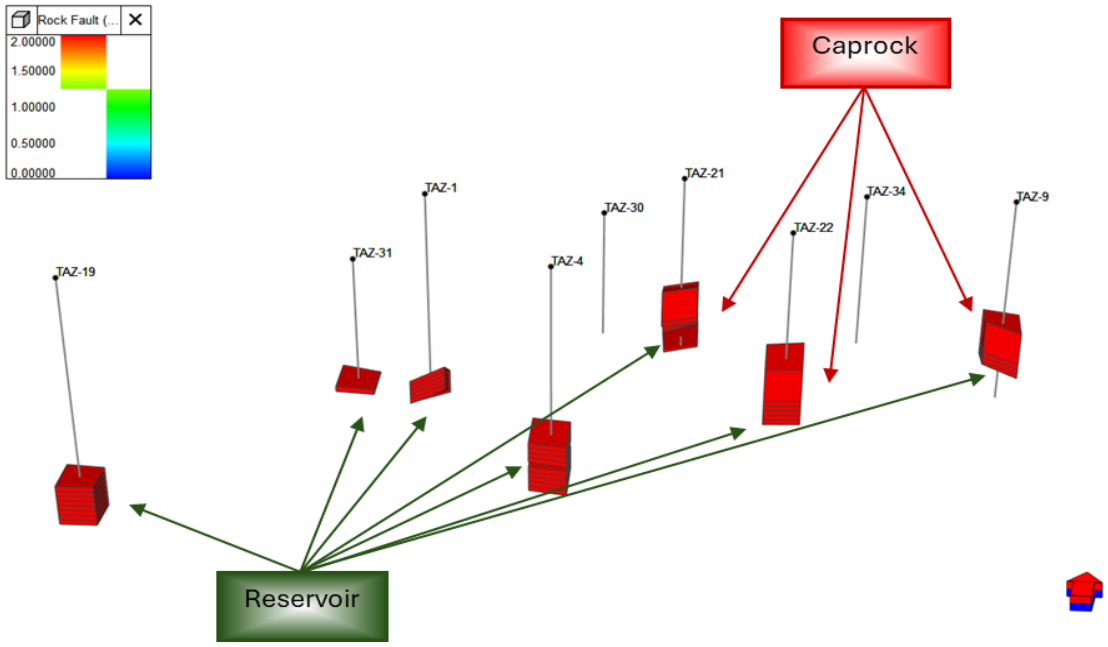


Figure 74. Visualization of the wells, reservoir and caprock @ Case 1

(source: tNavigator ; Edited by the author)

### 9.3.4.2 Case 2

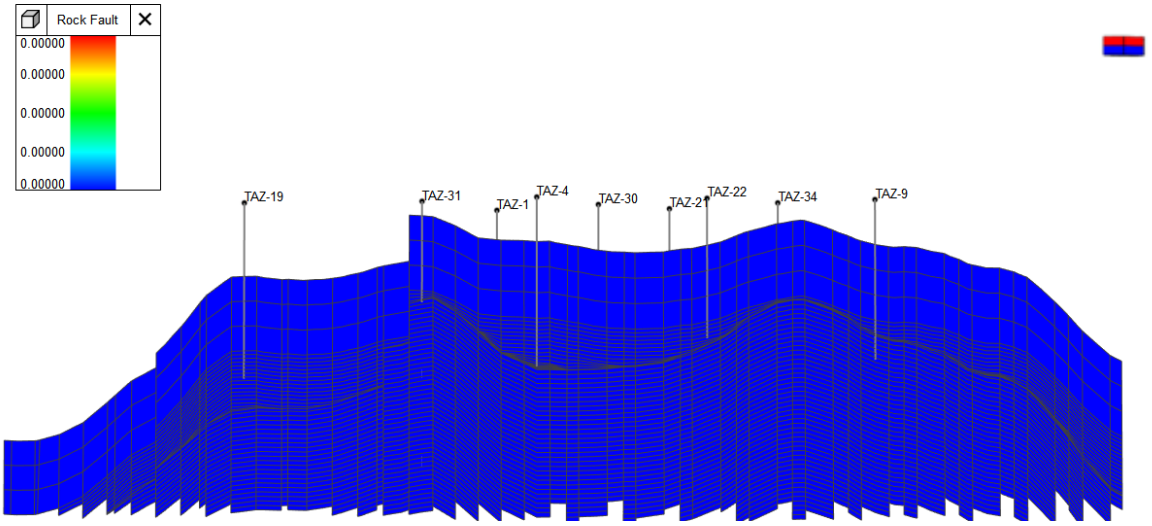


Figure 75. Cross-sectional view of Tázlár wells @ Case 2
(source: tNavigator ; Edited by the author)

| | Permeability | Young modulus [MPa] | Poisson ratio | Friction angel (theta) [°] | cohesion [MPa] |
|---|---|---|---|---|---|
| Reservoir | 30 | 900,000 | 0.35 | 32 | 40 |
| Cap rock | 0.00001 | 300,000 | 0.10 | 14 | 40 |

There are no damages at Case 2 simulation.

### 9.3.4.3 Case 3

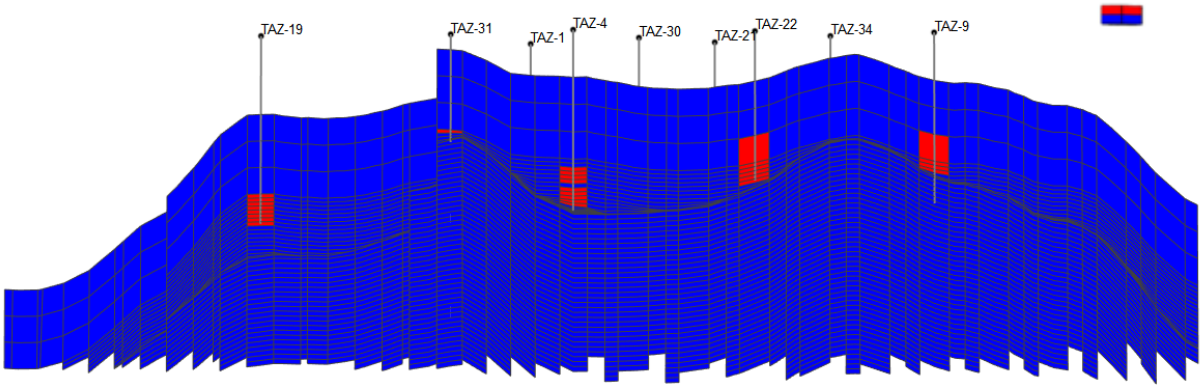


Figure 76. Cross-sectional view of Tázlár wells @ Case 3
(source: tNavigator ; Edited by the author)

| | Permeability | Young modulus [MPa] | Poisson ratio | Friction angel (theta) [°] | cohesion [MPa] |
|---|---|---|---|---|---|
| Reservoir | 10 | 300,000 | 0.17 | 0 | 6 |
| Cap rock | 0.00001 | 50,000 | 0.10 | 0 | 14 |

There are well sites damage in Case 3.

### 9.3.4.4 Case 4

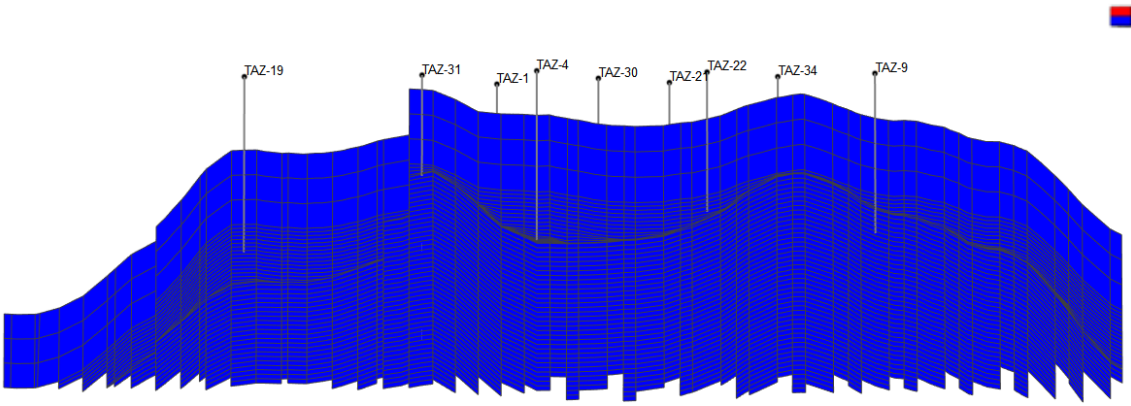


Figure 77. Cross-sectional view of Tázlár wells @ Case 4
(source: tNavigator ; Edited by the author)

| | Permeability | Young modulus [MPa] | Poisson ratio | Friction angel (theta) [°] | cohesion [MPa] |
|---|---|---|---|---|---|
| Reservoir | 10 | 900,000 | 0.35 | 32 | 40 |
| Cap rock | 0.00001 | 300,000 | 0.10 | 14 | 40 |

There are no damages at Case 4 simulation.

### 9.3.4.5 Case 5

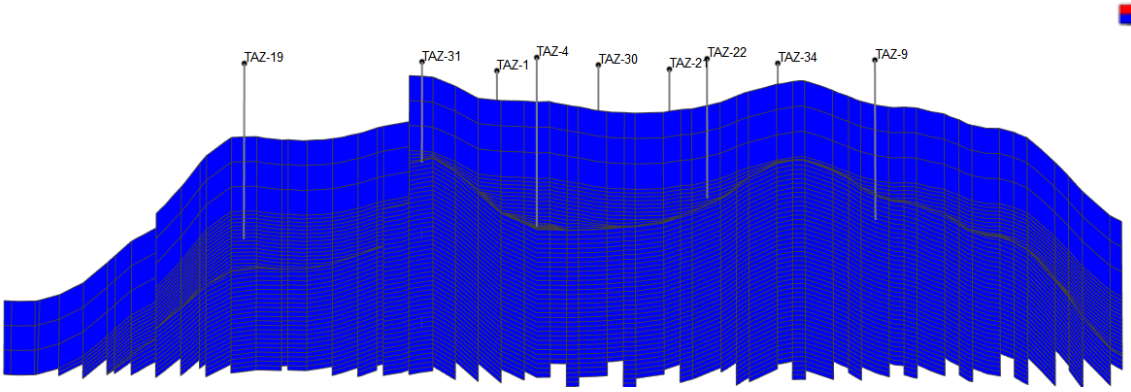


Figure 78. Cross-sectional view of Tázlár wells @ Case 5
(source: tNavigator ; Edited by the author)

| | Permeability | Young modulus [MPa] | Poisson ratio | Friction angel (theta) [°] | cohesion [MPa] |
|---|---|---|---|---|---|
| Reservoir | 30 | 300,000 | 0.17 | 32 | 40 |
| Cap rock | 0.00001 | 50,000 | 0.10 | 14 | 40 |

There are no damages at Case 5 simulation.

### 9.3.4.6 Case 6

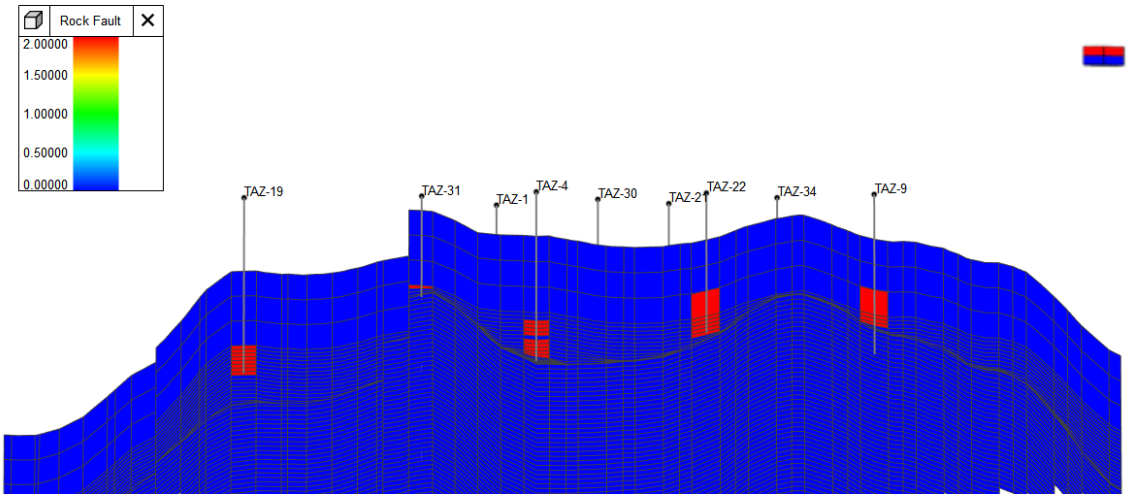


Figure 79. Cross-sectional view of Tázlár wells @ Case 6
(source: tNavigator ; Edited by the author)

| | Permeability | Young modulus [MPa] | Poisson ratio | Friction angel (theta) [°] | cohesion [MPa] |
|---|---|---|---|---|---|
| Reservoir | 30 | 900,000 | 0.35 | 0 | 6 |
| Cap rock | 0.00001 | 300,000 | 0.10 | 0 | 14 |

There are well site damages in Case 6.

The only parameter which seems to affect the rock failure is the theta, the friction angel. If 0° value is used, in every case the same failure occurred in the simulation runs. If the friction angle is higher than 0°, no failure could be observed.

### 9.3.4.7 Additional cases

In the previous six simulation cases, the behavior of the storage formation was modeled under extreme parameter values, spanning a broad spectrum. This approach was intended to explore the system's response under boundary conditions and to identify potential damage mechanisms. The results suggested that further simulations were warranted to investigate the influence of additional friction angle values on damage occurrence. The parameter combination of the runs were the following. (on Table 26.)

Table 26. Parameters of additional run scenarios
(Edited by the author)

| | | Permeability | Young modulus [MPa] | Poisson ratio | Friction angel (theta) [°] | cohesion [MPa] |
|---|---|---|---|---|---|---|
| **7. Case - min** | Reservoir | 10 | 300,000 | 0.17 | 16 | 40 |
| | Cap rock | 0.00001 | 50,000 | 0.10 | 7 | 40 |
| **7. Case - max** | Reservoir | 30 | 900,000 | 0.35 | 16 | 6 |
| | Cap rock | 0.00001 | 300,000 | 0.10 | 7 | 14 |
| **8. Case - min** | Reservoir | 10 | 300,000 | 0.17 | 8 | 40 |
| | Cap rock | 0.00001 | 50,000 | 0.10 | 4 | 40 |
| **8. Case - max** | Reservoir | 30 | 900,000 | 0.35 | 8 | 6 |
| | Cap rock | 0.00001 | 300,000 | 0.10 | 4 | 14 |
| **9. Case - min** | Reservoir | 10 | 300,000 | 0.17 | 4 | 40 |
| | Cap rock | 0.00001 | 50,000 | 0.10 | 2 | 40 |
| **9. Case - max** | Reservoir | 30 | 900,000 | 0.35 | 4 | 6 |
| | Cap rock | 0.00001 | 300,000 | 0.10 | 2 | 14 |
| **10. Case - min** | Reservoir | 10 | 300,000 | 0.17 | 2 | 40 |
| | Cap rock | 0.00001 | 50,000 | 0.10 | 1 | 40 |
| **10. Case - max** | Reservoir | 30 | 900,000 | 0.35 | 2 | 6 |
| | Cap rock | 0.00001 | 300,000 | 0.10 | 1 | 14 |
| **11. Case - min** | Reservoir | 10 | 500,000 | 0.25 | 37 | 20 |
| | Cap rock | 0.00001 | 60,000 | 0.30 | 25 | 3 |
| **11. Case - max** | Reservoir | 30 | 500,000 | 0.25 | 37 | 20 |
| | Cap rock | 0.00001 | 60,000 | 0.30 | 25 | 3 |

Consequently, a series of supplementary simulation scenarios were defined. To refine the estimation of the friction angle between the storage formation and the cap rock, an interval halving method was used. This iterative technique allowed for a more precise approximation of the critical friction angle values associated with structural damage.
Finally, the last simulation case incorporated the most representative literature-based average values for the lithology of the Tázlár formation. This provided a realistic benchmark for evaluating the mechanical behavior of the system under typical geological conditions.

In neither case was there any damage, so the cross-sectional visualizations will not be included in the dissertation. (would be the same as were on Figure 75, 77, 78.)

#### 9.3.4.8 Conclusions and notes

After further simulations, it can be concluded that damage only occurred in cases where the friction angle was 0°. Approximating the friction angle value using the interval halving method, there were no cases where damage occurred at values other than 0°. Based on the data in the literature, there was no change even at the most typical values, all while complying with the previously defined boundary conditions.

It should be noted that in reality if a failure has occurred during production history, it is uncertain how it behaves during the storage period or when the reservoir is fully filled and the average pressure is close to its initial value.

The model, due to the average permeability represents an ideal case, like a homogeneous reservoir, which never happens in nature especially in case of these rocks, where the permeability tends to be low, but the rock has natural fractures which drive every flow in the reservoir.

The model ran with different locations and different perforation depths for the $CO_2$ injection, but there is no significant difference between the runs due to the average permeability. The vertical permeability is 10% of the horizontal permeability in all cases.

The best producer's location should be selected for injections, to avoid increasing the pressure locally.

The main message of this evaluation is that before deciding which depleted oil or gas reservoir is suitable for CCS, detailed rock mechanics measurements are necessary to be able to decide which reservoir is the most secure to store $CO_2$ for a long period of time.

### 9.3.5 ROOF DEFORMATION

The roof deformation by the end of the production history is significant in all cases, due to the huge pressure depletion of the reservoir, which disappears by the end of the $CO_2$ injection.

This deformation also can help fracture propagation within the caprock, depending on the elasticity of the marl or clay.

The simulation of the roof deformation based on the production history and the $CO_2$ injection rates and parameter, when the well sites and structures are not damaged.

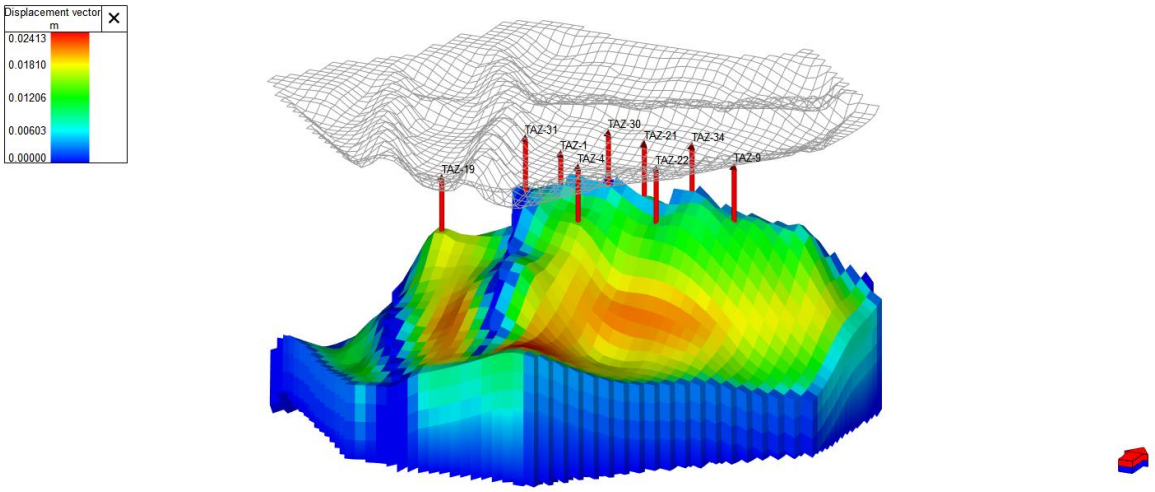


Figure 80. Roof deformation during the production
(source: tNavigator ; Edited by the author)

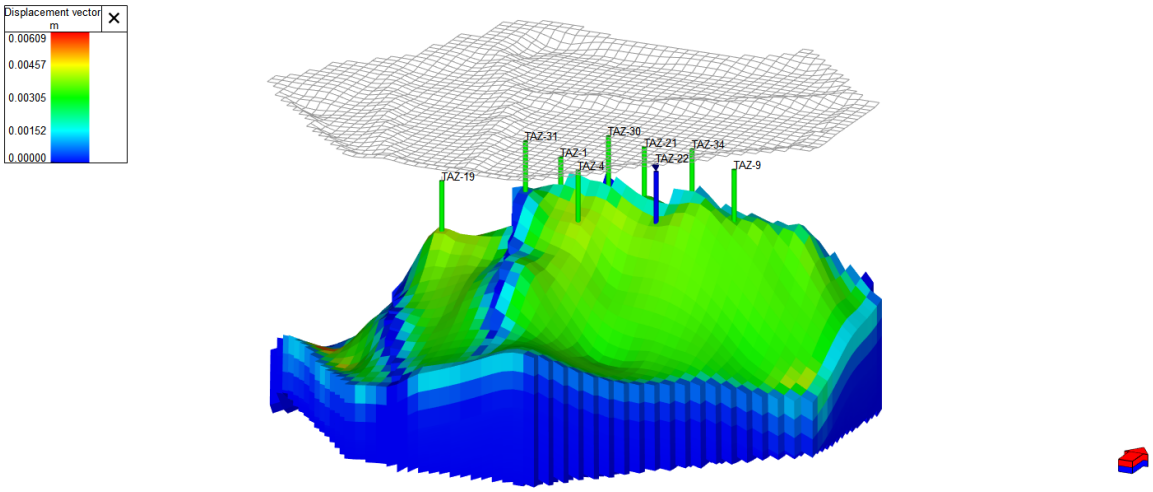


Figure 81. Roof deformation during the $CO_2$ injection
(source: tNavigator ; Edited by the author)

### 9.3.6 INCORPORATION THE RESULT OF THE MCT MEASUREMENTS

One of the output of the mCT measurements was new porosity-permeability correlations for the selected core sample.

Based on the mCT measurements, the calculated correlations come form the flooded section (495-700 slices). The measured permeability values are in unusable high range, at 100%, 25% and 12% eff. volume, represent higher quality rock or these slices with higher porosity probably cross a fracture, and their use would paint a completely extreme (unrealistic) picture of the storage facility. It has been concluded that not to use them as the base of the permeability calculation.

At 2% of eff. volume, the porosity – permeability dotes are in a same range, where the 10 mD and 30 mD minimal and maximal permeability values originally assume. Shown on Figure 82.

The correlation describing the flatter curve was used:

$$K = 0.3436 \cdot e^{1.3884 \cdot \varphi} \quad (27)$$

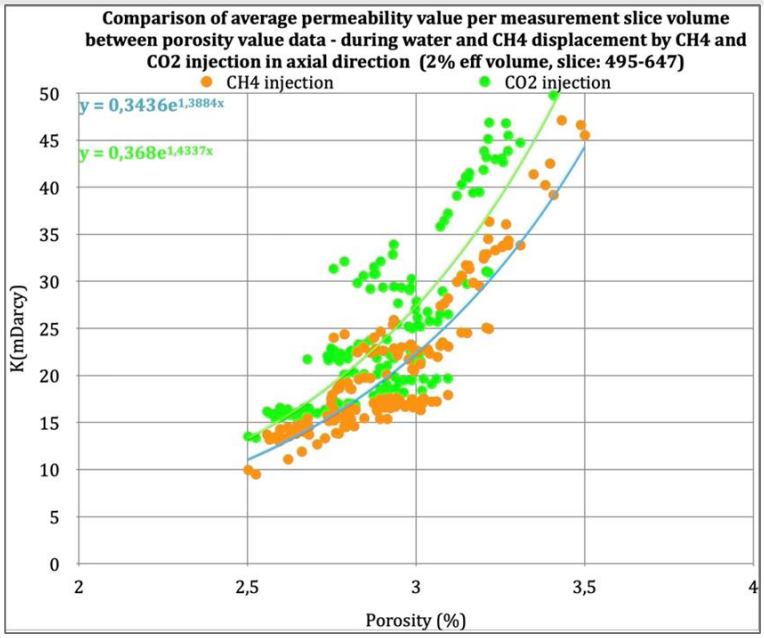


Figure 82. Visualization of porosity – permeability correlation @ 2% eff. volume
(Same as Figure 55.)
(source: tNavigator ; Edited by the author)

The calculated permeability distribution is the following:

Applying the porosity-permeability correlation derived from the core sample results in an average of approximately 14 mD. This is comparable to the “theoretic” minimum average of 10 mD, indicating that the outcomes do not significantly deviate from earlier scenarios. The results of core measurement suggest that, due to the selection of high-quality core samples chosen to ensure successful laboratory analysis, unfortunately, the data does not accurately represent the entire reservoir. As a result, the measurements tend to overestimate actual reservoir performance.

Given the rock poor quality and the fact that these types of reservoirs tend to be fractured, the permeability distribution calculated based on a poro-perm correlation given to the matrix gives too low permeability; the wells can’t produce their historical volume and on their production rates in the numerical simulation model.

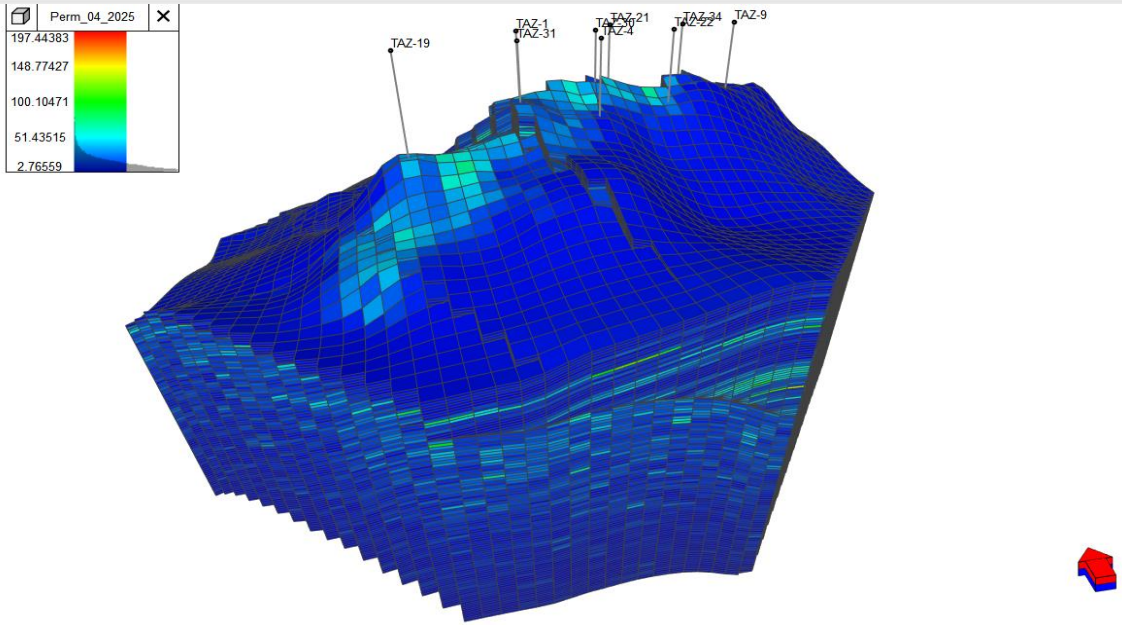


Figure 83. The calculated permeability distribution
(source: tNavigator ; Edited by the author)

The correlation was the following:

$$K = e^{0.306 \cdot \phi - 6.142} \quad (28)$$

The originally, field based correlation was confirmed: not usable and not realistic, based on the previous verified correct production history matching disfigurement. (see Figure 84.)

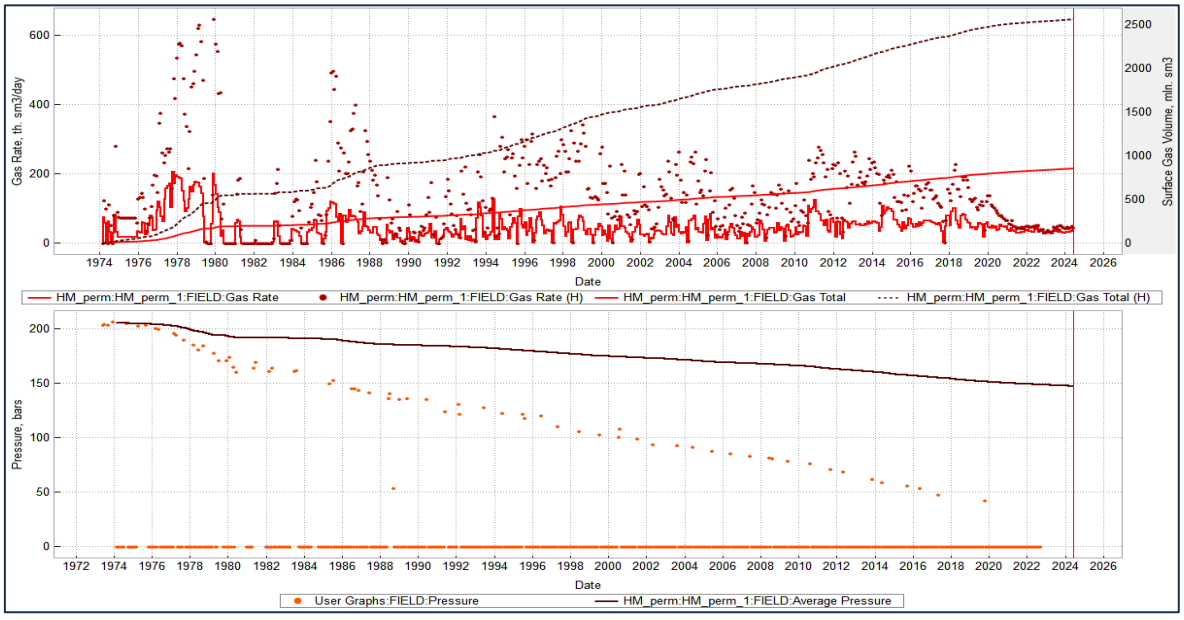


Figure 84. History matching with field based poro-perm correlation
(source: tNavigator ; Edited by the author)

# 10. CONCLUSIONS, SUMMARY AND THESES

The research makes several significant technical contributions to CCS knowledge and methodology development.

The application of medical CT scanners for detailed reservoir characterization represents a novel approach that provides cost-effective, high-resolution analysis of core samples. The methodology enables comprehensive evaluation of porosity distributions, fracture networks, and structural heterogeneity essential for storage assessment.

Integration of mCT analysis with controlled displacement experiments offers unique capabilities for understanding $CO_2$ storage processes. Monitoring of displacement fronts and saturation changes provides fundamental insights into storage mechanisms at the pore scale. This knowledge supports the development of improved injection strategies and reservoir management techniques.

Comprehensive experimental programs combining multiple analytical techniques provide robust validation of characterization methodologies. The integration of CT imaging, laboratory measurements, and microscopy analysis ensures accurate understanding of reservoir properties and storage behavior.

This multi-technique approach establishes best practices for future storage site assessment.

Advanced geomechanical modeling approaches demonstrate practical methods for assessing storage security and operational constraints. The integration of reservoir simulation with mechanical analysis provides comprehensive evaluation of injection scenarios and associated risks. These capabilities are essential for safe and effective storage implementation.

In order to simulate real-world processes at laboratory scale and to model conditions that most closely resemble the presumed implementation, the following boundary conditions were applied:

- $CO_2$ was injected in a supercritical state under both static and dynamic flooding scenarios;
- The model design incorporated field and laboratory data accumulated over decades and utilized by MOL Plc.;
- The values for pressure and temperature used in the simulations were derived from known conditions at the start of field development and at the end of production;
- Core samples previously extracted from wells were selected based on defined criteria, and only those were used for the experiments;
- The origin and quantity of the examined core samples were predetermined;

- The number of tests that could be conducted was constrained by the available financial resources;
- The resulting database served as the foundation of the research;
- The model can be refined in the future through the analysis and integration of additional samples. During the research, the aim was to enhance the experimental methodology and improve the accuracy of the results.

**1.)** The measurement program for static $CO_2$ flooding and static holding was defined according to the following parameters, same as Table 11. (Edited by the author).

| **$CO_2$ flooding** | **Duration (weeks)** | **Temperature (°C)** | **Pressure (bar)** |
|---|---|---|---|
| Before $CO_2$ flooding | - | 23 | - |
| I. cycle of $CO_2$ flooding | 1 | 50 | 65 |
| II. cycle of $CO_2$ flooding | 1 | 100 | 90 |
| III. cycle of $CO_2$ flooding | 2 | 100 | 90 |
| IV. cycle of $CO_2$ flooding | 1 | 135 | 90 |
| V. cycle of $CO_2$ flooding | 1 | 135 | 90 |
| VI. cycle of $CO_2$ flooding | 2 | 135 | 90 |

The measurement program for static $CO_2$ saturation and static holding was defined based on the following parameters: saturation durations, temperature and pressure values were determined in consideration of the resources and laboratory equipment specifications (core holder cell, $CO_2$ gas cylinder, manometer) available at the Research Institute of Applied Earth Sciences, University of Miskolc. For the first saturation cycle, was defined to include $CO_2$ saturation in its gaseous state, followed by exposure to several temperatures above the critical point of $CO_2$, under the maximum pressure achievable under laboratory conditions (90 barg).

Following the measurement of basic rock parameters, 5 out of the available 18 core samples were selected for further testing. Selection was based on the highest porosity and permeability values, as well as the aim to represent different reservoir units and lithologies, in order to obtain the most comprehensive dataset possible from the measurements.

After the $CO_2$ treatment contact time elapsed, the cores were removed from the pressure-retaining cell. The rock samples were then dried in an oven until constant mass was achieved, after which repeated He porosity and $N_2$ permeability measurements were performed. Subsequently, the cores were returned to the cell, and the next flooding cycle commenced. After 6 measurement cycles, an increase in porosity and permeability was observed between the initial and final states for samples CT-1/1 (quartz-rich clay shale),

CT-3/1 (conglomerate), and CT-8/1 (sandstone). These findings were corroborated by thin-section petrographic analyses. In these samples from the Tázlár field, $CO_2$ induced dissolution processes, although no crystallization or carbonate precipitation was observed. For sample CT-10/1 (bioclastic marl), He porosity increased after the I. saturation cycle, decreased during the II. and III. cycles, and then showed a clear increase again following the IV.-V.-VI. treatments. $N_2$ permeability initially showed a slight decrease, followed by a marked increase after the fourth to sixth treatments.

In the case of sample CT-11/1 (bioclastic limestone), He porosity increased after the I. and II. $CO_2$ flooding cycles, but subsequent cycles led to a decrease or stagnation. $N_2$ permeability decreased after the I. and V. treatments, while slight increases were observed following the other cycles.

**2.)** It was the first application of medical-grade CT scanners for geological reservoir analysis in Hungary. Quantitative 3D characterization of porosity, permeability. The measurement program was developed for dynamic $CO_2$ flooding using micro-CT (mCT) rock analysis. The objective was to model hydrocarbon production under laboratory conditions following the reproduction of initial reservoir conditions and formation fluids and subsequently simulate $CO_2$ injection based on the current reservoir state—mirroring the process as it would occur at field scale. The initial reservoir temperature was 128 °C; however, due to the technical limitations of the mCT equipment, this temperature could not be achieved during measurement. Nevertheless, a temperature of 90 °C was sufficient to maintain $CO_2$ in a supercritical state at the applied pressure steps, enabling realistic simulation of field conditions. The mCT technology allowed for the visualization of flow patterns and the determination of porosity and permeability values throughout the following experimental steps:

a.) Establishing the initial state: the sample was held under vacuum until its mass stabilized.

b.) Flooding the dry sample with ion-exchange water at room temperature. The injected volume was 10 $cm^3$, with an estimated pore volume of 0.8 $cm^3$.

c.) Performing mCT measurement on the water-saturated sample.

d.) Injecting an additional 10 $cm^3$ of ion-exchanged water to ensure full saturation, with pressure increased up to 100 barg.

e.) Performing mCT measurement on the fully saturated sample.

f.) Increasing pressure to the initial reservoir pressure of 207 barg.

g.) Performing mCT measurement.

h.) Raising the temperature to 90 °C.

i.) Performing mCT measurement.

j.) First $CH_4$ flooding cycle at 207 barg and 90 °C. Injected volume: 10 cm³.

k.) Performing mCT measurement.

l.) Second $CH_4$ flooding cycle at 207 barg and 90 °C. Injected volume: 10 cm³.

m.) Performing mCT measurement.

n.) Adjusting to current reservoir pressure: 30 barg.

o.) Performing mCT measurement.

p.) Increasing pressure to 100 barg. First $CO_2$ flooding cycle at 100 barg and 90 °C. Injected volume: 10 cm³.

q.) Performing mCT measurement.

r.) Increasing pressure to 207 barg. Second $CO_2$ flooding cycle at 207 barg and 90 °C. Injected volume: 10 cm³.

s.) Performing mCT measurement.

Based on the experiments, the following observations were made:

**3.)** During mCT measurement, the cylindrical rock specimen is reconstructed slice by slice (with slice thickness depending on the resolution of the equipment). The evaluation of the measurement is based on average parameters calculated for each individual slice.

**4.)** Calibration confirmed that measurement noise did not influence the results.

**5.)** The mCT technique is capable of distinguishing between three different fluids—water, methane, and supercritical $CO_2$ —under reservoir conditions, based on their density differences.

**6.)** During the $CO_2$ injection/methane displacement process, a steady-state condition was not achieved. $CO_2$ did not fully traverse the sample, thus relative permeability could not be determined. A total of 10 cm³ of $CO_2$ was injected into a pore volume of 0.8 cm³. This more than tenfold volumetric ratio was based on preliminary estimation. Since real-time monitoring of the flooding process was not possible, the extent of flooding could only be inferred retrospectively from the measurement results. For future repetitions of the experiment, either the duration of the measurement or the volume of injected $CO_2$ should be increased. However, financial resources were not available to repeat the measurements.

**7.)** As steady-state flow was not achieved and $CO_2$ did not fully penetrate the pore space, permeability calculations must rely on new in-situ interpretations at the slice level. For a given porosity, multiple permeability values may be associated; however, some slices exhibit similar behavior. At different effective volume percentages (2%, 12%, 25%, and 100%), distinct new porosity–permeability correlations were established, as summarized in the following table.

Calculated Porosity-permeability correlations
(Edited by the author)

| Effective volume | Porosity-permeability correlation |
|---|---|
| 100% | $K = 23.291 \cdot e^{0.0994 \cdot \varphi}$ |
| 25% | $K = 6.8474 \cdot e^{0.1887 \cdot \varphi}$ |
| 12% | $K = 2.7628 \cdot e^{0.3329 \cdot \varphi}$ |
| 2% | $K = 0.3436 \cdot e^{1.3884 \cdot \varphi}$ |

e - Euler number and φ - porosity (%)

**Thesis 1) "Clarifying the presence or absence of an active aquifer"**

By integrating the production history of the Tázlár field, formation pressure measurement data, and the static PVT model into a new software platform (tNavigator)—which had not previously been used for this field—it was demonstrated that, contrary to earlier assumptions, the field does not possess an active aquifer and no water influx occurs within the reservoir. Using this data, a high-accuracy history match was achieved both at the individual well level and for the entire field, under the assumption of an aquifer-free system. When an active aquifer was assumed, the simulated data showed very limited correlation with the measured data.

Clarifying the presence or absence of an active aquifer is of critical importance for $CO_2$ storage, as the presence of large volumes of formation water influences $CO_2$ flow behavior, available pore volume, dissolution potential, and formation pressure, ultimately affecting the volume of $CO_2$ that can be injected.

**Thesis 2) "Derivation of porosity-permeability relationships across different lithologies"**

**8.)** The calibrated dynamic model (history-matched, assuming a homogeneous reservoir with a permeability of 30 mD—both boundary conditions derived from the static model developed and used by MOL Plc.) revealed that the commonly used porosity–permeability correlation:

$$K = e^{0.306 \cdot \varphi - 6.142}$$

is not suitable for characterizing the reservoir when considering known field data. This correlation has also appeared in previous production review plans.

**9.)** One of the output of the mCT measurements was new porosity-permeability correlations for the selected core sample.

Based on the mCT measurements, the calculated correlations come form the flooded section (495-700 slices). The measured permeability values are in unusable high range, at

100%, 25% and 12% eff. volume, represent higher quality rock or these slices with higher porosity probably cross a fracture, and their use would paint a completely extreme (unrealistic) picture of the storage facility. It has been concluded that not to use them as the base of the permeability calculation.
At 2% of eff. volume, the porosity – permeability dotes are in a same range, where the 10 mD and 30 mD minimal and maximal permeability values originally assume. Shown on Figure 82.

The correlation describing the flatter curve was used:

$$K = 0.3436 \cdot e^{1.3884 \cdot \varphi}$$

The calculated permeability distribution is the following:

Applying the porosity-permeability correlation derived from the core sample results in an average of approximately 14 mD. This is comparable to the “theoretic” minimum average of 10 mD, indicating that the outcomes do not significantly deviate from earlier scenarios.

**Thesis 3) “Novel integration of CT and mCT technologies for reservoir-scale heterogeneity analysis”**

Among the porosity–permeability correlations obtained from the mCT measurements, the one assuming the lowest permeability value—when implemented into the dynamic model—resulted in a better match (14 mD). Thus, using the porosity–permeability correlation derived from the mCT measurement that assumes the lowest (and most realistic) permeability yielded a more accurate history match in the dynamic simulation. Nevertheless, the sample used in the measurement cannot be considered representative, and the reservoir itself is not homogeneous. However, it was confirmed that by conducting additional similar measurement programs, the porosity–permeability correlation for the field can be significantly refined.

**10.)** Geomechanical sensitivity analyses were also conducted. In the absence of measured rock physical parameters, literature data were used to make several inferences regarding the reservoir, the caprock, and surface conditions. Based on the simulation program and the boundary conditions summarized in the following table, the following results were obtained (same as Table 24):

| | | Permeability | Young modulus [MPa] | Poisson ratio | Friction angel (theta) | cohesion |
|---|---|---|---|---|---|---|
| **1. Case - min** | Reservoir | 30 | 300,000 | 0.17 | 0 | 6 |
| | Cap rock | 0.00001 | 50,000 | 0.10 | 0 | 14 |
| **2. Case - max** | Reservoir | 30 | 900,000 | 0.35 | 32 | 40 |
| | Cap rock | 0.00001 | 300,000 | 0.10 | 14 | 40 |
| **3. Case - min** | Reservoir | 10 | 300,000 | 0.17 | 0 | 6 |
| | Cap rock | 0.00001 | 50,000 | 0.10 | 0 | 14 |
| **4. Case - max** | Reservoir | 10 | 900,000 | 0.35 | 32 | 40 |
| | Cap rock | 0.00001 | 300,000 | 0.10 | 14 | 40 |
| **5. Case - combination 1** | Reservoir | 30 | 300,000 | 0.17 | 32 | 40 |
| | Cap rock | 0.00001 | 50,000 | 0.10 | 14 | 40 |
| **6. Case - combination 2** | Reservoir | 30 | 900,000 | 0.35 | 0 | 6 |
| | Cap rock | 0.00001 | 300,000 | 0.10 | 0 | 14 |

The following boundary conditions were used in the simulations:

- Initial and current reservoir pressures and temperatures
  - Initial reservoir pressure, temperature: 207 barg ; 128°C
  - Current reservoir pressure, temperature: 30 barg ; 128°C
- Maximum available layer pressure at initial layer pressure: 200 barg
- Amount of injected $CO_2$ 1,2 Mt/year (planned storage volume by MOL Plc.)
- Overburden: marble

Findings:

**Thesis 4) "Implementation of field-calibrated geomechanical models using tNavigator"**

Damage to the reservoir, wellbore vicinity, or caprock during $CO_2$ injection occurred only when the rock's internal friction angle was assumed to be 0°. No other parameter variation led to fracturing of the formation. Based on literature data, six different simulation cases were run using various extreme values for both the reservoir and the caprock, as summarized in the table above.

**11.)** The results of the six simulation run, suggested that further simulations were warranted to investigate the influence of additional friction angle values on damage occurrence. Consequently, a series of supplementary simulation scenarios were defined. To refine the estimation of the friction angle between the storage formation and the cap rock, an interval halving method was used. This iterative technique allowed for a more precise approximation of the critical friction angle values associated with structural damage.

Finally, the last simulation case incorporated the most representative literature-based average values for the lithology of the Tázlár formation. This provided a realistic benchmark for evaluating the mechanical behavior of the system under typical geological conditions. Confirmed: No other parameter variation led to fracturing of the formation.

**12.)** According to the surface deformation simulation results, the ground surface has subsided by more than 20 mm in certain areas since the start of production, based on known production and pressure data. Under the projected injection rate of 1.2 Mt/year and a maximum allowable reservoir pressure of 207 barg, these surface deformations are expected to reverse, returning to pre-production conditions.

**13.)** If the maximum allowable reservoir pressure during injection is increased to twice the initial reservoir pressure (~400 barg), the reservoir fractures and wellbore damage occur in all cases.

**Thesis 5) "Estimation of safe $CO_2$ injection parameters"**

Simulations were also conducted assuming 10 mD and 30 mD permeability values. The main conclusion from the model runs is that the results are not dependent on permeability. Using an average permeability value renders the model homogeneous, which does not accurately represent the reservoir. The only difference caused by using minimum versus maximum permeability is the time required to reach the maximum reservoir pressure. With an average permeability of 10 mD, the maximum pressure of 207 barg is reached in approximately 75 years, whereas with 30 mD, it is reached after 25 years.

**14.)** The total injectable volume differs slightly according to the simulation results. Assuming an average permeability of 10 mD, the reservoir reaches near-maximum pressure in about 35 years. Over the following 40 years, the inflow rate becomes minimal until the maximum reservoir pressure is reached. This is due to the low permeability and the limited pressure differential, as the bottomhole pressure is capped at 207 barg. In contrast, assuming an average permeability of 30 mD, the reservoir reaches the maximum allowable pressure after 25 years, during which time the total injected $CO_2$ volume is approximately 10% higher than in the previous case.

Laboratory experimental programs utilize limited sample sets that may not fully represent field-scale heterogeneity. Scaling effects between laboratory and field conditions require careful consideration in applying experimental results to actual storage operations. Additional testing of diverse sample types would strengthen confidence in regional storage assessment.

Geomechanical property databases for Hungarian reservoir rocks remain limited, requiring reliance on literature values and analogous field data. Direct measurement programs for key geomechanical parameters would significantly improve modeling accuracy and reduce uncertainty in risk assessment. Enhanced characterization of caprock properties is particularly important for storage security evaluation.

Long-term storage behavior prediction relies on relatively short-term experimental programs that may not capture all relevant processes. Extended experimental programs and field monitoring data are needed to validate long-term storage security predictions. Understanding of geochemical reactions requires longer-term studies to assess mineral trapping potential.

**Thesis 6) "Simulation based specified values of Tázlár field reservoir properties"**

The dynamic simulation ensures values about Tázlár reservoir properties, these numbers obtained can then provide a foundation for further economic analyses.

| **The calculated total injected $CO_2$ after 25 years** | **@10 mD** | **@30 mD** |
|---|---|---|
| Total injected $CO_2$ volume | 3.08 billion $m^3$ | 3.36 billion $m^3$ |
| Total injected $CO_2$ mass | 6.31 Mt | 6.89 Mt |

| | |
|---|---|
| **Original Gas in Place** | 3.02 billion $m^3$ |
| **Pore Volume @ Reservoir Conditions** | 21.20 $Mm^3$ |
| **Total gas production** | 2,557.78 $Mm^3$ |

The integrated analysis estimates $CO_2$ storage capacity of ~7 million tons (3.36 billion $m^3$), with structural and residual trapping mechanisms dominating initially, followed by gradual increases in solubility and mineral trapping over time.

At reservoir conditions, above $CO_2$ critical pressure and temperature, $CO_2$ behaves like a supercritical fluid, with a density often 2–3 times that of methane at the same reservoir pressure. This means that for the same pore space, more standard cubic meters of $CO_2$ molecules are storable than methane molecules.

This research provides essential foundation for advancing $CO_2$ storage implementation in Hungary and similar geological settings worldwide. Continued development of characterization methodologies, experimental validation, and demonstration projects will accelerate the deployment of this critical climate change mitigation technology.

# 11. REFERENCES

Adriana Paluszny, Caroline C. Graham, Katherine A. Daniels, Vasiliki Tsaparli, Dimitrios Xenias, Saeed Salimzadeh, Lorraine Whitmarsh, Jon F. Harrington, Robert W. Zimmerman, (2020) Caprock integrity and public perception studies of carbon storage in depleted hydrocarbon reservoirs, International Journal of Greenhouse Gas Control, Volume 98, 2020, 103057, ISSN 1750-5836, https://doi.org/10.1016/j.ijggc.2020.103057. (https://www.sciencedirect.com/science/article/pii/S1750583619306590)

Akin, S., Kovscek, A.R., (2003). Computed tomography in petroleum engineering research. Geol. Soc. London. Special Publ. 215, 23-38.

Al Baroudi, Hisham & Awoyomi, Adeola & Patchigolla, Kumar & Anthony, Edward. (2021). A review of large-scale CO2 shipping and marine emissions management for carbon capture, utilisation and storage.

Alalwan, H. A., & Alminshid, A. H. (2021). CO2 capturing methods: Chemical looping combustion (CLC) as a promising technique. The Science of the total environment, 788, 147850. https://doi.org/10.1016/j.scitotenv.2021.147850

Al-Bayati, D., Saeedi, A., Myers, M., White, C., Xie, Q., Clennell, B., 2018. Insight investigation of miscible SCCO2 Water Alternating Gas (WAG) injection performance in heterogeneous sandstone reservoirs. J. CO2 Util. 28, 255-263. doi:10.1016/j.jcou.2018.10.010.

Alsarhan, L.M., Alayyar, A.S., Alqahtani, N.B., Khdary, N.H., 2021. Circular Carbon Economy (CCE): A Way to Invest CO2 and Protect the Environment, a Review. Sustainability 13, 11625. doi:10.3390/su132111625.

Al-Shargabi, M., Davoodi, S., Wood, D.A., Rukavishnikov, V.S., Minaev, K.M., 2022. Car-bon Dioxide Applications for Enhanced Oil Recovery Assisted by Nanoparticles: Re-cent Developments. ACS Omega 7, 9984-9994. doi:10.1021/acsomega.1c07123.

Aminu, M.D., Nabavi, S.A., Rochelle, C.A., Manovic, V., 2017. A review of developments in carbon dioxide storage. Appl. Energy 208, 1389-1419. doi:10.1016/j.apenergy.2017.09.015.

Anjana Krishnan, Amrita Nighojkar, Balasubramanian Kandasubramanianb (2023) Emerging towards zero carbon footprint via carbon dioxide capturing and sequestration, Carbon Capture Science & Technology 9 (2023) 100137

Askaripour, Mahdi & Saeidi, Ali & Mercier-Langevin, Patrick & Rouleau, Alain. (2022). A Review of Relationship between Texture Characteristic and Mechanical Properties of Rock. Geotechnics. 2. 262-296. 10.3390/geotechnics2010012.

Bachu, S. (2000). Sequestration of CO2 in geological media: Criteria and approach for site selection in response to climate change. Energy Conversion and Management, 41(9), 953-970.

Bachu, S., & Adams, J.J. (2003). Sequestration of CO2 in geological media in response to climate change: capacity of deep saline aquifers to sequester CO2 in solution. Energy Conversion and Management, 44(20), 3151-3175.

Beaubien, S.E., Jones, D.G., Gal, F., Barkwith, A.K.A.P., Braibant, G., Baubron, J.C., Ciotoli, G., Graziani, S., Lister, T.R., Lombardi, S., Michel, K., Quattrocchi, F., Strutt, M.H., 2013. Monitoring of near-surface gas geochemistry at the Weyburn, Canada, CO2-EOR site, 2001-2011. Int. J. Greenh. Gas Control 16, S236-S262. doi:10.1016/j.ijggc.2013.01.013.

Bin Pan, Xia Yin, Stefan Iglauer, (2021a) Rock-fluid interfacial tension at subsurface conditions: Implications for H2, CO2 and natural gas geo-storage, International Journal of Hydrogen Energy, Volume 46, Issue 50, 2021, Pages 25578-25585, ISSN 0360-3199, https://doi.org/10.1016/j.ijhydene.2021.05.067. https://www.sciencedirect.com/science/article/pii/S0360319921018218)

Bin Pan, Xia Yin, Weiyao Zhu, Yongfei Yang, Yang Ju, Yujie Yuan, Lijie zhang, Stefan Iglauer, (2022) Theoretical study of brine secondary imbibition in sandstone reservoirs: Implications for H2, CH4, and CO2 geo-storage, International Journal of Hydrogen Energy, Volume 47, Issue 41, 2022, Pages 18058-18066, ISSN 0360-3199, https://doi.org/10.1016/j.ijhydene.2022.03.275. (https://www.sciencedirect.com/science/article/pii/S0360319922014252)

Bobok E. (2012) Fluid dynamics, Miskolci Egyetem, ISBN: 2310011937799

Bongole, K., Sun, Z., Yao, J., Mehmood, A., Yueying, W., Mboje, J., Xin, Y., 2019. Multi-fracture response to supercritical CO 2 -EGS and water-EGS based on thermo-hydro-mechanical coupling method. Int. J. Energy Res. 4743. doi:10.1002/er.4743.

Brown ET, Bray JW, Santarelli FJ (1989) Influence of stress-dependent elastic moduli on stresses and strains around axisymmetric boreholes. Rock Mech Rock Engng 22:189-203

Bukka, V. Rohit, and Sarin, Pankaj (2024) Effects of Particle Size Reduction on the Pore Structure and Accessibility in Natural Porous Materials. United States: N. p., 2024. Web. doi:10.1021/acs.energyfuels.4c00194. (https://www.sciencedirect.com/science/article/pii/B9780444635334000019)

Burrows, L.C., Haeri, F., Cvetic, P., Sanguinito, S., Shi, F., Tapriyal, D., Goodman, A., Enick, R.M., 2020. A Literature Review of CO 2, Natural Gas, and Water-Based Fluids for Enhanced Oil Recovery in Unconventional Reservoirs. Energy & Fuels 34, 5331¬5380. doi:10.1021/acs.energyfuels.9b03658.

Celia, M. A., S. Bachu, J. M. Nordbotten, and K. W. Bandilla (2015), Status of CO2 storage in deep saline aquifers with emphasis on modeling approaches and practical simulations, Water Resour. Res., 51, 6846–6892, doi:10.1002/2015WR017609.

Chandra, Naveen & Patra, P. & Bisht, Jagat & Ito, Akihiko & Umezawa, Taku & Saigusa, Nobuko & Morimoto, Shinji & Aoki, Shuji & Janssens-Maenhout, G. & Fujita, Ryo & Takigawa, Masayuki & Watanabe, Shingo & Saitoh, Naoko & Canadell, Josep. (2020). Emissions from the Oil and Gas Sectors, Coal Mining and Ruminant Farming Drive Methane Growth over the Past Three Decades. Journal of the Meteorological Society of Japan. 99. 10.2151/jmsj.2021-015.

Cheng, C.Y., Kuo, C.C., Yang, M.W., Zhuang, Z.Y., Lin, P.W., Chen, Y.F., Yang, H.S., Chou, C.T., 2021. CO2 Capture from Flue Gas of a Coal-Fired Power Plant Using Three-Bed PSA. Process. Energies 14, 3582. doi:10.3390/en14123582.

Cheng, X., Mei, K., Li, Z., Zhang, X., Guo, X., (2016) Research on the interface structure during unidirectional corrosion for oil-well cement in H2S based on computed tomography technology. Ind. Eng. Chem. Res. 55, 10889-10895.

CHIQUET, P., BROSETA, D., THIBEAU, S., 2007. Wettability alteration of caprock minerals by carbon dioxide. Geofluids 7, 112-122. doi:10.1111/j.1468-8123.2007.00168.x.

Czarnota, R., Janiga, D., Stopa, J., Wojnarowski, P., 2017. Determination of minimum miscibility pressure for CO 2 and oil system using acoustically monitored separator. J. CO2 Util. 17, 32-36. doi:10.1016/j.jcou.2016.11.004.

Dudek, J., Janiga, D., Wojnarowski, P., 2021. Optimization of CO2-EOR process management in polish mature reservoirs using smart well technology. J. Pet. Sci. Eng. 197, 108060. doi:10.1016/j.petrol.2020.108060.

Esmaeil Koohestanian, Farhad Shahraki, (2021) Review on principles, recent progress, and future challenges for oxy-fuel combustion CO2 capture using compression and purification unit, Journal of Environmental Chemical Engineering, Volume 9, Issue 4, 2021, 105777, ISSN 2213-3437, https://doi.org/10.1016/j.jece.2021.105777. (https://www.sciencedirect.com/science/article/pii/S2213343721007545)

Esterhuizen, Gabriel & Bajpayee, T.S. & Ellenberger, J.L. & Murphy, Michael. (2013). Practical estimation of rock properties for modeling bedded coal mine strata using the Coal Mine Roof Rating. 47th US Rock Mechanics / Geomechanics Symposium 2013. 3. 1634-1647.

European Commission (2021). Regulation (EU) 2021/1119 establishing the framework for achieving climate neutrality ('European Climate Law'). Official Journal of the European Union.

European Commission. (2019). "Directive 2009/31/EC on the Geological Storage of Carbon Dioxide." Retrieved from European Commission.

Farrell, N.J.C., Healy, D., Taylor, C.W., 2014. Anisotropy of permeability in faulted porous sandstones. J. Struct. Geol. 63, 50-67. doi:10.1016/j.jsg.2014.02.008.

Feldkamp, L.A., Davis, L.C., & Kress, J.W. (1984). Practical cone-beam algorithm. Journal of the Optical Society of America A, 1(6), 612-619.

Feng, D., Li, X., Wang, X., Li, J., Zhang, X., 2018. Capillary filling under nanoconfinement: The relationship between effective viscosity and water-wall interactions. Int. J. Heat Mass Transf. 118, 900-910. doi:10.1016/j.ijheatmasstransfer.2017.11.049.

Feng, F., Wu, J., Zeng Liang, C., Weber, M., Zhang, S., Chung, T.S., 2023. Syner-gistic dual-polymer blend membranes with molecularly mixed macrocyclic cavitands for efficient pre-combustion CO2 capture. Chem. Eng. J. 470, 144073. doi:10.1016/j.cej.2023.144073.

Földes, T. (2015). Standardized Imaging Protocols for Geological CT Scanning. Geophysical Journal International, 201 (2), 123-135.

Földes, T., & Kovács, A. (2012). Advances in Non-Destructive Rock Analysis Using CT Technology. Geoscientific Instrumentation, Methods, and Data Systems, 31 (2), 203-210.

Földes, T., Kiss, J., & Tóth, G. (2010). Innovations in Geological CT Analysis: Techniques and Applications. Journal of Applied Geophysics, 70 (1), 86-98.

Fuhar Dixit, Karl Zimmermann, Majed Alamoudi, Leili Abkar, Benoit Barbeau, Madjid Mohseni, Balasubramanian Kandasubramanian, Kevin Smith, (2022) Application of MXenes for air purification, gas separation and storage: A review Renewable and Sustainable Energy Reviews, Volume 164, 2022, 112527, ISSN 1364-0321, https://doi.org/10.1016/j.rser.2022.112527. https://www.sciencedirect.com/science/article/pii/S1364032122004282)

Gan, M., Zhang, L., Miao, X., Oladyshkin, S., Cheng, X., Wang, Y., Shu, Y., Su, X., & Li, X. (2020). Application of computed tomography (CT) in geologic CO2 utilization and storage research: A critical review. Journal of Natural Gas Science and Engineering, 83, 103591.

Gaus, I., 2010. Role and impact of CO2-rock interactions during CO2 storage in sedimen-tary rocks. Int. J. Greenh. Gas Control 4, 73-89. doi:10.1016/j.ijggc.2009.09.015.

Gilliland, E.S., Ripepi, N., Conrad, M., Miller, M.J., Karmis, M., 2013. Selection of monitoring techniques for a carbon storage and enhanced coalbed methane recovery pilot test in the Central Appalachian Basin. Int. J. Coal Geol. 118, 105-112. doi:10.1016/j.coal.2013.07.007.

Global CCS Institute (2020). Global status of CCS 2020. Global Carbon Capture and Storage Institute.

Hamza, A., Hussein, I.A., Al-Marri, M.J., Mahmoud, M., Shawabkeh, R., Aparicio, S., 2021. CO2 enhanced gas recovery and sequestration in depleted gas reservoirs: A review. J. Pet. Sci. Eng. 196, 107685. doi:10.1016/j.petrol.2020.107685.

Hayder A. Alalwan, Alaa H. Alminshid,(2021) CO2 capturing methods: Chemical looping combustion (CLC) as a promising technique, Science of The Total Environment, Volume 788, 2021, 147850, ISSN 0048-9697, https://doi.org/10.1016/j.scitotenv.2021.147850. (https://www.sciencedirect.com/science/article/pii/S0048969721029211)

Hendriks, C.A., Blok, K., 1993. Underground storage of carbon dioxide. Energy Convers. Manag. 34, 949-957. doi:10.1016/0196-8904(93)90041-8.

Hoek E (2007) Practical Rock Engineering. Rock science.

Hoek E, Brown ET (1980) Underground excavations in rock. Inst Min Metall London

Holloway, S., Savage, D., 1993. The potential for aquifer disposal of carbon dioxide in the. UK. Energy Convers. Manag. 34, 925-932. doi:10.1016/0196-8904(93)90038-C.

Hounsfield, G.N. (1973). Computerized transverse axial scanning (tomography): Part 1. Description of system. British Journal of Radiology, 46(552), 1016-1022.

Iglauer. S.. A. Z. Al-Yaseri. R. Rezaee. and M. Lebedev (2015). CO2 wettability of caprocks: Implications for structural storage capacity and containment security. Geophys. Res. Lett.. 42. 9279–9284. doi:10.1002/2015GL065787.

Intergovernmental Panel on Climate Change. Climate Change 2014: Mitigation of Climate Change: Working Group III Contribution to the IPCC Fifth Assessment Report. Cambridge University Press; 2015.

International Energy Agency (2020). Energy Technology Perspectives 2020: Clean Energy Transitions Programme. IEA Publications.

IPCC, 2019. Global warming of 1.5 °C: an IPCC special report on the impacts of global warming of 1.5 °C above pre-Industrial levels and related global greenhouse gas emission pathways, in the Context of Strengthening the Global Response to the Threat of Climate Change. In: Masson-Delmotte, Valerie, Zhai, Panmao, Portner, Hans-Otto, Roberts, Debra, Skea, Jim, Shukla, Priyadarshi R., Pirani, Anna, Moufouma-Okia, Wilfran, Pean,

Clotilde, Pidcock, Roz, Connors, Sarah, Robin Matthews, J.B., Chen, Yang, Zhou, Xiao, Gomis, Melissa I., Lonnoy, Elisabeth, Maycock, Tom, Tignor, Melinda, Waterfield, T. (Eds.), Sustainable Development, and Efforts to Eradicate Poverty. https://www.ipcc.ch/sr15/.

J. A. Hudson & J. P. Harrison (1997) Engineering Rock Mechanics - An Introduction to the Principles - Part 1

J. Schön, Physical Properties of Rocks, Volume 65: Fundamentals and Principles of Petrophysics. Netherlands. 2015. Print.

Jaeger JC, Cook NGW (1979) Fundamentals of rock mechanics, 3rd edition. Chapman & Hall

Jay M. Korde and Balasubramanian Kandasubramanian (2019) Fundamentals and Effects of Biomimicking Stimuli-Responsive Polymers for Engineering Functions, Industrial & Engineering Chemistry Research 2019 58 (23), 9709-9757 DOI: 10.1021/acs.iecr.9b00683

Jenkins, C., Chadwick, A., Hovorka, S.D., 2015. The state of the art in monitor-ing and verification—Ten years on. Int. J. Greenh. Gas Control. 40, 312-349. doi:10.1016/j.ijggc.2015.05.009.

Jia Liu, Jan Baeyens, Yimin Deng, Tianwei Tan, Huili Zhang, (2020) The chemical CO2 capture by carbonation-decarbonation cycles, Journal of Environmental Management, Volume 260, 2020, 110054, ISSN 0301-4797, https://doi.org/10.1016/j.jenvman.2019.110054. (https://www.sciencedirect.com/science/article/pii/S0301479719317724)

Kalair, A., Abas, N., Saleem, M.S., Kalair, A.R., Khan, N., 2021. Role of energy storage systems in energy transition from fossil fuels to renewables. Energy Storage 3. doi:10.1002/est2.135.

Kalender, W. A. (1994). Spiral CT: Current Concepts and Applications. **International Journal of Radiation Oncology, Biology, Physics, 30**(1), 123-139.

Kalender, W. A., Wolf, H., Suess, C., & Klotz, E. (1999). Comparison of the Sensitivity of Different Multi-Detector Computed Tomography (MDCT) Scanners for Detecting Low-Contrast Signals in Phantoms. **European Radiology, 9**(7), 1409-1414.

Karagianni, A. & Karoutzos, Georgios & Ktena, Stella & Vagenas, Nikolaos & Vlachopoulos, Ioannis & Sabatakakis, Nikolaos & Koukis, George. (2017). ELASTIC PROPERTIES OF ROCKS. Bulletin of the Geological Society of Greece. 43. 1165. 10.12681/bgsg.11291.

Kaza, R. K., Platt, J. F., Goodsitt, M. M., Al-Hawary, M. M., Dhanani A. E., Wasnik, A. P., Neville, A. M., & Francis, I. R. (2010). Emerging Techniques in Oncologic Imaging. **Radiographics, 30**(3), 836-854.

Kiss, J., Tóth, G., & Földes, T. (2014). 3D Visualization Techniques in Geological CT Imaging. **Journal of Structural Geology, 67**(1), 1-10.

Kovari K, Tisa A, Einstein HH, Franklin JA (1983) Suggested methods for determining the strength of rock materials in triaxial compression: revised version. Int J Rock Mech Min Sci Geomech Abstr 20, 283-290

Kubovics. I. (1993): Kőzetmikroszkópia I-II. Nemzeti Tankönyvkiadó. Budapest.

Lawrence M. Anovitz.& David R. Cole; Characterization and Analysis of Porosity and Pore Structures. Reviews in Mineralogy and Geochemistry 2015;; 80 (1): 61–164. doi: https://doi.org/10.2138/rmg.2015.80.04

Lee, C.T., Mohammad Rozali, N.E., Van Fan, Y., Klemes, J.J., Towprayoon, S., 2018. Low-carbon emission development in Asia: energy sector, waste management and environmental management system. Clean Technol. Environ. Policy 20, 443-449. doi:10.1007/s10098-018-1512-8.

Lianyang Zhang (2005) Engineering Properties of Rocks - Elsevier GEO-Engineering Book Series, Volume 4, 1st Edition

Li-ping, H., Ping-ping, S., Xin-wei, L., Qi-Chao, G., Cheng-sheng, W., Fangfang, L., 2015. Study on CO2 EOR and its geological sequestration potential in oil field around Yulin city. J. Pet. Sci. Eng. 134, 199-204. doi:10.1016/j.petrol.2015.06.002.

Liu, Tao & Zhao, Guanghui. (2025). Study on Enhanced Geothermal System of Carbon Dioxide Fracturing Dry Hot Rock. Academic Journal of Science and Technology. 14. 36-38. 10.54097/q5n4pm12.

Liu, Y., Rui, Z., 2022. A Storage-Driven CO2 EOR for a Net-Zero Emission Target. Engineering 18, 79-87. doi:10.1016/j.eng.2022.02.010.

Lucile Trevisan, Mélanie Bordignon, (2020) Screening Life Cycle Assessment to compare CO2 and Greenhouse Gases emissions of air, road, and rail transport: An exploratory study, Procedia CIRP, Volume 90, 2020, Pages 303-309, ISSN 2212-8271, https://doi.org/10.1016/j.procir.2020.01.100. (https://www.sciencedirect.com/science/article/pii/S2212827120302675)

MacQuarrie, K.T.B., Mayer, K.U., 2005. Reactive transport modeling in fractured rock: A state-of-the-science review. Earth-Science Rev. 72, 189-227. doi:10.1016/j.earscirev.2005.07.003.

McPhee, C., Reed, J., & Zubizarreta, I. (2015). Core analysis: A best practice guide. Elsevier.

MedWrench. Siemens SOMATOM Plus Specifications. MedWrench. Available from: https://www.medwrench.com/equipment/857/siemens-somatom-plus. (Downloaded: 25/June/2024)

Meier, Trixi & Gross, Daniel & Hanenkamp, Nico. (2021). COMPARISON OF SPRAYABILITY AND SOLUBILITY OF BIO-BASED LUBRICANTS WITH LIQUID CARBON DIOXIDE. MM Science Journal. 2021. 5077-5084. 10.17973/MMSJ.2021_11_2021155.

Meng Z, Peng S, Ling B (2000) characteristics of strength and deformation for sedimentary rocks under different confining stresses. J of China Coal Society 25(1):15-18 (in Chinese)

Meng, Z., Zhang, J. & Peng, S. Influence of sedimentary environments on mechanical properties of clastic rocks. Environ Geol 51, 113–120 (2006). https://doi.org/10.1007/s00254-006-0309-y

Michael, K., Golab, A., Shulakova, V., Ennis-King, J., Allinson, G., Sharma, S., & Aiken, T. (2010). Geological storage of CO2 in saline aquifers—A review of the experience from existing storage operations. International Journal of Greenhouse Gas Control, 4(4), 659-667.

Mikulcic, H., Ridjan Skov, I., Dominkovic, D.F., Wan Alwi, S.R., Manan, Z.A., Tan, R., Duic, N., Hidayah Mohamad, S.N., Wang, X., 2019. Flexible Carbon Capture and Utilization technologies in future energy systems and the utilization pathways of captured CO2. Renew. Sustain. Energy Rev. 114, 109338. doi:10.1016/j.rser.2019.109338.

Ministry of Innovation and Technology (2020). National Energy and Climate Plan of Hungary. Government of Hungary.

Mogensen, K., Masalmeh, S., 2020. A review of EOR techniques for carbonate reservoirs in challenging geological settings. J. Pet. Sci. Eng. 195, 107889. doi:10.1016/j.petrol.2020.107889.

Molnár F.. Szentpéteri K. (2005): Opak ásványok mikroszkópos vizsgálata. Hantken Kiadó. Budapest.

Nicol, A., Carne, R., Gerstenberger, M., Christophersen, A., 2011. Induced seismicity and its implications for CO2 storage risk. Energy Procedia 4, 3699-3706. doi:10.1016/j.egypro.2011.02.302.

Nowrouzi, I., Manshad, A.K., Mohammadi, A.H., 2020. The mutual effects of injected fluid and rock during imbibition in the process of low and high salinity carbonated water injection into carbonate oil reservoirs. J. Mol. Liq. 305, 112432. doi:10.1016/j.molliq.2019.112432.

Orlic, B., 2016. Geomechanical effects of CO 2 storage in depleted gas reservoirs in the Netherlands: Inferences from feasibility studies and comparison with aquifer storage. J. Rock Mech. Geotech. Eng. 8, 846-859. doi:10.1016/j.jrmge.2016.07.003.

Pawar, R.J., Bromhal, G.S., Carey, J.W., Foxall, W., Korre, A., Ringrose, P.S., Tucker, O., Watson, M.N., White, J.A., 2015. Recent advances in risk assessment and risk management of geologic CO2 storage. Int. J. Greenh. Gas Control. 40, 292-311. doi:10.1016/j.ijggc.2015.06.014.

Peng S, Meng Z (2002) Theory and practice of mining engineering geology. Geological Press (in Chinese)

Peng S, Qu H, Luo L, Wang L, Duan Y (2000) Complete stress-strain and permeability experiments. J China Coal Society 25(2):113-116 (in Chinese)
Peng S, Wang J (2001) Safe mining over confining aquifers. Coal Industry Press (in Chinese)

RadiologyInfo.org. CT Scans. Radiology Info. Available from: https://www.radiologyinfo.org/en/info.cfm?pg=ct. (Downloaded: 25/June/2024)

Ranaee, E., Khattar, R., Inzoli, F., Blunt, M.J., Guadagnini, A., 2022. Assessment and uncertainty quantification of onshore geological CO2 storage capacity in China. Int. J. Greenh. Gas Control. 121, 103804. doi:10.1016/j.ijggc.2022.103804.

Raza, A., Glatz, G., Gholami, R., Mahmoud, M., Alafnan, S., 2022. Carbon mineralization and geological storage of CO2 in basalt: Mechanisms and technical challenges. Earth-Sci. Rev. 229, 104036. doi:10.1016/j.earscirev.2022.104036.

Rissman, J., Bataille, C., Masanet, E., Aden, N., Morrow, W.R., Zhou, N., Elliott, N., Dell, R., Heeren, N., Huckestein, B., Cresko, J., Miller, S.A., Roy, J., Fennell, P., Cremmins, B., Koch Blank, T., Hone, D., Williams, E.D., de la Rue du Can, S., Sisson, B., Williams, M., Katzenberger, J., Burtraw, D., Sethi, G., Ping, H., Danielson, D., Lu, H., Lorber, T., Dinkel, J., Helseth, J., 2020. Technologies and policies to decarbonize global industry: Review and assessment of mitigation drivers through 2070. Appl. Energy 266, 114848. doi:10.1016/j.apenergy.2020.114848.

Schembre, J.M., Kovscek, A.R., (2001). Direct measurement of dynamic relative permeability from CT monitored spontaneous imbibition experiments. SPE Annual Technical Conference and Exhibition. Society of Petroleum Engineers, New Orleans, Louisiana, p. 11.

Scherer, G.W., Celia, M.A., Prévost, J.H., Bachu, S., Bruant, R., Duguid, A., Fuller, R., Gasda, S.E., Radonjic, M., Vichit-Vadakan, W., 2005. Leakage of CO2 Through Abandoned Wells, in: Carbon Dioxide Capture for Storage in Deep Geologic Formations. Elsevier 827-848. doi:10.1016/B978-008044570-0/50136-7.

Siemens Healthcare. Computed Tomography. Siemens Healthineers. Available from: https://www.siemens-healthineers.com/computed-tomography. (Downloaded: 25/June/2024)

Sunil Kumar, Jalal Foroozesh, Katriona Edlmann, Mohamed Gamal Rezk, Chun Yan Lim, (2020) A comprehensive review of value-added CO2 sequestration in subsurface saline aquifers, Journal of Natural Gas Science and Engineering, Volume 81, 2020, 103437, ISSN 1875-5100, https://doi.org/10.1016/j.jngse.2020.103437. (https://www.sciencedirect.com/science/article/pii/S1875510020302912)

Suping Peng & Jincai Zhang (2007) Engineering Geology for Underground Rocks

Szabó, A., Harnos, Z., & Simon, J. (2019). "CO2 Storage Potential in Hungary's Depleted Oil and Gas Fields." Energy Policy Journal, 67(2), 89-97.

Szabó, A., Tóth, J., & Czinege, Z. (2020). Assessment of potential CO2 storage sites in the Pannonian Basin. Journal of Geological Research, 45(3), 123-138.

Teng Zhou, Huaiwei Shi, Xuechong Ding, Yageng Zhou,(2021) Thermodynamic modeling and rational design of ionic liquids for pre-combustion carbon capture, Chemical Engineering Science, Volume 229, 2021, 116076,ISSN 0009-2509, https://doi.org/10.1016/j.ces.2020.116076. (https://www.sciencedirect.com/science/article/pii/S0009250920306084)

Veres GP, Tamás Földes, István Szunyog, (2024) Assessment of core samples through the analysis of CT measurements and its implications for CO2 sequestration potential in a Hungarian depleted oil field, Results in Engineering, Volume 24, 2024, 103241, ISSN 2590-1230, https://doi.org/10.1016/j.rineng.2024.103241. (https://www.sciencedirect.com/science/article/pii/S2590123024014956)

Veres, GP (2022) – Supercritical CO2 injection in moderate-tight hydrocarbon reservoirs, a preliminary case study, Scientia et Securitas (Open Access) (2732-2688): 4 pp 1-9 (2022).

Veres, GP (2021), Magyarország energiastratégiája a klímasemlegesség tükrében, Multidiszciplináris tudományok, 11. kötet. (2021) 1 sz. pp. 69-75; https://doi.org/10.35925/j.multi.2021.1.7

W. Tanikawa & Zand T. Shimamoto (2006) Klinkenberg effect for gas permeability and its comparison to water permeability for porous sedimentary rocks - Hydrology and Earth System Sciences Discussions

Wei, N., Li, X., Wang, Y., Zhu, Q., Liu, S., Liu, N., Su, X., 2015. Geochemical impact of aquifer storage for impure CO 2 containing O 2 and N 2: Tongliao field experiment. Appl. Energy 145, 198-210. doi:10.1016/j.apenergy.2015.01.017.

Xu, X., Saeedi, A., Liu, K., 2017. An experimental study of combined foam/surfactant polymer (SP) flooding for carbone dioxide-enhanced oil recovery (CO2-EOR). J. Pet. Sci. Eng. 149, 603-611. doi:10.1016/j.petrol.2016.11.022.

Yang, G., Ma, X., Wen, D., Li, X., Diao, Y., Cao, W., Liu, D., Wang, S., Shao, W., 2021. Numerical study of CO2 geological storage combined with saline water recovery and optimization of injection-production schemes in eastern Junggar Basin of China. Int. J. Greenh. Gas Control. 110, 103404. doi:10.1016/j.ijggc.2021.103404.

Zhang, D., Song, J., 2014. Mechanisms for Geological Carbon Sequestration. Procedia IUTAM 10, 319-327. doi:10.1016/j.piutam.2014.01.027.

Zhao, N., Xu, T., Wang, K., Tian, H., Wang, F., 2018. Experimental study of physical-chemical properties modification of coal after CO 2 sequestration in deep unmineable coal seams. Greenh. Gases Sci. Technol. 8, 510-528. doi:10.1002/ghg.1759.

Zou, C., Wu, S., Yang, Z., Pan, S., Wang, G., Jiang, X., Guan, M., Yu, C., Yu, Z., Shen, Y., 2023. Progress, challenge and significance of building a carbon industry system in the context of carbon neutrality strategy. Pet. Explor. Dev. 50, 210-228. doi:10.1016/S1876-3804(22)60382-3.

# 12. LIST OF PUBLICATIONS RELATED TO THIS THESIS

Veres, Gábor Pál ; Földes, Tamás ; Szunyog, István (2024) Assessment of core samples through the analysis of CT measurements and its implications for CO2 sequestration potential in a Hungarian depleted oil field, RESULTS IN ENGINEERING 24 Paper: 103241 , 14 p. (2024), ***Rank: D1***

Veres, Gábor Pál (2021) Magyarország energiastratégiája a klímasemlegesség tükrében, MULTIDISZCIPLINÁRIS TUDOMÁNYOK: A MISKOLCI EGYETEM KÖZLEMÉNYE 11 : 1 pp. 69-75. , 7 p. (2021)

Veres, Gábor Pál (2022) Supercritical CO2 injection in moderate-tight hydrocarbon reservoirs, a preliminary case study, SCIENTIA ET SECURITAS 3 : 3 pp. 176-184. , 9 p. (2022)

Veres, Gábor Pál ; Vadászi, Mariann (2021) Az ipari szén-dioxid-leválasztás eljárásainak összehasonlító elemzése, MAGYAR ENERGETIKA 28 : 4 pp. 26-30. , 5 p. (2021)

# 13. ACKNOWLEDGMENTS

I would like to express my sincere gratitude to my supervisor Dr. István Szunyog, for their invaluable guidance, patience and continuous support throughout this research journey. Their insightful feedback and encouragement have been instrumental in shaping this dissertation.

I extend my appreciation to MOL Hungarian Oil and Gas Company, and for Hungarian Upstream colleagues for providing access to the Tázlár field data and core samples that formed the foundation of this research.

Special thanks to Dr. Béla Kelemen, for their support as an industrial leader and as a private mentor.

My gratitude goes to the Research Institute of Applied Earth Sciences and Institute of Exploration Geosciences , last but not least for Institute of Mining and Energy – University of Miskolc, for providing the research facilities and academic environment that made this work possible. The laboratory staff and technical experts deserve special recognition for their assistance with experimental procedures and analysis.

I am deeply grateful to TOMOGEO Ltd. particularly Tamás Földes, for sharing expertise in CT analysis and providing access to advanced imaging facilities that were essential for this research. Their technical knowledge and collaboration significantly enhanced the quality of this work.

I would like to acknowledge Andrea Lövei for their expertise and contribution to the geomechanical modeling component of this research. Their technical insights were invaluable for developing robust simulation models.

Finally, I wish to extend my sincere appreciation to my family, whose steadfast support, enduring patience, and unwavering belief in my abilities have been the cornerstone of this academic journey. Your encouragement has sustained me through moments of doubt and has been a constant source of strength throughout the challenges of this endeavor.

I am also deeply grateful to Kitti, whose presence in my life has brought renewed clarity and joy. Her compassion, understanding, and quiet confidence in me have provided invaluable reassurance during the final stages of this work.

I dedicate this dissertation to my beloved son, Zsombor.

# 14. APPENDICES

## 14.1 APPENDIX 1.

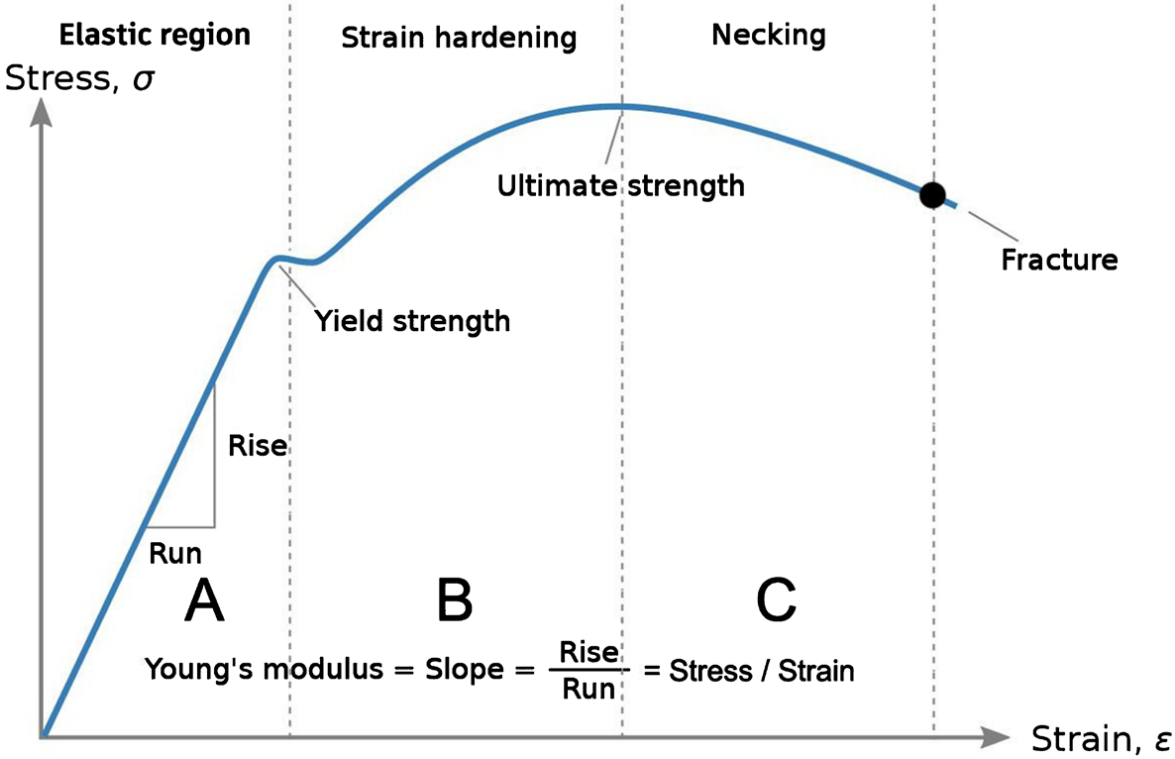


Figure 85. A typical stress-strain curve
(source: Alsayed, 2021)

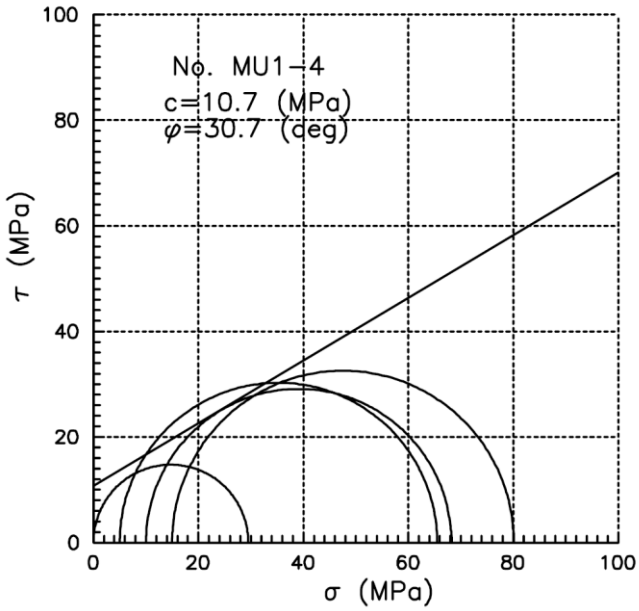


Figure 86. Mohr circles and strength envelope from triaxial tests in mudstone
(source: Peng and Zhang, 2007)

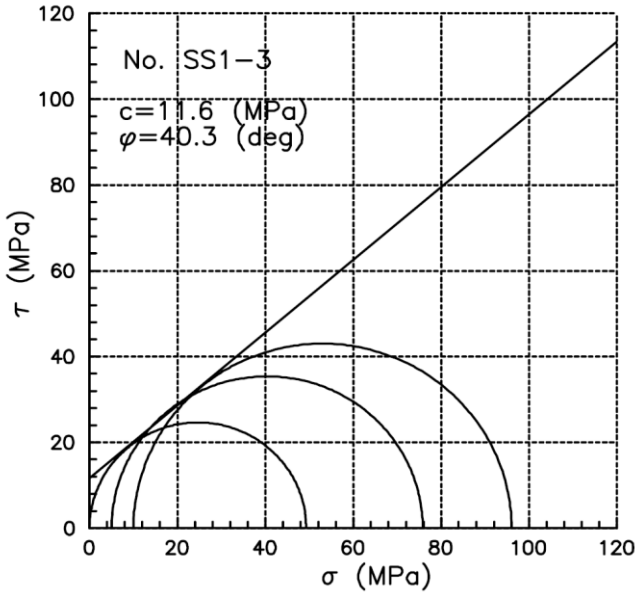


Figure 87. Mohr circles and strength envelope from triaxial tests in sandy shale (source: Peng and Zhang, 2007)

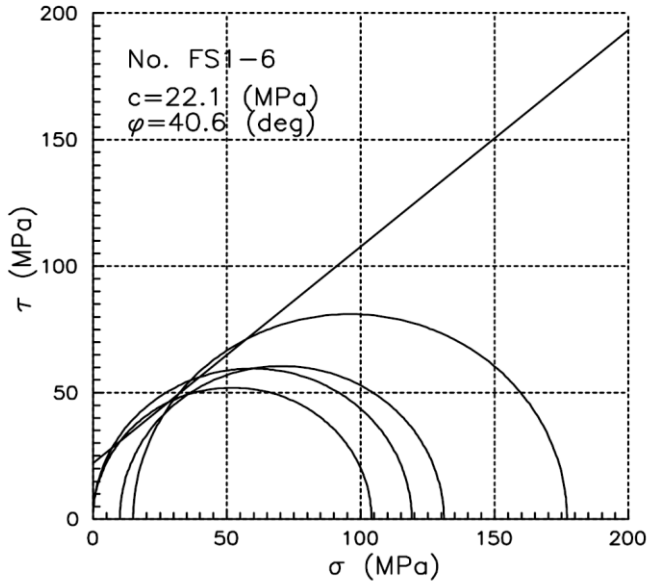


Figure 88. Mohr circles and strength envelope from triaxial tests in fine-grained sandstone (source: Peng and Zhang, 2007)

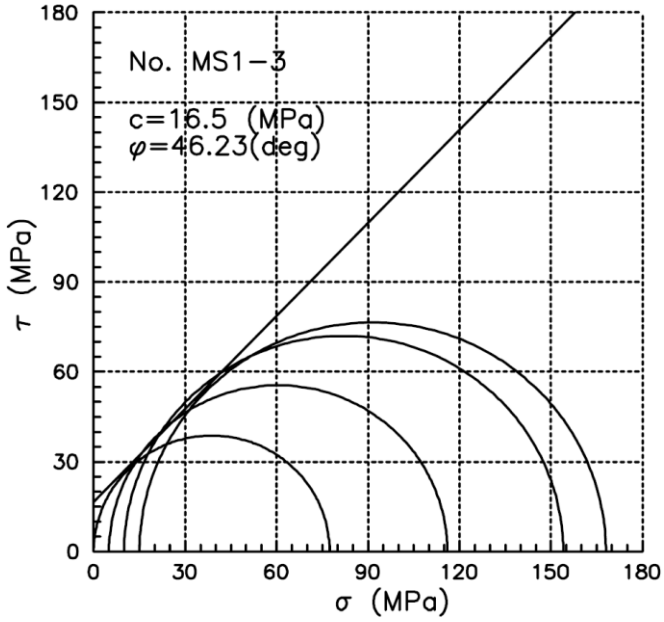


Figure 89. Mohr circles and strength envelopes from triaxial tests in medium grained sandstone
(source: Peng and Zhang, 2007)

## 14.2 APPENDIX 2.

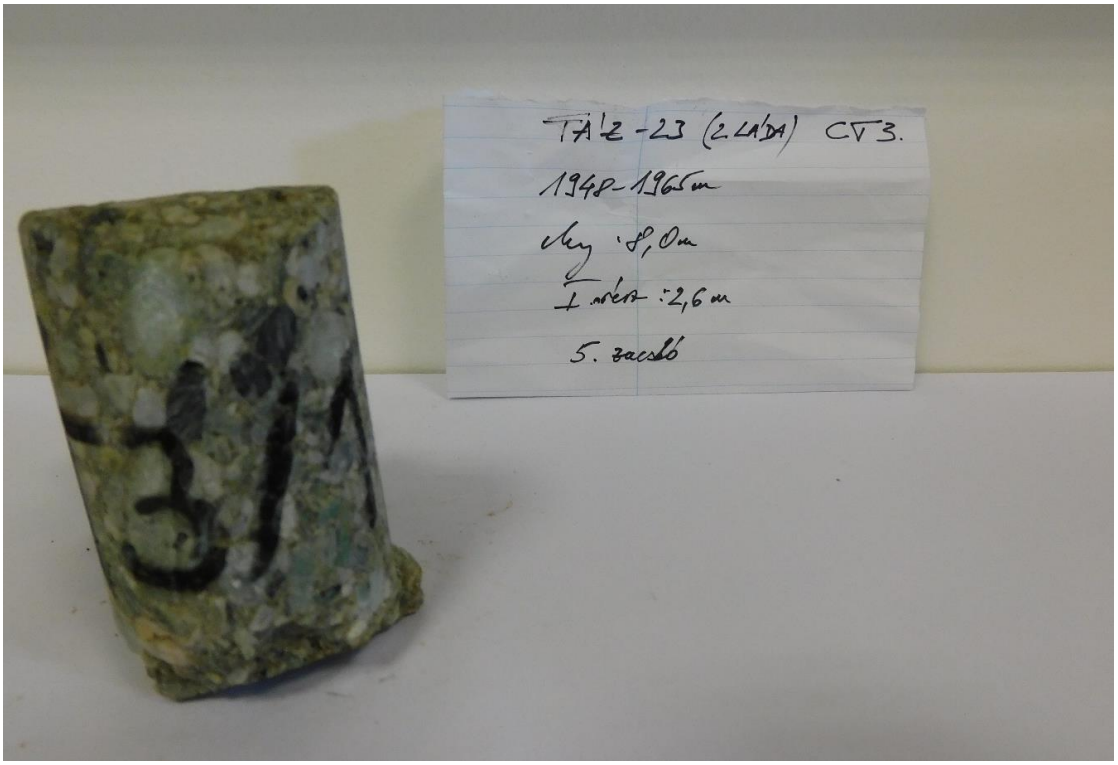


Figure 90. Design of the CT-3/1 rock core

(Recorded by the author)

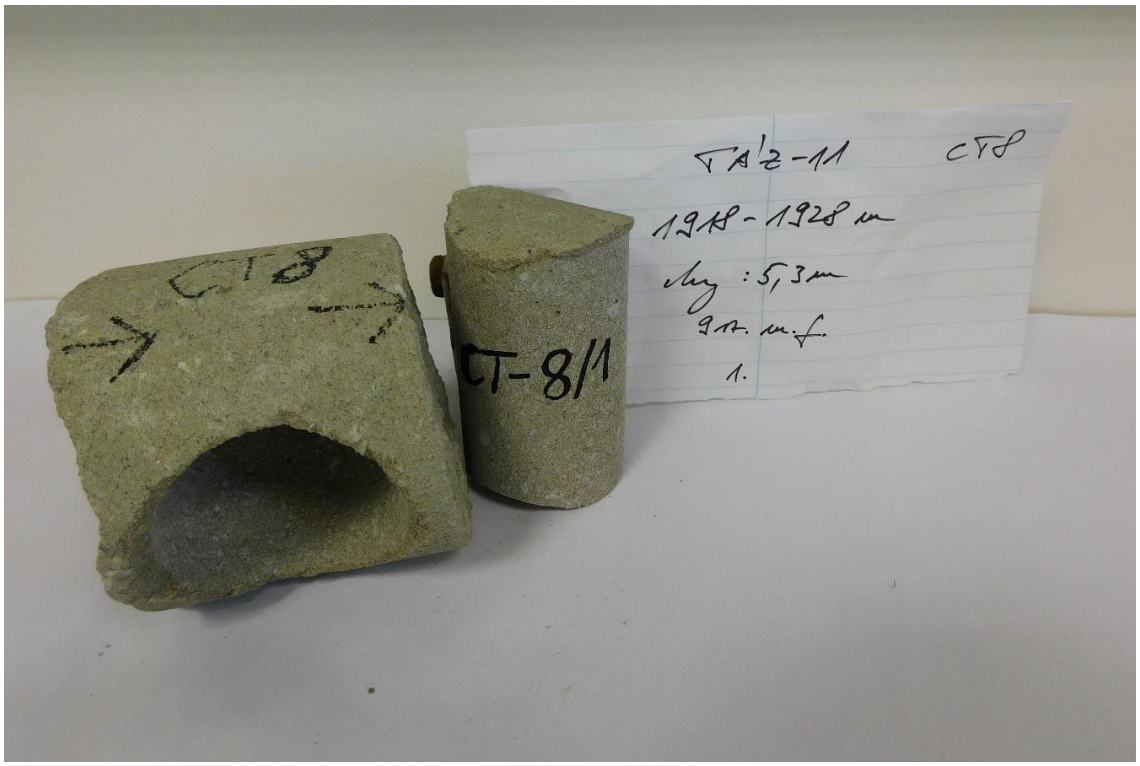


Figure 91. Design of the CT-8/1 rock core

(Recorded by the author)

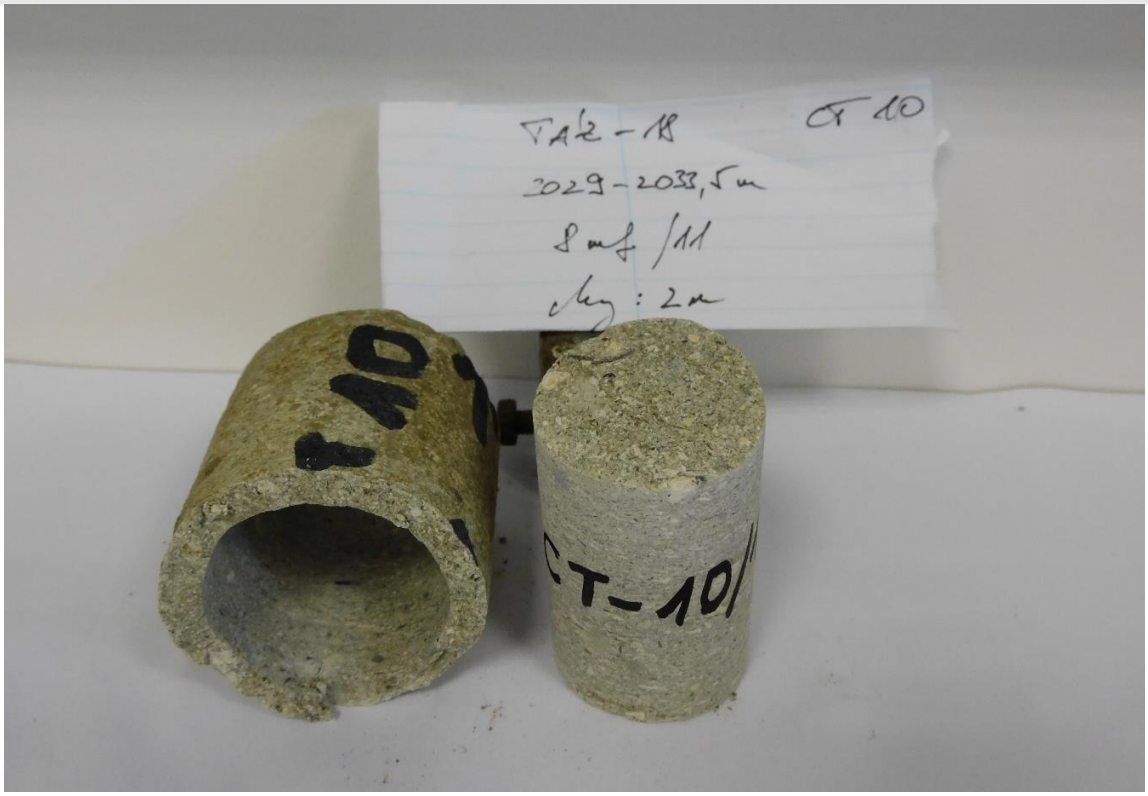


Figure 92. Design of the CT-10/1 rock core
(Recorded by the author)


Figure 93. Design of the CT-11/1 rock core
(Recorded by the author)

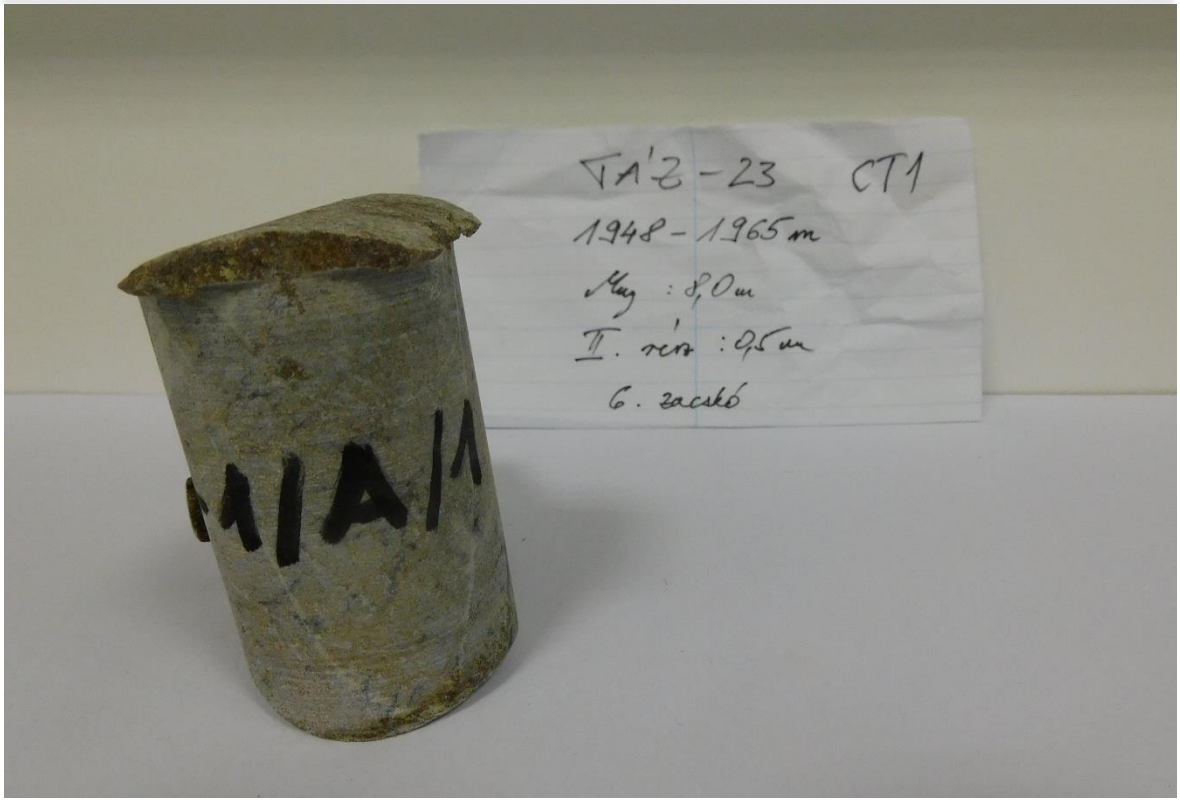


Figure 94. Design of the CT-1A/1 rock core

(Recorded by the author)

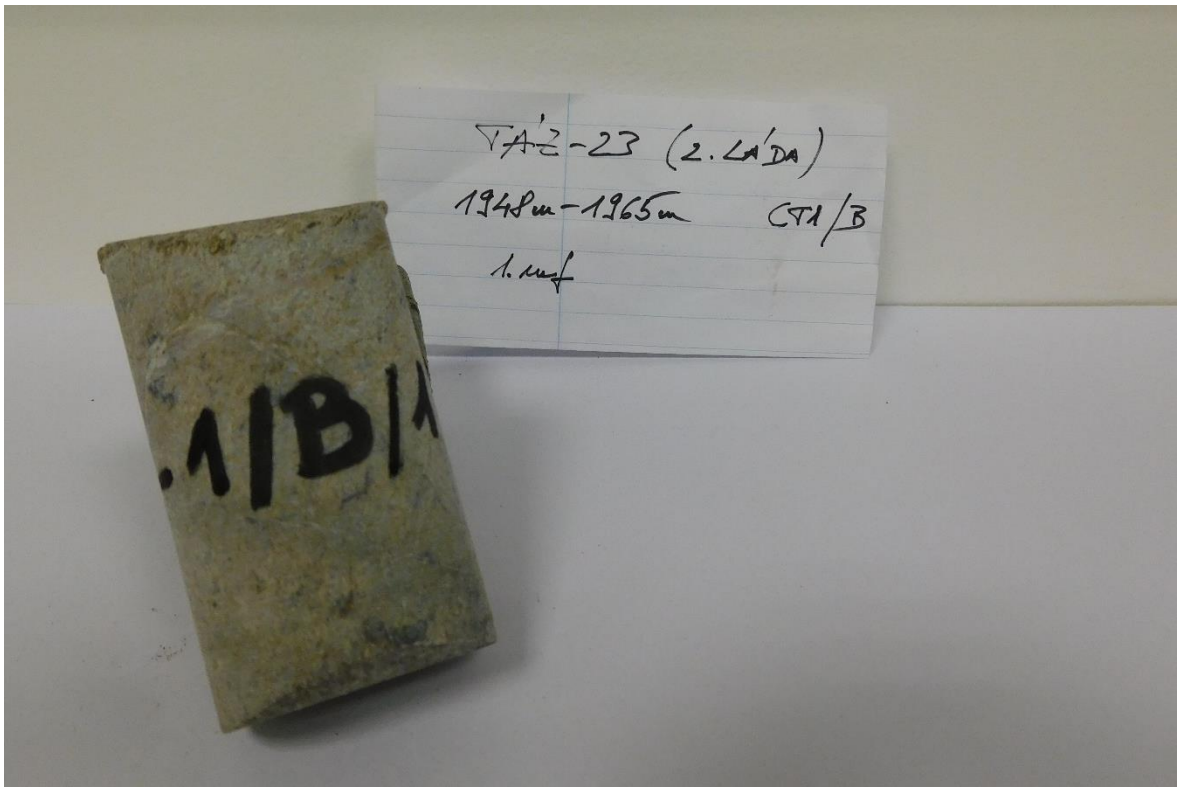


Figure 95. Design of the CT-1B/1 rock core

(Recorded by the author)

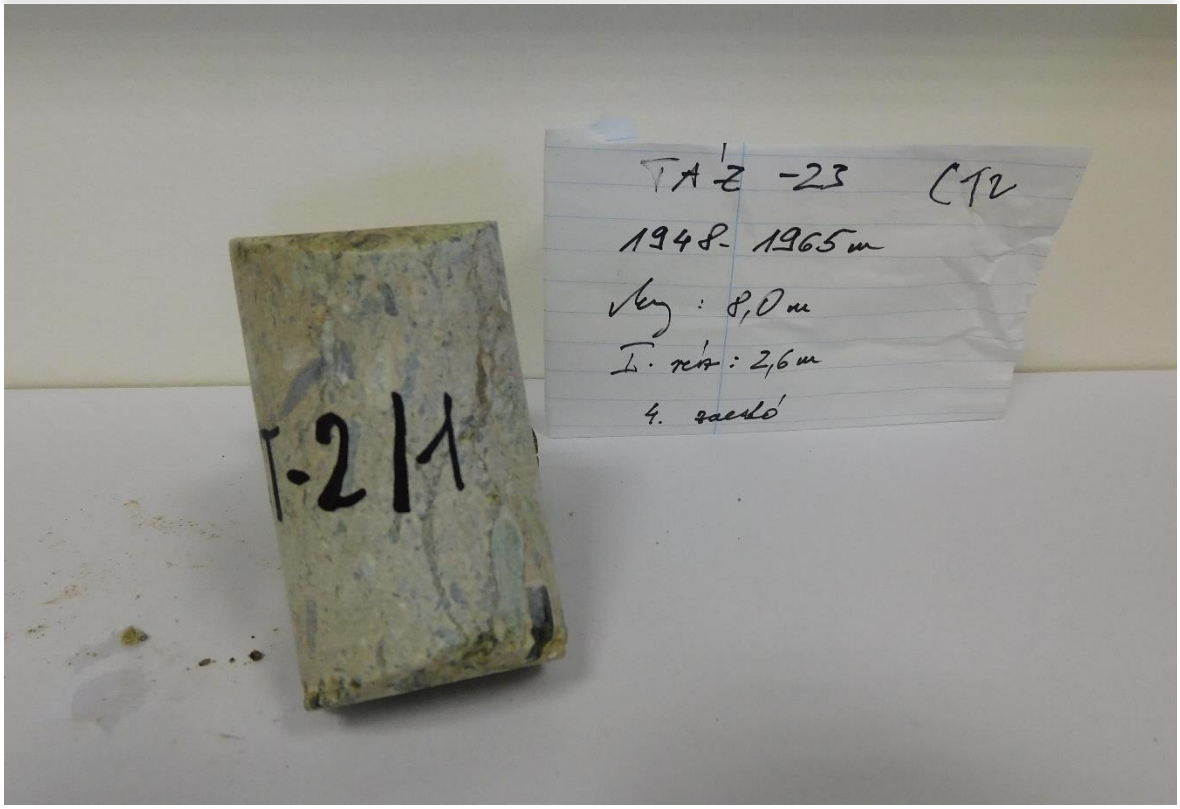


Figure 96. Design of the CT-2/1 rock core
(Recorded by the author)

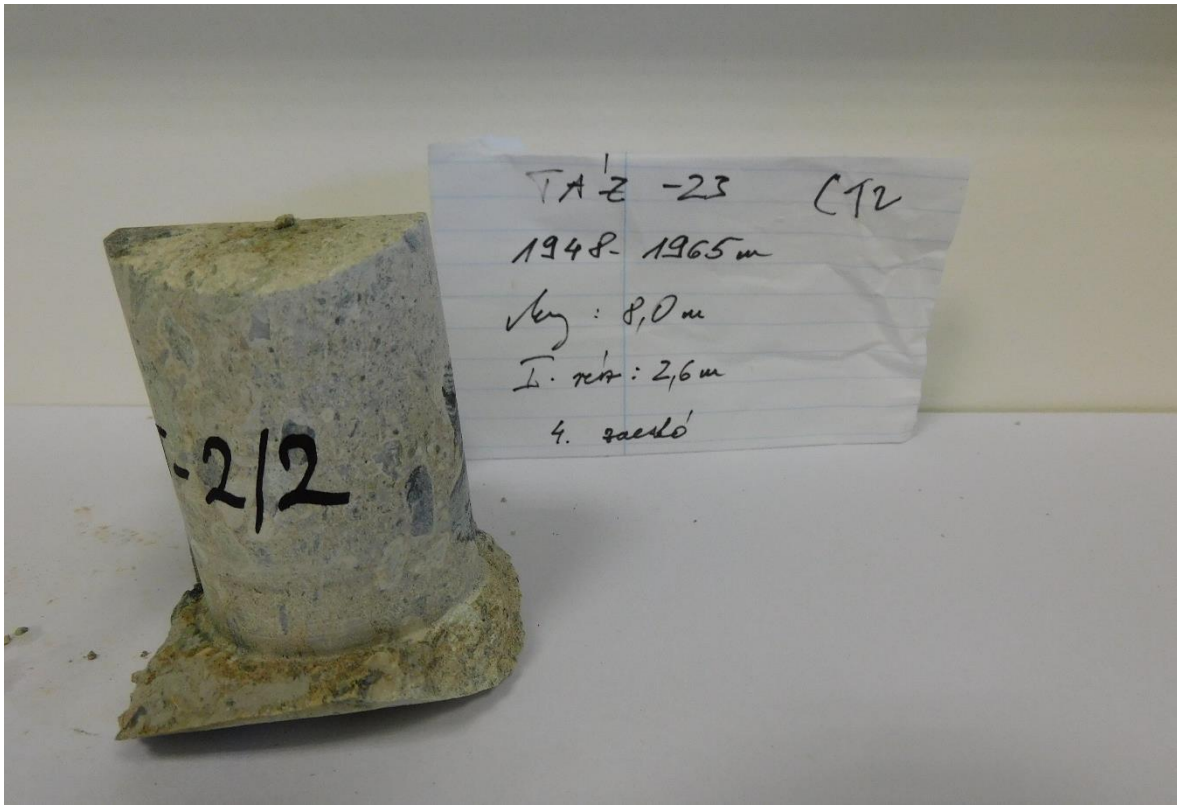


Figure 97. Design of the CT-2/2 rock core
(Recorded by the author)

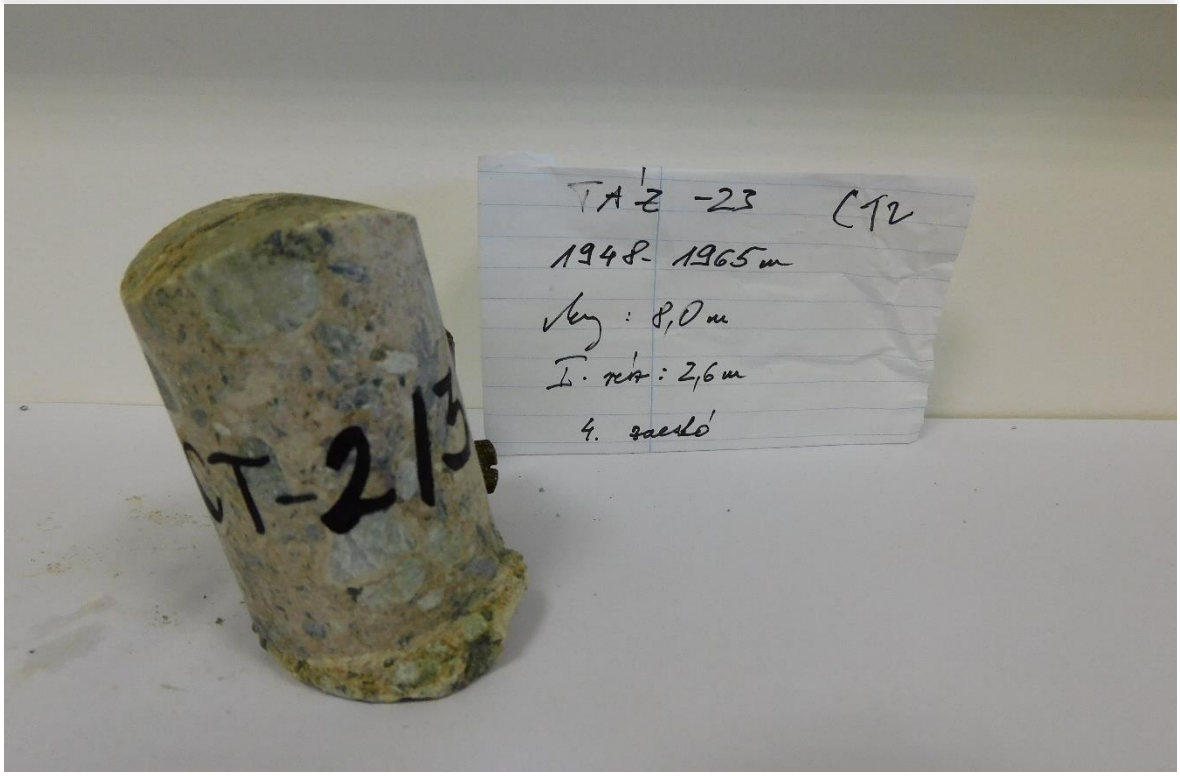


Figure 98. Design of the CT-2/3 rock core
(Recorded by the author)

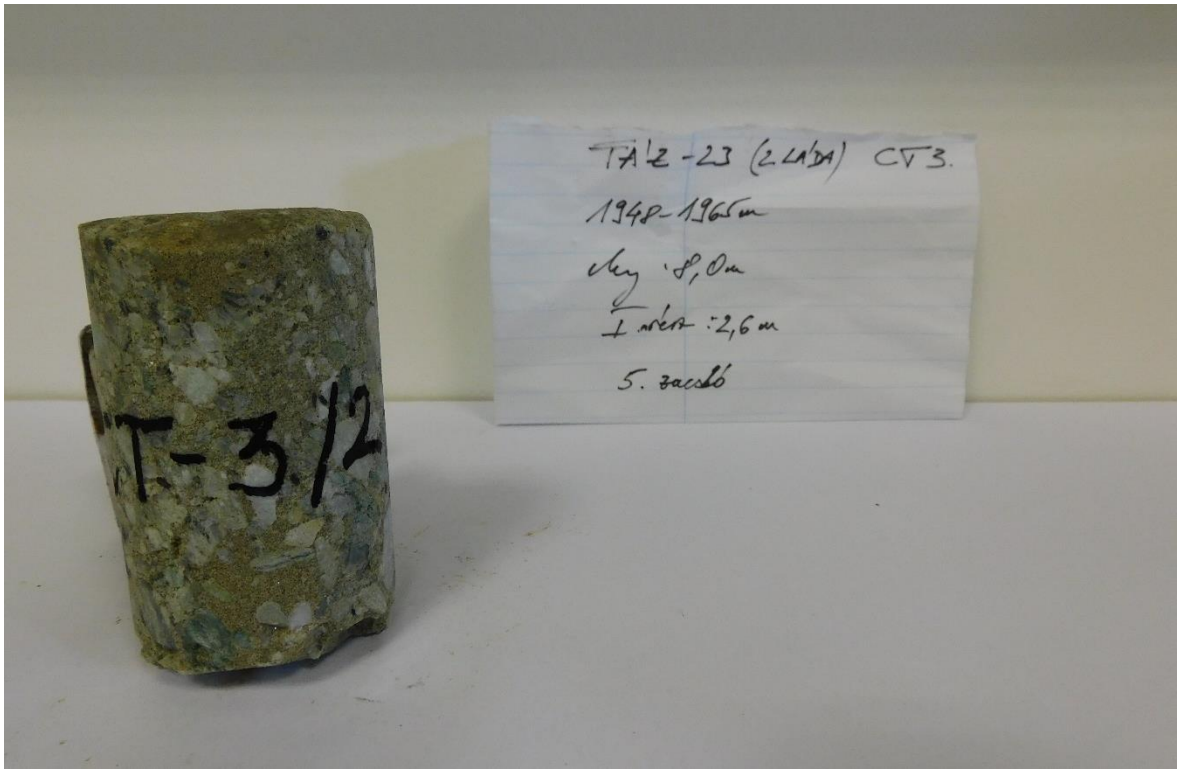


Figure 99. Design of the CT-3/2 rock core
(Recorded by the author)


Figure 100. Design of the CT-4/1 rock core
(Recorded by the author)

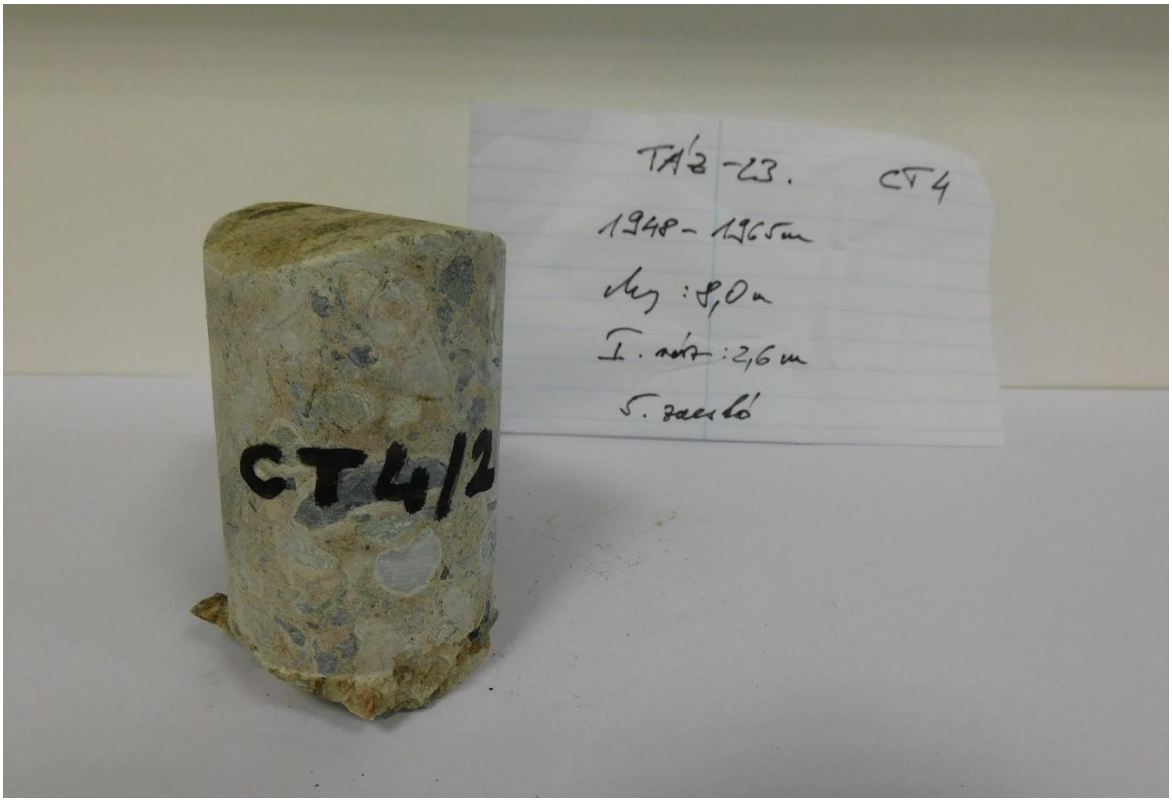


Figure 101. Design of the CT-4/2 rock core
(Recorded by the author)


Figure 102. Design of CT-5/1, CT-5/2 and CT-5/3 cores
(Recorded by the author)

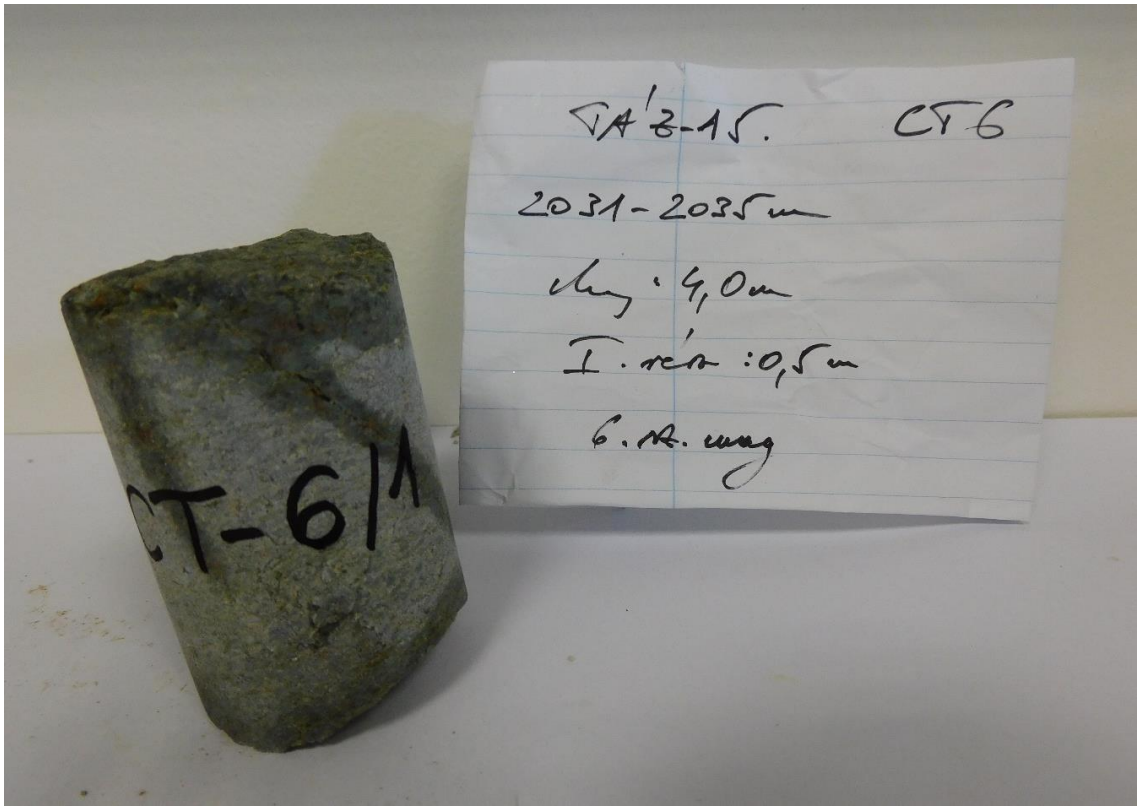


Figure 103. Design of the CT-6/1 rock core
(Recorded by the author)

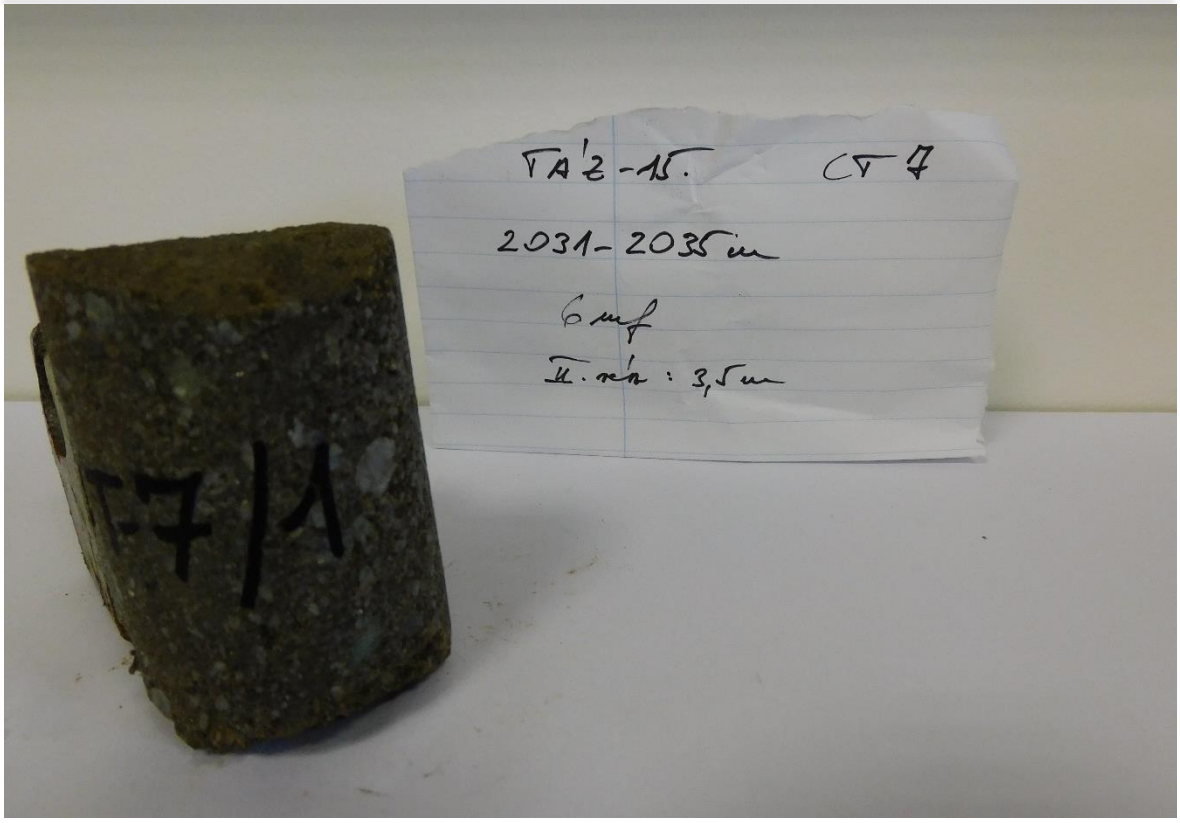


Figure 104. Design of the CT-7/1 rock core
(Recorded by the author)

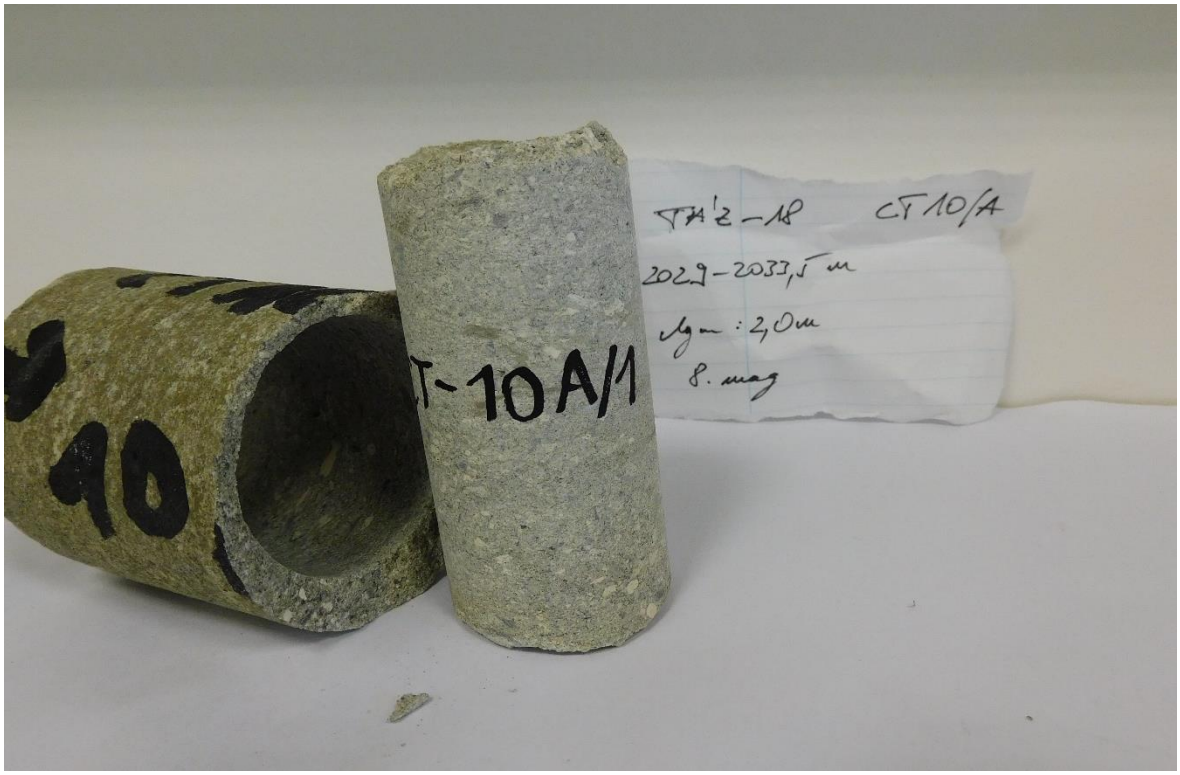


Figure 105. Design of the CT-10A/1 rock core
(Recorded by the author)

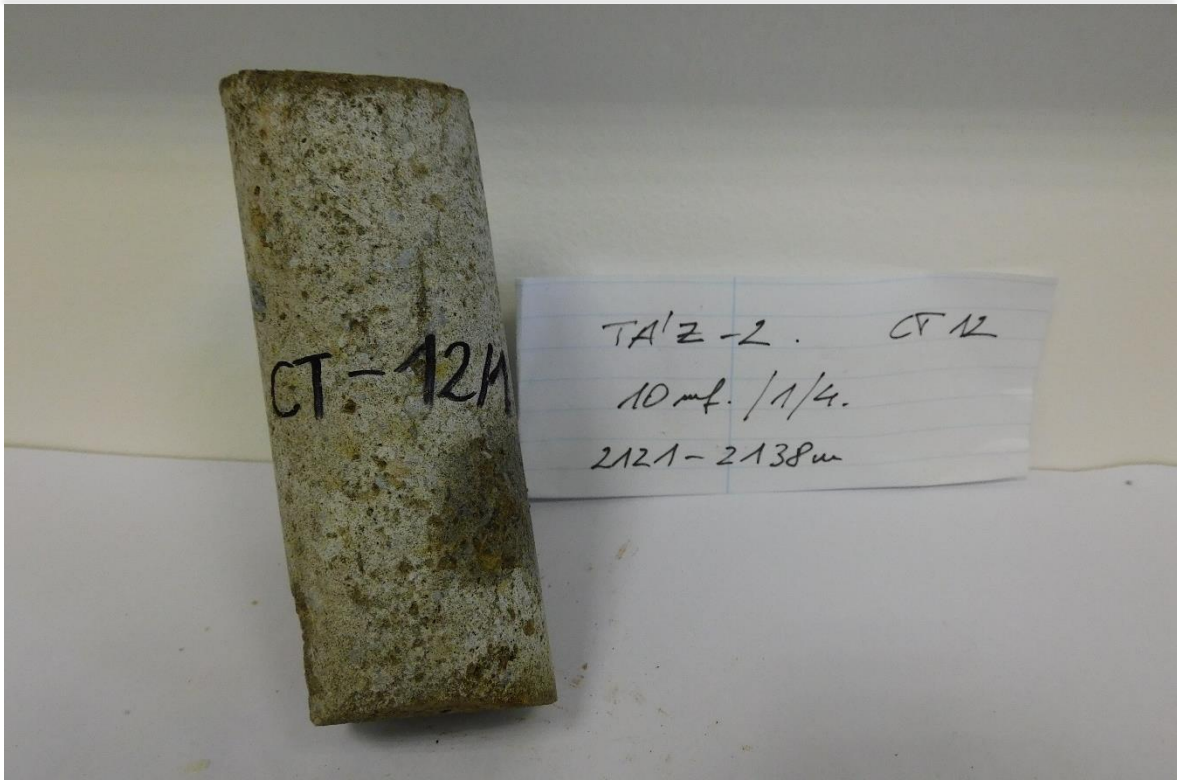


Figure 106. Desing of the CT-12/1 rock core
(Recorded by the author)

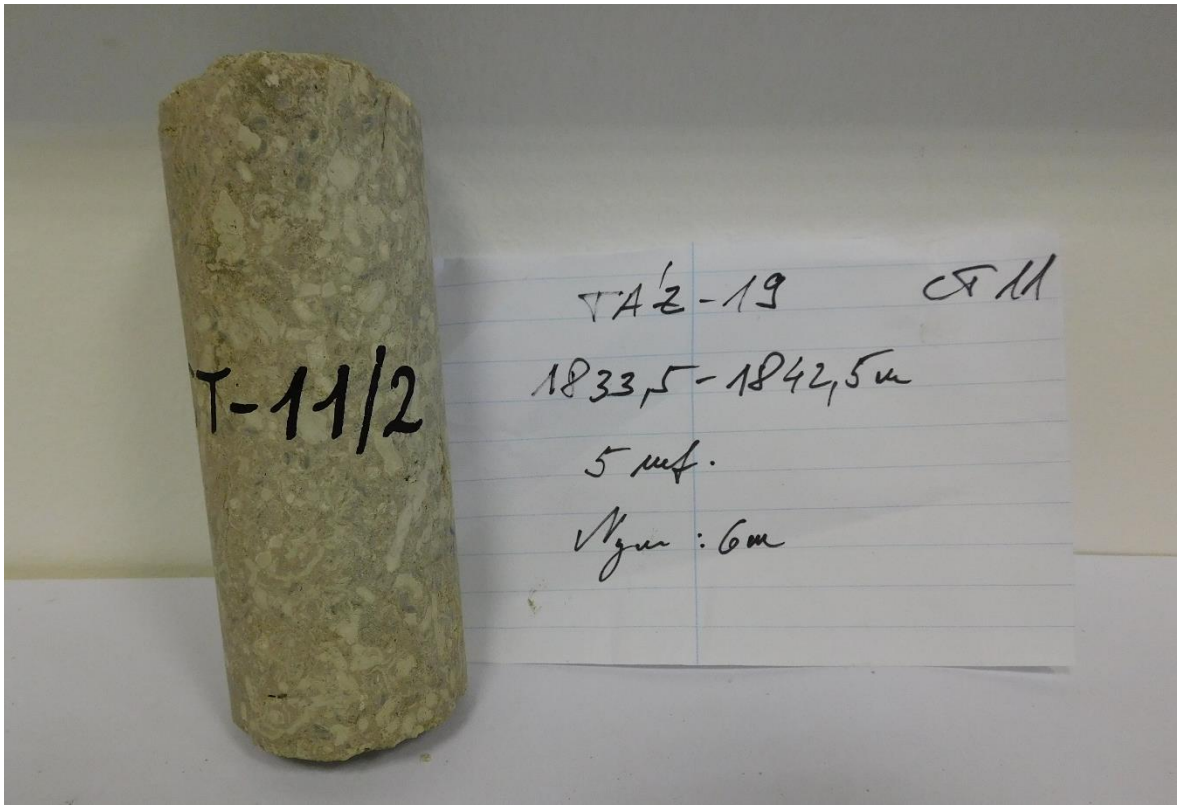


Figure 107. Design of the CT-11/2 rock core
(Recorded by the author)

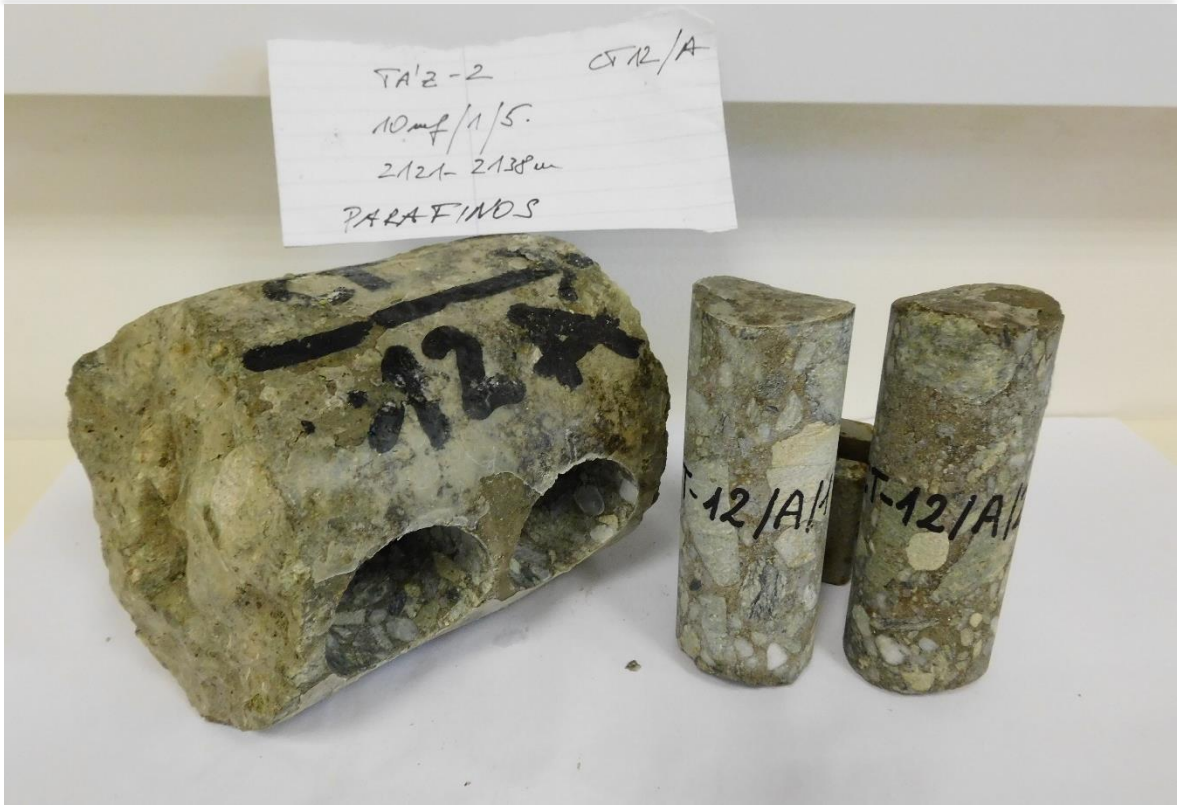


Figure 108. Design of the CT-12A/1 rock core
(Recorded by the author)

## 14.3 APPENDIX 3.

Untreated sample (CT 1/1):

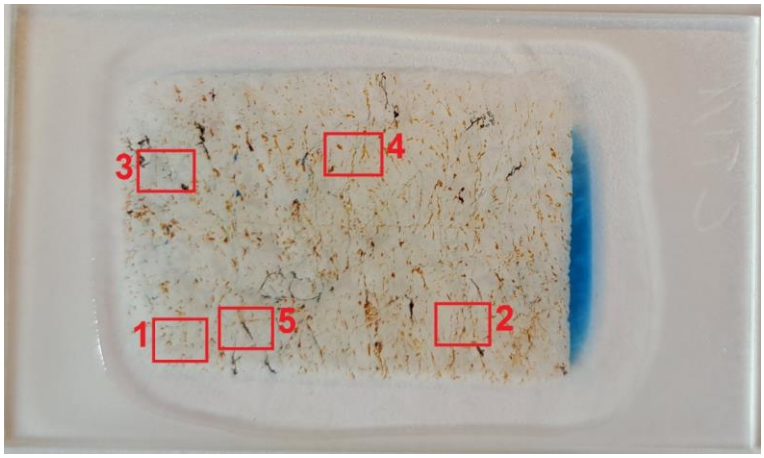


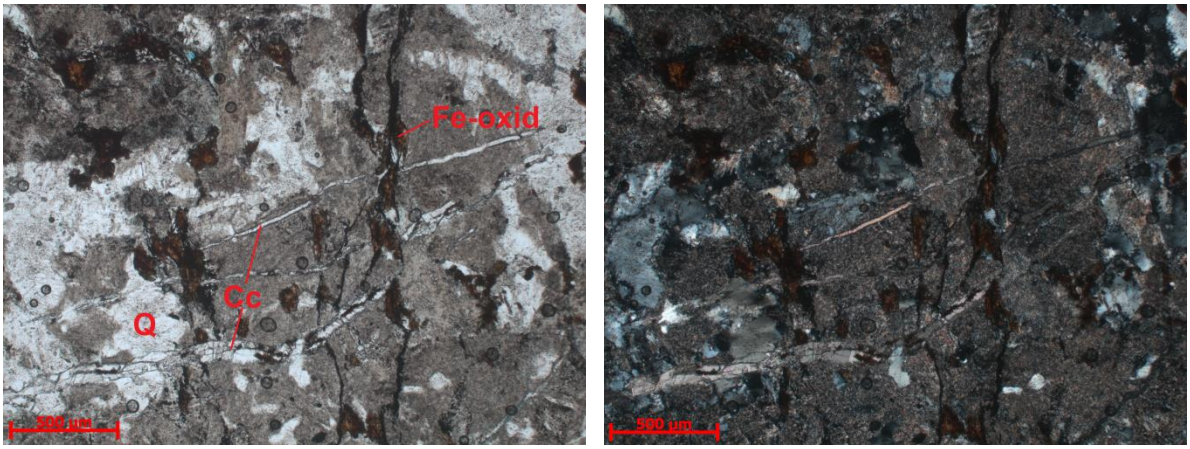


Figure 109. Cracks/voids filled with Fe oxide and calcite (Cc) and quartz (Q) grains in the microcrystalline matrix (1N on the left, XN on the right)
(source: UoM)

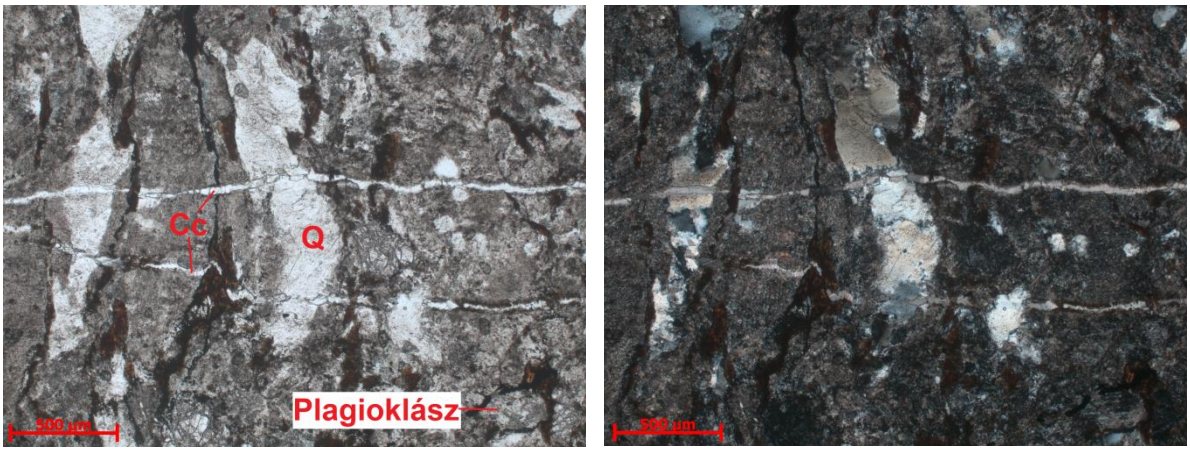


Figure 110. Veins/cracks filled with calcite (Cc) intersecting a quartz (Q) grain and a broken plagioclase grain in the microcrystalline matrix (1N on the left, XN on the right)
(source: UoM)

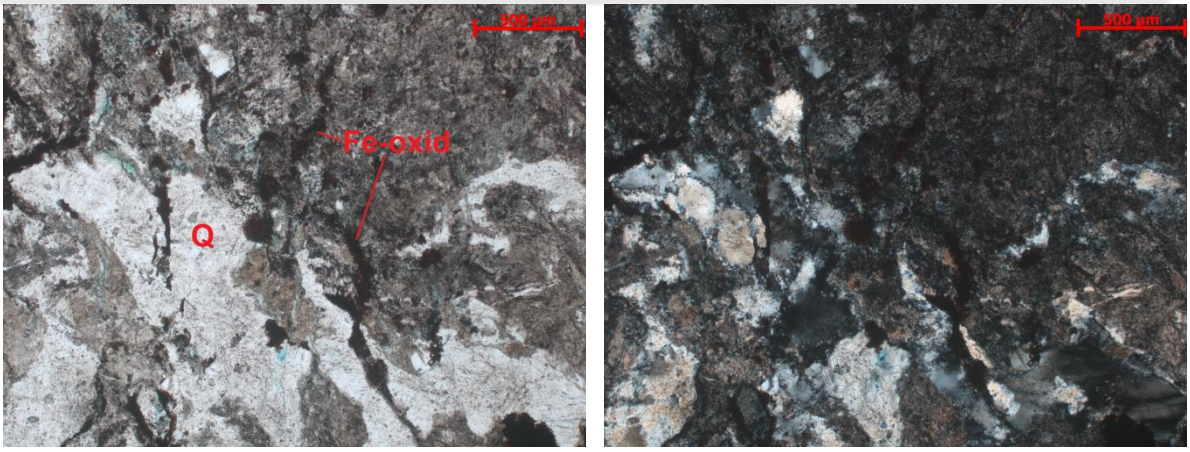


Figure 111. Unfilled microcracks (blue) in and along quartz (Q) grains and in the microcrystalline matrix, 1N on the left, XN on the right
(source: UoM)

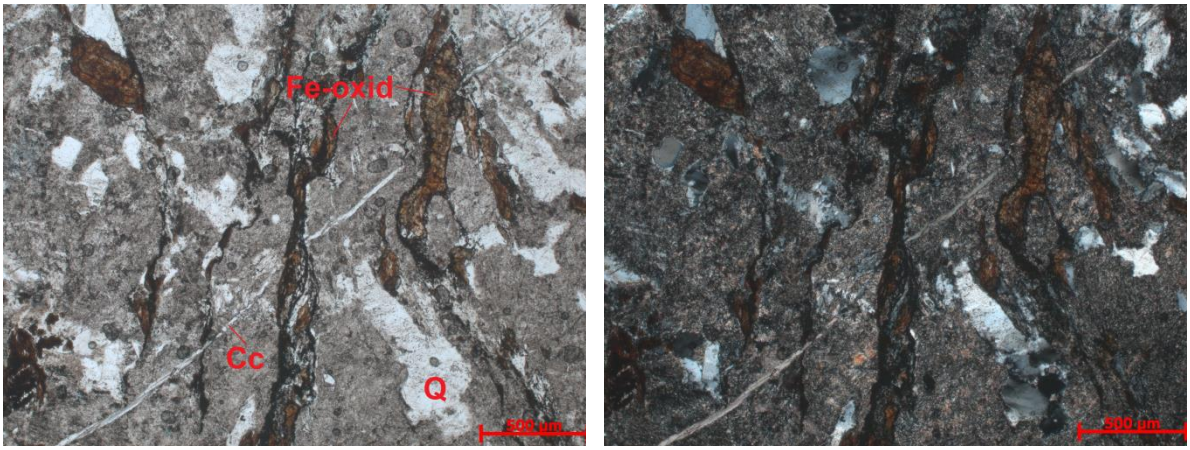


Figure 112. Directionally oriented cracks filled with Fe oxide and angularly closing cracks filled with calcite (Cc) and quartz (Q) grains (left 1N, right XN)
(source: UoM)

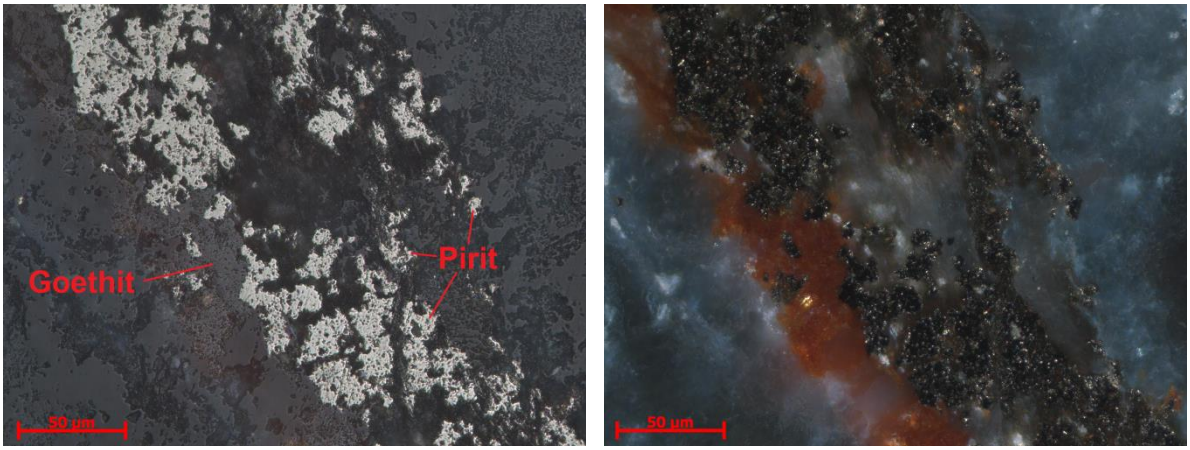


Figure 113 Pyrite and goethite in incident light (left 1N, right XN)
(source: UoM)

$CO_2$ treated sample (CT 1/1):


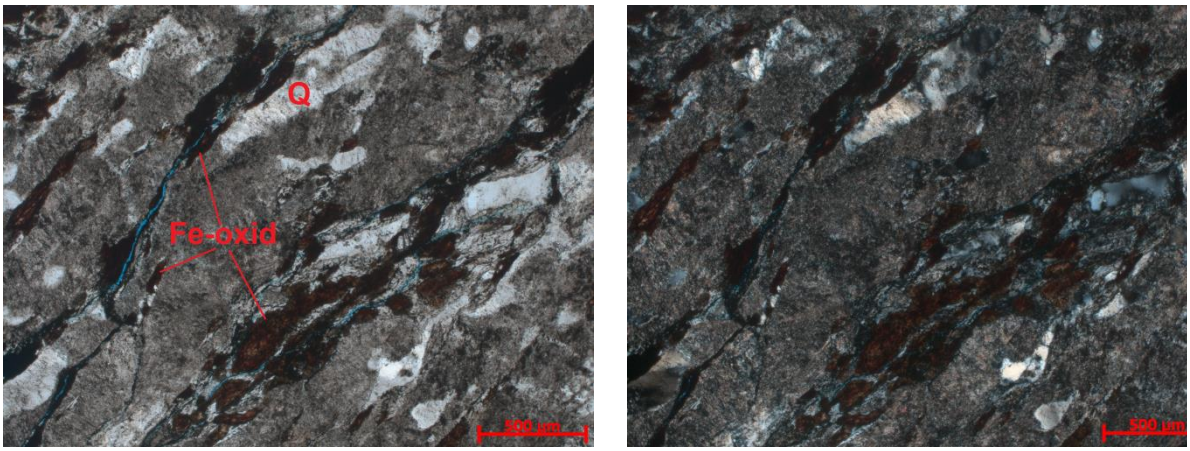


Figure 114. Unfilled cracks (blue) along quartz (Q) grains and Fe-oxide-filled veins, 1N on the left, XN on the right
(source: UoM)

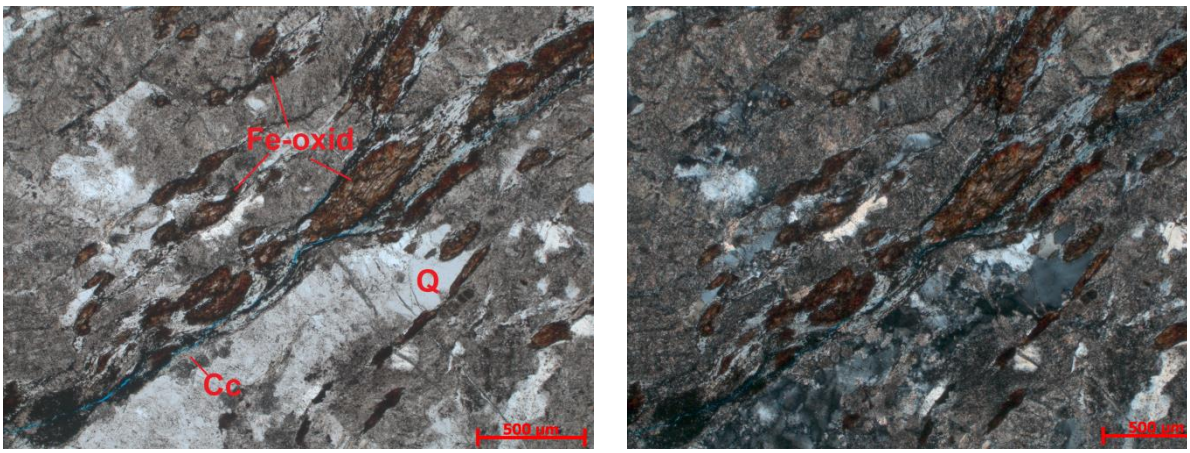


Figure 115. Unfilled cracks along quartz (Q) and calcite (Cc) lenses and Fe-oxide-filled veins (blue), 1N on the left, XN on the right
(source: UoM)

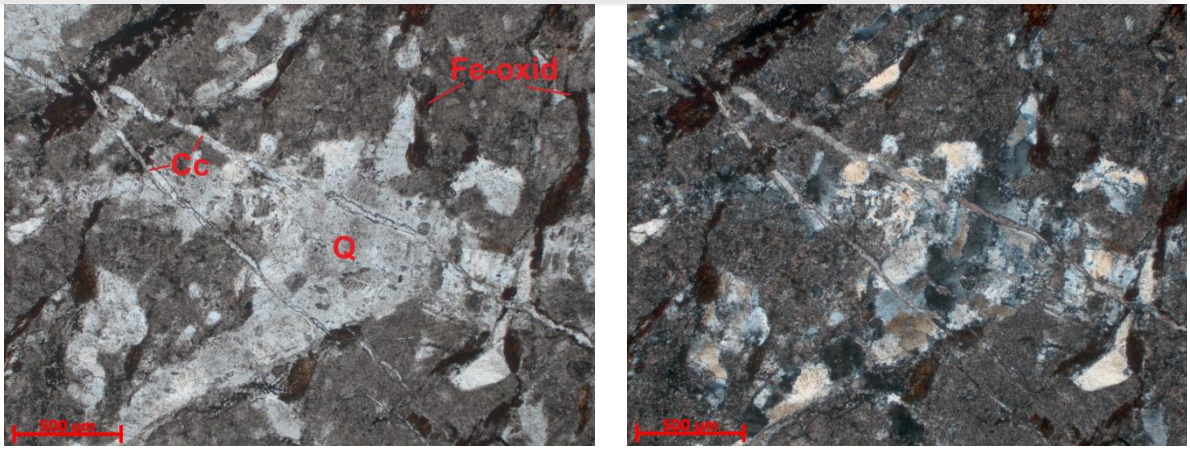


Figure 116. Quartz (Q) lens and Fe oxide-filled cracks intersected by calcite (Cc) filled veins (left 1N, right XN)
(source: UoM)

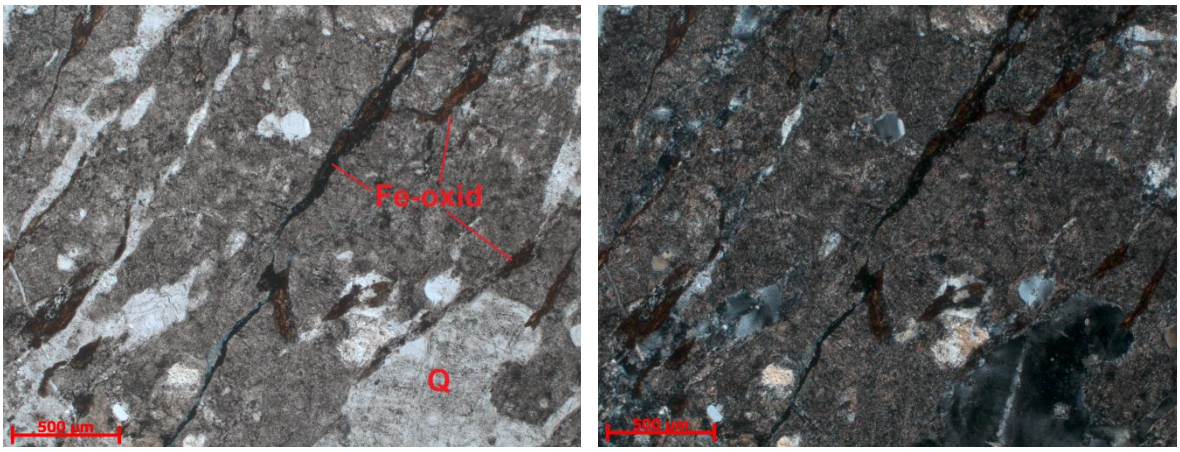


Figure 117. Unfilled cracks (blue) along quartz (Q) grains and Fe-oxide filled veins, 1N on the left, XN on the right
(source: UoM)

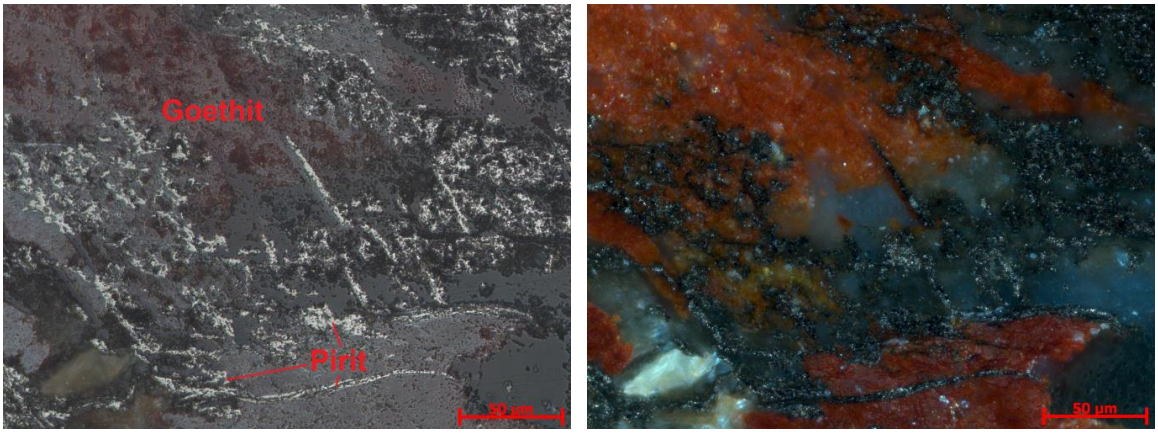


Figure 118. Pyrite and goethite in incident light (left 1N, right XN)
(source: UoM)

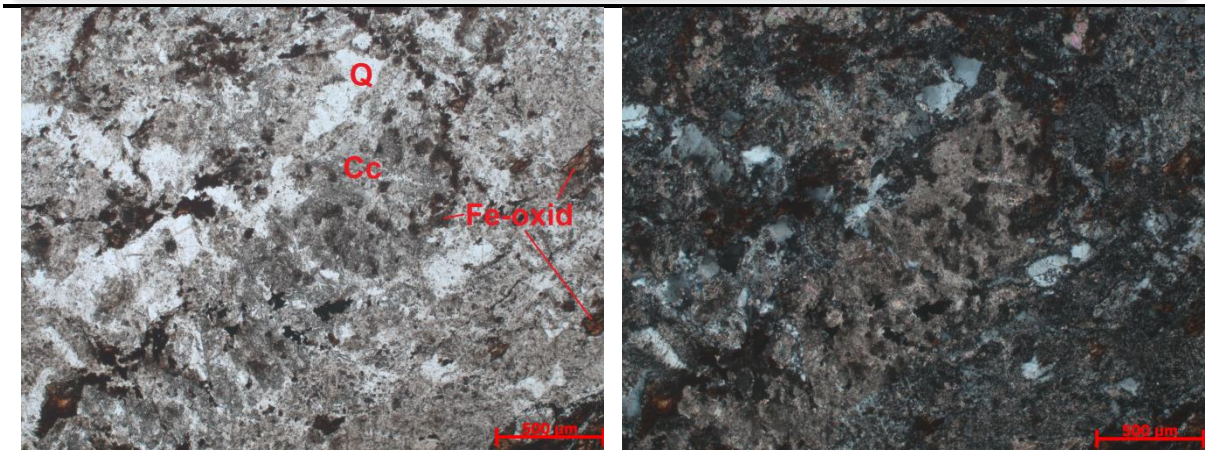


Figure 119. Microcrystalline calcites at the site of a disintegrated mineral (plagioclase?). Quartz (Q) grains and Fe-oxide (1N on left, XN on right)
(source: UoM)

Untreated sample (CT 3/1):

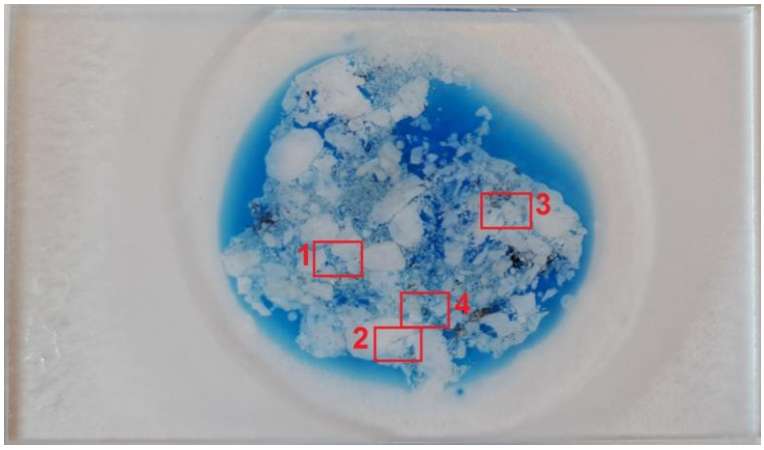


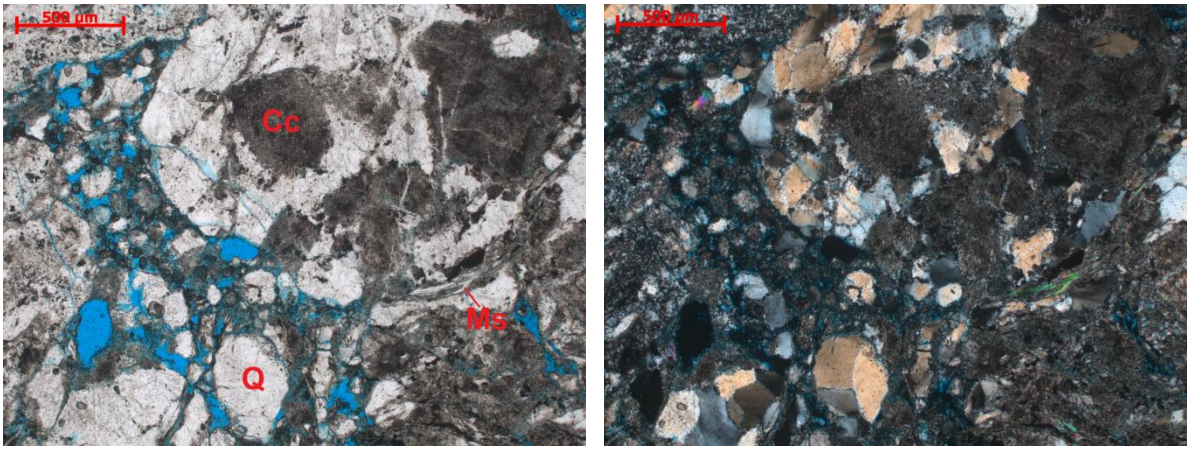


Figure 120. Quartz (Q) grains, muscovite (Ms) plates and microcrystalline calcite (Cc), 1N on the left, XN on the right
(source: UoM)

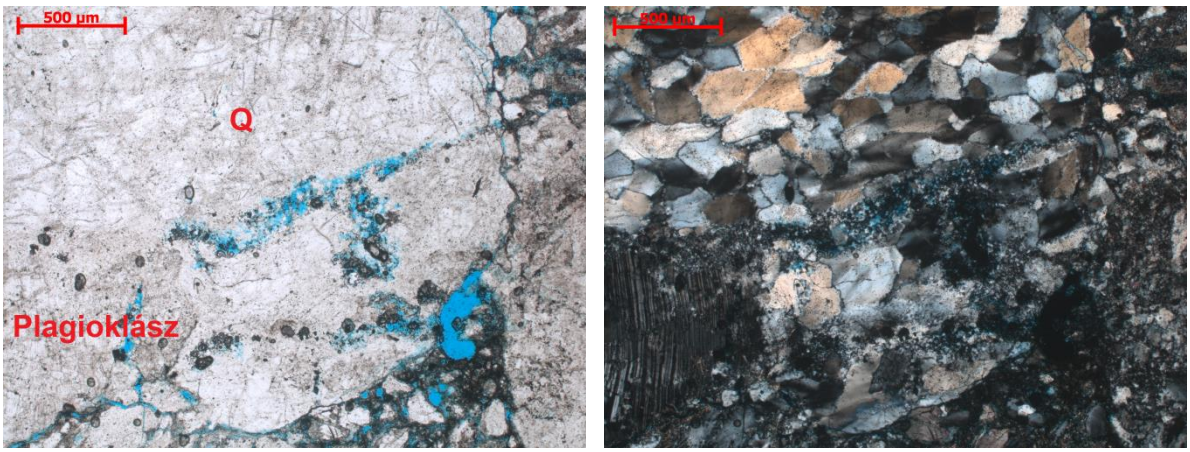


Figure 121. Quartz (Q) with two different appearances (coarse crystal and fine crystal) and polysynthetically iced plagioclase (1N on the left, XN on the right)
(source: UoM)

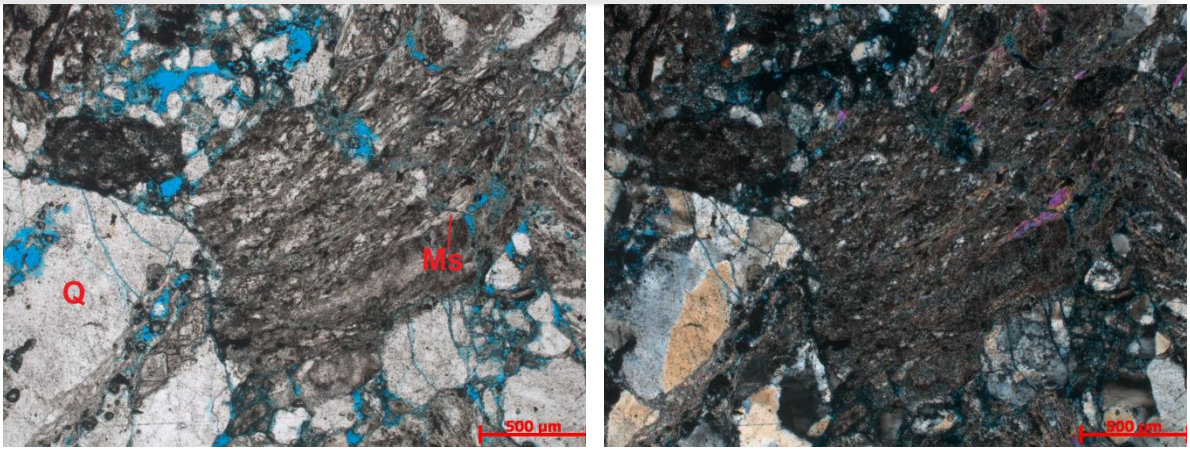


Figure 122. Fractured quartz (Q) grains and muscovite (Ms) plates (1N on left, XN on right)
(source: UoM)

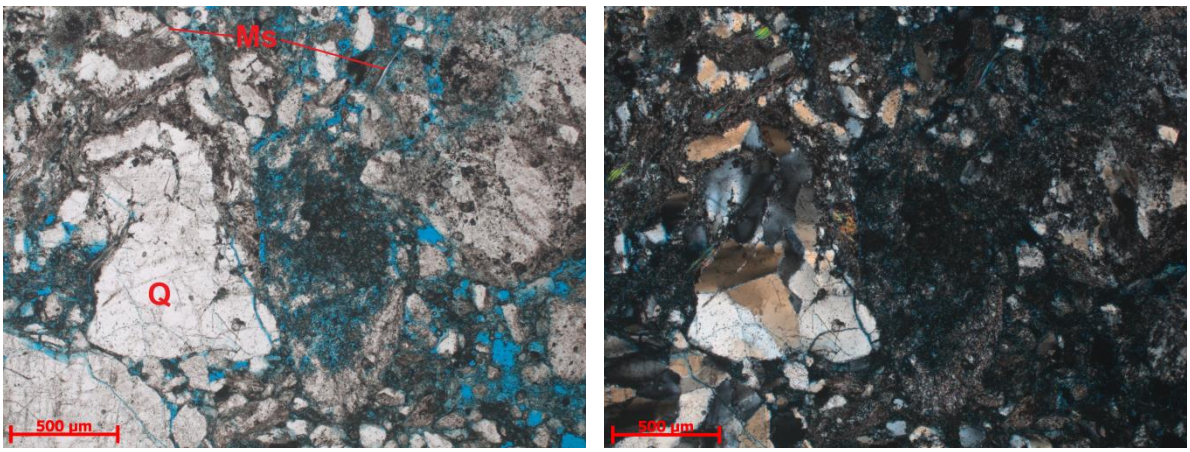


Figure 123. Fractured quartz (Q) grains and muscovite (Ms) plates (1N on left, XN on right)
(source: UoM)

$CO_2$ treated sample (CT 3/1):

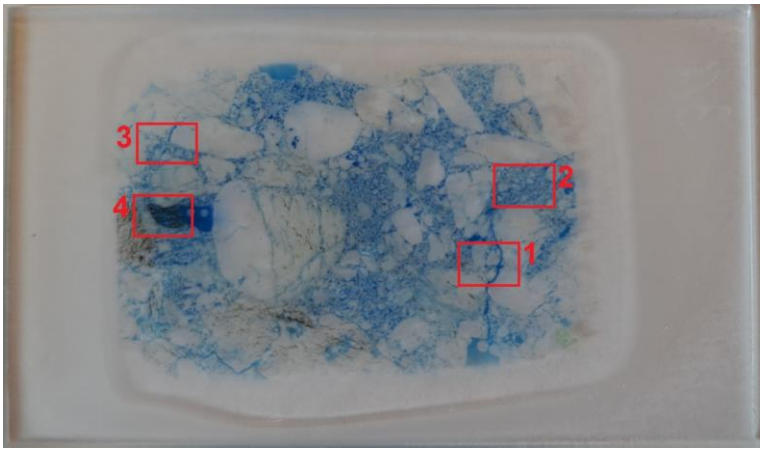


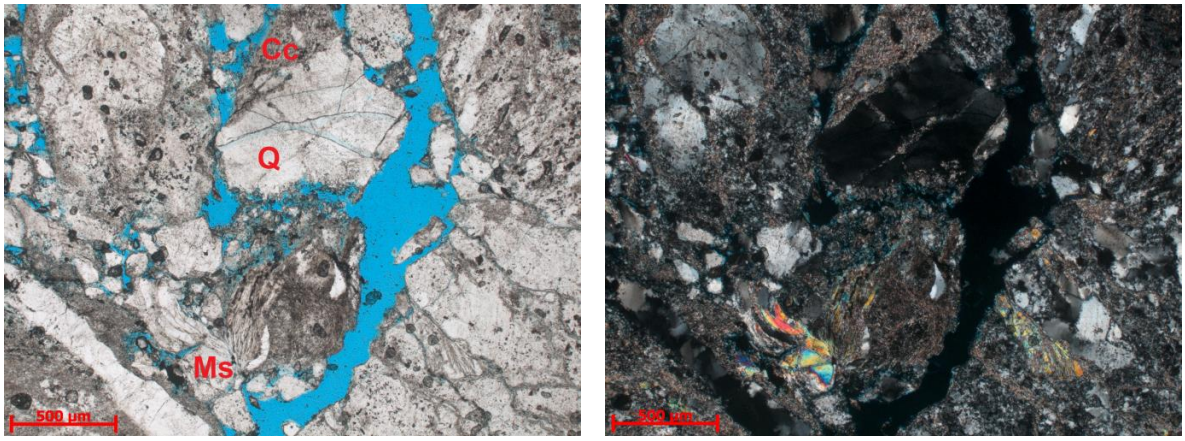


Figure 124. Fractured quartz (Q) grains, muscovite (Ms) plates and microcrystalline calcite (Cc) clusters with increased intergranular space and cracks (blue), 1N on the left, XN on the right

(source: UoM)

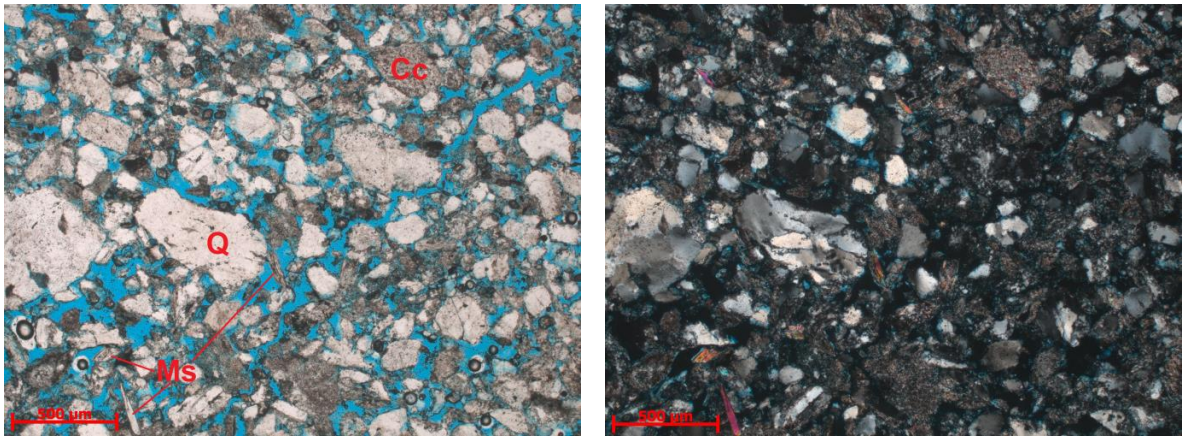


Figure 125. Quartz (Q) grains, muscovite (Ms) plates and microcrystalline calcite (Cc) clusters with increased intergranular space (blue), 1N on the left, XN on the right

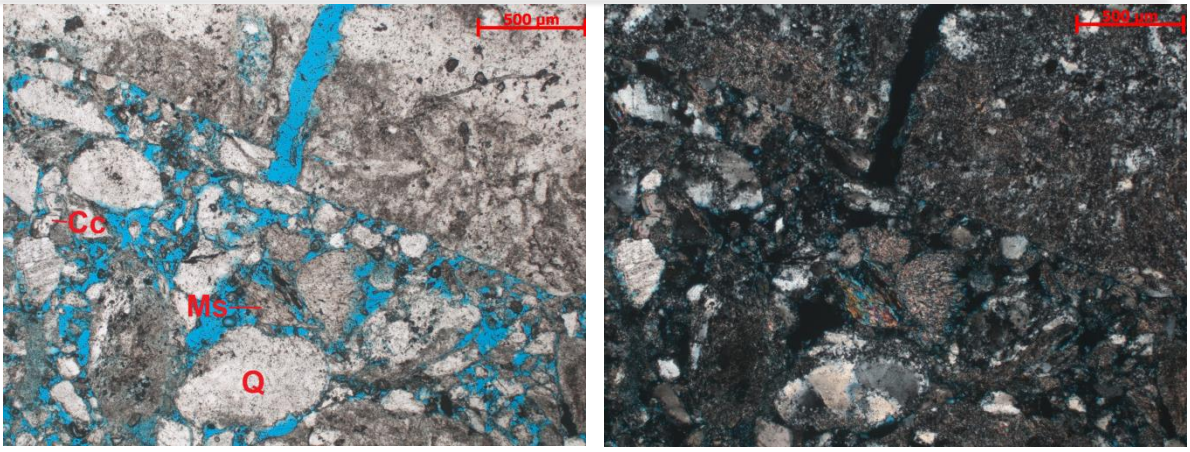


Figure 126. Quartz (Q) grains, muscovite (Ms) plates and calcite (Cc) crystals with increased intergranular space (blue), and a highly fractured mineral (feldspar?) split in two (1N left, XN right)
(source: UoM)

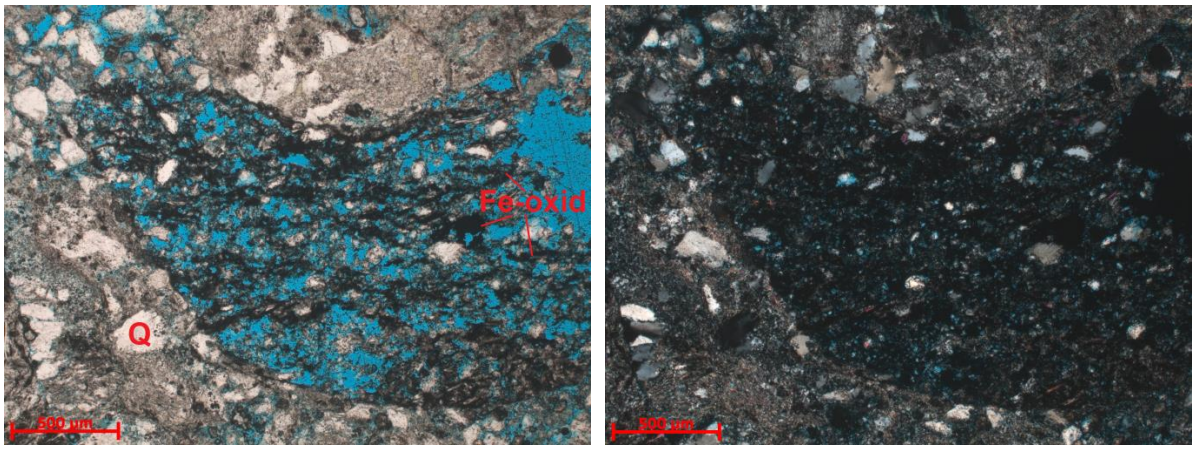


Figure 127. Quartz (Q) grains and remnants of a highly disaggregated, disseminated, Fe-oxidized mineral with increased intergranular space (blue), 1N on the left, XN on the right
(source: UoM)

Untreated sample (CT 8/1):

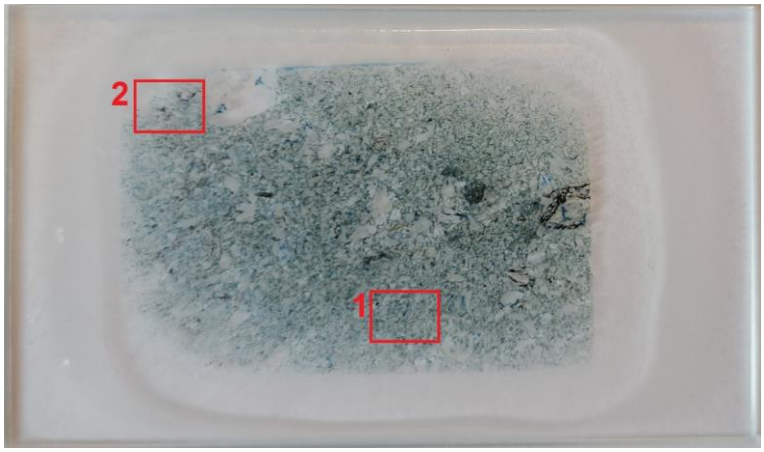


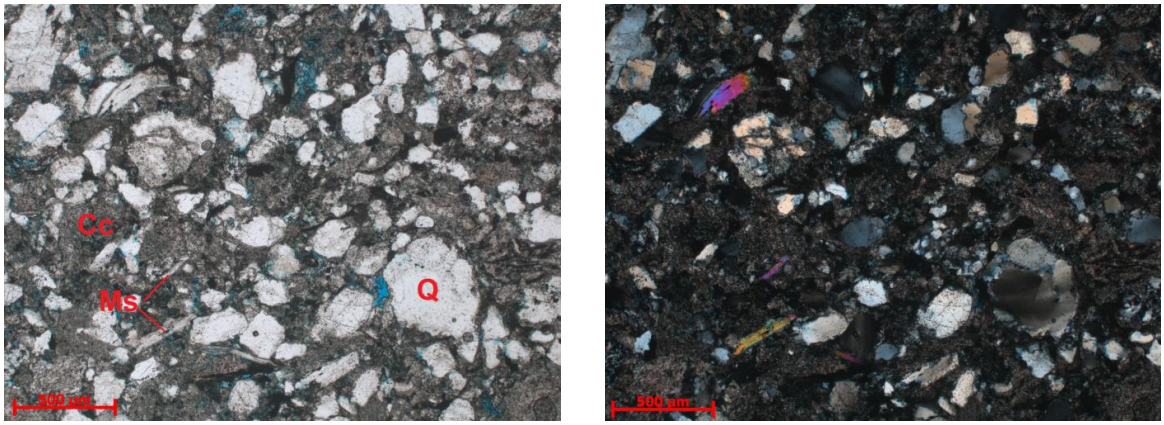


Figure 128. Quartz (Q) grains, muscovite (Ms) plates and microcrystalline calcite (Cc), 1N on the left, XN on the right
(source: UoM)

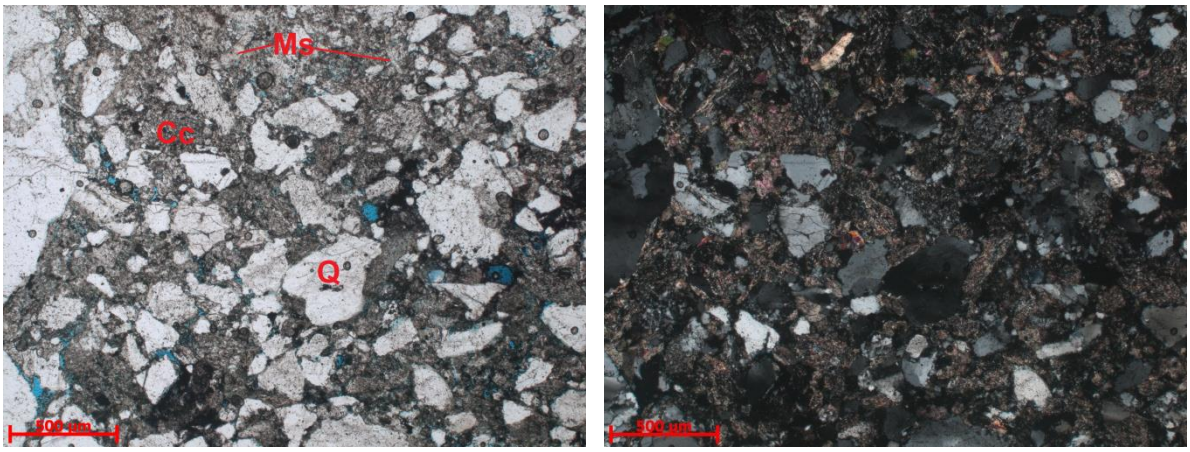


Figure 129. Quartz (Q) grains, muscovite (Ms) plates and microcrystalline calcite (Cc), 1N on the left, XN on the right
(source: UoM)

$CO_2$ treated sample (CT 8/1):

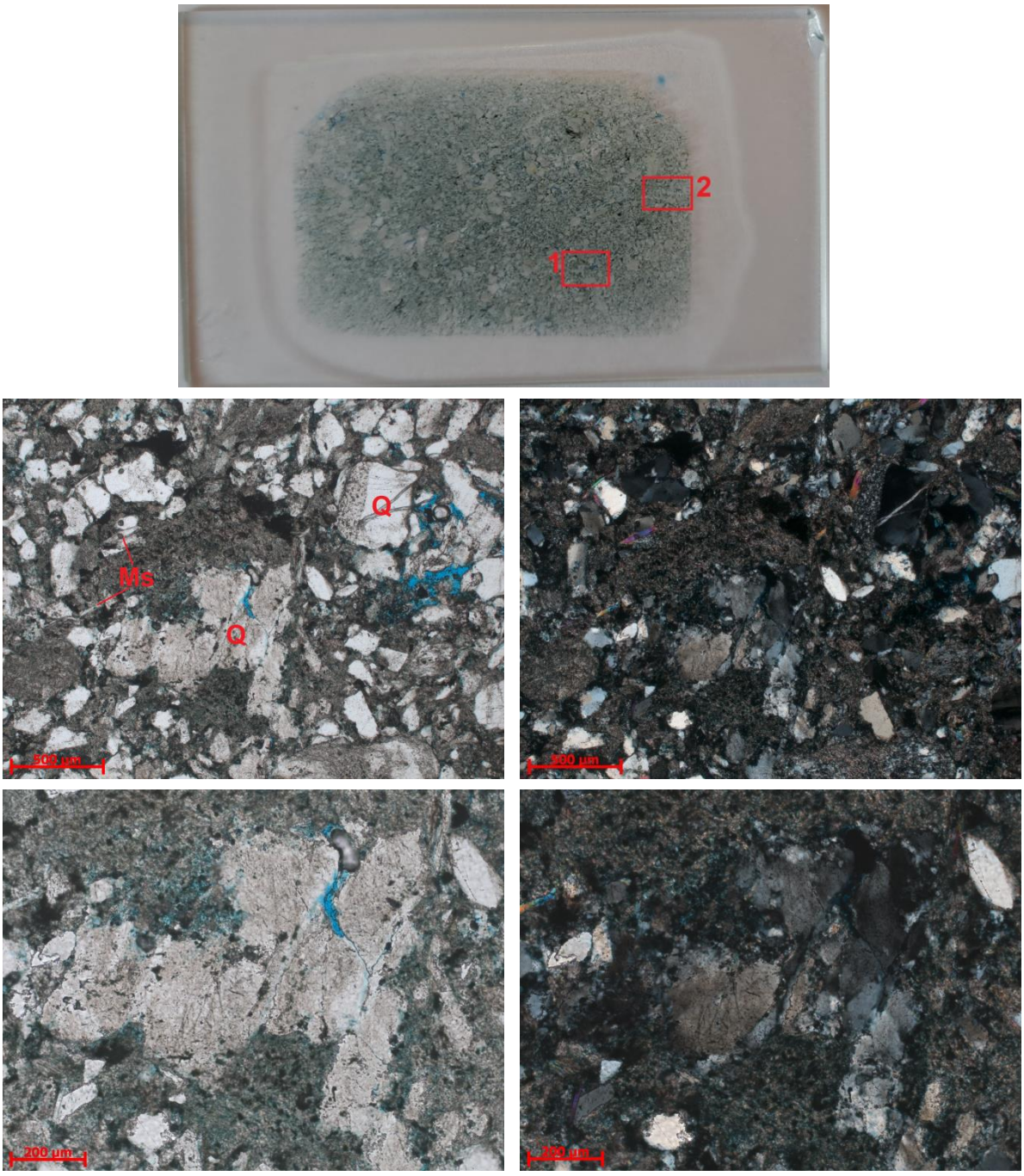


Figure 130. Quartz (Q) grains and muscovite (Ms) sheets with increased intergranular space (blue). Bottom: enlarged image of the polycrystalline quartz stack shown in the image above, Left 1N, right XN
(source: UoM)

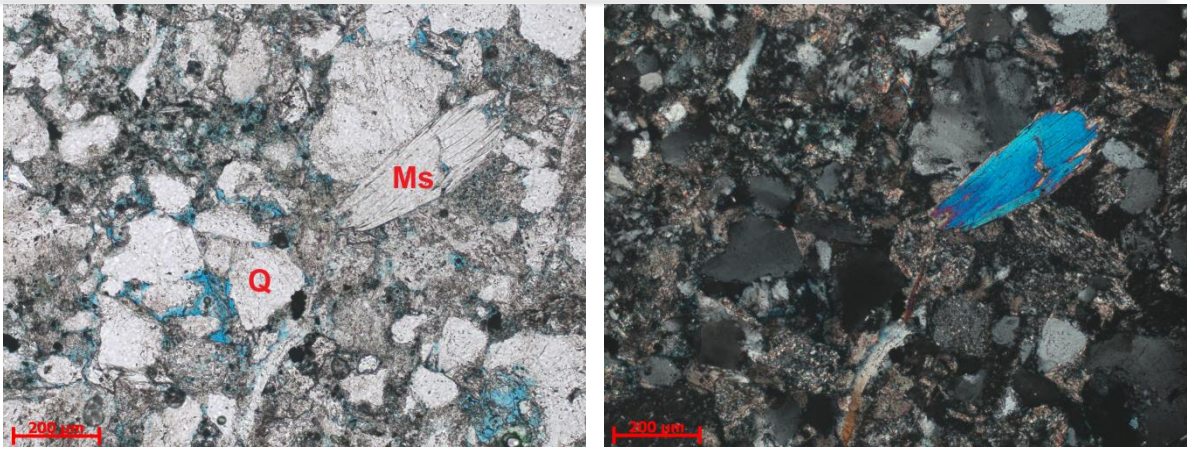


Figure 131. Quartz (Q) grains and muscovite (Ms) with increased intergranular space (blue). 1N on the left, XN on the right
(source: UoM)

Untreated sample (CT 10/1):

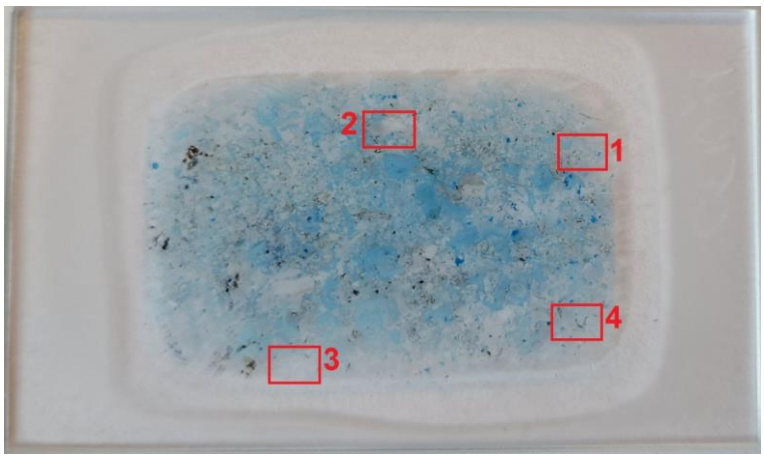


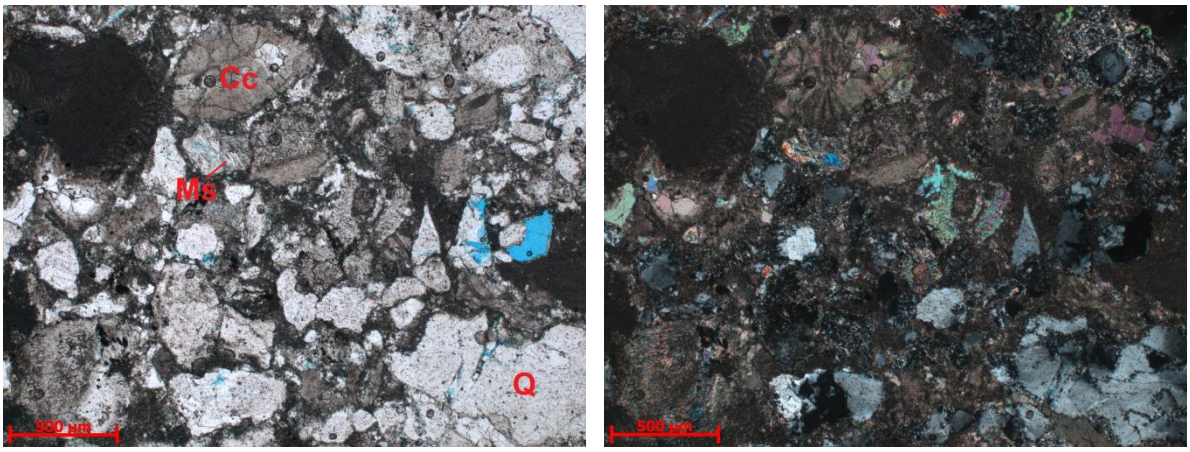


Figure 132. Quartz (Q) grains, muscovite (Ms) plates and calcite (Cc), 1N on the left, XN on the right
(source: UoM)

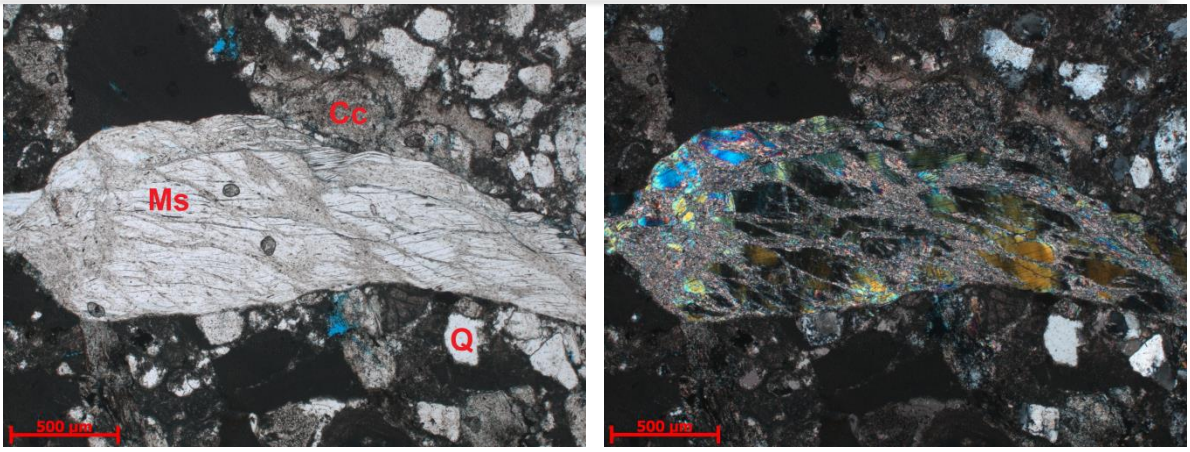


Figure 133. Quartz (Q) grains, muscovite (Ms) plates and calcite (Cc), 1N on the left, XN on the right
(source: UoM)

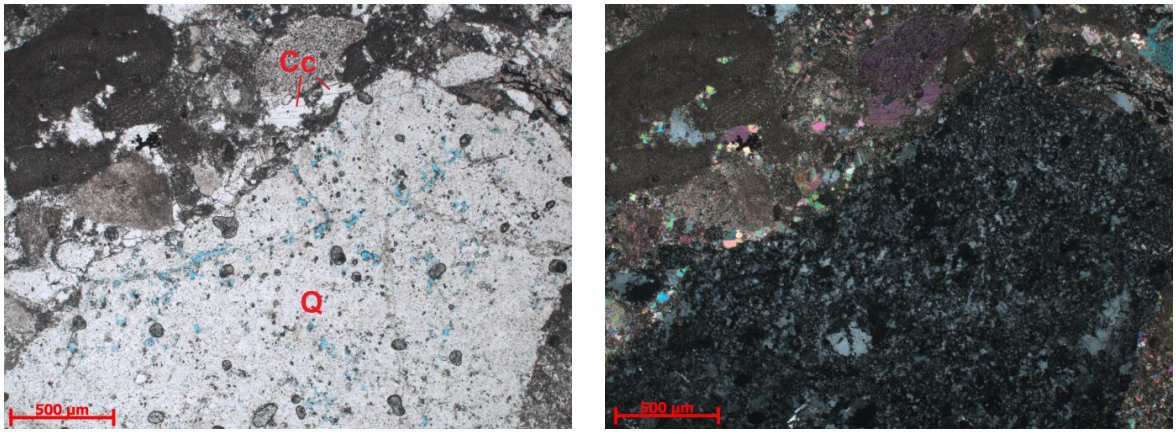


Figure 134. Polycrystalline quartz (Q) cluster with cracks and pores (blue) and xenomorphic calcite (Cc) grains and calcareous fossils (1N on the left, XN on the right)
(source: UoM)

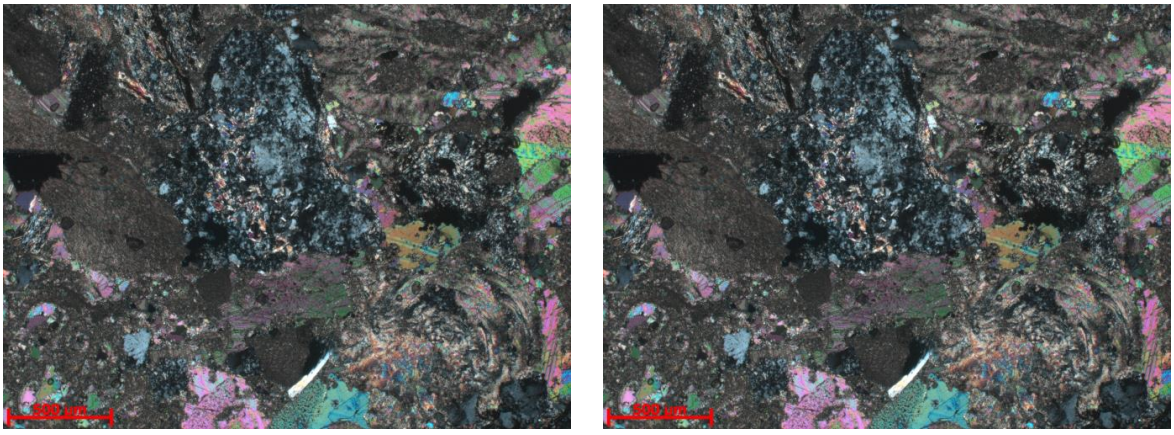

Figure 135. Polycrystalline quartz (Q) cluster with cracks and pores (blue) and xenomorphic calcite (Cc) grains and calcareous fossils (1N on the left, XN on the right)
(source: UoM)

$CO_2$ treated sample (CT 10/1):

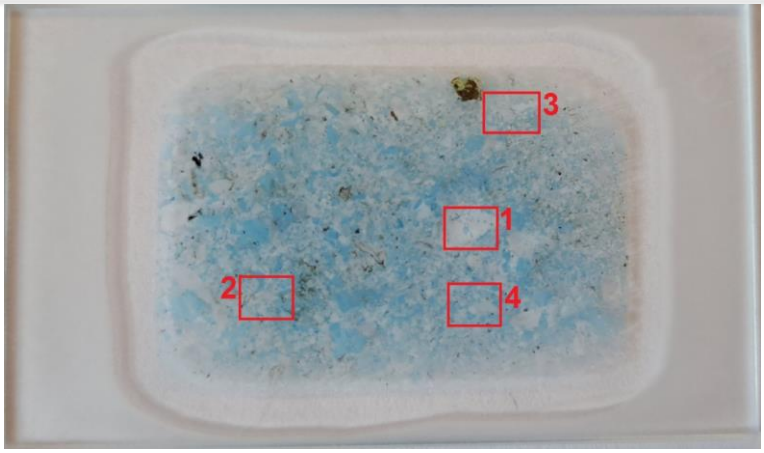


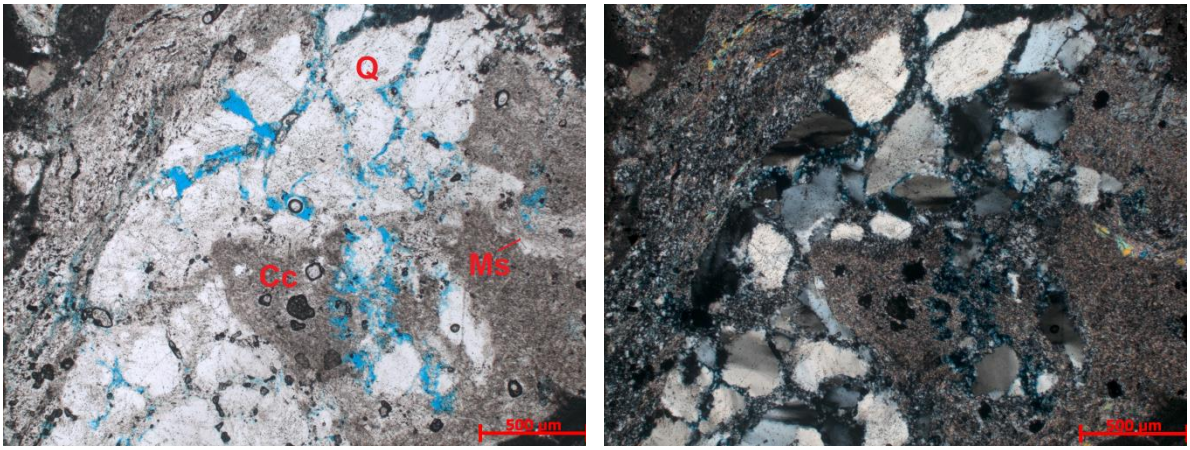


Figure 136. Quartz (Q) grains, muscovite (Ms) plates and calcite (Cc) with increased intergranular space (blue), 1N on the left, XN on the right
(source: UoM)

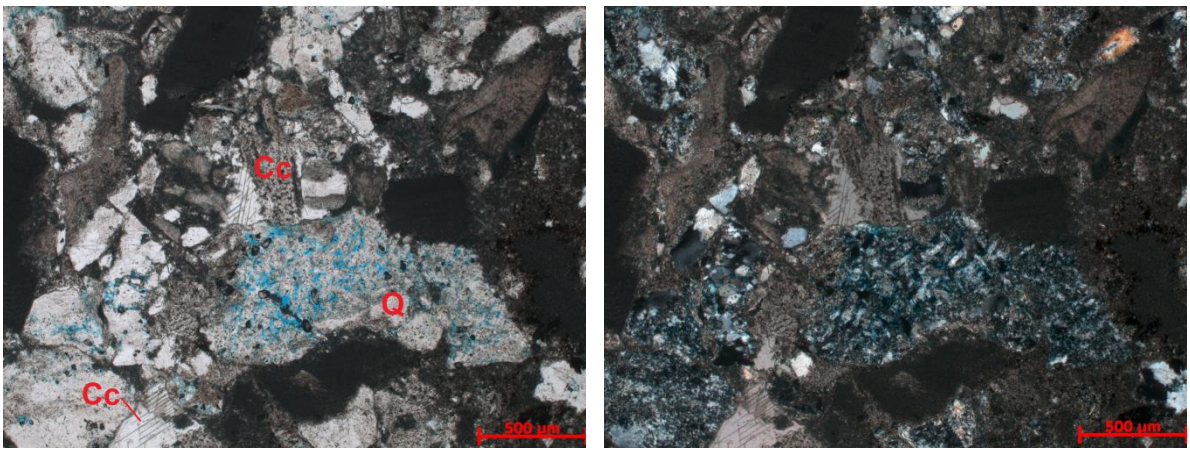


Figure 137. Polycrystalline quartz (Q) cluster with cracks and pores (blue) and xenomorphic calcite (Cc) grains and calcareous fossils (1N on the left, XN on the right)
(source: UoM)

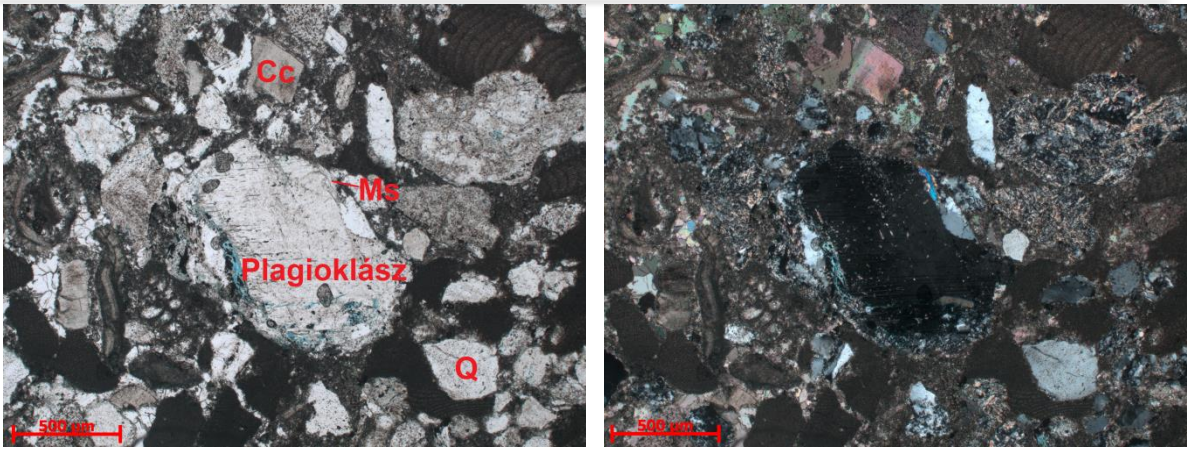


Figure 138. Polysynthetically twinned plagioclase, quartz (Q) grains, muscovite (Ms) plates, calcite (Cc) and calcareous fossils (1N on the left, XN on the right) (source: UoM)

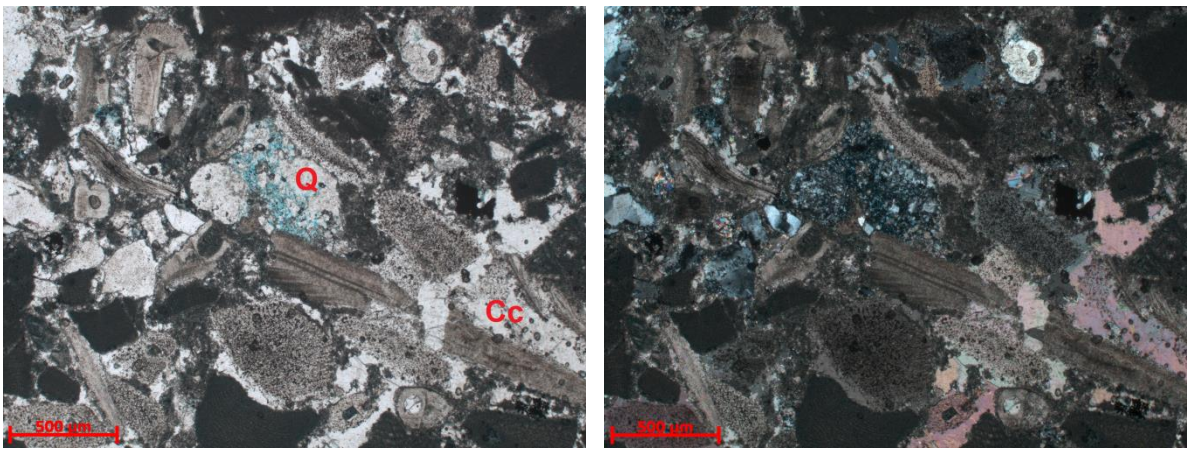


Figure 139. Polycrystalline quartz (Q) cluster with cracks and pores (blue) and xenomorphic calcite (Cc) grains and calcareous fossils (1N on the left, XN on the right) (source: UoM)

Untreated sample (CT 11/1):

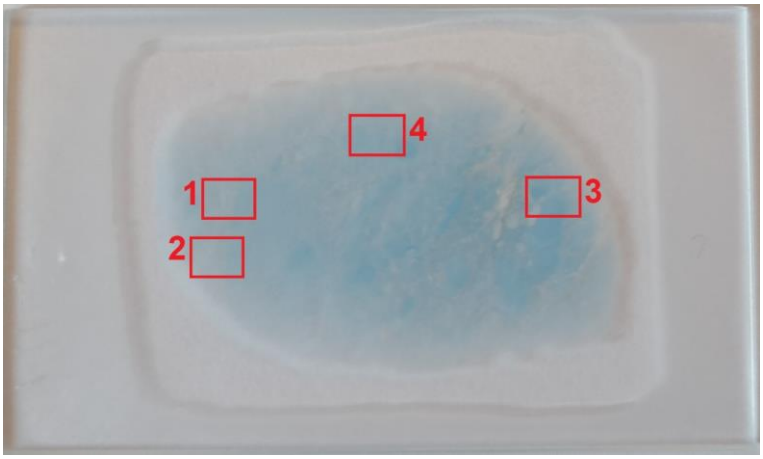


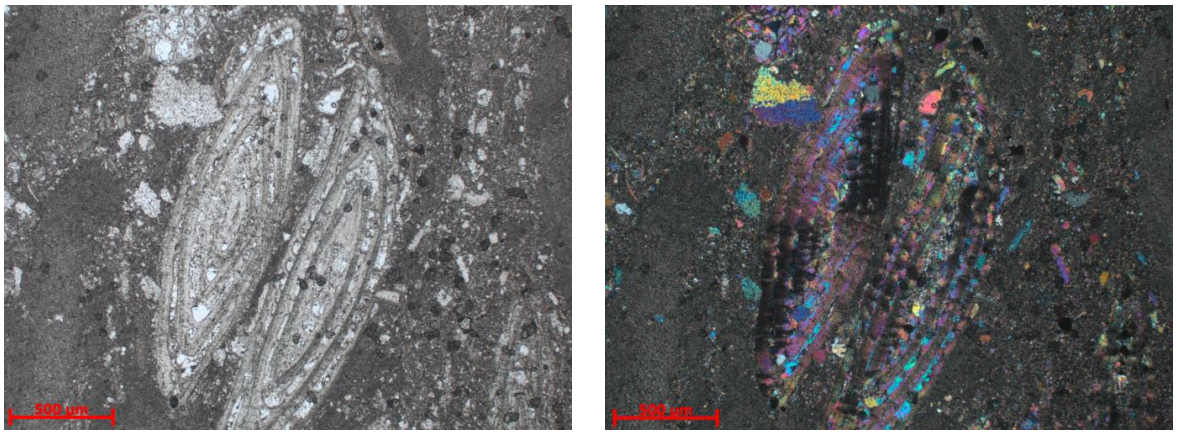

Figure 140. Calcareous fossils filled with calcite and xenomorphic calcite grains in the microcrystalline calcite matrix (1N on the left, XN on the right)
(source: UoM)

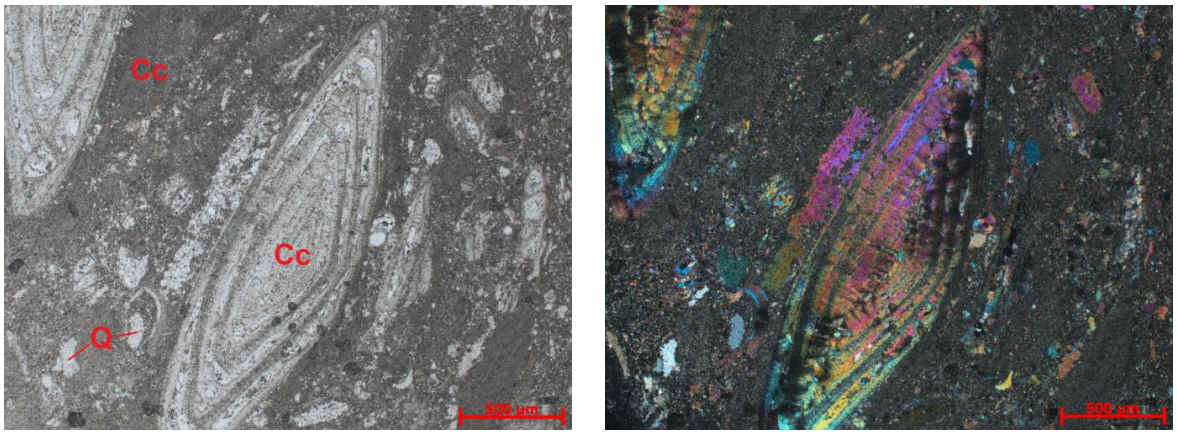


Figure 141. Calcareous fossils filled with calcite (Cc), xenomorphic calcite grains and some quartz (Q) grains in the microcrystalline calcitic matrix (1N on the left, XN on the right)
(source: UoM)

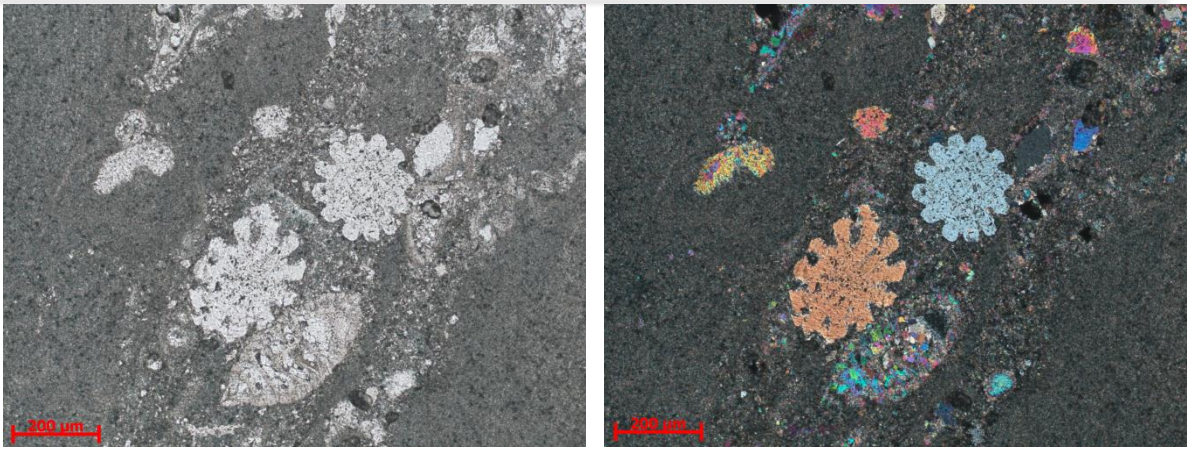

Figure 142. Calcareous fossils filled with calcite and xenomorphic calcite grains in the microcrystalline calcite matrix (1N on the left, XN on the right)
(source: UoM)

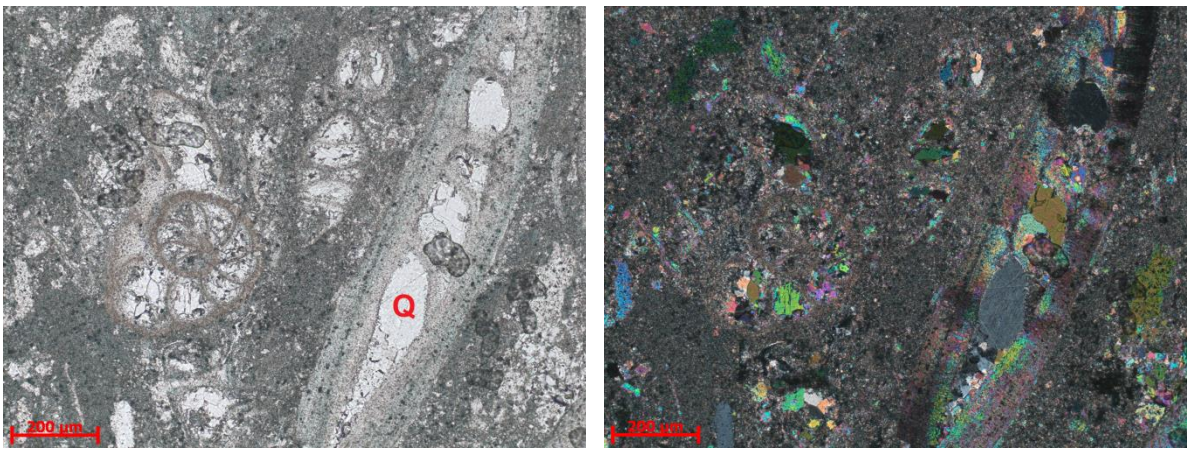


Figure 143. Limestone fossils filled with calcite and xenomorphic calcite grains in the microcrystalline calcite matrix. The fossil on the right is quartz (Q) inclusions (1N on the left, XN on the right)
(source: UoM)

$CO_2$ treated sample (CT 11/1):

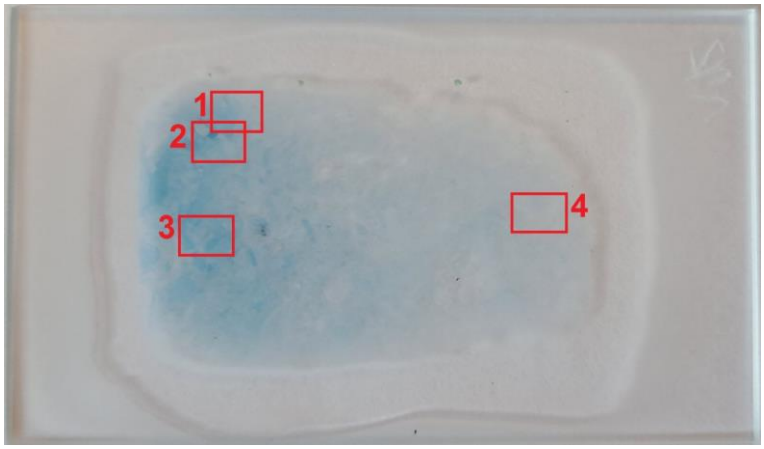


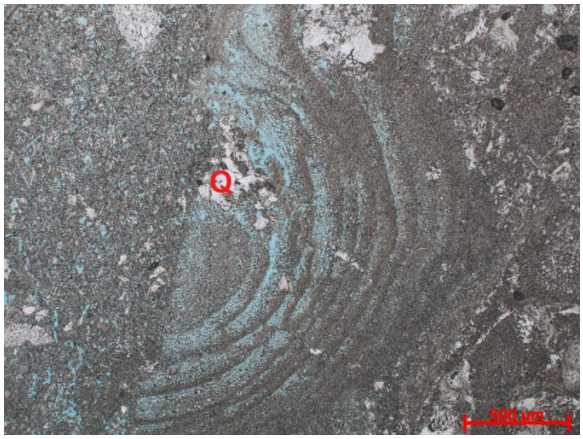


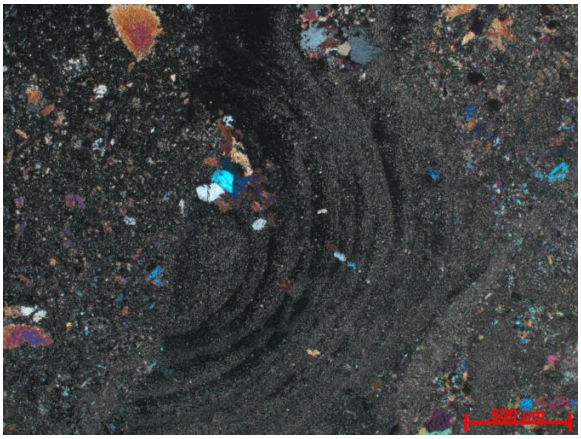

Figure 144. Limestone fossils filled with microcrystalline calcite and xenomorphic calcite and quartz (Q) grains in the microcrystalline calcite matrix. The increased pore space (blue) is clearly visible. 1N on the left, XN on the right
(source: UoM)

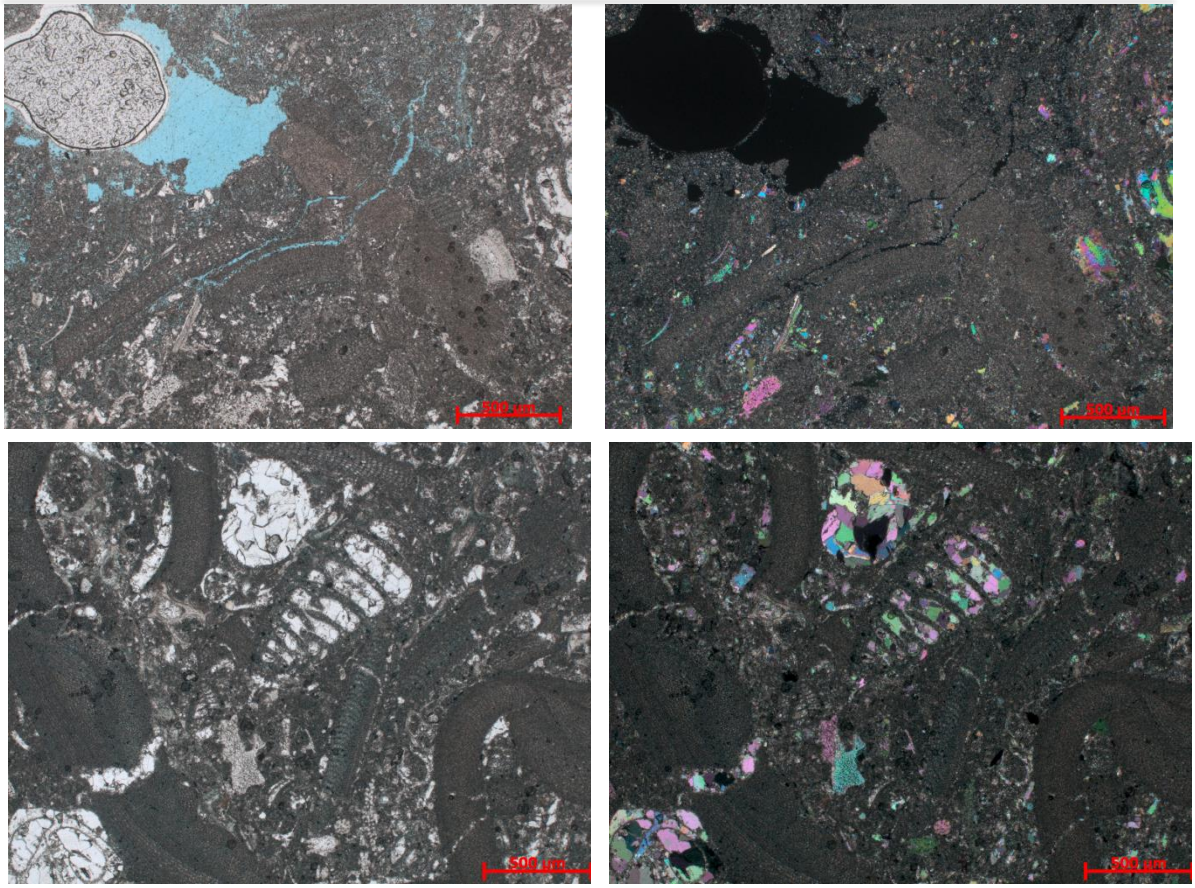

Figure 145. Limestone fossils filled with calcite and xenomorphic calcite grains in the microcrystalline calcite matrix. Left 1N, right XN
(source: UoM)

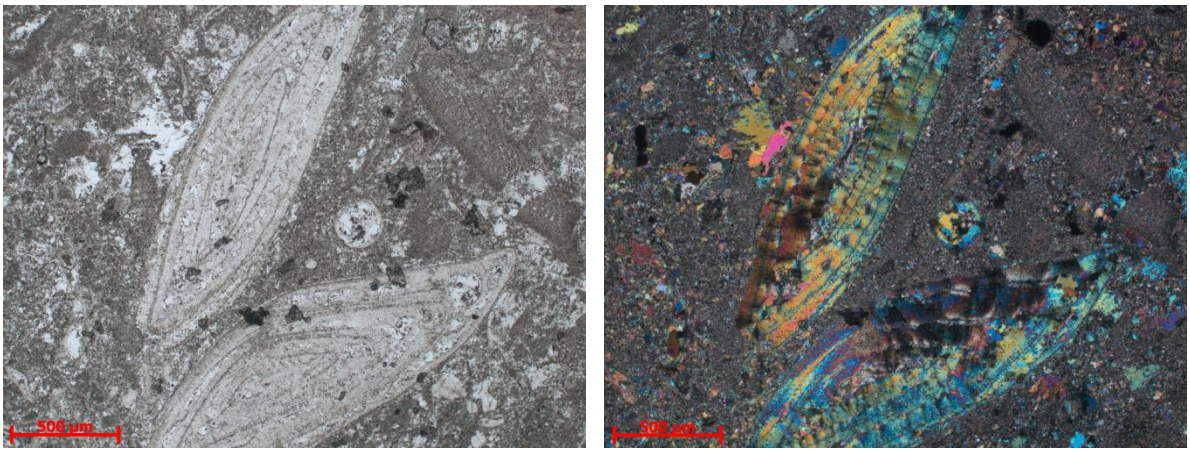

Figure 146. Limestone fossils filled with calcite and xenomorphic calcite grains in the microcrystalline calcite matrix. Left 1N, right XN
(source: UoM)

## 14.4 APPENDIX 4.

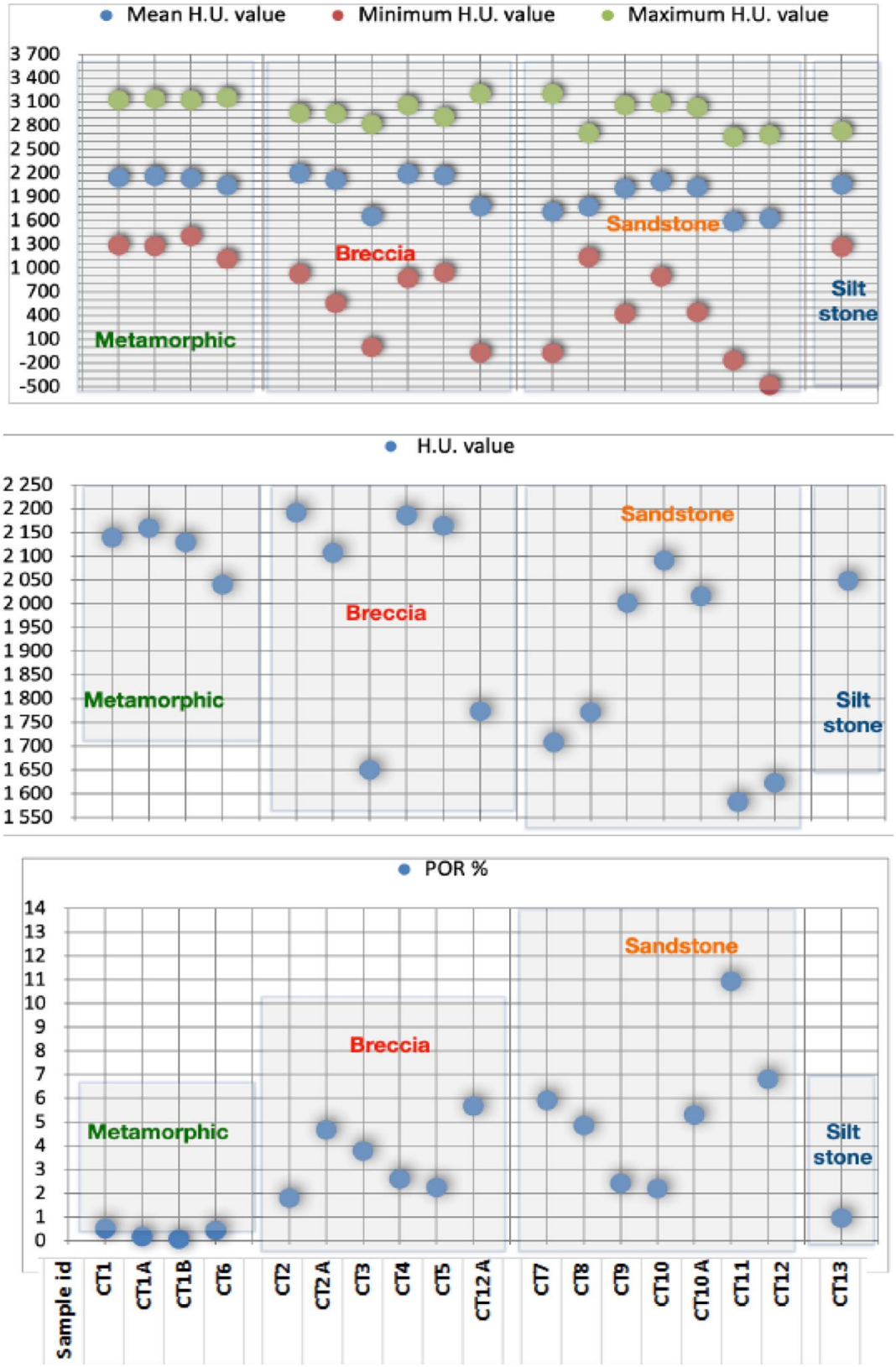


Figure 147. Visualization summary of the measured data.
(Edited by the author)

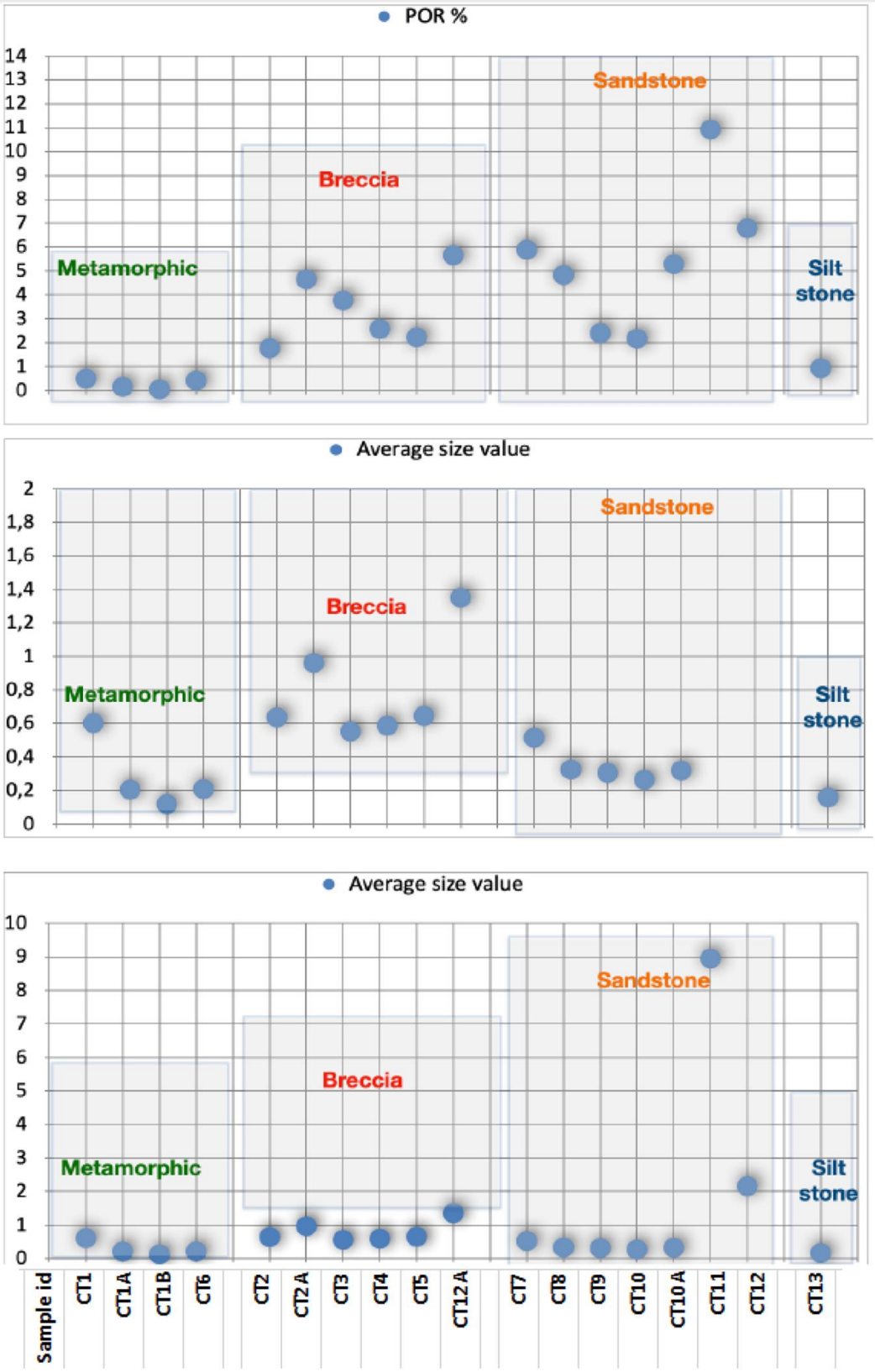


Figure 148. Visualization summary of the measured data – average porosity value per sample
(Edited by the author)

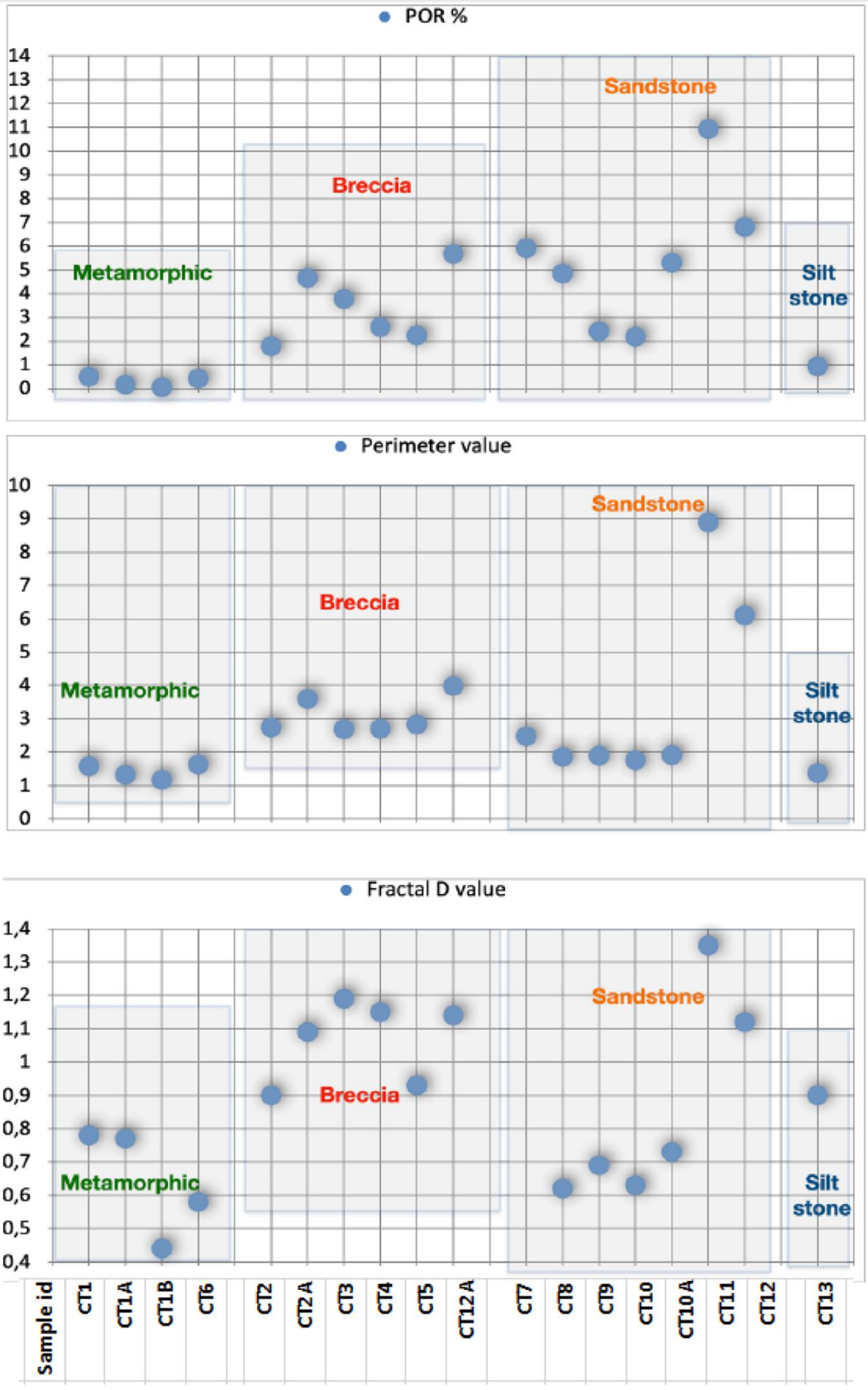


Figure 149. Visualization summary of the measured data
(Edited by the author)

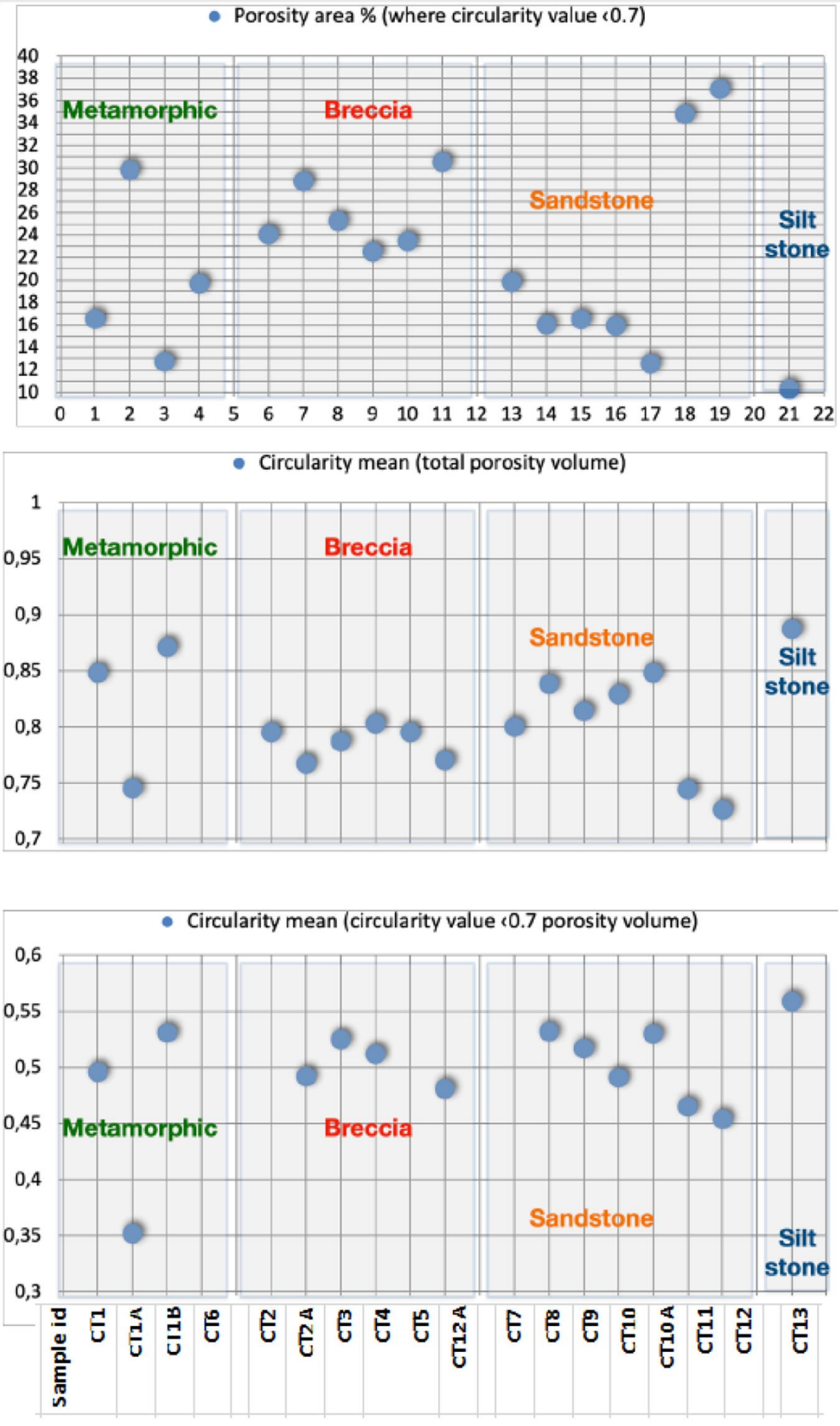


Figure 150. Visualization summary of the measured data
(Edited by the author)

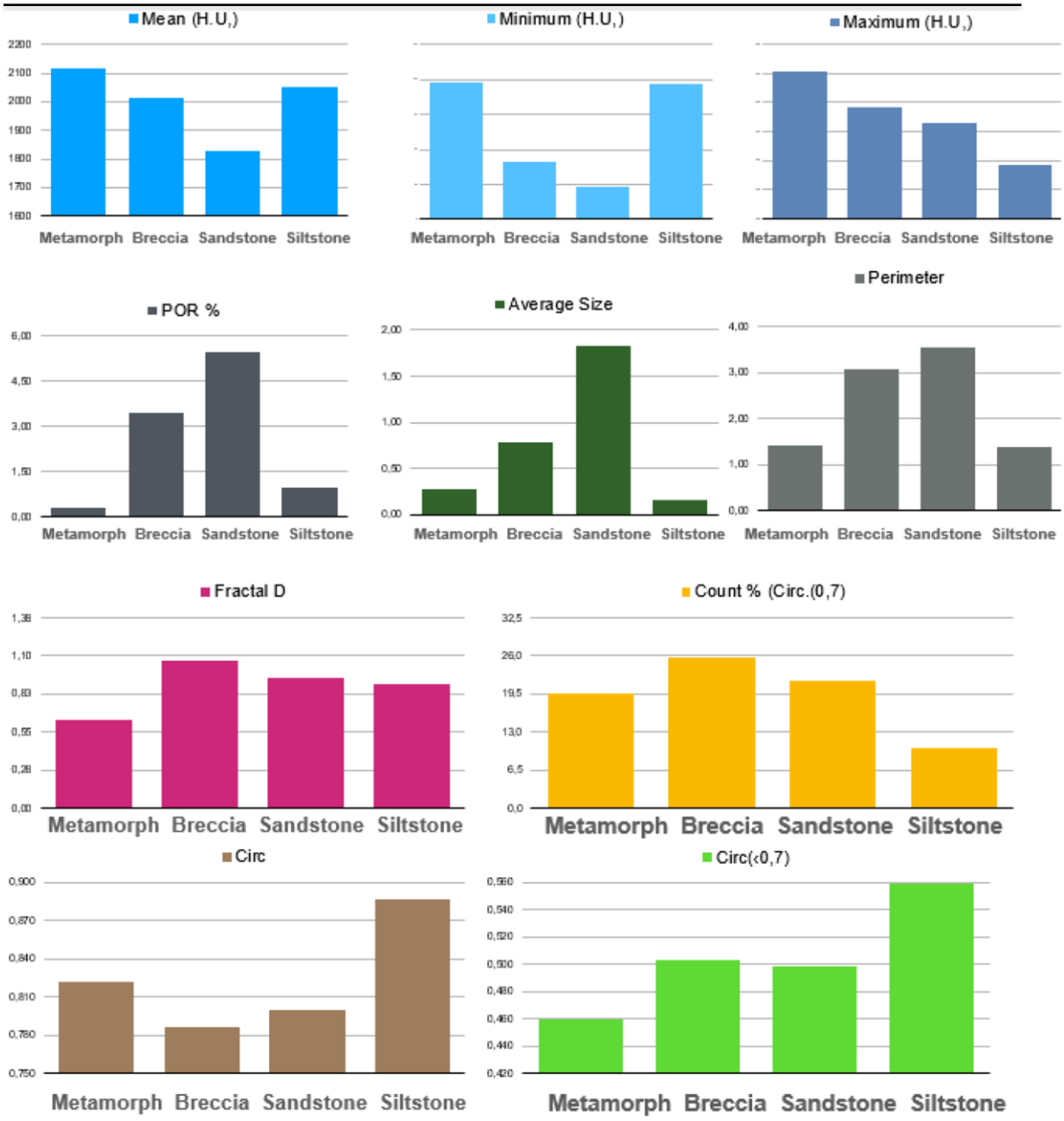


Figure 151. Comparison of average data of different rock types
(Edited by the author)

## 14.5 APPENDIX 5.

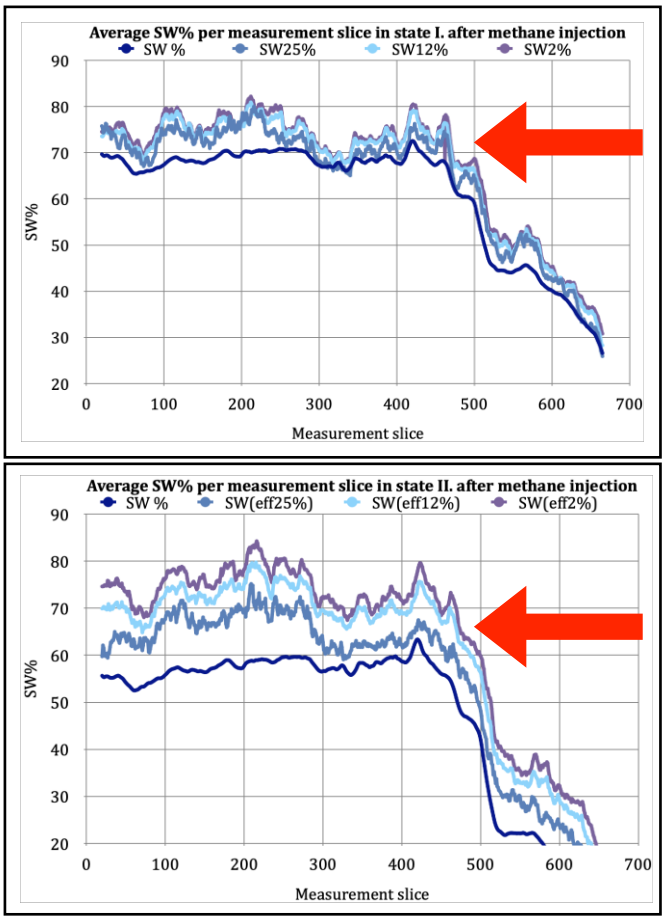


Figure 152. Average SW% per measurement slice in states I. and II. with different effective volumes after $CH_4$ injection
(Edited by the author, source TOMOGEO Ltd.)

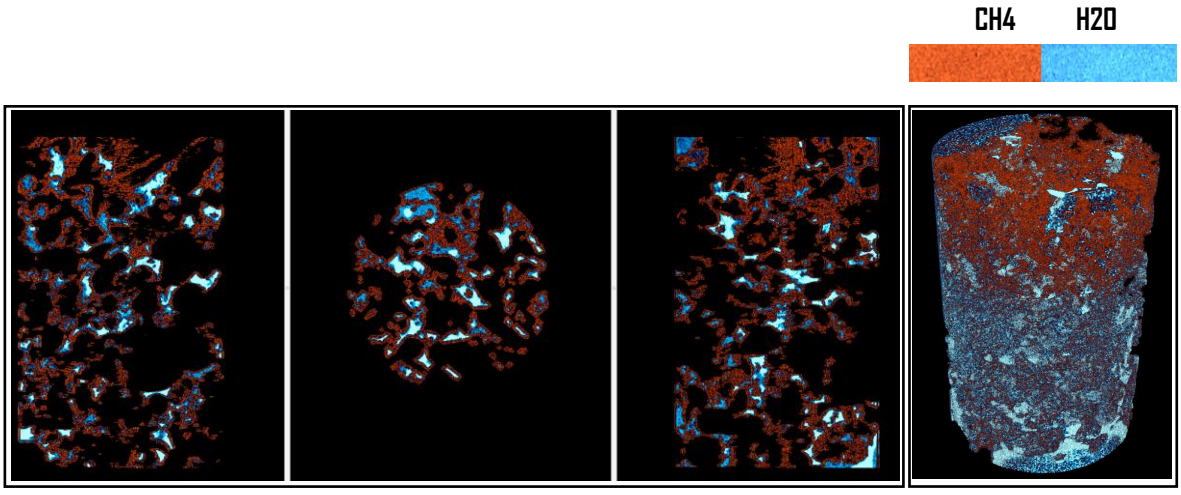


Figure 153. Visualization of fluid saturation in state II. after $CH_4$ injection. Total effective volume
(Edited by the author, source TOMOGEO Ltd.)

Table 27. Table of summarized mCT operation and measurement data

(Edited by the author, source TOMOGEO Ltd.)

Yellow mark: where T or P changes happen

| Operation | mCT measurement | Injection pressure (bar) | PWST (bar) | Temp. (°C) | $H_2O$ inj. volume ($cm^3$) | $CH_4$ inj. volume ($cm^3$) | $CO_2$ inj. volume ($cm^3$) | State |
|---|---|---|---|---|---|---|---|---|
| Calibration measurement | + | | | | | | | |
| Vacuum cleaning | | | | | | | | |
| 1) Dry core measurement | + | Closed | - | | | | | |
| 2) Dry core measurement | + | | | | | | | |
| Water injection | | 0 >5 | 0->10 | Room | +10 | | | |
| Wet core mCT measurement | + | 5 | 10 | Room | | | | |
| Pressure increase | | 5->90 | 10->100 | Room | +10 | | | |
| Core mCT measurement after pressure increase | + | 90 | 100 | Room | | | | |
| Pressure increase | | 90->200 | 100->207 | Room | | | | |
| Core mCT measurement after pressure increase | + | 200 | 207 | Room | | | | |
| Temperature increase | | 200 | 207 | Room -> 90°C | | | | |

| | | | | | | | | |
|---|---|---|---|---|---|---|---|---|
| Core mCT measurement after temperature increase | + | 200 | 207 | | | | | |
| 1) $CH_4$ inj. | | 200 | 207 | 90°C | | +10 | | |
| 1) Core mCT measurement after $CH_4$ inj. | + | 200 | 207 | 90°C | | | | $CH_4$ I. |
| 2) $CH_4$ inj. | | 200 | 207 | 90°C | | +10 | | |
| 2) Core mCT measurement after $CH_4$ inj. | + | 200 | 207 | 90°C | | | | $CH_4$ II. |
| Pressure reduction | | 200->30 | 207->30 | 90°C | | | | |
| Core mCT measurement after pressure reduction | + | 30 | 37 | 90°C | | | | |
| Pressure increase | | 30->100 | 30->107 | 90°C | | | | |
| Core mCT measurement after pressure increase | + | 100 | 107 | 90°C | | | | |
| 1) $CO_2$ inj. | | 100 | 107 | 90°C | | | +10 | |
| 1) Core mCT measurement after $CO_2$ inj. | + | 100 | 107 | 90°C | | | | $CO_2$ I. |
| 2) $CO_2$ inj. | | 100->200 | 107->207 | 90°C | | | | |
| 2) Core mCT measurement after $CO_2$ inj. | + | 200 | 207 | 90°C | | | | $CO_2$ II |

## 14.6 APPENDIX 6.

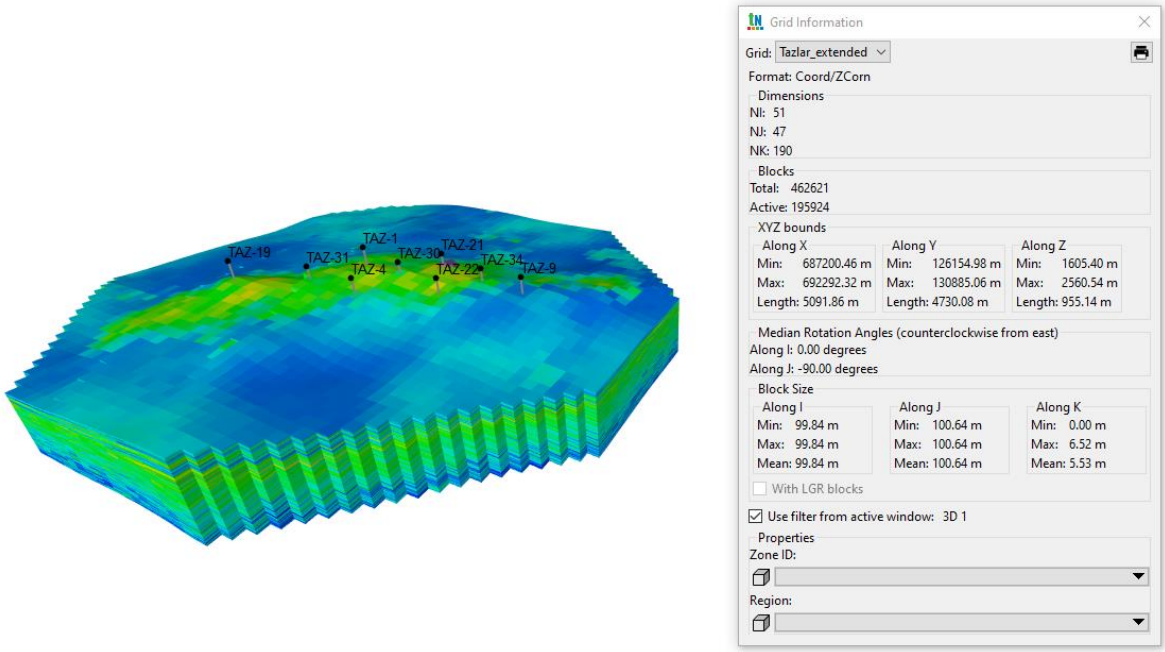


Figure 154. 3D Storage dimensions
(source: tNavigator ; Edited by the author)

# 14.7 APPENDIX 7.

### Táz-4 well

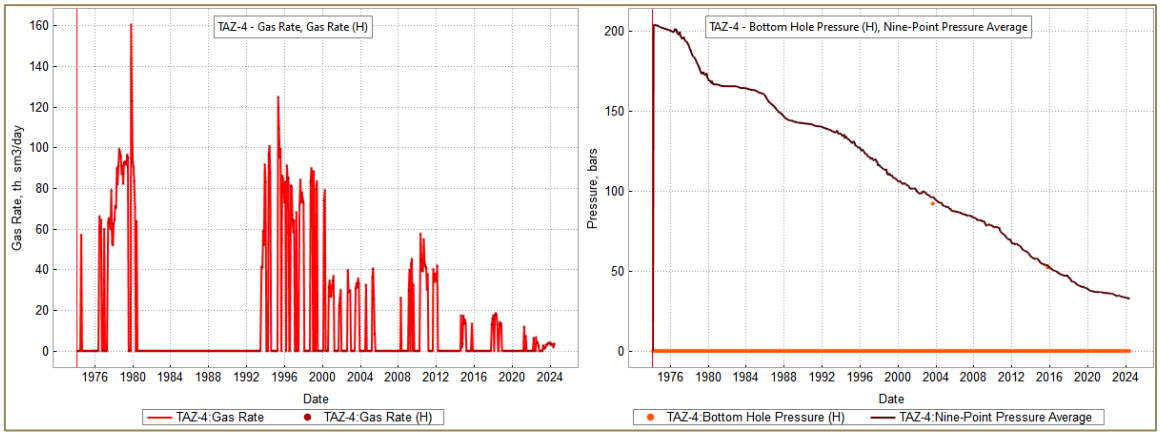


Figure 155. History matching of Táz-4 well
(source: tNavigator ; Edited by the author)

### Táz-9 well

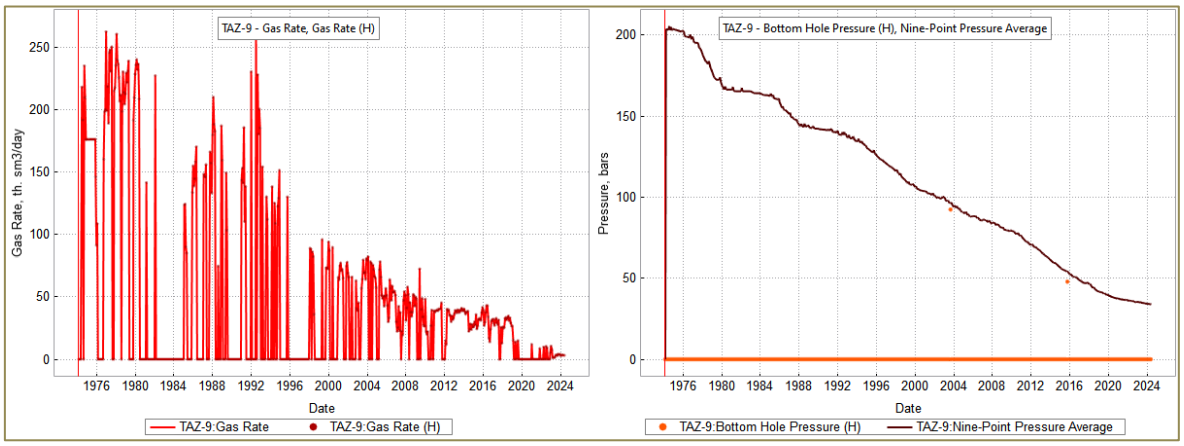


Figure 156. History matching of Táz-9 well
(source: tNavigator ; Edited by the author)

### Táz-30 well

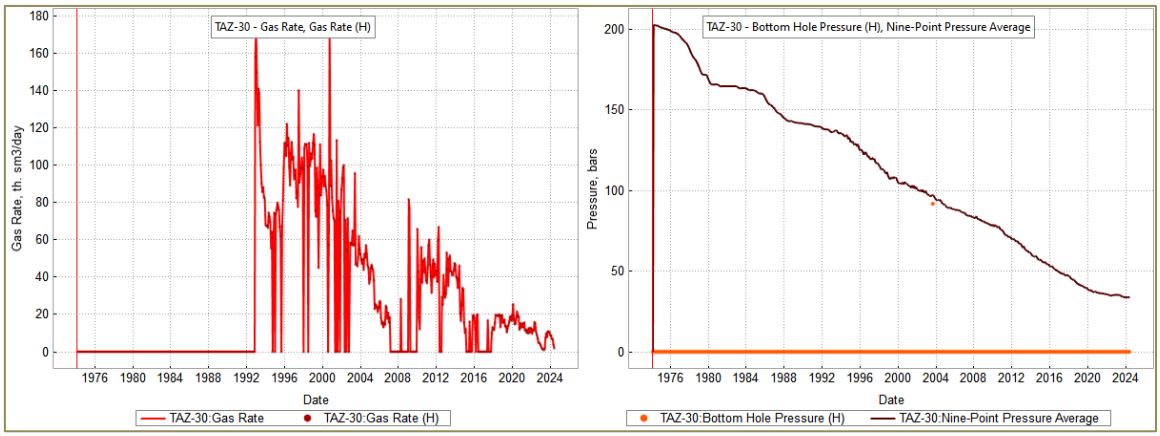


Figure 157. History matching of Táz-30 well
(source: tNavigator ; Edited by the author)

## Táz-31 well

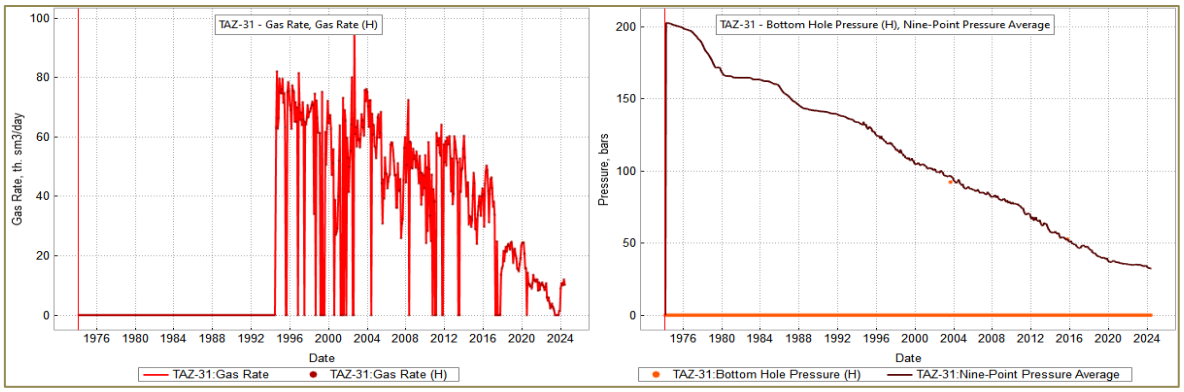


Figure 158. History matching of Táz-31 well
(source: tNavigator ; Edited by the author)

## Táz-34 well

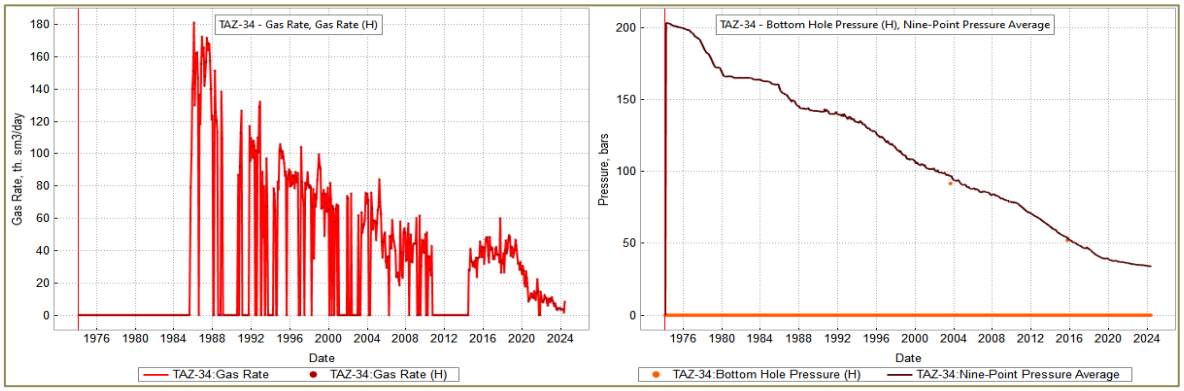


Figure 159. History matching of Táz-34 well
(source: tNavigator ; Edited by the author)

## 14.8 APPENDIX 8.

Table 28. Rock parameters
(source: Rutqvist, J. 2012)

| Rock Type | ρ (lb/ft³) [kg/m³] | Porosity % | E (ksi [GPa]) | Poisson's Ratio |
|---|---|---|---|---|
| Igneous | (138 - 187) [2210 - 3000] | 0.10 - 22.10 | (1450 - 14504) [10 - 100] | 0.10 - 0.40 |
| Granite | (158 - 164) [2530 - 2620] | 1.02 - 2.87 | (4351 - 10153) [30 - 70] | 0.17 |
| Diorite | (175 - 187) [2800 - 3000] | 0.10 - 0.50 | (4351 - 14504) [30 - 100] | 0.10 - 0.20 |
| Gabbro | (170 - 187) [2720 - 3000] | 0.20 - 3.57 | (5802 - 14504) [40 - 100] | 0.20 - 0.35 |
| Rhyolite | (150 - 162) [2400 - 2600] | 0.40 - 4.00 | (1450 - 7252) [10 - 50] | 0.20 - 0.40 |
| Andesite | (156 - 175) [2500 - 2800] | 0.20 - 8.00 | (1450 - 10153) [10 - 70] | 0.20 |
| Basalt | (138 - 173) [2210 - 2770] | 0.22 - 22.10 | (5802 - 11603) [40 - 80] | 0.10 - 0.20 |
| Sedimentary | (114 - 172) [1820 - 2760] | - | (725 - 13053) [5 - 90] | 0.10 - 0.30 |
| Conglomerate | (154 - 172) [2470 - 2760] | - | (1450 - 13053) [10 - 90] | 0.10 - 0.15 |
| Sandstone | (119 - 161) [1910 - 2580] | - | (2176 - 7252) [15 - 50] | 0.14 |
| Shale | (125 - 150) [2000 - 2400] | - | (725 - 4351) [5 - 30] | 0.10 |
| Mudstone | (114 - 170) [1820 - 2720] | - | (725 - 10153) [5 - 70] | 0.15 |
| Dolomite | (137 - 169) [2200 - 2700] | - | (4351 - 10153) [30 - 70] | 0.15 |
| Limestone | (167 - 170) [2670 - 2720] | - | (2901 - 10153) [20 - 70] | 0.30 |
| Metamorphic | (136 - 206) [2180 - 3300] | - | (725 - 13053) [5 - 90] | 0.15 - 0.30 |
| Gneiss | (163 - 195) [2610 - 3120] | 0.32 - 1.16 | (4351 - 11603) [30 - 80] | 0.24 |
| Schist | (162 - 178) [2600 - 2850] | 10.00 - 30.00 | (725 - 8702) [5 - 60] | 0.15 - 0.25 |
| Phyllite | (136 - 206) [2180 - 3300] | - | (1450 - 12328) [10 - 85] | 0.26 |
| Slate | (169 - 174) [2710 - 2780] | 1.84 - 3.64 | (2901 - 13053) [20 - 90] | 0.20 - 0.30 |
| Marble | (157 - 179) [2510 - 2860] | 0.65 - 0.81 | (4351 - 10153) [30 - 70] | 0.15 - 0.30 |
| Quartzite | (163 - 167) [2610 - 2670] | 0.40 - 5.90 | (7252 - 13053) [50 - 90] | 0.17 |

Table 29. Basic data of the wells in Tázlár

(Edited by the author, source MOL Plc.)

| Well Nr. | Surface X (EOV) | Surface Y (EOV) | Bottom X (EOV) | Bottom Y (EOV) | Elevation [m] | Depth (MD) | Miocene roof [MD m] | Miocene roof [tsza m] | Opalocene-Precambrian roof [MD m] | Opalocene-Precambrian roof [tsza m] | Year of Drilling |
|---|---|---|---|---|---|---|---|---|---|---|---|
| **Táz-1** | 689601.14 | 128544.88 | 689601.14 | 128544.89 | 128.39 | 1948.0 | 1825.0 | -1696.61 | 1893.0 | -1764.61 | 1966 |
| **Táz-2** | 690695.9 | 129510.83 | 690695.84 | 129510.84 | 127.24 | 2212.0 | 2072.5 | -1944.11 | 2174.0 | -2045.44 | 1967 |
| **Táz-3** | 689048.73 | 129354.17 | 689048.73 | 129354.18 | 128.46 | 2146.5 | 2030.0 | -1901.54 | 2097.5 | -1969.04 | 1967 |
| **Táz-4** | 690079.26 | 127909.68 | 690079.26 | 127909.69 | 125.50 | 1904.5 | 1794.0 | -1667.23 | 1871.5 | -1744.62 | 1967 |
| **Táz-5** | 688047.39 | 128674.96 | 688047.39 | 128674.97 | 127.00 | 2246.5 | 2094.0 | -1964.76 | 2182.0 | -2052.34 | 1967 |
| **Táz-6** | 688079.89 | 127181.64 | 688079.83 | 127181.76 | 125.00 | 2146.0 | 2031.0 | -1905.84 | 2077.0 | -1951.84 | 1968 |
| **Táz-7** | 690656.41 | 127178.33 | 690656.41 | 127178.34 | 124.00 | 2195.0 | 1982.0 | -1856.51 | 2172.0 | -2046.23 | 1967 |
| **Táz-8** | 688536.12 | 130098.62 | 688535.36 | 130098.55 | 127.19 | 2603.5 | 2112.0 | -1984.81 | 2599.0 | -2471.81 | 1967 |
| **Táz-9** | 691328.1 | 128647.49 | 691328.1 | 128647.5 | 128.00 | 2047.1 | 1796.5 | -1667.88 | 1817.0 | -1688.31 | 1968 |
| **Táz-10** | 688935.98 | 128775.68 | 688935.41 | 128776.11 | 127.50 | 2200.0 | 2013.0 | -1884.15 | 2072.0 | -1943.00 | 1968 |
| **Táz-11** | 691257.87 | 129244.28 | 691257.87 | 129244.29 | 128.50 | 2201.5 | 1906.0 | -1775.32 | 1927.5 | -1796.78 | 1968 |
| **Táz-12** | 690646.03 | 130072.69 | 690645.33 | 130072.61 | 128.69 | 2334.0 | 2126.0 | -1996.02 | 2331.5 | -2201.41 | 1969 |
| **Táz-13** | 689757.59 | 130286.65 | 689757.59 | 130286.66 | 126.43 | 2339.5 | 2142.0 | -2013.75 | 2306.0 | -2177.49 | 1968 |
| **Táz-14** | 689230.23 | 129594.92 | 689230.03 | 129594.91 | 127.00 | 2176.0 | 2025.0 | -1897.57 | 2131.0 | -2003.49 | 1969 |
| **Táz-15** | 688991.63 | 129066.52 | 688991.63 | 129066.53 | 129.00 | 2130.0 | 1997.0 | -1867.25 | 2031.0 | -1909.95 | 1969 |
| **Táz-16** | 689874.1 | 129330.49 | 689873.54 | 129330.36 | 127.50 | 2200.5 | 2021.0 | -1892.53 | 2120.0 | -1991.10 | 1969 |
| **Táz-17** | 691726.85 | 127993.63 | 691726.85 | 127993.64 | 128.50 | 2150.5 | 1994.5 | -1864.93 | 2120.0 | -1990.31 | 1970 |
| **Táz-18** | 689115.79 | 126817.63 | 689115.76 | 126818.04 | 123.00 | 2092.4 | 1957.0 | -1821.98 | 2081.0 | -1945.78 | 1970 |
| **Táz-19** | 688830.48 | 127796.52 | 688830.48 | 127796.53 | 122.50 | 1935.0 | 1826.0 | -1702.60 | 1900.5 | -1777.00 | 1971 |
| **Táz-20** | 688173.11 | 129562.03 | 688172.43 | 129562.01 | 130.00 | 2461.0 | 2116.5 | -1985.42 | 2433.0 | -2301.47 | 1971 |
| **Táz-21** | 690343.48 | 128731.63 | 690343.48 | 128731.64 | 127.00 | 2000.0 | 1786.5 | -1658.71 | 1803.0 | -1675.18 | 1973 |
| **Táz-22** | 690638.9 | 128274.67 | 690638.9 | 128274.68 | 126.50 | 2000.0 | 1797.5 | -1671.11 | 1833.0 | -1706.61 | 1973 |
| **Táz-23** | 688669.18 | 126984.25 | 688669.18 | 126984.26 | 124.00 | 2060.0 | 1942.0 | -1816.66 | 1970.0 | -1844.55 | 1974 |
| **Táz-24** | 689693.4 | 127445.01 | 689693.4 | 127445.02 | 124.00 | 2100.0 | 1823.0 | -1698.25 | 1843.0 | -1718.23 | 1975 |
| **Táz-25** | 689030.68 | 128356.45 | 689030.68 | 128356.46 | 124.00 | 2148.5 | 1961.5 | -1836.46 | 2009.5 | -1884.37 | 1975 |
| **Táz-26** | 692056.66 | 129057.27 | 692056.66 | 129057.28 | 128.00 | 2090.0 | 1929.0 | -1800.92 | 2003.0 | -1874.92 | 1975 |
| **Táz-27** | 688012.9 | 127670.64 | 688012.9 | 127670.65 | 125.50 | 2120.0 | 2047.5 | -1921.06 | 2083.5 | -1957.00 | 1978 |
| **Táz-28** | 688401.11 | 127226.22 | 688401.11 | 127226.23 | 125.00 | 2100.0 | 1965.5 | -1838.91 | 1972.0 | -1845.38 | 1978 |
| **Táz-29** | 688516.61 | 126725.61 | 688516.61 | 126725.62 | 125.50 | 2100.0 | 2019.0 | -1892.65 | 2040.0 | -1913.54 | 1978 |
| **Táz-30** | 690131.74 | 128378.2 | 690131.74 | 128378.21 | 128.50 | 2100.0 | 1740.0 | -1610.78 | 1745.5 | -1616.27 | 1979 |
| **Táz-31** | 689546.48 | 127986.22 | 689546.48 | 127986.23 | 127.50 | 2100.0 | 1751.0 | -1622.53 | 1758.0 | -1629.53 | 1979 |
| **Táz-32** | 688435.74 | 127625.6 | 688435.74 | 127625.61 | 126.50 | 2100.0 | 1959.0 | -1832.20 | 2022.0 | -1895.16 | 1979 |
| **Táz-33** | 688961.31 | 126992.77 | 688961.31 | 126992.78 | 125.50 | 2100.0 | 1939.5 | -1813.33 | 2000.0 | -1873.75 | 1979 |
| **Táz-34** | 690868.69 | 128631.96 | 690868.69 | 128631.97 | 130.00 | 2099.5 | - | - | 1777.0 | -1646.03 | 1980 |
| **Táz-35** | 690372.56 | 127912.49 | 690372.56 | 127912.5 | 128.00 | 2100.0 | 1882.0 | -1753.47 | 1974.5 | -1845.84 | 1980 |